

University of Bath



PHD

Mathematical and numerical modelling of peristaltic flow and absorption in the small intestine

Leger, Andre J. P.

Award date:
2005

Awarding institution:
University of Bath

[Link to publication](#)

General rights

Copyright and moral rights for the publications made accessible in the public portal are retained by the authors and/or other copyright owners and it is a condition of accessing publications that users recognise and abide by the legal requirements associated with these rights.

- Users may download and print one copy of any publication from the public portal for the purpose of private study or research.
- You may not further distribute the material or use it for any profit-making activity or commercial gain
- You may freely distribute the URL identifying the publication in the public portal ?

Take down policy

If you believe that this document breaches copyright please contact us providing details, and we will remove access to the work immediately and investigate your claim.

Download date: 22. May. 2019

Mathematical and Numerical Modelling of Peristaltic Flow and Absorption in the Small Intestine

submitted by

André J.P. Léger

for the degree of Doctor of Philosophy

of the

University of Bath


Department of Mathematical Sciences

July 2005

COPYRIGHT

Attention is drawn to the fact that copyright of this thesis rests with its author. This copy of the thesis has been supplied on the condition that anyone who consults it is understood to recognise that its copyright rests with its author and that no quotation from the thesis and no information derived from it may be published without the prior written consent of the author.

This thesis may be made available for consultation within the University Library and may be photocopied or lent to other libraries for the purposes of consultation.

Signature of Author 

André J.P. Léger

UMI Number: U601974

All rights reserved

INFORMATION TO ALL USERS

The quality of this reproduction is dependent upon the quality of the copy submitted.

In the unlikely event that the author did not send a complete manuscript and there are missing pages, these will be noted. Also, if material had to be removed, a note will indicate the deletion.



UMI U601974

Published by ProQuest LLC 2013. Copyright in the Dissertation held by the Author.
Microform Edition © ProQuest LLC.

All rights reserved. This work is protected against
unauthorized copying under Title 17, United States Code.



ProQuest LLC
789 East Eisenhower Parkway
P.O. Box 1346
Ann Arbor, MI 48106-1346

UNIVERSITY OF BATH
LIBRARY
35 26 OCT 2005
PhD.....

2005 OCT 26

Summary

The nature of flow and absorption in the small intestine is of particular interest and importance to Unilever in the emerging area of Health and Food. Unilever are interested in designing Optimal Systems for the delivery of nutrients and functionally active material to the gut lining. In doing so they must understand how substances flow in the intestine and how this flow affects the absorption of drugs. In this thesis we model mathematically the way fluid flows under the action of peristalsis and how the complex flow patterns lead to enhanced absorption of therapeutic solute in the intestine.

We mathematically model peristaltic flow of fluid flowing in a vibrating peristaltic axisymmetric domain. We derive an asymptotic expression for the peristaltic velocity profile from Stokes slow flow equations which we solve by a perturbation expansion in the small wave curvature. We elucidate the complex flow patterns of peristalsis; trapping (circulating flow) and reflux, through particle paths. We apply the peristaltic velocity, \mathbf{u} , to the 2D dispersion model

$$c_t + \mathbf{u} \cdot \nabla c = D \nabla^2 c,$$

for the motion of solute with concentration c in a peristaltic flow. Fundamental to the project is the appropriate modelling of drug absorption which we approximate by a suitable boundary condition. We model passive absorption at the epithelial wall in the intestine by

$$-D \mathbf{n} \cdot \nabla c = K_a c,$$

a diffusive flux condition for the solute at the boundary with permeability K_a . As a first step to understanding solute behaviour in a peristaltic domain, we consider the 1D asymptotic equation applied by Stoll et al. [73] for the mean concentration behaviour \bar{c} of a solute in a cylinder where the fluid flow is Poiseuille

$$\bar{c}_t + U_e \bar{c}_{xx} = D_e \bar{c}_x - K_e \bar{c}.$$

The coefficients U_e, D_e, K_e are related to the overall flow field. Stoll et al. had applied this 1D equation to the movement of solute in the intestine, however, we show the conditions for applying his asymptotic analysis are not met. We then numerically solve the peristaltic dispersion model, which is a moving boundary problem, by a moving rectangular domain transformation and applying finite differences. We solve the model concurrently with the Poiseuille dispersion model for the same parameters and compare the results. We show that more solute is absorbed in a peristaltic flow as a result of trapping and that peristalsis retards solute motion. This an efficient means for mixing slow diffusing therapeutics as solute travels backwards from one region of circulation to another.

Acknowledgements

I would like to begin by thanking my supervisors Alastair Spence and Chris Budd for their contribution to this Thesis. Over the past few years I have developed as an academic as a result of their help and advice. I have enjoyed their humour at our meetings and I thank them for their endless patience, especially with the writing of this thesis. The phrase ‘pretty plain you no verb’ will always bring a smile to my face.

I thank Alastair, who was also my personal tutor as an undergraduate, for his guidance over the many years. I am extremely grateful to him for the opportunity to work on this project and also for his encouragement and support over the past year as I lectured for the Department of Mathematical Sciences. I would like to thank Chris for his enthusiasm on this project, for introducing me to the European Study Groups with Industry and broadening my horizons. I am grateful to have had the opportunity to learn so much from him. I further thank Jonathan Evans for his willingness and much needed help throughout this project, whenever I was stuck he was there.

In addition, I thank Pawel Plucinski my Chemical Engineering Supervisor for his support, and my industrial advisers at Unilever; John Melrose, Stephen Moore, Guoping Lian and Michael Butler. I thank Unilever and the EPSRC for their financial support.

Furthermore, I would like to thank Mark, Darrel, Bob and Adam of Computer Support whose help, patience and friendship has kept this project running smoothly. Likewise, much thanks go to Dawn for her time and friendship. Thanks also to Keith and Jill and the rest of the Department of Mathematical Sciences.

I have thoroughly enjoyed my time at the University and much of that is thanks to my good friends, Andy, Mark, Dave, Aids and Stef. Thanks go to my officemates; Brad, Simone, Melina, Damien, Petra and Patrick for creating an enjoyable work environment.

Finally a big thank you for my family, especially my parents. They have provided the love and support throughout my education. I thank them for their sacrifices to do so. I would not have achieved this without them.

Contents

1	Introduction	1
1.1	Functional Foods and Unilever	1
1.2	The Thesis	3
1.2.1	Chapter 2: Background and Simple Models	4
1.2.2	Chapter 3: Modelling Peristaltic Flow	4
1.2.3	Chapter 4: Dispersion Models in Cylindrical Flow with Application to the Intestine	6
1.2.4	Chapter 5: The Peristaltic Dispersion Model	7
1.2.5	Chapter 6: Numerical Methods for the Fluid Flow and for the Dispersion Models	9
1.2.6	Brief Summary of New Work	10
2	Background and Simple Models	12
2.1	How is Food Digested?	12
2.2	The Small Intestine	13
2.3	Fluid Mechanics in the Intestine	14
2.4	Absorption Models for the Intestine	16
2.4.1	The Mass Balance Approach	16
2.4.2	The Compartmental and Transit Model	17
2.4.3	The Dispersion Models	19
2.5	Oral Drug Absorption	20
2.6	Advanced Simulation Software for Intestinal Absorption Models	22
2.6.1	Example 1: STELLA	22
2.6.2	Example 2: GASTROPLUS	23
2.7	Summary	24
3	Modelling Peristaltic Flow	25
3.1	Literature Review	26
3.2	Deriving Peristaltic Flow	28
3.2.1	Simulating Peristaltic Motion by a Moving Boundary	29
3.2.2	The Peristaltic Boundary Conditions for the Biharmonic Equations	30

3.2.3	Nondimensionalising the Biharmonic Problem	31
3.3	The Trivial Case ($\alpha = 0$): Deriving Poiseuille Flow	32
3.4	The Non-trivial case ($\alpha \neq 0$): Solving the Biharmonic Equations by a Perturbation Expansion	32
3.4.1	Determining the Limits of the Semi-Analytic Streamfunction	33
3.4.2	Determining The Semi-Analytic Peristaltic Velocities	36
3.5	Pumping and Copumping: A Consequence of Peristaltic Flow	36
3.5.1	Determining The Pressure Gradient	37
3.5.2	Relating the Fluid Flow Rates to the Pressure Gradient	38
3.5.3	The Intestine as a Pump	39
3.6	Describing Fluid Particle Motion	41
3.6.1	Peristaltic Phenomenon 1: Reflux	41
3.6.2	Peristaltic Phenomenon 2: Trapping	41
3.6.3	The Different Types of Peristaltic Flow	42
3.6.4	Understanding the Behaviour of the Semi-Analytic Streamfunction	43
3.6.5	High Flow Rate Behaviour of the Fluid Flow	47
3.6.6	Determining the Amount of Wave Frame Recirculation	50
3.6.7	Particle Paths	51
3.6.8	Evolution Of an Initial Condition of Passive Particles	53
3.6.9	A Measure of Peristaltic Induced Convective Dispersion	58
3.7	Summary	65
4	Dispersion Models in Cylindrical Flow with Application to the Intes- tine	66
4.1	Introduction to 1D Dispersion Models	68
4.1.1	Modelling Solute Transport	69
4.1.2	Modelling Absorption	69
4.1.3	Modelling Diffusion	70
4.2	Modelling Passive Absorption in the Intestine	71
4.3	Introduction to 2D Dispersion Models	72
4.3.1	Introducing Radial Diffusion	73
4.3.2	A Simple Solvable 2D Problem	74
4.4	Averaging the Concentration Behaviour for Poiseuille Flow	76
4.4.1	Taylor's Solute Dispersion for an Impermeable Membrane	78
4.4.2	Applying Taylor's 1D Averaged Equation to the Intestine In the Absence of Absorption	80
4.4.3	Solute Dispersion for a Permeable Membrane	82
4.4.4	Compensating for Long Time Behaviour: Deriving The Fictitious Initial Condition	88
4.4.5	Modelling Peristalsis by Enhanced Diffusion	91

4.5	Comparing the Numerical Solution of the Full 2D model with the Numerical Solution of the 1D Asymptotic Equation	92
4.5.1	Approximating the Numerically Obtained Mean Solute Concentration of the 2D Dispersion Model by a 1D Dispersion Equation	93
4.5.2	Comparing the Numerical Solutions of the Models	95
4.6	Summary	97
5	The Peristaltic Dispersion Model	100
5.1	Deriving the 2D Peristaltic Dispersion Model	102
5.1.1	Conditions for a Maintained Source at the Inlet	105
5.1.2	Comparing the Peristaltic Dispersion Model with the Poiseuille Dispersion Model	106
5.2	Solving the Peristaltic Dispersion Model	107
5.3	Results of the 2D Peristaltic Dispersion Model	110
5.3.1	Case A - Slow Flow	111
5.3.2	Case A - Fast Flow	117
5.3.3	Case B - Centreline Trapping	123
5.3.4	Case C - No Trapping	129
5.3.5	Case D - No Trapping, Reflux	135
5.3.6	Case E - Trapping and Reflux	141
5.4	Discussion of the Behaviour of Solute Motion under Peristaltic Flow with Application to the Intestine	147
5.5	Weak Peristaltic Forces: A Superimposed Oscillatory Profile in the Mean Solute Concentration	148
5.6	Comparing Peristaltic Dispersion with Poiseuille Flow with Enhanced Diffusion	149
5.6.1	Enhanced Absorption by Peristalsis	150
5.7	Summary	154
6	Numerical Methods for the Fluid Flow and for the Dispersion Models	156
6.1	Numerically Solving the 1D Dispersion Model	157
6.1.1	Discretising the 1D Dispersion Equation on a Uniform Mesh	158
6.1.2	Determining a Well-Posed Numerical Scheme	159
6.1.3	A Diffusion Transformation of the 1D Dispersion Equation	161
6.1.4	Refinement Techniques of 1D Partial Differential Equations	161
6.1.5	Formulation of a Moving Mesh Partial Differential Equation	162
6.1.6	The Choice of Monitor Function and Smoothing	164
6.1.7	A Comparison of the Different Numerical Schemes for the 1D Dispersion Equation	164
6.2	Numerically Solving The 2D Poiseuille Dispersion Model	167

6.2.1	Applying a 2D Finite Difference Scheme to the Poiseuille Dispersion Model	167
6.2.2	A 2D Moving Mesh Scheme	168
6.3	Numerically Solving the Peristaltic Dispersion Model	169
6.3.1	Discretising the 2D Model with Finite Difference Operators	171
6.3.2	Numerical Scheme Instability	172
6.4	Summary	173
7	Conclusions	174
7.1	Modelling Peristaltic Fluid Flow in the Intestine	175
7.2	Modelling Solute Behaviour in a Peristaltic Flow	175
7.3	Stoll's Approach to Modelling Solute in the Intestine	176
7.4	What Aspects of the Thesis are New?	177
7.4.1	Modelling Peristaltic Flow	177
7.4.2	Dispersion Models in Cylindrical Flow with Application to the Intestine	178
7.4.3	The Peristaltic Dispersion Model	179
7.5	Final Thoughts	179
7.6	Future Work	179
A	Future Work 1: Modelling A Peripheral Layer of Water	181
A.1	Previous Efforts to Model the Peripheral Layer	182
A.2	Rederiving the Biharmonic Equations for Fluid Flow with a Radially Varyation in Viscosity	183
A.3	Deriving Fluid Flow in the Presence of a Peripheral Layer	184
A.3.1	Modelling the Peripheral Layer by a Weak Variation in the Viscosity	185
A.3.2	An Example of the Effect of a Weak Drop in the Viscosity on The Effective Velocity	187
A.3.3	Modelling the Peripheral Layer by a Boundary Layer Function for the Viscosity	188
A.3.4	The Effects of Modelling a Peripheral Layer on the Concentration Profile from the 2D Dispersion Model	189
A.4	Relaxing the No-Slip Condition	191
A.5	Summary	193
B	Future Work 2: Modelling the Villi as a Porous Membrane	194
B.1	Modelling Fluid Flow in a Porous Medium	196
B.1.1	Darcy's Law	196
B.1.2	The Brinkmann Model	196
B.2	The Porous Dispersion Model	198
B.2.1	Deriving the Velocity Profile	198

B.2.2	Defining a Dispersion Model	199
B.2.3	Asymptotic Analysis	199
C	Modelling Peristaltic Flow	200
C.1	Boundary Conditions for the Biharmonic Equations	200
C.2	Reflux in the Pumping Range	201
C.3	Flow Rate/Pressure Drop versus Amplitude Ratio	203
D	Dispersion Models	204
D.1	Poiseuille Dispersion Asymptotic Coefficients	204
E	Numerical Methods	206
E.1	A Finite Difference Approach to Numerically Solving the Biharmonic Problem	206
E.1.1	Determining the Peristaltic Velocities from the Solution of the Biharmonic Problem in the Rectangular Domain	209
E.1.2	Determining the Pressure Gradients from the Tangential Vorticity Solution of the Biharmonic Problem in the Rectangular Frame	210
E.1.3	Determining the Fixed Frame Velocities by Linearly Interpolating the Numerically Solved Wave Frame Velocities of the Biharmonic Problem	211
E.2	How to Apply the Low Pass Filter to Remove Noise	214

List of Figures

1-1	The Compartmental & Transit Model	4
1-2	The Nondimensionalised Model for the Peristaltic Flow of Fluid with Streamfunction $\hat{\psi}$ and Tangential Vorticity $\hat{\phi}$	5
1-3	Evolution of an Initial Condition consisting of 10^6 passive particles which are dyed black at the centreline. The flow exhibits Trapping and Reflux ($\alpha = 0.5, \hat{\psi}_w = -0.4$). The frames correspond to $T = 0, 1, \dots, 4$ cycles of flow.	6
1-4	The Nondimensionalised Peristaltic Dispersion Model	8
1-5	An Example of a Solute Concentration Profile in a Peristaltic Flow with Centreline Trapping	8
1-6	An Example of a Solute Concentration Profile in a Poiseuille Flow	9
2-1	The Small Intestine (The Figure has been adapted from [73])	13
2-2	The Villi Structure (The Figure has been adapted from [73])	14
2-3	The Compartmental & Transit Model	17
3-1	One Wavelength of the Peristaltic Axisymmetric Deformable Tube	29
3-2	The Nondimensionalised Model for the Peristaltic Flow of Fluid with Streamfunction $\hat{\psi}$ and Tangential Vorticity $\hat{\phi}$	31
3-3	Contour Plots of $g(\hat{x}, \hat{r})$ a Measure of the Relative Size of $\hat{\psi}_{0,\hat{x},\hat{x}}$ to $\hat{\phi}_0$ for $\hat{\psi}_w = 0.2$	34
3-4	Contour Plots of $E_{\psi,2}$ a Measure of the Relative Size of $\epsilon^4 \hat{\psi}_{2,xx}$ to $\hat{\phi}_0 + \epsilon^2 \hat{\phi}_2$ for $\hat{\psi}_w = 0.2, \epsilon = 0.2$	35
3-5	A Graph of the Different Flow Regions and Behaviour for Arbitrary Flow Rate $\hat{\psi}_w$ and Amplitude Ratio α	42
3-6	Contour Plots of the Streamfunction for Cases A,B,C,D with amplitude of vibration $\alpha = 0.2$	43
3-7	Surface Plots of the Streamfunction for Cases A,B,C with amplitude of vibration $\alpha = 0.2$ to Illustrate Lemma 2	44
3-8	An Example Graph to Show Regions of Detached Streamline Trapping ($\alpha = 0.3, \hat{\psi}_w = 0$)	46

3-9	A Contour Plot of the Proportion of Volume of 1 Wavelength undergoing Recirculation as the Flow Rate and Amplitude of Vibration Varies. . . .	51
3-10	Evolution of 9 Particle Paths starting at Maximum and Minimum Points of Occlusion for 5 periods in Case B when $\alpha = 0.2$ and $\hat{\psi}_w = -0.2$	52
3-11	Evolution of 9 Particle Paths starting at Maximum and Minimum Points of Occlusion for 5 periods in Case D when $\alpha = 0.2$ and $\hat{\psi}_w = -0.5$	53
3-12	Evolution of 9 Particle Paths for 5 seconds in Cases A,C,E,F,G.	54
3-13	Evolution of an Initial Condition consisting of 10^6 passive particles for Case A: $\alpha = 0.2, \hat{\psi}_w = -0.1$. The frames correspond to $T = 0, 1, \dots, 4$ cycles of flow.	55
3-14	Evolution of an Initial Condition consisting of 10^6 passive particles for Case B: $\alpha = 0.2, \hat{\psi}_w = -0.2$. The frames correspond to $T = 0, 1, \dots, 4$ cycles of flow.	56
3-15	Evolution of an Initial Condition consisting of 10^6 passive particles for Case C: $\alpha = 0.2, \hat{\psi}_w = -0.4$. The frames correspond to $T = 0, 1, \dots, 4$ cycles of flow.	56
3-16	Evolution of an Initial Condition consisting of 10^6 passive particles for Case D: $\alpha = 0.2, \hat{\psi}_w = -0.5$. The frames correspond to $T = 0, 1, \dots, 4$ cycles of flow.	57
3-17	Evolution of an Initial Condition consisting of 10^6 passive particles for Case E: $\alpha = 0.5, \hat{\psi}_w = -0.4$. The frames correspond to $T = 0, 1, \dots, 4$ cycles of flow.	57
3-18	Measuring Dispersion and Radial Mixing from Particle Paths for all types of possible Peristaltic Flow Cases.	61
3-19	Measuring Dispersion and Radial Mixing from Particle Paths for Time Mean Flow Rate $Q/Q_0 = 0.5$	62
3-20	Measuring Dispersion and Radial Mixing from Particle Paths for Time Mean Flow Rate $Q/Q_0 = 1$	63
3-21	Measuring Dispersion and Radial Mixing from Particle Paths for Time Mean Flow Rate $Q/Q_0 = 1.5$	64
4-1	A 2D Plug Flow Dispersion Model in a Cylindrical Tube	73
4-2	A Solvable 2D Plug Flow Dispersion Model in a Cylindrical Tube	74
4-3	A Comparison of the Numerical Solution of the Mean Solute Concentration from the full 2D Poiseuille Dispersion Model (Blue) with the Numerical Solution of the Mean Solute Concentration from the 1D Taylor Dispersion equation (Red).	81
4-4	A Comparison of the Numerical Solution of the full 2D Poiseuille Dispersion Model with the Numerical Solution of the 1D Macrotransport Dispersion equation.	96

5-1	The Peristaltic Dispersion Model	104
5-2	A Graph of Flow Rate, $\hat{\psi}_w$, versus Amplitude of Vibration, α , indicating the Region of Purely Positive Horizontal Velocity	106
5-3	Mean Solute Concentration for the Peristaltic Dispersion Model and the Poiseuille Dispersion Model, and their 1D Dispersion Approximation with the the FFT of the Peristaltic Solution, for a Fast Diffusing Solute, $P_{er} = 100$, when $\alpha = 0.1$, $\hat{\psi}_w = 0$ and $D_{ar} = 1$	111
5-4	Mean Solute Concentration for the Peristaltic Dispersion Model and the Poiseuille Dispersion Model, and their 1D Dispersion Approximation with the the FFT of the Peristaltic Solution, for A Slow Diffusing Solute, $P_{er} = 1000$, when $\alpha = 0.1$, $\hat{\psi}_w = 0$ and $D_{ar} = 1$	111
5-5	Mass Absorbed for the Peristaltic and Poiseuille Dispersion Models for a Fast Diffusing Solute, $P_{er} = 100$, when $\alpha = 0.1$, $\hat{\psi}_w = 0$ and $P_{er} = 1000$, $D_{ar} = 1$	112
5-6	Mass Absorbed for the Peristaltic and Poiseuille Dispersion Models for a Slow Diffusing Solute, $P_{er} = 1000$, when $\alpha = 0.1$, $\hat{\psi}_w = 0$ and $P_{er} = 1000$, $D_{ar} = 1$	112
5-7	Peristaltic Contour Plots when $\hat{\psi}_w = 0$, $P_{er} = 100$, $\alpha = 0.1$, $D_{ar} = 1$. .	113
5-8	Poiseuille Contour Plots when $\hat{\psi}_w = 0$, $P_{er} = 100$, $\alpha = 0.1$, $D_{ar} = 1$. .	114
5-9	Peristaltic Contour Plots when $\hat{\psi}_w = 0$, $P_{er} = 1000$, $\alpha = 0.1$, $D_{ar} = 1$. .	115
5-10	Poiseuille Contour Plots when $\hat{\psi}_w = 0$, $P_{er} = 1000$, $\alpha = 0.1$, $D_{ar} = 1$. .	116
5-11	Mean Solute Concentration for the Peristaltic Dispersion Model and the Poiseuille Dispersion Model, and their 1D Dispersion Approximation with the the FFT of the Peristaltic Solution, for a Fast Diffusing Solute in Case A, $P_{er} = 100$, when $\alpha = 0.1$, $\hat{\psi}_w = 1$ and $D_{ar} = 1$	117
5-12	Mean Solute Concentration for the Peristaltic Dispersion Model and the Poiseuille Dispersion Model, and their 1D Dispersion Approximation with the the FFT of the Peristaltic Solution, for A Slow Diffusing Solute in Case A, $P_{er} = 1000$, when $\alpha = 0.1$, $\hat{\psi}_w = 1$ and $D_{ar} = 1$	117
5-13	Mass Absorbed for the Peristaltic and Poiseuille Dispersion Models for a Fast Diffusing Solute, $P_{er} = 100$, when $\alpha = 0.1$, $\hat{\psi}_w = 1$ and $P_{er} = 1000$, $D_{ar} = 1$	118
5-14	Mass Absorbed for the Peristaltic and Poiseuille Dispersion Models for a Slow Diffusing Solute, $P_{er} = 1000$, when $\alpha = 0.1$, $\hat{\psi}_w = 1$ and $P_{er} = 1000$, $D_{ar} = 1$	118
5-15	Peristaltic Contour Plots for Case A when $\hat{\psi}_w = 1$, $P_{er} = 100$, $\alpha = 0.1$, $D_{ar} = 1$	119
5-16	Poiseuille Contour Plots for Case A when $\hat{\psi}_w = 1$, $P_{er} = 100$, $\alpha = 0.1$, $D_{ar} = 1$	120

5-17	Peristaltic Contour Plots for Case A when $\hat{\psi}_w = 1$, $P_{er} = 1000$, $\alpha = 0.1$, $D_{ar} = 1$	121
5-18	Poiseuille Contour Plots for Case A when $\hat{\psi}_w = 1$, $P_{er} = 1000$, $\alpha = 0.1$, $D_{ar} = 1$	122
5-19	Mean Solute Concentration for the Peristaltic Dispersion Model and the Poiseuille Dispersion Model, and their 1D Dispersion Approximation with the the FFT of the Peristaltic Solution, for a Fast Diffusing Solute in Case B, $P_{er} = 100$, when $\alpha = 0.2$, $\hat{\psi}_w = -0.2$ and $D_{ar} = 1$	123
5-20	Mean Solute Concentration for the Peristaltic Dispersion Model and the Poiseuille Dispersion Model, and their 1D Dispersion Approximation with the the FFT of the Peristaltic Solution, for A Slow Diffusing Solute in Case B, $P_{er} = 1000$, when $\alpha = 0.2$, $\hat{\psi}_w = -0.2$ and $D_{ar} = 1$	123
5-21	Mass Absorbed for the Peristaltic and Poiseuille Dispersion Models for a Fast Diffusing Solute, $P_{er} = 100$, when $\alpha = 0.2$, $\hat{\psi}_w = -0.2$ and $P_{er} = 1000$, $D_{ar} = 1$	124
5-22	Mass Absorbed for the Peristaltic and Poiseuille Dispersion Models for a Slow Diffusing Solute, $P_{er} = 1000$, when $\alpha = 0.2$, $\hat{\psi}_w = -0.2$ and $P_{er} = 1000$, $D_{ar} = 1$	124
5-23	Peristaltic Contour Plots for Case B when $\hat{\psi}_w = -0.2$, $P_{er} = 100$, $\alpha =$ 0.2 , $D_{ar} = 1$	125
5-24	Poiseuille Contour Plots for Case B when $\hat{\psi}_w = -0.2$, $P_{er} = 100$, $\alpha = 0.2$, $D_{ar} = 1$	126
5-25	Peristaltic Contour Plots for Case B when $\hat{\psi}_w = -0.2$, $P_{er} = 1000$, $\alpha = 0.2$, $D_{ar} = 1$	127
5-26	Poiseuille Contour Plots for Case B when $\hat{\psi}_w = -0.2$, $P_{er} = 1000$, $\alpha = 0.2$, $D_{ar} = 1$	128
5-27	Mean Solute Concentration for the Peristaltic Dispersion Model and the Poiseuille Dispersion Model, and their 1D Dispersion Approximation with the the FFT of the Peristaltic Solution, for a Fast Diffusing Solute in Case C, $P_{er} = 100$, when $\alpha = 0.1$, $\hat{\psi}_w = -0.38$ and $D_{ar} = 1$	129
5-28	Mean Solute Concentration for the Peristaltic Dispersion Model and the Poiseuille Dispersion Model, and their 1D Dispersion Approximation with the the FFT of the Peristaltic Solution, for A Slow Diffusing Solute in Case C, $P_{er} = 1000$, when $\alpha = 0.1$, $\hat{\psi}_w = -0.38$ and $D_{ar} = 1$	129
5-29	Mass Absorbed for the Peristaltic and Poiseuille Dispersion Models for a Fast Diffusing Solute, $P_{er} = 100$, when $\alpha = 0.1$, $\hat{\psi}_w = -0.38$ and $P_{er} = 1000$, $D_{ar} = 1$	130
5-30	Mass Absorbed for the Peristaltic and Poiseuille Dispersion Models for a Slow Diffusing Solute, $P_{er} = 1000$, when $\alpha = 0.1$, $\hat{\psi}_w = -0.38$ and $P_{er} = 1000$, $D_{ar} = 1$	130

5-31	Peristaltic Contour Plots for Case C when $\hat{\psi}_w = -0.38$, $P_{er} = 100$, $\alpha = 0.1$, $D_{ar} = 1$	131
5-32	Poiseuille Contour Plots for Case C when $\hat{\psi}_w = -0.38$, $P_{er} = 100$, $\alpha = 0.1$, $D_{ar} = 1$	132
5-33	Peristaltic Contour Plots for Case C when $\hat{\psi}_w = -0.38$, $P_{er} = 1000$, $\alpha = 0.1$, $D_{ar} = 1$	133
5-34	Poiseuille Contour Plots for Case C when $\hat{\psi}_w = -0.38$, $P_{er} = 1000$, $\alpha = 0.1$, $D_{ar} = 1$	134
5-35	Mean Solute Concentration for the Peristaltic Dispersion Model and the Poiseuille Dispersion Model, and their 1D Dispersion Approximation with the the FFT of the Peristaltic Solution, for a Fast Diffusing Solute in Case D, $P_{er} = 100$, when $\alpha = 0.3$, $\hat{\psi}_w = -0.43$ and $D_{ar} = 1$	135
5-36	Mean Solute Concentration for the Peristaltic Dispersion Model and the Poiseuille Dispersion Model, and their 1D Dispersion Approximation with the the FFT of the Peristaltic Solution, for A Slow Diffusing Solute in Case D, $P_{er} = 1000$, when $\alpha = 0.3$, $\hat{\psi}_w = -0.43$ and $D_{ar} = 1$	135
5-37	Mass Absorbed for the Peristaltic and Poiseuille Dispersion Models for a Fast Diffusing Solute, $P_{er} = 100$, when $\alpha = 0.3$, $\hat{\psi}_w = -0.43$ and $P_{er} = 1000$, $D_{ar} = 1$	136
5-38	Mass Absorbed for the Peristaltic and Poiseuille Dispersion Models for a Slow Diffusing Solute, $P_{er} = 1000$, when $\alpha = 0.3$, $\hat{\psi}_w = -0.43$ and $P_{er} = 1000$, $D_{ar} = 1$	136
5-39	Peristaltic Contour Plots for Case D when $\hat{\psi}_w = -0.43$, $P_{er} = 100$, $\alpha = 0.3$, $D_{ar} = 1$	137
5-40	Poiseuille Contour Plots for Case D when $\hat{\psi}_w = -0.43$, $P_{er} = 100$, $\alpha = 0.3$, $D_{ar} = 1$	138
5-41	Peristaltic Contour Plots for Case D when $\hat{\psi}_w = -0.43$, $P_{er} = 1000$, $\alpha = 0.3$, $D_{ar} = 1$	139
5-42	Poiseuille Contour Plots for Case D when $\hat{\psi}_w = -0.43$, $P_{er} = 1000$, $\alpha = 0.3$, $D_{ar} = 1$	140
5-43	Mean Solute Concentration for the Peristaltic Dispersion Model and the Poiseuille Dispersion Model, and their 1D Dispersion Approximation with the the FFT of the Peristaltic Solution, for a Fast Diffusing Solute in Case E, $P_{er} = 100$, when $\alpha = 0.4$, $\hat{\psi}_w = -0.3$ and $D_{ar} = 1$	141
5-44	Mean Solute Concentration for the Peristaltic Dispersion Model and the Poiseuille Dispersion Model, and their 1D Dispersion Approximation with the the FFT of the Peristaltic Solution, for A Slow Diffusing Solute in Case E, $P_{er} = 1000$, when $\alpha = 0.4$, $\hat{\psi}_w = -0.3$ and $D_{ar} = 1$	141

5-45	Mass Absorbed for the Peristaltic and Poiseuille Dispersion Models for a Fast Diffusing Solute, $P_{er} = 100$, when $\alpha = 0.4$, $\hat{\psi}_w = -0.3$ and $P_{er} = 1000$, $D_{ar} = 1$	142
5-46	Mass Absorbed for the Peristaltic and Poiseuille Dispersion Models for a Slow Diffusing Solute, $P_{er} = 1000$, when $\alpha = 0.4$, $\hat{\psi}_w = -0.3$ and $P_{er} = 1000$, $D_{ar} = 1$	142
5-47	Peristaltic Contour Plots for Case E when $\hat{\psi}_w = -0.3$, $P_{er} = 100$, $\alpha = 0.4$, $D_{ar} = 1$	143
5-48	Poiseuille Contour Plots for Case E when $\hat{\psi}_w = -0.3$, $P_{er} = 100$, $\alpha = 0.4$, $D_{ar} = 1$	144
5-49	Peristaltic Contour Plots for Case E when $\hat{\psi}_w = -0.3$, $P_{er} = 1000$, $\alpha = 0.4$, $D_{ar} = 1$	145
5-50	Poiseuille Contour Plots for Case E when $\hat{\psi}_w = -0.3$, $P_{er} = 1000$, $\alpha = 0.4$, $D_{ar} = 1$	146
5-51	The Mean Solute Concentration for the Peristaltic Dispersion Model and the Poiseuille Dispersion Model with Enhanced Diffusion.	150
5-52	Solute Mean Concentration for the Peristaltic and Poiseuille Diffusion Model for a Radially Nonuniform Initial Condition.	151
5-53	Mass Absorbed for the Peristaltic and Poiseuille Diffusion Model for a Radially Nonuniform Initial Condition.	151
5-54	Peristaltic Contour Plots for Radially Non-Uniform Initial Condition for Case B when $\hat{\psi}_w = -0.2$, $P_{er} = 100$, $\alpha = 0.2$, $D_{ar} = 1$	152
5-55	Poiseuille Contour Plots for Radially Non-Uniform Initial Condition for Case B when $\hat{\psi}_w = -0.2$, $P_{er} = 100$, $\alpha = 0.2$, $D_{ar} = 1$	153
6-1	The Effects of an Inappropriate Inlet Boundary Condition in the Numerical Scheme on the Solute Concentration Profile at time $\check{t} = 10$ when $U_e = 1e - 2$, $D_e = 1e - 4$	160
6-2	The Peristaltic Dispersion Model	169
6-3	The Peristaltic Dispersion Model in the Rectangular Domain	171
6-4	The Mean Solute Concentration of the Peristaltic Dispersion Model when using different Finite Difference Operators on the Convection Term for an example of Peristaltic Flow with Negative Velocities present. Example: Case D after 4 periods when $\epsilon = 0.156$, $\alpha = 0.3$, $\hat{\psi}_w = -0.45$, $P_{eh} = 1000$, $D_{ar} = 1$	172
A-1	Velocity Profile for varying Orders of the Perturbation Expansion	187
A-2	The Effects of a Peripheral Layer Modelled by a Boundary Layer Function on the Fluid Flow Profile and Effective Velocity on (i) an equidistributed mesh and (ii) a uniform mesh.	190

A-3	The Effects of a Peripheral Layer on the 2D Dispersion Model	190
C-1	Flow Types for various Amplitude Ratio	203
D-1	A Comparison of Moffat's and Stoll's Absorption Coefficient α^*	204
D-2	Asymptotic Coefficients	205
E-1	The Peristaltic Biharmonic Problem in the Rectangular Computational Domain	207
E-2	A Model to Display How to Determine Wave Frame Peristaltic Velocities from the Streamfunction Solution of the Biharmonic Problem	209
E-3	A Model to Display How to Determine Pressure Gradients from the Tangential Vorticity Solution of the Biharmonic Problem	210

List of Notation

Symbol	Definition	Page
δ_0	Displacement	15
A	Local amplitude	15
ω	Angular frequency	15
α	Phase lag	15
J_w	Concentration wall flux	16
P_w	Membrane permeability	16
C_w	Drug concentration at wall	16
I_n	n^{th} Intestine compartment	18
Y_s	Percentage dose in stomach	17
K_s	Gastric emptying constant	17
Y_n	Percentage dose in compartment n	18
K_t	Transit rate constant	18
K_{an}	Absorption rate constant in compartment n	18
K_{dn}	Degradation rate constant in compartment n	18
Y_a	Percentage dose absorbed	18
Y_d	Percentage dose degraded	18
F_a	Fraction dose absorbed	18
c	Concentration in the intestine	19
α	Dispersion coefficient	19
u	Plug flow velocity	19
K	Absorption rate	19
S_{pH}	pH dependent Solubility	22
P	Drug permeability	22
A	Surface area	22
M	Mass flux absorbed	22
\mathbf{u}	Fluid velocity	28
ρ	Density	28
∇p	Pressure gradient	28
ν	Kinematic viscosity	28
μ	Viscosity	28
L_{-1}	Laplacian in polar coordinates	28
Re	Reynolds number	28
ω	Vorticity	28
ψ	Stokes stream function	29
ω	Stokes vorticity	29

Symbol	Definition	Page
u	Axial velocity	29
v	Transverse velocity	29
ϕ	Tangential velocity	29
f	Moving boundary	29
h	Average radius of nondisturbed cylinder	29
η	Wave amplitude	29
σ	Wave speed	29
λ	Wavelength	29
t	Time	29
x	Fixed frame axial coordinate	29
r	Fixed frame axial coordinate	30
L_x	Length of domain	30
-	Wave Frame variables	30
	$(u, v, f, r, x, p, L, \psi, \omega, \phi) \mapsto (\bar{u}, \bar{v}, \bar{f}, \bar{r}, \bar{x}, \bar{p}, \bar{L}, \bar{\psi}, \bar{\omega}, \bar{\phi})$	
q	Wave frame flow rate	31
$\bar{\psi}_w$	Boundary flow rate condition	31
$\hat{\psi}_w$	Dimensionless boundary condition flow rate	31
α	Amplitude of vibration	31
ϵ	Wave number	31
$\hat{\cdot}$	Dimensionless wave frame variable	31
	$(\bar{u}, \bar{v}, \bar{f}, \bar{r}, \bar{x}, \bar{p}, \bar{\psi}, \bar{\omega}, \bar{\phi}) \mapsto (\hat{u}, \hat{v}, \hat{f}, \hat{r}, \hat{x}, \hat{p}, \hat{\psi}, \hat{\omega}, \hat{\phi})$	
ψ_{wp}	Poiseuille flow rate	32
U_0	Poiseuille flow centreline velocity	32
\bar{V}	Mean velocity	32
$E_{\psi,0}$	Approximate error measurement of $\hat{\psi}$ to leading order	34
$E_{\psi,2}$	Approximate error measurement of $\hat{\psi}$ to $O(\epsilon^2)$	35
\hat{U}	Wave frame centreline velocity for Poiseuille flow	36
$\nabla \hat{p}_\lambda$	Wavelength pressure change	37
$\hat{\psi}_{w0}$	Zero pumping flow rate	38
$\nabla \hat{p}_0$	Zero flow rate pressure gradient	38
Q	Instantaneous volume flow rate	38
\bar{Q}	Time mean volume flow rate	38
\hat{Q}	Dimensionless time mean volume flow rate	38
\hat{Q}_0	Zero pressure drop time mean volume flow rate	38
\bar{x}	Mean axial position of particles	58
σ_x^2	Variance of particles axial position	58
D	Instantaneous dispersion coefficient	58
K	Cycle dispersion coefficient	58

Symbol	Definition	Page
q	Radial position of particle in rectangular domain	59
\bar{q}	Mean radial position of particles in rectangular domain	59
σ_q^2	Variance of particles radial position	59
s	Skewness of particles radial position	59
c	Solute concentration	69
J	Solute flux	69
u	Plug flow speed	69
ϕ	Initial Solute Concentration Profile	69
K	Absorption coefficient	69
\tilde{x}	Dimensionless axial coordinate (fixed frame)	69
\hat{t}	Dimensionless Time	69
\bar{D}_a	Axial Damköhler number	69
M_0	Initial mass present	70
$M(t)$	Mass present at time t	70
$M_A(t)$	Mass absorbed up to time t	70
P_e	Axial Péclet number	71
D	Diffusion coefficient	70
J^D	Diffusive solute flux	70
D_{ar}	Radial Damköhler number	72
R_0	Radial length of cylinder	73
\tilde{r}	Dimensionless radial coordinate (fixed frame)	74
ℓ	Relative length of cylinder	74
P_{er}	Radial Péclet number	74
J_0	Bessel function of zeroth order	75
J_1	Bessel function of first order	75
β_n	Transcendental number	75
\bar{c}	Cross-sectional average solute concentration	76
τ	Asymptotic time condition	79
U_e	Effective velocity	80
D_m	Effective dispersion contribution from molecular diffusion	80
D_c	Effective dispersion contribution from convective dispersion	80
d	Asymptotic distance condition	80
\hat{c}	Fourier transform of solute concentration	82
F_n	Eigenfunction	83
p_n	Eigenvalue	83
Φ	Normalisation condition	85
K_e	Effective absorption coefficient	85
α^*	Effective absorption factor	85

Symbol	Definition	Page
γ^*	Effective velocity factor	85
$M(D_{ar})$	Contribution factor from convective dispersion	85
B	Field equation	86
Ω	Effective dispersion factor	87
A	Fictitious function	88
\bar{A}^*	Fictitious initial condition	88
P_0^∞	Local moment	88
u	Taylor vortex-like axial velocity	91
v	Taylor vortex-like axial velocity	91
A	Time dependent field strength	91
d_i	Length of rectangular unit cell in x_i direction	91
Γ	Field strength	91
d^*	Circular diameter	91
D_m	Molecular diffusion	91
D_{en}	Enhanced diffusion	91
K_h	Numerically obtained effective absorption coefficient	93
U_h	Numerically obtained effective velocity coefficient	93
D_h	Numerically obtained effective dispersion coefficient	93
\hat{c}	Laplace transform of the solute concentration	93
w	Diffusion transformation of the solute concentration	94
F	Least squares minimised function	94
M_Γ	Laplace transform of the solute concentration	95
\sim	Dimensionless fixed frame variable	103
	$(\hat{u}, \hat{v}, \hat{f}, \hat{r}, \hat{x}, \hat{t}) \mapsto (\tilde{u}, \tilde{v}, \tilde{f}, \tilde{r}, \tilde{x}, \tilde{t})$	103
P_{eh}	Radial Péclet number in peristaltic domain	103
Δ_{-x}	Upwinding finite difference operator in x direction	158
Δ_{+x}	Downwinding finite difference operator in x direction	158
Δ_{0x}	Central difference finite difference operator in x direction	158
δ_{0x}^2	Second order central difference finite difference operator	158
$\delta\tilde{x}$	Spatial step in \tilde{x} direction	158
\mathbf{c}	Discrete solute concentration vector from method of lines	158
A	Sparse matrix from method of lines	158
α	Diffusion transformation term 1	161
β	Diffusion transformation term 2	161
M	Monitor function	162
I	Functional from deriving an adaptive mesh	163
τ	MMPDE smoothing parameter	163
ξ	Computational coordinate mapped from physical coordinate \tilde{x} .	163

Symbol	Definition	Page
E	Equidistribution term from finite difference	164
c^*	Analytical solution of 1D dispersion model	164
m_{err}	Mass conservation error	165
L_2	L2 error	165
M_{aerr}	Mass absorbed error	165
χ	Fixed frame rectangular domain transformation: $\tilde{x} \mapsto \chi$	169
κ	Fixed frame rectangular domain transformation: $\tilde{r} \mapsto \kappa$	169
τ	Fixed frame Rectangular domain transformation: $\tilde{t} \mapsto \tau$	169
a_i, b_i	Fixed frame domain transformation tensors	170
ν	Rate of exponential decay in viscosity term	183
J_3	Bessel function of order 3	186
J_4	Bessel function of order 4	186
μ_c	Viscosity of peripheral layer at membrane	185
δ	Slip velocity	189
S_a	Surface area of intestine	194
μ_c	Apparent viscosity	197
u^f	Free fluid velocity	198
u^p	Porous seepage velocity	198
γ	Slip coefficient	198
k	Permeability	198
v	Solute concentration in the villi	199
$\hat{\chi}$	Wave frame rectangular domain transformation: $\hat{x} \mapsto \hat{\chi}$	206
$\hat{\kappa}$	Wave frame rectangular domain transformation: $\hat{r} \mapsto \hat{\kappa}$	206
$g_{\hat{\kappa}}$	Domain transformation tensor	207
$g_{\hat{\kappa}\hat{\kappa}}$	Domain transformation tensor	207
$g_{\hat{\chi},\hat{\kappa}}$	Domain transformation tensor	207
$\delta\hat{\chi}$	Spatial step in $\hat{\chi}$ direction	207
$\delta\hat{\kappa}$	Spatial step in $\hat{\kappa}$ direction	207
A, B, D, I	Discretised biharmonic equations in matrix form	209
$\Delta\chi$	Spatial step in χ direction	211
$\Delta\kappa$	Spatial step in κ direction	211
\mathbf{f}	Fast Fourier transform of solute concentration	214
\mathbf{g}	Noise reduction vector	214
h	Reduced noise Fourier transform of solute concentration	214

Chapter 1

Introduction

The nature of flow and absorption in the small intestine is of particular interest and importance to Unilever in the emerging area of Health and Food. Unilever are interested in designing Optimal Systems for the delivery of nutrients and functionally active material to the gut lining, such as the optimal particle size for delivery and the development of more readily digestible foods. In this introduction we discuss how the boom in the functional foods market has motivated Unilever to support the work of this thesis. We briefly discuss Chapter by Chapter the structure of the thesis and present a summary of the new work.

1.1 Functional Foods and Unilever

With the mapping of the human genome to the strains and challenges associated with increased life expectancy, media coverage on issues of health has been fervent as advances have been made in the last decade. Consequently, the increasingly aware public are taking a greater look at their health and the potential benefits afforded to them. This is highlighted by public surveys showing they view diet as more important in attaining better health than exercise [26].

Hectic lifestyles and longer working hours have left the public precipitous in following dietary guidelines and differentiating between various diets and foodstuffs. Fad diets and confusion have left consumers seeking nutritional support to prevent and fend off chronic diseases associated with ageing. Nutrition has had to adapt to the new challenges of a changing society. As a result, pharmaceuticals (Novartis) to food and food ingredient companies (Unilever) have recognised the potential of the new market, given the current advances and understanding of nutrient properties. Intense research into identifying and implementing food ingredients with the potential for health benefits has begun, resulting in the booming ‘Neutraceuticals and Functional Foods’ market, the fastest growing sector of our food industry [26].

Neutraceuticals and Functional foods, or alternatively by other named phrases

pharmaconutrients and dietary integrators, are substances that are a food¹ or form foods² providing health and medical benefits beyond that of common nutrition. The rising pharmacological applications of certain nutrients affecting the human body at a cellular level is blurring the thin line between nutraceuticals and drugs³. Recent examples of simple functional foods appearing lately in supermarkets and commercials are calcium enriched water and orange juice, but most noticeably is the headlining 'cholesterol reducing margarine' Benecol, which acts more as a drug than as a supplement by preventing the absorption of cholesterol into the blood.

However, an exploding market will appeal to irresponsible companies whose products fail to live up to their claims. Hence, manufacturers must authenticate any health claim with scientific evidence and prove that functional foods are safe for consumption. Unilever is interested in designing delivery systems for their own functional foods, e.g. Slim Fast, to contain added health benefit. One current aim is to prevent absorption of sugars in the Gastro-Intestinal (GI) tract to reduce the onset of Diabetes Type II. To do this requires a better understanding of fluid dynamics in the small intestine and to then factor in the fluid flow properties in the optimal design of their product.

Case Study Questions

Consequently Unilever have posed the following questions that this thesis will help answer.

- How do substances flow in the small intestine?
- Can we model this flow mathematically?
- How does the fluid flow in the small intestine affect solute motion and consequently its absorption?
- Were Stoll et al. [73] correct in assuming a 1D asymptotic dispersion equation to describe the motion and absorption of solute in the intestine? If not what is a more suitable model?

This PhD is the first part in a series of connected projects aimed at understanding the small intestine at Unilever. Projects currently in place are concerned with (i) physically modelling the intestine in a lab, (ii) modelling absorption rates of solute flow in a cylinder to develop a suitable boundary condition for passive absorption and (iii) developing optimal transport systems for Unilever products.

¹Food example: Oats, whose health benefits have recently been uncovered

²Food Ingredient examples: Polyunsaturated fatty acids (omega-3 and omega-6) and antioxidants

³Definition: A drug is a pharmacologically active substance that will potentiate, antagonize or otherwise modify any physiological or metabolic function

Food and The Intestine

Upon ingestion foodstuff becomes emulsified from chewing and rolled into a bolus which is squeezed down the oesophagus by a muscle contraction into the stomach. From here the food is mixed with gastric juices and passes from the stomach to the small intestine by contractions of the lower end of the stomach. It is here in the small intestine that foodstuffs are absorbed at the membrane. On average the small intestine is 3m in length [73] and has many bends as it is wrapped around for efficient storage in the body. Hence fluid flowing in the intestine must traverse round bends. It does so by complex intestinal contractions that send waves down the intestine. The principle wave for transporting digested food is *peristalsis*, a longitudinal contraction (see §2.3). However, across the length of the small intestine there exists a pressure gradient between the opening and outlet. This change in pressure combined with peristalsis determines the nature of the fluid flow.

1.2 The Thesis

We answer Unilever's questions in this thesis by mathematically modelling peristaltic flow to determine the complex flow patterns: trapping and reflux, which we illustrate through particle paths (Chapter 3). We apply the peristaltic velocity \mathbf{u} to the 2D dispersion model

$$c_t + \mathbf{u} \cdot \nabla c = D \nabla^2 c,$$

for the motion of solute with concentration c in a peristaltic flow. Fundamental to the project is the appropriate modelling of drug absorption which we do through a suitable boundary condition. We model passive absorption at the epithelial wall in the intestine by

$$-D \mathbf{n} \cdot \nabla c = K_a c,$$

a diffusive flux condition for the solute at the boundary with permeability K_a . As a first step to understanding solute behaviour in a peristaltic domain we derive the averaged solute concentration behaviour \bar{c} in a cylinder where the fluid flow is Poiseuille (Chapter 4). Stoll et al. [73] applied this method to modelling the mean concentration of a solute in the intestine. We show that the conditions to apply the asymptotic analysis to derive the 1D equation for \bar{c} are not appropriate given the anatomical parameters of the intestine. We then numerically solve the peristaltic dispersion model with the Poiseuille dispersion model for the same parameters and compare the results (Chapter 5). We show more solute is absorbed in a peristaltic flow from trapping and that peristalsis retards solute motion. This is an efficient means for mixing slow diffusing therapeutics as solute travels backwards from one region of circulation to another.

1.2.1 Chapter 2: Background and Simple Models

In Chapter 2 we begin the thesis with background knowledge of the intestine. First we describe the physical make up of the intestine and in particular describe intestinal motility, the random motions occurring in the intestine propelling food along it. We also discuss previous intestinal absorption models. There are two types, 1) the compartmental models which form a system of odes and 2) dispersion models which are governed by pdes. Case 1, favoured by pharmacologists, represent the intestine by a series of compartments, each with their own properties.

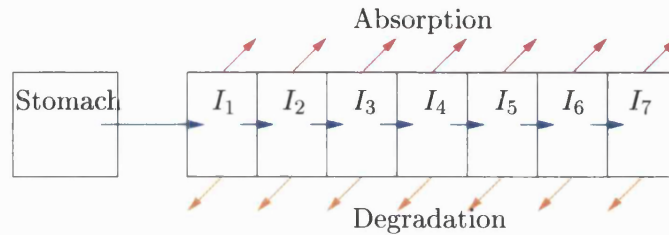


Figure 1-1: The Compartmental & Transit Model

This model is very simple and parameters are fitted to determine the compartment absorption and degradation rates. This model forms the basis of GASTROPLUS, an advanced simulation software package to model drug absorption by following the concentration of the therapeutic through a system of compartments involving a series of compartments for the intestine, the intestinal wall and the blood stream. Such a model cannot describe in a continuous sense the distribution of solute concentration in the intestine. Hence chemical engineers have favoured the 1D dispersion models for the drug's concentration (Ho et al. [28]). However, in time this has evolved to a 1D asymptotic equation for the mean solute concentration of a 2D Poiseuille dispersion model [73].

1.2.2 Chapter 3: Modelling Peristaltic Flow

To understand how substances flow in the intestine we discuss previous efforts to model flow in the intestine by peristalsis. We then model mathematically peristaltic flow to derive the peristaltic velocities. We do this by modelling a viscous inhomogeneous fluid flow in a tube that is moving under the action of standing peristaltic waves induced by a vibrating boundary with location

$$\tilde{r} = f(\tilde{x}, \tilde{t}) = 1 + \alpha \cos(2\pi(\tilde{x} - \tilde{t})).$$

We apply Lubrication Theory to simplify the Navier-Stokes equations to obtain the biharmonic equations for the fluid streamfunction ψ and tangential vorticity ϕ in a frame moving with the speed of the wave $(\hat{x}, \hat{r}) = (\tilde{x} - \tilde{t}, \tilde{r})$.

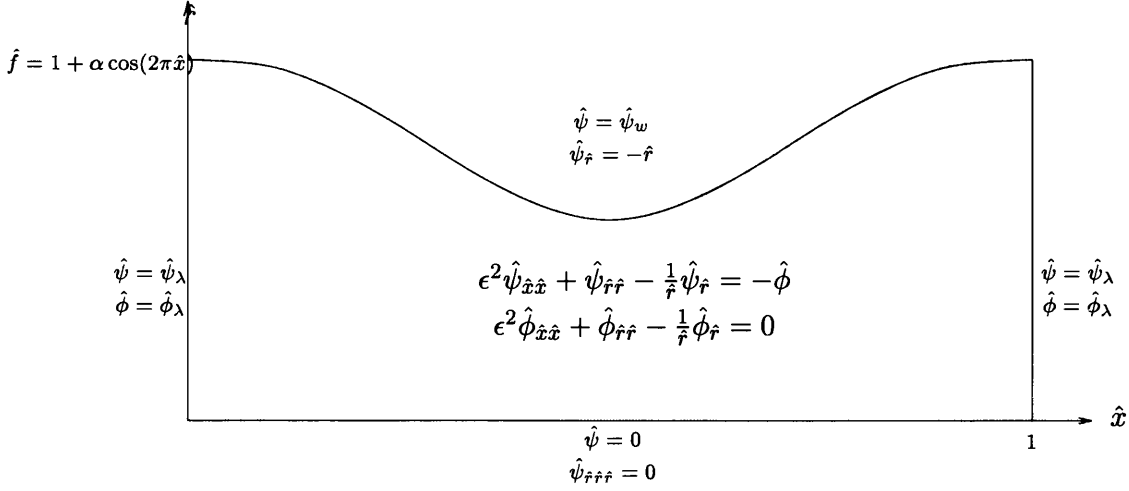


Figure 1-2: The Nondimensionalised Model for the Peristaltic Flow of Fluid with Streamfunction $\hat{\psi}$ and Tangential Vorticity $\hat{\phi}$

We solve the streamfunction model in Figure 1-2 by a perturbation expansion for the small wave number⁴ ϵ as a function of the flow rate $\hat{\psi}_w$. We determine the peristaltic velocities up to order $O(\epsilon^4)$ and show that they simplify to Poiseuille flow in the absence of vibration, $\alpha = 0$. For the leading order solution when $\alpha \neq 0$, we determine the existence of 5 types of peristaltic flow that depend on the amplitude of vibration α and the flow rate $\hat{\psi}_w$. The different flows elucidate two important features of peristaltic flow (i) *trapping* where fluid particles circulate in the wave frame and (ii) *reflux* where the net motion of the particles close to the boundary after one period is retrograde. We illustrate these fluid motions by plotting the exotic particle paths, see example Figure 1.2.2.

We study the convective dispersion of the peristaltic flow in the absence of diffusion and illustrate the behaviour of the oscillatory flow, namely centreline trapping, which induces large radial mixing. Some analysis allows us to actually determine the amount of volume of fluid recirculating in the flow. We wish to model the motion of a solute in a peristaltic flow to represent therapeutic motion in the intestine. Hence we consider the 2D dispersion model

$$c_t + \mathbf{u} \cdot \nabla c = D \nabla^2 c, \quad (1.2.1)$$

for the solute concentration with peristaltic velocity \mathbf{u} . However, first we consider the trivial case in the next Chapter when $\alpha = 0$ and the model (1.2.1) reduces to the Poiseuille dispersion equation (1.2.2).

⁴The wave number is the ratio of the height of the wave to the wavelength

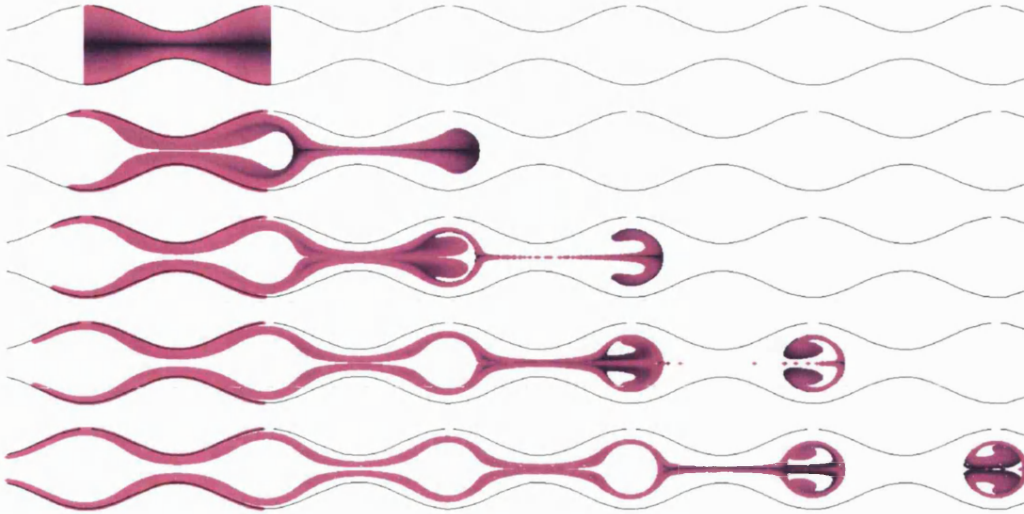


Figure 1-3: Evolution of an Initial Condition consisting of 10^6 passive particles which are dyed black at the centreline. The flow exhibits Trapping and Reflux ($\alpha = 0.5, \hat{\psi}_w = -0.4$). The frames correspond to $T = 0, 1, \dots, 4$ cycles of flow.

1.2.3 Chapter 4: Dispersion Models in Cylindrical Flow with Application to the Intestine

In this Chapter we look at the averaged solute concentration behaviour in a cylinder where the fluid flow is Poiseuille. The full concentration profile satisfies the 2D Poiseuille dispersion model,

$$c_t + u(r)c_x = D\nabla^2 c. \quad (1.2.2)$$

To understand the dispersion effects of a nonuniform velocity we start from the basics and build up from a 1D model to the desired 2D model. We then apply asymptotic analysis to reduce the 2D model to a 1D equation for the mean concentration \bar{c} . We start by describing the 1D model of solute concentration in a cylinder with plug flow u , solute diffusion D and solute absorption K , such that the solute concentration satisfies

$$c_t + uc_x = Dc_{xx} - Kc,$$

a *convection-diffusion-reaction* equation. We motivate extending 1D model to the 2D Poiseuille convection diffusion equation (1.2.2) to take into account *convective dispersion* from Poiseuille flow. Fundamental to modelling solute motion in the intestine is the modelling of absorption at the epithelial wall, hence, we describe passive absorption at the boundary with permeability K_a by

$$-D\mathbf{n} \cdot \nabla c = K_a c, \quad (1.2.3)$$

a Robin boundary condition. In dimensionless form the boundary condition satisfies $\mathbf{n} \cdot \nabla c = -D_{ar}c$, where D_{ar} is the radial Damköhler number which describes whether the membrane is diffusion limited or absorption limited. This 2D model has been investigated before and has been applied to the intestine by Stoll et al. [73]. They used a macrotransport approach to reduce the model to a 1D equation for the cross sectional average of the solute concentration. To understand their approach we consider first the simpler impermeable case, described by Taylor [74]. We describe Taylor's long time asymptotics which approximates Poiseuille solute transport, (1.2.2), in an impermeable tube to a 1D asymptotic equation

$$\bar{c}_t + U_e \bar{c}_x = D_e \bar{c}_{xx},$$

for the mean solute concentration \bar{c} . We describe two important parameters governing the application of asymptotics: they are 1) the tube length ratio ℓ and 2) the Péclet number P_{er} which describes whether convection dominates diffusion or vice versa. We show that the conditions to apply the asymptotic analysis in the intestine for a non-absorbable tracer are not met. We then describe the permeable wall case where the asymptotic form of this equation is the most advanced dispersion model describing solute motion in the intestine [73]. However, we observed different results from [73]. This required reworking the asymptotic analysis by Lungu and Moffatt [52] who reduced the model (1.2.2) with the boundary condition (1.2.3) to a 1D asymptotic equation

$$\bar{c}_t + U_e \bar{c}_x = D_e \bar{c}_{xx} - K_e \bar{c}. \quad (1.2.4)$$

We show that the long time asymptotics by Moffatt and by Stoll match with the exception of the effective absorption coefficient which is stated incorrectly by Stoll et al. in [73], [10], [6], resulting in high levels of absorption. To apply (1.2.4) to a physical example, Stoll et al. derived a fictitious initial condition to validate their model for short time. However, we show that this fictitious term is insufficient by 1) reworking its derivation in our dimensionless coordinates and then 2) compare the numerical solution of the asymptotic equation (1.2.4) with the numerical solution of the full model (1.2.2) and (1.2.3). Furthermore Stoll had modelled peristalsis simply by enhanced diffusion as a function of the strength of the peristaltic flow. We state the formula in its full form from [10], and show that its application is in contradiction to its derivation.

1.2.4 Chapter 5: The Peristaltic Dispersion Model

In this Chapter we incorporate the leading order peristaltic velocities, derived in Chapter 3, in the 2D dispersion model (1.2.1) We numerically solve the Peristaltic dispersion model, shown in full with boundary condition in Figure 1-4, to determine the effects of peristaltic flow on (i) the solute concentration profile and (ii) absorption. However,

we need a base to compare our model against and we solve the Poiseuille dispersion model concurrently. Hence we compare the concentration profile and the amount of mass absorbed for the peristaltic dispersion model and Poiseuille dispersion model, for the same instantaneous mean volume flow rate and therapeutic parameters. In solving the peristaltic model we apply the domain transformation

$$(\chi, \kappa, \tau) = \left(\tilde{x}, \frac{\tilde{r}}{\tilde{f}(\tilde{x}, \tilde{t})}, \tilde{t} \right),$$

to move from a moving peristaltic ‘physical’ domain to a fixed rectangular ‘computational’ domain.

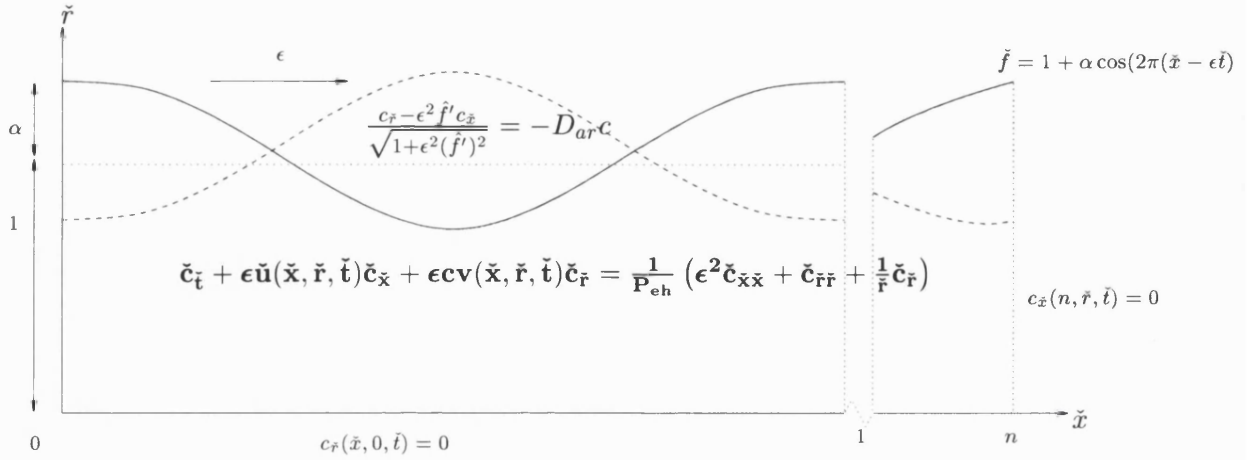


Figure 1-4: The Nondimensionalised Peristaltic Dispersion Model

Our numerical results show peristaltic flow gives rise to an oscillatory mean solute concentration profile. Using contour plots we show that in the presence of trapping the peristaltic solute concentration profile looks nothing like that of the Poiseuille concentration profile, the flows are too dissimilar. We observe from the peristaltic flow of a solute that solute is constantly brought to the wall by trapping enhancing absorption. What this model reveals that can not be illustrated in the particle paths is that solute does not just stick to one region of trapping it diffuses backwards into other regions of trapping, greatly increasing the convective dispersion of the solute.

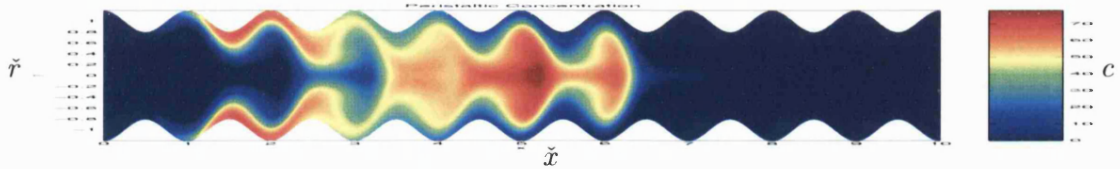


Figure 1-5: An Example of a Solute Concentration Profile in a Peristaltic Flow with Centreline Trapping

In Figure 1-5, solute has diffused from the leading wave of circulating flow into a trailing wave (darkest red), and it continues to do so with time. This has implications to the movement of food/drugs in the intestine. The villi are largest at the entrance to the intestine, and most nutrients are absorbed in the first quarter of the intestine [75]. Hence peristalsis is responsible for improving absorption of nutrients as it brings the solute closer to the epithelial wall and keeps solute at the entrance of the tube whilst constantly mixing it. This is unlike Poiseuille flow where most solute convects down the centreline (see Figure 1-6).

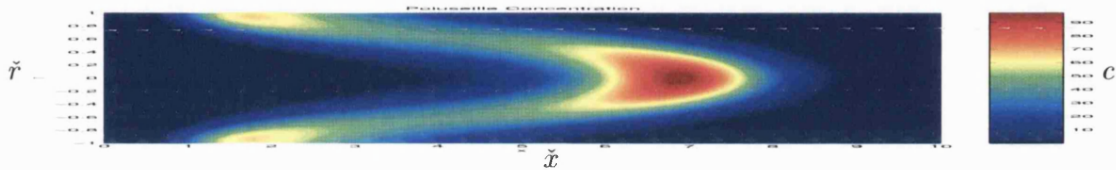


Figure 1-6: An Example of a Solute Concentration Profile in a Poiseuille Flow

In the presence of trapping, we show that solute movement is far too complicated to be modelled by enhanced diffusion in a Poiseuille model by showing that the peristaltic mean solute concentration and the Poiseuille mean solute concentrations, found for enhanced diffusion, are quite dissimilar for the same flow rate. It becomes even more apparent from varying the initial condition where solute is now placed at the centerline of the tube and we observe that more mass is absorbed and more mixing occurs from trapping which is not seen in a Poiseuille flow.

1.2.5 Chapter 6: Numerical Methods for the Fluid Flow and for the Dispersion Models

In this thesis we are dealing in general with equations too complicated to have an analytical solution. We apply a finite difference numerical scheme to solve the dispersion models (1.2.2) and (1.2.4) in one and two dimensions. The different numerical schemes for the 1D case are (i) standard upwinding difference method, (ii) a 1D diffusion transformation of (1.2.4) to $w_t = Dw_{xx}$ followed by finite difference and (iii) a moving mesh equation. The latter schemes are designed to reduce numerical dispersion from applying upwinding to the convection term. We solve (1.2.4) where the solution is known and show that the 1D diffusion transformation reduces numerical dispersion more than the moving mesh approach. Hence we show the error in the amount of mass absorbed and the amount of mass present in the domain is reduced. However, absorption in the intestine is not uniform down the gut, $K = K(x)$, and the diffusion transformation would no longer hold in this case. Hence it is necessary to develop the complex moving mesh approach. In the 2D case, there is no diffusion transformation and we can only improve accuracy by locating grid points in regions of sharp solution change located at

the boundary layer induced by absorption across the wall.

1.2.6 Brief Summary of New Work

In this thesis we derive a peristaltic dispersion model to measure absorption in the intestine. This is an alternative model to the standard Compartmental and Transit Models which simplify solute motion by assuming fluid is transported by plug flow. This basic assumption of fluid flow neglects mixing effects that are induced by a peristaltic flow. However, we capture the mixing by determining peristaltic velocities and applying them to a 2D dispersion model.

We derive the peristaltic flow using a power series expansion in ϵ , the wave number, on the Stokes flow equations in streamfunction-vorticity form. We analyse the breakdown of the leading order solution when the amplitude of vibration α of the peristaltic wave increases. However, to analyse peristaltic flow we assume ϵ is sufficiently small so that we need only consider leading order terms. We consider fluid flow not only when the pressure gradient is positive [64] but when it is negative. Through analysis we describe the behaviour of peristaltic flow for all types of flow rates (pressure gradients) and amplitude of vibrations. In particular this analysis allows us to quantify the proportion of recirculating fluid per wavelength of the peristaltic wave. Hence we can determine the fluid flow conditions for maximum mixing effects.

We implement the fluid flow in the 2D dispersion model $c_t + \mathbf{u} \cdot \nabla c = D \nabla^2 c$ with passive absorption on the boundary modelled by the flux condition $-D \mathbf{n} \cdot \nabla c = Kc$. We consider the trivial case when $\alpha = 0$, the Poiseuille Dispersion Model. In [74] and [52] the authors have shown it is possible to average the solute concentration across the cylinder cross-section to obtain a 1D asymptotic equation of the 2D model for the mean solute concentration. However, this 1D equation is valid *only* after a significant time has passed. The asymptotic equation has been derived for two cases, (i) an impermeable boundary by Taylor [74] and (ii) the permeable case Brenner et al. [10] Stoll et al. [73]. The macrotransport approach by Stoll et al. [73] needed to be reworked from a different perspective as we had obtained erroneous results when reproducing their results. We reworked the asymptotic analysis by Lungu and Moffatt [52] to correspond with that of Brenner et al. [10] and we observed three errors in the model by Stoll et al.; (i) the absorption coefficient is stated incorrectly in the book on Macrotransport Processes by Brenner et al. [10] and consequently in the paper by Stoll et al. [73], (ii) the fictitious initial condition is meant to make the asymptotic equation valid for all time, but by reworking the analysis in dimensionless form and numerically solving both 2D and 1D models, we observe that the initial condition fails to do so, (iii) the enhanced diffusion equation is derived for small Péclet number by a perturbation expansion but is applied in practice for large Péclet number.

The main part of this thesis is concerned with solving the Peristaltic dispersion in

Chapter 5. We observe the following interesting behaviour of the peristaltic flow on the mean solute concentration:

- Oscillations in the mean solute concentration which for weak peristaltic forces can be filtered to reveal an underlying Poiseuille mean solute concentration.
- When comparing the mean solute concentrations of the peristaltic dispersion model to that of the Poiseuille dispersion the advance of the solute in the peristaltic flow is retarded if there is centreline trapping.
- Peristaltic dispersion is too complex to model by Poiseuille dispersion plus enhanced diffusion.
- Peristalsis enhances absorption by (i) inducing enhanced radial mixing and (ii) reducing the distance solute has to diffuse to be absorbed.

Hence peristalsis optimises absorption in the intestine by retarding solute motion and circulating solute towards the membrane.

Chapter 2

Background and Simple Models

In this Chapter we describe the physiological make up of the intestine and the physical factors occurring within. We review previous intestinal absorption models which are mainly being developed by pharmacologists. The most common is the CAT model, where the intestine is modelled by a sequence of compartments, each with their own absorption and degradation rates. This model is the basis of GASTROPLUS, a simulation software package sold to pharmaceutical companies. We further review dispersion models used by chemical engineers which model continuously the spatial distribution of solute in the intestine. The dispersion model is mathematically the most complex intestinal absorption model that has been conceived to date.

2.1 How is Food Digested?

The ‘Digestion System’ is responsible for converting the food we eat into fuel for the body. Food is broken down into small molecules to be absorbed into the bloodstream. The process begins when food is chewed in the mouth. Saliva assists in softening the food which is then pushed into the throat by the tongue. Food then travels down the oesophagus to the stomach and at this point is known as the ‘bolus’. The muscles of the stomach twist and churn and strong acids and enzymes are released that dissolve the food until it becomes ‘chyme’, a creamy liquid mass. The stomach then empties the chyme into the small intestine at a rate that depends on the composition of the food in the stomach (fat/protein/carbohydrate). Carbohydrates are easy to dissolve and are released into the intestine much faster than say protein. More enzymes are then released in the small intestine to break the food down further. The contents of the intestine are mixed together and absorbed across the intestinal lining into the bloodstream. The waste products are then propelled into the colon to be excreted some time later. We are interested in the small intestine which is responsible for the mixing and absorption of the chyme. We describe in the next section the physiological make up of the small intestine.

2.2 The Small Intestine

Virtually all nutrients in blood are absorbed by the small intestine. This is accomplished by the breaking down of large supramolecular aggregates into small molecules that can be absorbed across the epithelium (small intestine wall). Water and electrolytes (sodium, chloride, potassium) and essentially all dietary organic molecules (such as glucose, amino acids and fatty acids) are absorbed there. Consequently, the small intestine plays a vital role in water and acid-base balance. It is split into three segments: the duodenum, jejunum and the ileum, which make up 5, 50 and 45% of the length respectively. The average length of a human small intestine is somewhere in the region of 3m. Approximately 90% of all absorption from the gastrointestinal (GI) tract occurs here [73].

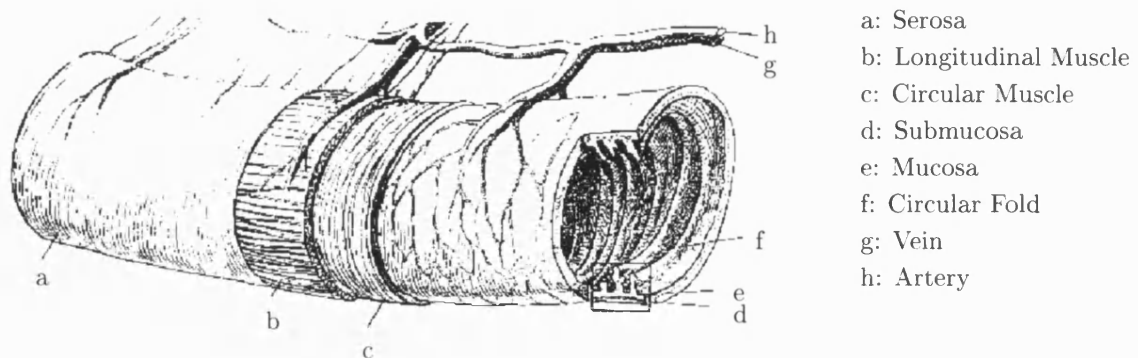


Figure 2-1: The Small Intestine (The Figure has been adapted from [73])

Taking the small intestine to be a simple cylinder, the luminal surface area would be on the order of one half square meter. However, the total exposed absorptive surface area is about $200m^2$, since the small intestine has three structural features that set it apart from other regions in the digestive tract and account for the huge absorptive surface area. The inner surface is not flat but comprised of circular folds known as *mucosal folds*, which increase surface area as well as aid in the mixing process of the chyme¹. Along the mucosa are small projections known as *villi* which themselves contain small projections known as *microvilli*. There are about 20,000 villi and 10 billion microvilli per square inch of the small intestine. Each villus brings in fresh oxygenated blood and sends out nutrient-enriched blood. In addition the villi constantly sway to stir up the chyme. Due to the decrease in the size and the number of mucosal folds and villi in the ileum, absorption primarily occurs in the duodenum and jejunum.

There are two distinct states of activity in the small intestine, where each state is associated with distinctive patterns of motility. The post meal cycle has two main types of motility: *segmentation* contractions that chop, mix and roll the chyme and

¹ *Chyme* - A semiliquid mass of partially digested food that passes from the stomach through the pyloric sphincter into the small intestine

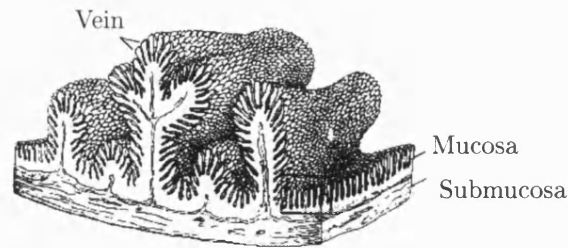


Figure 2-2: The Villi Structure (The Figure has been adapted from [73])

peristalsis, that slowly moves the chyme towards the large intestine. The second cycle occurs between meals, when the lumen is mostly empty. A sequence of 'housekeeping' contractions, propagate from the stomach through the entire small intestine, sweeping the undigested food clear and is the cause of 'growing'. Chyme moves at a rate where the residue of one meal leaves the ileum as another enters the stomach [75].

The most important and most common form of intestinal motility is segmentation which causes chyme to mix with digestive juices and exposes the chyme to the absorptive surface of the mucosa repeatedly. A common scenario is a small mass of food lies in one of the intestinal loops, suddenly constrictions at regular intervals along the tract cut the mass into little ovoid pieces. Moments later these segments are divided into two masses, and immediately after the separation neighbouring particular masses rush together and merge to form new segments. Then new segments are divided and a third series of segments are formed when neighbouring particles unite and so forth.

Peristalsis contractions are short lived weak contractions by nature move very slowly at 1 to 2 cm per second and die out after travelling just a few centimeters. However, following the distension of the duodenum as the stomach empties, intense peristaltic contractions occur that sweep the food through greater distances, and with greater speed. There are also *pendular* movements present in the small intestine that are contractions swaying back and forth.

The ileocecal sphincter that separates the colon from the terminal ileum is normally closed. Unabsorbed chyme delivered to the terminal ileum several hours after eating can remain there undergoing further segmentation, peristalsis and absorption for quite some time before exiting the ileum.

2.3 Fluid Mechanics in the Intestine

Kinematics and *Dynamics* are two branches of Mechanics, the study of motion. Kinematics deals with the motion of a body relative to a reference frame. However, Dynamics studies the forces associated with motion and the properties of the material in motion. Intestinal motility is practically unstudied from either the kinematic or

dynamic viewpoint. Empirical investigations that have dealt with intestinal motion are generally referred to as *transit studies* and take a very simple kinematic viewpoint. Usually a radioactive marker or radiopaque particles are ingested and their intestinal motion described. Average velocities of the marker over given distances are sometimes obtained. However, this is far short of a thorough quantitative description of motion over the entire intestine, or even a part of it.

For a greater understanding of intestinal motility it is necessary to investigate the interaction between chyme and the epithelial wall. A dynamic model is required, as it deals with the causes of the motion as opposed to just describing the motion (kinematics). Determining how the properties of the particle and the forces acting on it move the particle adds a greater complexity to a model. For the small intestine, fluid particles in the lumen are acted on by viscous forces from the intestinal wall, internal pressure in the lumen and gravity. Very little is known about the complex properties of chyme and early attempts to model have assumed that the luminal contents have simple physical properties. Chyme is assumed to be a highly viscous Newtonian fluid allowing for Stokes flow approximations to be made. The intestinal wall is also considered to be a simple axisymmetric tube with a propagating boundary prescribed by a periodic function. One of the first papers to describe the intestine in such a way was by Lew, Fung and Lowenstein [47]. However, instead of a peristaltic boundary a series of traveling axisymmetric, infinitely long, nodal constrictions are considered. Two fundamental solutions are given, (i) where the peristaltic flow is of pure transport, where the work done by peristalsis on the fluid is converted into mass transport with maximum effectiveness and (ii) peristaltic flow of pure compression and work done by the wall is used only to maintain the pressure gradient without any accompanying net transport of the fluid. This stands to reason because with the ileocecal valve closed, peristaltic flow of chyme must be of pure compression (although slight transport exists due to the distensibility of the luminal wall). In this case pressure builds up at the colon end of the intestine until the valve opens, allowing the pressure to help empty contents of the lumen. Vortex flow created by the peristalsis in the model moves chyme back and forth from the centre of the tube towards the tube wall, aiding in absorption. Pressure build up in the compression phase should also aid the absorption process [47].

Macagno and Christensen [53] claimed the terms *peristalsis*, *segmentation* and *pendular movements* were poorly defined and abandoned them in favour of simpler nomenclature. There are contractions of both the *circular* muscle layer and of the *longitudinal* muscle layer, which are both rhythmic; they repeat briefly and regularly, with a stereotyped time course. The contractions are also propagative, progressive or sweeping along the tube. Longitudinal muscle layer contractions can occur independently of the circular muscle layer. A simple model of longitudinal contractions of the wall was developed from observed data. In their notation the displacement δ_0 for points of a segment of duodenum is given by a simple equation $\delta_0 = A \cos(\omega t - \alpha)$, where A is the

local amplitude, α is the phase lag, and ω is the angular frequency of the slow wave.

Ring (circular muscular) contractions were studied by Christensen et al. [19] after taking systematic observations in the human duodenum. Once the statistics of the contractions were obtained, attempts were made to model ring contractions at a point in the duodenum as a series of independent events. However, results were unsatisfactory and a Markov type model was approached [67], where dependence on a given number of previous slow wave cycles were assumed. Success was achieved by assuming dependence on three previous slow wave cycles. Frequency distributions from experimental data and generated data from the Markov model were then compared using Chi-squared goodness of fit tests and were found to be statistically similar.

2.4 Absorption Models for the Intestine

Estimating the amount of drug absorbed is paramount in selecting therapeutic candidates when researching new drugs are developed. It is of particular interest to pharmaceutical scientists who are optimising drug delivery. A primary reason for developing predictive drug absorption models is to remove the need for *in vivo* studies in humans. In so doing, drug delivery strategies may be developed from the understanding of the rate limiting processes that affect drug absorption.

Intestinal Mechanics is fundamental to understanding how drugs flow and are absorbed in the intestine. However, previous drug absorption models have been very simple and neglected intestinal motility by assuming plug flow, constant velocity of flow at all points in the intestine. Predictive therapeutic models may be split into two types: *Compartmental and Transit* model and *Dispersion* models. The first treats the intestine as a series of connected compartments with concentration determined by a first order differential equation [77]. However, in the dispersion model concentration satisfies a convective dispersion pde, to take into account the spatial distribution of solute concentration (Ho et al. [73]). We discuss the uses of both models citing their advantages and disadvantages.

2.4.1 The Mass Balance Approach

Some approaches to modelling oral drug absorption have focussed on the actual epithelial boundary of the small intestine whereby a macroscopic mass balance approach (MMBA) is applied for passive and non-passive drugs (Sinko et al. [68]). It is recognised that drug dissolution and permeability are the main parameters that control the rate and extent of drug absorption (Amidon et al. [3]). Mass balance occurs due to a wall flux $J_w = P_w C_w$, and fraction dose absorbed is then estimated as a function of the membrane permeability, P_w , and membrane drug concentration C_w . This flux condition is applied to two models in their steady state 1) the mixing tank model

(MT), where the contents of the intestine are assumed to be uniform and spatially independent, and 2) the complete radial mixing tank (CRM), a spatially dependent process (Sinko et al. [68]). The fraction dose absorbed for amoxicilin is then estimated for initial doses of high and low solubility and permeability with *in situ* and *in vitro* obtained parameters.

2.4.2 The Compartmental and Transit Model

The most commonly used model for calculating the amount of drug absorbed in the small intestine is the Compartmental and Transit Model (CAT) (Yu et al. [77]). The flow of solute in the small intestine is deemed similar to that of flow through a series of connected, well mixed compartments where the rate of transfer of the drug from one compartment to the next is proportional to the amount of drug present in the current compartment (the drug transfers in a ‘1st order fashion’). The number of compartments subsequently increased from the original one compartment model to better fit experimental results, until Yu et al. [77] determined the optimal number to be seven. For a non-absorbing non-degrading tracer, an increasing number of compartments were added until the residual sum of squares error (SSE) of the transit time compared to the experimental result became small. The physiologically changing features of the gastrointestinal tract make the seven compartment approach reasonable, where each compartment represents the different portions of the small intestine. The first compartment is comprised of the duodenum and part of the jejunum. The jejunum also occupies part of the second and third compartment and the ileum makes up the remaining compartments.

It is assumed that the drug dissolves instantaneously and the amount of absorption in the stomach and colon is negligible compared to the amount absorbed in the small intestine.

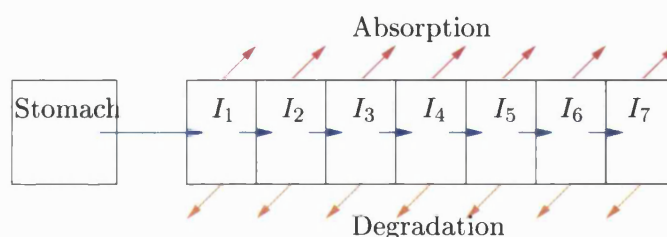


Figure 2-3: The Compartmental & Transit Model

The following equation (2.4.1) governs the percentage of dose of drug in the stomach Y_s where the drug leaves the stomach compartment in a 1st order fashion with gastric emptying constant K_s

$$\frac{dY_s}{dt} = -K_s Y_s. \quad (2.4.1)$$

The main equation (2.4.2) calculates the fraction dose Y_n in compartment n (denoted in Figure 2-3 by I_n for intestinal compartment n) for $n = 1, \dots, 7$.

$$\frac{dY_n}{dt} = K_t Y_{n-1} - K_t Y_n - K_{an} Y_n - K_{dn} Y_n, \quad n = 1, 2, \dots, 7. \quad (2.4.2)$$

In (2.4.2), for each compartment $n = 1, \dots, 7$, the uniform transit rate constant is denoted by K_t , the absorption rate constant by K_{an} and the degradation rate constant by K_{dn} . Yu et al. [77] factored into the drug absorption coefficient a compartment dependent saturable absorption coefficient and a compartment independent passive absorption parameter. Simply summing the rate of absorption in each compartment yields the total rate of absorption in the intestine:

$$\frac{dY_a}{dt} = \sum_{n=1}^7 K_{an} Y_n.$$

Similarly the rate of degradation over the small intestine is the sum of degradation over the 7 compartments:

$$\frac{dY_d}{dt} = \sum_{n=1}^7 K_{dn} Y_n.$$

Consequently the fraction of the dose of the drug absorbed by the intestine as time tends to infinity is given by

$$F_a = \frac{Y_a}{100} = \int_0^{\infty} \sum_{n=1}^7 \frac{K_{an} Y_n}{100} dt.$$

Hence deriving the rate of absorption and degradation as well as the total amount of drug absorbed is very easy.

The CAT model is given by a set of first order ordinary differential equations describing plug flow through the intestine where experimental data is used to reasonably estimate transfer and absorption rate parameters. It has undergone various changes to incorporate passive and saturable absorption as well as degradation (Yu et al. [77]). Here the results of the varying size of oral doses of Cefatrizine, an Amino- β -lactam antibiotic, were used to explain the observed oral plasma concentration time profiles. In general, the model offers reasonable accuracy by the model, however, physiological effects can only be incorporated discretely for each compartment and as a result the models fail to describe spatially, in a continuous sense, the distribution of a drug. However, the CAT model exceeds the mass balance models and the single tank models in terms of effectiveness and versatility.

2.4.3 The Dispersion Models

A one dimensional dispersion model was originally applied by Ho et al. [28] to simulate oral drug absorption of a non-absorbable non-degradable drug. The equation takes the form $c_t = Dc_{xx} - uc_x$, where solute travels axially in the x direction with concentration c . The plug flow velocity is denoted by u and is determined from the mean intestinal transit speed by assuming constant velocity in the intestine. The dispersion coefficient D incorporates molecular diffusion and physiological effects. In general an analytical solution is not always obtainable for the dispersion model. This is true also for the full convection diffusion reaction (CDR) model $c_t = Dc_{xx} - uc_x - Kc$, where an absorption rate K is taken into account. The downside of the dispersion model is its inability to factor in (i) the physiological differences of the duodenum and the ileum and (ii) a reasonable way to incorporate gastric emptying as a function of volume (Yu et al. [77]). This has allowed the simpler ode CAT model to be favoured over the more complex pde model.

The CAT, MMBA and 1D dispersion models have all assumed that there are no radial inhomogeneities in the solute concentration and in the fluid flowing along the small intestine. This assumption neglects a more complex underlying phenomena known as ‘convective dispersion’ which is discussed in Stoll et al. [73]. This phenomena and the work of Stoll form the basis of Chapter 4. Convective dispersion is a consequence of viscous forces whereby fluid particles on the boundary of the tube obey the no-slip condition and as a result neighbouring particles move at slower speeds when compared to particles occupying the centerline. Let us consider a dissolved therapeutic *in situ*. It will exhibit dispersion in part from (i) molecular diffusion and (ii) from axial convection. As the boundary of the wall becomes increasingly permeable, solute particles close to the membrane that occupy slower streamlines are removed. Hence the remaining therapeutic particles towards the center of the tube occupy faster streamlines. Consequently, the centroid of concentration travels faster than the mean flow speed and as a result the enhanced dispersion from axial convection diminishes.

The 2D model can actually be approximated by a 1D process after a significant amount of time has passed. This happens when all radial positions have been sampled by the remaining solute resulting in the removal of all radial inhomogeneities. This chromatographic effect was seen by Taylor (1953) [74] when solute travelled in a tube with impermeable walls (see §4.4.1). The mean concentration profile was then solved for asymptotically long time. In the presence of permeable walls the asymptotic mean profile was solved to account for the loss of conservation of mass by Sankarasubramanian and Gill (1973) [4] and also by Lungu and Moffatt (1982) [52] (see §4.4.3). Similarly a paper by Stoll et al. used Macrotransport Theory by Brenner and Edwards (1993) [10], to reduce the axisymmetrical 2D model of the small intestine to a 1D model. The advantage of applying the asymptotic analysis is that it is both easier and quicker to

solve numerically a 1D pde than a 2D pde. The Macrotransport approach by Brenner [10] is similar to the analysis applied by Sankarasubramanian et al. but takes general form to encompass a wide variety of transport processes involving enhanced dispersion phenomena not just that seen in Poiseuille flow in a permeable tube.

2.5 Oral Drug Absorption

In the previous section we discussed models that predict absorption from the intestine that vary in complexity. However, the models form only one part of what is known as the "Oral Drug Absorption" (alternatively Oral Drug Bioavailability²) process. This process follows the course of a drug from being orally administered to its movement to the intestine, its absorption from the lumen, to reaching the systemic circulation. Starting off as a solid drug, there are two main steps involved in reaching circulation, they are *dissolution* and *absorption*. Before absorption the therapeutic must be dissolved. Using in vitro³ methods the dissolution process has become fairly well understood to predict dissolution in vivo⁴. However, the absorption process is still not fully known. Grass et al. ([23]) stated there are two factors, physical and physiological, that affect oral drug absorption.

The physical parameters depend on the drugs physicochemical characteristics they include a) *solubility*, b) *dissolution rate*, c) *molecular size*, d) *partition coefficient*, e) *chemical degradation* and f) *delivery system*.

These factors determine how easily the compound can be dissolved, whether it is absorbed by passive or active absorption, and how strong the compound stands up to degradation before it can be absorbed. All of these parameters may be influenced by the choice of delivery system, whether it be tablet, capsule, suspension, solution or modified release, these systems will determine where and when the drug can be absorbed [23] and [2].

Physiological factors are the properties of the gastrointestinal tract that aid or hinder absorption: a) *binding/complexation*; therapeutics may undergo binding or complexation in the intestine, that is where the compounds that compose the drug react to the lumen contents, such as enzymes. Consequently the amount of absorbable therapeutic reduces. b) *regional pH*; local pH plays an important role in the GI tract and is responsible for (i) varying dissolution rates of solid dose forms [2], (ii) the degradation rates and (iii) the permeability of the lumen. c) *intestinal permeability*; there is variation in the permeability throughout the intestine, this stems from the decreasing size of i) the lumen and ii) the number of villi, both affecting the absorption surface area. d) *gastric and intestinal transit* which determines how long the drug is available

²Bioavailability refers to the fraction of dose reaching systemic circulation

³In Vitro: in an artificial environment outside the living organism

⁴In Vivo: within a living organism

for absorption, and e) *first pass extraction*.

First pass extraction has been defined to be the loss of therapeutic between two points; the point where the drug is administered to the point where systemic concentration is measured. Main loss of therapeutic is attributed to gut metabolism and hepatic⁵ elimination. Other sites of degradation occur in the lungs and blood, although eliminations here are minor in comparison. However, the liver is most responsible and extracts therapeutic at a rate dependent on the hepatic flow rate and plasma binding [2]. The contribution from the liver in reducing bioavailability is considerable enough to warrant designing any dosing regimen around it. It is particularly difficult to estimate the correct dosage when drugs undergo extensive first pass metabolism, since factors such as age, gender, enzyme activity and food become increasingly responsible for fraction dose absorbed and are responsible for the observed wide inter-individual variability. Hence for such easily metabolised drugs to achieve desired plasma concentration levels much larger oral doses than those administered by IV⁶ doses is required.

We have shown that it is essential for any therapeutic model to take into account 1) as many physical and physiological parameters as possible and 2) as much feasible experimental testing to corroborate the model. The foundations of any predictive dispersion model is the 1D intestinal absorption pde reviewed in the (2.4.3). From this equation we can extend the model to include additional parameters. The dispersion equation is complex in comparison to the CAT equation and so very little has been done to improve the dispersion model. However, Stoll et al. have attempted to additionally model 1) convective dispersion from Poiseuille flow, 2) enhanced diffusion from peristalsis and 3) hepatic extraction [73]. Their model also assumes instantaneous dissolution of therapeutic, an assumption used to simplify the model by removing the dissolution phase. Without this assumption the model would require coupling the dispersion equation with a dissolution equation [3].

By considering the physical and physiological factors we can elucidate the weaknesses of the CAT model. It is unable to account for a number of factors: the pH dependence of solubility, the drug dissolution rate, the delivery system and first pass elimination in the gut and in the liver to name a few. For drugs with low permeability and low solubility (e.g. controlled release drugs), it is possible that absorption will be incomplete by the time the therapeutic reaches the colon. In this case colonic absorption will account for a significant amount of the overall mass absorbed [2], [23]. Conversely, for highly soluble and highly permeable drugs (in the case of immediate release drugs), colonic absorption will be negligible and absorption taking place in the stomach will play an increasing role. Hence, the addition of a further two compartments to model absorption in the stomach and colon would make the CAT model more effective (Grass et al. [23]). We review more advanced compartmental models which improve upon the

⁵Hepatic: acting on or occurring in the liver

⁶IV is short for 'intravenous' which means: within a vein.

CAT model by considering further physical and physiological parameters.

2.6 Advanced Simulation Software for Intestinal Absorption Models

Primary research into therapeutic models is still mainly undertaken by pharmaceutical researchers⁷. To extend a dispersion model would require in depth mathematical knowledge, hence, the CAT model has been the favoured model to build upon. It simply requires experimental pharmacokinetic data and can quickly solve for the absorption and degradation kinetics by parameter fitting to plasma concentration [77]. It is made even simpler by removing the user from the hard-coding of the model's equations by modelling the equations in a software package and presenting the user with a GUI (Graphical User Interface) of the model.

2.6.1 Example 1: STELLA

One such example of a simulation software packages is STELLA (Structural Thinking Experimental Learning Laboratory with Animation). It is fronted by a GUI that actually allows the user to graphically build his own variant of the CAT system [23]. An advantage of such a system is the ease with which alterations can be made to the model using graphics rather than manually amending the hard code and the equations. This is a major reason why dispersion models have been less favoured. In STELLA data may be entered numerically or graphically, such as a graph of experimental data, without having to prescribe mathematical functions.

In Grass et al. [23], STELLA was used to simulate gastrointestinal absorption. However, what sets this apart from the work by Yu et al. [77], is that each intestinal segment is represented by their own compartment. Rather than 7 compartments for just the small intestine, instead the stomach, duodenum, jejunum, ileum and colon, were represented by their own compartment. This introduced two additional absorbing compartments; the stomach and the colon. As in the CAT model, the gastrointestinal transit times for each segment are estimated using literature. What stands STELLA apart from the CAT model is that absorption in each compartment is determined by (i) the solubility of the compound as a function of the segments pH, S_{pH} , (ii) surface area A and (iii) drug permeability P . The mass flux absorbed is subsequently given by the simple formula $M_t = P.A.S_{pH}$ per compartment.

An important part of the oral drug process is metabolism. This is a factor not considered by Yu [77], however, the model by Grass et al. [23] circumvented this by testing non-metabolisable compounds. Hence, by applying a two compartment pharmacokinetic model for the elimination of a therapeutic after it has been absorbed. Grass et al.

⁷See Advanced Drug Delivery Reviews journal

were able to fit the elimination constants using plasma concentrations. However, this model can only be used for validation purposes since the data for the plasma kinetics is unavailable during the screening process of a drug. This form of elimination is post-absorption, but what is more important is pre-absorption elimination, e.g. metabolism, as most drugs are highly metabolisable. We now consider the advanced CAT (ACAT) model, the most advanced oral drug absorption model. The ACAT models not only metabolism but a significant number of other physiological parameters.

2.6.2 Example 2: GASTROPLUS

GASTROPLUS is a more advanced simulation software based on the advanced CAT model by Agoram et al. [2]. The ACAT model describes the movement of a drug through a series of compartments, namely the standard 7 intestinal compartments plus compartments for the stomach and colon. The model captures the motion of a therapeutic from when it is released, to its dissolution, its luminal degradation, its metabolic extraction and finally to its absorption as well as exsorption. In reality drug movement from the lumen is not unidirectional, but depends on the concentration gradient. This implies that solute can move in either direction at the epithelial wall. However, unlike in the CAT model, the luminal barrier is not treated as a thin wall, but rather as a further series of compartments that absorbed luminal therapeutic must pass through, they are the enterocyte and surrounding tissue.

The ACAT models a system of equations representing 18 compartments (9 GI and 9 enterocyte) and captures six states of a therapeutic; unreleased, undissolved, dissolved, degraded, metabolized and absorbed. There are a further three states for excreted material as well, they are unreleased, undissolved and dissolved. Similar to the CAT model, the total amount of drug absorbed is the sum over all the compartments that absorb material. Intercompartmental movement is modelled by four main rate constants known as the transfer rate k_t , the dissolution rate k_d , the absorption rate k_a and the degradation rate constant k_{deg} .

In the CAT model the transfer rate K_t is considered to be uniform but in GASTROPLUS the rate is adjusted based on the volume of each compartment. In this new model the rate constant for dissolution is a function of particle size density, the lumen concentration, the diffusion coefficient and the solubility of the drug as a function of pH. The absorption rate now depends on the effective permeability of the drug multiplied by a correction term for the change in permeability as a result in surface area and pH. In each compartment the absorption rate coefficient is rescaled according to pH and passive diffusion (known as log D).⁸ The parameter log D is used to represent passive diffusion and is determined by the size and the shape of a drug's molecule as

⁸Passive Diffusion involves carriers, channels, or direct diffusion through a membrane, as opposed to Active Diffusion where a source of energy is required to move the carrier and its materials against the concentration gradient, e.g. Glucose in the intestine.

well as the molecule's acid and base dissociation constants which are a function of the GI tract's pH. Similarly, the luminal degradation rate is found from experimentation as a function of pH.

2.7 Summary

Therapeutic absorption models fall into two categories, (i) compartment models and (ii) dispersion models. Compartment models are a system of simple odes describing the absorption, degradation, and transit of solute in a series of compartments that represent the stomach, segments of the intestine and the colon. The model parameters are fitted to experimental results. The compartment models are simple enough to be extended to follow the course of a therapeutic from its oral admission to movement in the intestine, its absorption in the lumen to finally its circulation in the blood stream. This drug process is known as 'oral drug absorption' and takes into account further factors such as pH and hepatic elimination. The extended models are used in software packages, such as STELLA or GASTROPLUS. The software is presented by a GUI which removes the user from the maths and coding. However, the compartment models simplify solute motion in the intestine to just bulk flow and do not give us an idea of how solute behaves in the lumen. The solute concentration profile is also only given in a discrete sense. However, a dispersion model is more informative and describes the solute concentration profile in a continuous sense. It elucidates 'convective dispersion', this is where therapeutic solute exhibits diffusion from axial convection of fluid by Poiseuille flow.

We wish to investigate the effects of intestinal flow, which is more complex than Poiseuille flow, on solute behaviour. In this Chapter we have discussed motion in the intestine known as intestinal motility. It is particularly difficult to model as there has been much debate on how to define the flow. Previous terms included peristalsis, segmentation and pendular movements but they were seen as poorly defined. Circular and longitudinal contractions are preferred definitions and describe propagating waves down the lumen. Longitudinal contractions were modelled by a sinusoidal function whereas ring contractions were represented by Markov type models. We wish to model these intestinal contractions but rather than modelling random waves we model a constant standing wave propagating down the intestine, based on the longitudinal contractions. This fluid motion has already been studied and contrary to the aforementioned definitions is known as 'peristaltic motion'. We ultimately wish to model the effect of the 'peristaltic' waves on solute concentration and how it differs from the effects of Poiseuille flow.

Chapter 3

Modelling Peristaltic Flow

In this Chapter we consider the fluid dynamics when fluid is pumped through a deformable cylinder with a peristaltic wave propagating on the boundary. Using the Stokes' slow flow equation for an axisymmetric domain, we derive the nondimensionalised biharmonic equations of the streamfunction and tangential vorticity. We solve the biharmonic problem for two cases, (i) when there are no vibrations so that the flow is Poiseuille, and (ii) for a vibrating tube where we derive the peristaltic velocities in the wave frame. For the latter we model the propagating wave by prescribing a sinusoidal boundary function. We obtain two dimensionless parameters; α , the amplitude of wave vibration, and $\epsilon = h/\lambda$, the wave number or sometimes referred to as the wave curvature, the ratio of the height of the tube to the wavelength. For sufficiently long wavelengths, the wave number is sufficiently small so that a perturbation expansion in ϵ^2 may be sought to solve for the streamfunction. The leading order solution yields a Poiseuille-like solution for the velocity profile. However, our analysis reveals that for small curvature (i.e. small wave number), $\epsilon \approx 0.2$, the leading order solution begins to break down for large amplitude of vibration α and it is necessary to consider $O(\epsilon^2)$ terms to correct the semi-analytical solutions.

For zero curvature, $\epsilon = 0$, it is shown that in contrast to Poiseuille flow where positive flow is driven by a pressure drop between the inlet and the outlet, positive flow can occur in the presence of a pressure rise. There are two states of flow found known as *copumping* and *pumping*, occurring in the presence of a pressure drop and rise respectively. Phenomena known as *reflux* and *trapping* occur in these states and give rise to 5 possible types of fluid flow that are a linear combination of the effects of peristaltic phenomena and the effects of pressure rise or drop. We discuss how in the past application of anatomical parameters combined with inaccurate measurement of intestinal length has led to differing values for the flow rates $\hat{\psi}_w$ and pressure gradients Δp_λ . It was believed that flow in the intestine was copumping [5], however, it has now come to be accepted that it can also occur in the pumping case given the more accurate calculation of $\hat{\psi}_w$ and the valve like nature of the illeocecal sphincter. We highlight

properties of the fluid dynamics through particle paths that show radial mixing and the different types of peristaltic behaviour. We analyse the flow to determine a measure of the radial dispersion, an indication of the amount of radial mixing. We show this to decrease as the flow rate increases as peristaltic flow tends to Poiseuille flow. Our aim is to apply the semi-analytic peristaltic velocities to a 2D dispersion model $c_t + \mathbf{u} \cdot \nabla c = D \nabla^2 c$ with a suitable boundary condition for absorption.

3.1 Literature Review

The driving force of fluid motion in a distensible tube can be a pressure drop between the inlet and outlet, or it can be a result of pumping by a mechanism known as *Peristalsis*, which stems from the Greek *peri stalsis* meaning *around contraction*. Progressive waves propagate along the tube propelling the fluid by inducing travelling regions of expansion and contraction. Peristalsis is an efficient natural phenomena occurring in biological systems for the transportation and mixing of physiological fluids. It is a neuromuscular property of smooth muscle structure forming the tube whereby neural point stimulation induces sequential squeezing of muscle fibers (long cells that construct the muscle) sending waves of muscular contractions along the passage. Observed in oesophageal swallowing of food boli, peristalsis mainly accounts for the movement of food and its waste derivatives, such as chyme in the GI tract, mixing food in the stomach and intra-uterine propulsion. Peristaltic motion has desirable fluid pumping characteristics and has consequently been copied and adapted for many real life applications. One such machine is the roller pump where rotating rollers compress a stationary tube, usually to the point of complete occlusion and the rollers proceed to squeeze the fluid along [64]. This approach is used to prevent contact of the propelled fluid with the mechanical pumping parts in cases of pumping blood or corrosive fluids. Also tiny mechanical devices have been designed to mix reagents and chemicals in small scale experiments where simple mixing methods are required for such small devices [17].

Peristalsis has been studied and documented from a biological standpoint since it was first described by Bayliss and Starling (1899). However, it was not until the late 60s where initial attempts to describe the motion began to understand the fluid dynamics of the propulsion. Experimental work on peristaltic pumping by Latham (1966) was soon followed by one of the first mathematical models describing peristalsis by Burns and Parkes [12]. An infinite train of travelling¹ sinusoidal peristaltic waves were considered to pump an incompressible fluid in a channel and an axisymmetric tube. Inertia free motion was assumed, that is the fluid is sufficiently viscous to simplify the Navier-Stokes equations which govern the fluid dynamics (see §3.2) and a perturbation solution was sought in terms of powers of the amplitude ratio of the wave, α . However,

¹Travelling waves refer to an extensible tube moving longitudinally, as opposed to standing waves that have pure transverse motion

no physiological applications were made by the authors. Soon after, Barton & Raynor [5] considered the axisymmetric case and removed the assumption of small amplitude and replaced it by long wavelength compared to radius of wave such that pressure can be seen to be uniform over the cross section. This enabled an analytical solution to be found for the velocities as a function of flow rate (when there is a zero pressure drop) and as a function of the sinusoidal function describing the wave. In many biological systems, viscous fluid boli are transported by such long wavelength peristaltic waves. Hence, the lubrication theory approximations were suitably justified for Barton et al. to reasonably compare their model to chyme movement in the small intestine.

Shapiro, Jaffrin & Weinberg [64] refined the definition of relatively long wavelength assumption to infinite wavelength to derive solutions for the channel case as well. They also assumed an integral number of waves between the inlet and outlet of the pump, removing time dependency of pressure to discover the conditions for the phenomena of *reflux* and *trapping*. These peristaltic flow characteristics occur when particles close to the wall travel with overall retrograde motion in the former case, and in the latter, a bolus of fluid travels approximately with speed of the wave with particles inside undergoing internal circulation. Reflux may in fact be responsible for bacteria movement from the bladder to the kidneys in the ureter against the flow of urine [64]. At this point urethral physiology became the main motivation for the study of peristalsis. These early models became the basis of all other studies where now most models assume a train of periodic sinusoidal waves pumping a Newtonian or non-Newtonian fluid through either a 2D symmetric channel or an axisymmetric tube. The governing equations are then obtained from simplifying the Navier-Stokes equations in one of two ways, either allowing arbitrary Reynolds numbers and assuming small wave amplitude to simplify or applying lubrication theory for arbitrary wave amplitudes. Analysis of flow is then conducted in either the *laboratory frame*, the fixed frame of reference, or in a reference frame moving with the velocity of the wave, known as the *wave frame* where the walls are stationary and some flows become steady (independent of time).

There are other physiological differences to consider in peristaltic pumping of biofluid, for example, viscosity variation of fluid being one. Typically there exists a peripheral layer of fluid at the wall of the pump with differing properties to the pumped fluid with one or both immiscible fluids being non-Newtonian. In the intestine the chyme bolus is surrounded by a thin layer of mucus which is less viscous. Shukla et al. [66] modified work by Barton and Raynor to include the effect of such a peripheral layer but modelled the mucus as a less viscous Newtonian fluid. Their results agreed more with physiological observations of chyme movement. However, their analysis was found to have violated conservation of mass by Brasseur et al. [9] who derived the peripheral layer problem for a channel, later derived by Rao et al. [63] for the axisymmetric case. In the channel case the peripheral layer has a profound effect on the overall pumping characteristics. If the layer adjacent to the wall is more viscous, the volume flow rate

increases when compared to a single fluid and vice versa for less viscous peripheral layer. Peristaltic pumping is a function of viscous forces with more efficient pumping when there is a higher viscous layer. However the intestine receives approximately 6 to 7 litres of fluid a day implying viscosity of the fluid increases the further from the wall. This ‘variable viscosity’ was just recently reviewed by Misery et al. [21] in the presence of an endoscope but the equations are analytically insoluble.

3.2 Deriving Peristaltic Flow

Consider a Newtonian fluid flowing in a cylindrical tube with constant viscosity and density (μ and ρ respectively). The flow velocity $\mathbf{u} = \mathbf{u}(\mathbf{x}, t)$ at any point \mathbf{x} and time t of the incompressible fluid is governed by the continuity equation $\nabla \cdot \mathbf{u} = 0$ and

$$\frac{\partial \mathbf{u}}{\partial t} + (\mathbf{u} \cdot \nabla) \mathbf{u} = -\frac{1}{\rho} \nabla p + \nu \nabla^2 \mathbf{u}, \quad (3.2.1)$$

the Navier-Stokes equation, where ∇p is the pressure gradient and $\nu = \mu/\rho$ is the kinematic viscosity. For an axisymmetric domain we use cylindrical polar coordinates (r, θ, x) where the Laplacian is given by

$$\nabla^2 = \frac{\partial^2}{\partial x^2} + \frac{\partial^2}{\partial r^2} + \frac{1}{r} \frac{\partial}{\partial r}. \quad (3.2.2)$$

Let us denote U and L to be the characteristic flow speed and length scale respectively of the fluid flow. The relative order of magnitude of the inertia term and the viscous term in the Navier-Stokes equation is

$$\frac{\|(\mathbf{u} \cdot \nabla) \mathbf{u}\|}{\|\nu \nabla^2 \mathbf{u}\|} \approx \frac{U^2/L}{\nu U/L^2} = \frac{UL}{\nu} = Re,$$

where Re is the Reynolds number, a dimensionless parameter. For a viscous fluid travelling at slow speed, $Re \ll 1$, the viscous forces $\nu \nabla^2 \mathbf{u}$ dominates the inertia forces $(\mathbf{u} \cdot \nabla) \mathbf{u}$, and it is sufficient to neglect the inertia term from the Navier-Stokes equation. We can further assume that the oscillations of the wall are such that $\sigma/\nu l = O(1)$ to neglect $u_t = 0$ [12]. Hence, the forces arising from pressure balance those coming from viscosity such that $\nabla p = \mu \nabla^2 \mathbf{u}$. We introduce *vorticity*, a measure of the amount of fluid rotating in the flow, which is defined by $\boldsymbol{\omega} = \nabla \times \mathbf{u}$. Taking the curl of vorticity yields the following identity $\nabla \times \boldsymbol{\omega} = \nabla \times (\nabla \times \mathbf{u}) = \nabla(\nabla \cdot \mathbf{u}) - \nabla^2 \mathbf{u}$. We assumed that the fluid is incompressible, $\nabla \cdot \mathbf{u} = 0$, hence the identity is reduced to $\nabla^2 \mathbf{u} = \nabla \times \boldsymbol{\omega}$. Therefore the Navier-Stokes flow for highly viscous fluid is satisfied by the *Stokes flow* (Slow flow) equation

$$\mu \nabla \times \boldsymbol{\omega} = \nabla p. \quad (3.2.3)$$

In the absence of any external forces acting on the fluid in the cylindrical tube we assume by axisymmetry of the domain there is no flow in θ direction, so $\mathbf{u} \equiv (v, 0, u)$ for radial and axial velocities $v \equiv v(r, x)$ and $u \equiv u(r, x)$ respectively. We now introduce the Stokes stream function $\psi = \psi(r, x)$ which is constant along any streamline and satisfies $\mathbf{u} = \nabla \times \left(\frac{\psi}{r} \mathbf{e}_\theta \right) = \left(-\frac{1}{r} \psi_x, 0, \frac{1}{r} \psi_r \right)$. Similarly vorticity $\boldsymbol{\omega} = \nabla \times \mathbf{u}$ in axisymmetric flow is defined by $\boldsymbol{\omega} = \omega \mathbf{e}_\theta$. The vorticity component and Stokes stream function satisfy

$$\boldsymbol{\omega} = \nabla \times \nabla \left(\times \left(\frac{\psi}{r} \mathbf{e}_\theta \right) \right) \Rightarrow -r\omega = \psi_{xx} + \psi_{rr} - \frac{1}{r} \psi_r := L_{-1}(\psi)$$

Noting that the curl of a gradient is zero, then taking the curl of the Stokes flow equation yields

$$\mu \nabla \times \nabla \boldsymbol{\omega} = \nabla \times (-\nabla p) = 0 \Rightarrow 0 = (r\omega)_{xx} + (r\omega)_{rr} - \frac{1}{r} (r\omega)_r := L_{-1}(r\omega)$$

We have obtained a biharmonic pde problem for Stokes stream function and tangential vorticity $\phi = r\omega$, as seen in Burns & Parkes [12].

$$L_{-1}(\psi) = -\phi, \quad L_{-1}(\phi) = 0.$$

3.2.1 Simulating Peristaltic Motion by a Moving Boundary

We consider a cylinder whose solid wall is allowed to undergo a vibration as a result of an infinite train of sinusoidal transverse waves propagating with speed σ in the positive x direction. The motion of the wall in time may be described by

$$r = f(x, t) = h + \eta \cos \left(\frac{2\pi}{\lambda} (x - \sigma t) \right),$$

for average radius of the nondisturbed cylinder h , amplitude of vibration η , wavelength λ and time t .

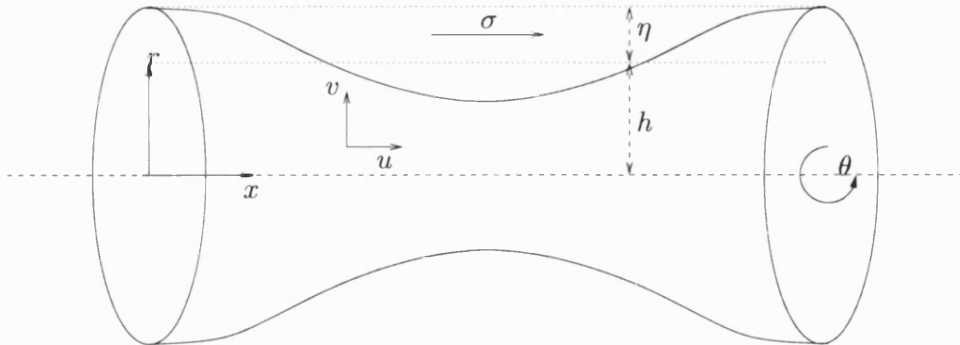


Figure 3-1: One Wavelength of the Peristaltic Axisymmetric Deformable Tube

Fluid flow in the presence of oscillating walls is unsteady but by assuming the length of the domain, L_x , is an integral number of waves $L/\lambda = n \in \mathbb{N}$ we can introduce a wave frame coordinate $(\bar{x} = x - \sigma t, \bar{r})$ moving with speed σ relative to the fixed frame (x, r) where flow in the moving frame is steady and flow in the fixed frame is now periodic. Hence, we introduce the following wave frame parameters denoted by a bar superscript

$$\begin{aligned} \bar{u}(\bar{x}, \bar{r}) &= \bar{u}(x - \sigma t, r) = u(x, r, t) - \sigma, & \bar{v}(\bar{x}, \bar{r}) &= \bar{v}(x - \sigma t, r) = v(x, r, t), \\ \bar{\psi}(\bar{x}, \bar{r}) &= \bar{\psi}(x - \sigma t, r) = \psi(x, r, t) - \frac{1}{2}r^2, & \bar{\phi}(\bar{x}, \bar{r}) &= \bar{\phi}(x - \sigma t, r) = \phi(x, r, t), \\ \bar{p}(\bar{x}, \bar{r}) &= \bar{p}(x - \sigma t, r) = p(x, r, t), & \bar{f}(\bar{x}) &= h + \eta \cos\left(\frac{2\pi}{\lambda}\bar{x}\right). \end{aligned}$$

As a result of the coordinate transformation the wave frame Stokes stream function satisfies the same biharmonic pde but in the corresponding wave frame parameters,

$$\bar{L}_{-1}(\bar{\psi}) = -\bar{\phi}, \quad \bar{L}_{-1}(\bar{\phi}) = 0.$$

3.2.2 The Peristaltic Boundary Conditions for the Biharmonic Equations

By axisymmetry we need only solve the problem for the positive domain $[0, \lambda] \times [0, \hat{f}(\hat{x})] \in \mathbb{R}$. The boundary conditions of the problem need to take into account the geometry of the domain and the fluid properties that are associated with transverse oscillating waves. For a regular solution to the biharmonic equations we impose boundary condition $\bar{\psi}_{\bar{r}\bar{r}\bar{r}}(\bar{x}, 0) = 0$ at the centreline (see Appendix §C.1 for proof). We also set the streamfunction to be constant, $\bar{\psi} = 0$, this implies particles on the axis move only on the axis since constant streamlines correspond to particle trajectories in the wave frame. To derive boundary conditions at the wall, we note fluid particles on the wall are subject to the motion of the wall.

For standing waves, a no-slip condition implies fluid in the wave frame on the boundary will be travelling backwards with speed of the wave $\bar{u} = (1/\bar{r})\bar{\psi}_{\bar{r}} = -\sigma$. By viscous effects fluid particles at the wall stick to the wall and consequently the particles move up and down so that they undergo transverse velocity of the wall $\bar{v} = -(1/\bar{r})\bar{\psi}_{\bar{x}} = f_t$. Hence we can rewrite the fluid velocity boundary conditions for the streamfunction as

$$\bar{\psi}_{\bar{r}} = -\sigma\bar{r}, \quad \bar{\psi}_{\bar{x}} = -f_t\bar{r}. \quad (3.2.4)$$

From boundary conditions (3.2.4) we determine a Dirichlet condition for $\bar{\psi}$ at the boundary, since the rate of change of $\bar{\psi}$ in the axial direction is

$$\frac{d\bar{\psi}}{d\bar{x}} = \frac{\partial\bar{\psi}}{\partial\bar{r}} \frac{d\bar{r}}{d\bar{x}} + \frac{\partial\bar{\psi}}{\partial\bar{x}} = (-\sigma f)f_{\bar{x}} - f f_t = 0.$$

Hence a first integral has been found for the stream function implying a constant

streamline on the boundary $\bar{\psi} = \bar{\psi}_0$. Integrating the axial velocity boundary condition, and applying appropriate symmetry conditions we determine the streamline on the boundary to be

$$\bar{\psi}(\bar{x}, \bar{f}) = \bar{\psi}(\bar{x}, 0) + \int_0^{\bar{f}} \bar{r}\bar{u}(\bar{x}, \bar{r})d\bar{r} = \int_0^{\bar{f}} \bar{r}\bar{u}(\bar{x}, \bar{r})d\bar{r} = \frac{q}{2\pi} = \bar{\psi}_w, \quad (3.2.5)$$

where $\bar{\psi}$ is proportional to the flow rate q , which is constant and independent of time and axial position in the domain. In fact, the flow rate $\bar{\psi}_w$ is linearly dependent on the pressure gradient over one wavelength $\Delta\bar{p}_\lambda$, see §3.5.2.

3.2.3 Nondimensionalising the Biharmonic Problem

We choose appropriate scales to characterise the various parameters and introduce the following dimensionless quantities denoted by the hat ^ superscript

$$\hat{x} = \frac{\bar{x}}{\lambda}, \quad \hat{r} = \frac{\bar{r}}{h}, \quad \hat{f} = \frac{\bar{f}}{h}, \quad \hat{t} = \frac{\sigma t}{\lambda}, \quad \hat{u} = \frac{\bar{u}}{\sigma}, \quad \hat{v} = \frac{\lambda\bar{v}}{h\sigma}, \quad \hat{\psi} = \frac{\bar{\psi}}{\sigma h^2}, \quad \hat{\phi} = \frac{\bar{\phi}}{\sigma}, \quad \hat{p} = \frac{h^2\bar{p}}{\lambda\mu\sigma}, \quad (3.2.6)$$

Hence the non-dimensionalisation of the axial and radial derivatives (3.2.5) yields the dimensionless biharmonic problem in the wave frame (Figure 3-2 below).

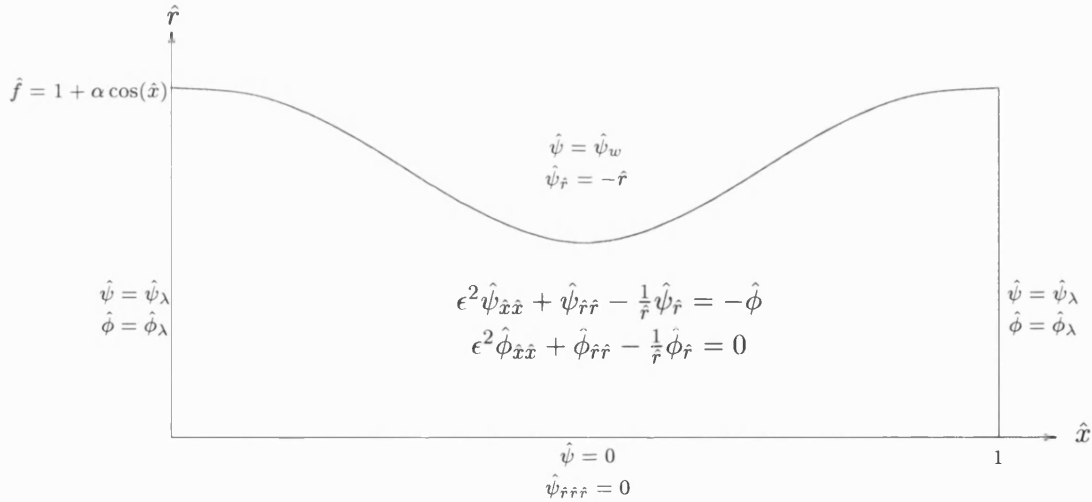


Figure 3-2: The Nondimensionalised Model for the Peristaltic Flow of Fluid with Streamfunction $\hat{\psi}$ and Tangential Vorticity $\hat{\phi}$

The Dirichlet boundary condition is given by the dimensionless flow rate $\hat{\psi}_w = q/2\pi\sigma h^2$. We introduce a further two dimensionless parameters: (i) the *amplitude ratio*, $\alpha = \eta/h$, the relative degree of deformation of the tube ($0 \leq \alpha < 1$), and (ii) the *wave number*, $\epsilon = h/\lambda$, a parameter describing the relationship between the slope and curvature of the wave. The nondimensionalised biharmonic problem can be solved numerically using

an appropriate rectangular domain transformation with finite difference (see Appendix E). However, for sufficiently small wave number, the biharmonic equations can be simplified to obtain an analytical solution in terms of a perturbation expansion in ϵ^2 .

3.3 The Trivial Case ($\alpha = 0$): Deriving Poiseuille Flow

We solve the nondimensionalised biharmonic equations for the trivial case when the amplitude of vibration is zero. For this case we consider the fixed frame and introduce dimensionless fixed frame coordinates $(\check{x}, \check{r}, \check{t})$ for which the biharmonic equations still hold. Note the check sign represents fixed frame dimensionless parameters. We assume that the flow has been established long enough to remove any axial inhomogeneities that may have existed. Hence there is invariance under translation in the \check{x} direction so that $\check{\psi} = \check{\psi}(\check{r})$ and the biharmonic equations are given by

$$\begin{aligned}\check{\psi}_{\check{r}\check{r}} - \frac{1}{\check{r}}\check{\psi}_{\check{r}} &= -\check{\phi}, \\ \check{\phi}_{\check{r}\check{r}} - \frac{1}{\check{r}}\check{\phi}_{\check{r}} &= 0.\end{aligned}\tag{3.3.1}$$

We still apply symmetry boundary conditions at the centreline but we must apply alternative boundary conditions at the wall, a Poiseuille flow rate $\hat{\psi}_{wp}$, with a no-slip condition $\check{\psi}_{\check{r}} = 0$ at the boundary $\check{r} = 1$. The streamfunction satisfies $\check{\psi}(\check{r}) = A\check{r}^4 + 2\check{r}^2$, and applying the boundary conditions at the wall the solution is given by

$$\check{\psi}(\check{r}) = \hat{\psi}_{wp} (2\check{r}^2 - \check{r}^4).$$

Hence, the Poiseuille velocities satisfy

$$\check{u}(\check{r}) = (4\hat{\psi}_{wp}) (1 - \check{r}^2) = U_0 (1 - \check{r}^2),$$

where U_0 is the centreline velocity. The mean fluid velocity \bar{V} is then found via

$$\bar{V} = \langle \check{u} \rangle = \frac{\int_0^1 \check{u}(\check{r})\check{r}d\check{r}}{\int_0^1 \check{r}d\check{r}} = 2 \int_0^1 \check{u}(\check{r})\check{r}d\check{r} = 2\hat{\psi}_{wp} = \frac{U_0}{2}.$$

Hence the Poiseuille flow in terms of the mean velocity $\check{u}(\check{r}) = 2\bar{V} (1 - \check{r}^2)$.

3.4 The Non-trivial case ($\alpha \neq 0$): Solving the Biharmonic Equations by a Perturbation Expansion

We expand the streamfunction and vorticity in a power series for the small wave number parameter ϵ^2 as follows:

$$\begin{aligned}\hat{\psi} &= \hat{\psi}_0 + \epsilon^2\hat{\psi}_2 + O(\epsilon^4), \\ \hat{\phi} &= \hat{\phi}_0 + \epsilon^2\hat{\phi}_2 + O(\epsilon^4).\end{aligned}\tag{3.4.1}$$

We are interested in parameters up to $O(\epsilon^2)$ since the $O(\epsilon), O(\epsilon^3)$ terms are zero and any other higher order terms $O(\epsilon^4)$ are sufficiently small that they may be neglected. Hence, upon substitution of (3.4.1) into the biharmonic equations we equate powers of ϵ^2 to obtain

$$O(1) \quad \hat{\phi}_{0,\hat{r}\hat{r}} - \frac{1}{\hat{r}}\hat{\phi}_{0,\hat{r}} = 0, \quad \hat{\psi}_{0,\hat{r}\hat{r}} - \frac{1}{\hat{r}}\hat{\psi}_{0,\hat{r}} = -\hat{\phi}_0, \quad (3.4.2)$$

$$O(\epsilon^2) \quad \hat{\phi}_{0,\hat{x}\hat{x}} + \hat{\phi}_{2,\hat{r}\hat{r}} - \frac{1}{\hat{r}}\hat{\phi}_{2,\hat{r}} = 0, \quad \hat{\psi}_{0,\hat{x}\hat{x}} + \hat{\psi}_{2,\hat{r}\hat{r}} - \frac{1}{\hat{r}}\hat{\psi}_{2,\hat{r}} = -\hat{\phi}_2, \quad (3.4.3)$$

The following boundary conditions at the membrane and symmetry axis must apply for each order of ϵ^2 :

$$\begin{aligned} O(1) \quad & \hat{\psi}_0(\hat{x}, 0) = 0, \quad \hat{\psi}_{0,\hat{r}\hat{r}\hat{r}}(\hat{x}, 0) = 0, \quad \hat{\psi}_0(\hat{x}, \hat{f}) = \hat{\psi}_w, \quad \hat{\psi}_{0,\hat{r}}(\hat{x}, \hat{f}) = 0, \\ O(\epsilon^2) \quad & \hat{\psi}_1(\hat{x}, 0) = 0, \quad \hat{\psi}_{2,\hat{r}\hat{r}\hat{r}}(\hat{x}, 0) = 0, \quad \hat{\psi}_2(\hat{x}, \hat{f}) = 0, \quad \hat{\psi}_{2,\hat{r}}(\hat{x}, \hat{f}) = 0. \end{aligned}$$

Solving the zeroth order biharmonic equations (3.4.2) and applying the peristaltic boundary conditions, the stream function and tangential velocity are given by

$$\begin{aligned} \psi_0(\hat{x}, \hat{r}) &= A(\hat{x})\hat{r}^4 + B(\hat{x})\hat{r}^2 = \left(-\frac{\hat{\psi}_w}{\hat{f}^4} - \frac{1}{2\hat{f}^2}\right)\hat{r}^4 + \left(\frac{2\hat{\psi}_w}{\hat{f}^2} + \frac{1}{2}\right)\hat{r}^2, \\ \phi_0(\hat{x}, \hat{r}) &= -8A(\hat{x})\hat{r}^2 = 8\left(\frac{\hat{\psi}_w}{\hat{f}^4} + \frac{1}{2\hat{f}^2}\right)\hat{r}^2. \end{aligned} \quad (3.4.4)$$

From the second order biharmonic equations (3.4.3) we expect the solution to be $O(\hat{r}^2)$ higher than the zeroth order and takes the form:

$$\psi_2(\hat{x}, \hat{r}) = C_1\hat{r}^6 + C_2\hat{r}^4 + C_3\hat{r}^2, \quad \phi_2(\hat{x}, \hat{r}) = D_1\hat{r}^4 + D_2\hat{r}^2, \quad (3.4.5)$$

Subsequently, substituting (3.4.5) and (3.4.4) into (3.4.3) the first order solution is

$$\begin{aligned} \hat{\psi}_2(\hat{x}, \hat{r}) &= -\left(\frac{A''}{12}\right)\hat{r}^6 + \left(\frac{A''\hat{f}^2}{6}\right)\hat{r}^4 - \left(\frac{A''\hat{f}^4}{12}\right)\hat{r}^2, \\ \hat{\phi}_2(\hat{x}, \hat{r}) &= A''(\hat{x})\hat{r}^4 + \left(-B'' - \frac{4A''\hat{f}^2}{3}\right)\hat{r}^2. \end{aligned} \quad (3.4.6)$$

3.4.1 Determining the Limits of the Semi-Analytic Streamfunction

In the literature, [5], [64], [66], the authors have only considered the leading order analytical solution where they assumed the curvature of the wave is exactly zero, $\epsilon = 0$. However, we look at a narrow deformable tube with wave number $\epsilon \leq 0.2$ ([5] used $h = 1.25\text{cm}$, $\lambda = 8.01\text{cm}$). This term may be sufficiently large to warrant considering higher order terms $O(\epsilon^2)$ for the solution of the streamfunction and peristaltic velocities. We determine numerically that the leading order solution depends also on on a small amplitude of vibration, α to remain valid. Consider the $O(1)$ solution for the streamfunction $\hat{\psi}_0$. By applying the leading order term we assume that $\epsilon^2\hat{\psi}_{0,\hat{x}\hat{x}}$ is

negligible compared to $\hat{\psi}_{\hat{r}\hat{r}} - \frac{1}{\hat{r}}\hat{\psi}_{\hat{r}}$, equivalently $-\hat{\phi}$, so that

$$|\epsilon^2 \hat{\psi}_{0,\hat{x}\hat{x}}| \ll |\hat{\phi}_0|$$

in equation $\hat{L}_{-1}(\hat{\psi}) = -\hat{\phi}$. It is similarly expected that $\epsilon^2 \hat{\phi}_{0,\hat{x},\hat{x}}$ is negligible. We define the following function

$$E_{\psi,0} = \epsilon^2 \frac{|\hat{\psi}_{0,\hat{x},\hat{x}}|}{|\hat{\psi}_{\hat{r}\hat{r}} - \frac{1}{\hat{r}}\hat{\psi}_{\hat{r}}|} = \epsilon^2 \frac{|\hat{\psi}_{0,\hat{x},\hat{x}}|}{|\hat{\phi}_0|} = \epsilon^2 |g(\hat{x}, \hat{r})|,$$

to be a measure of the relative size of $\epsilon^2 \hat{\psi}_{0,\hat{x},\hat{x}}$ to $\hat{\phi}_0$. To apply the leading order solution we would hope $E_{\psi,0} \ll 1$. We consider an example of peristaltic fluid flow with flow rate $\hat{\psi}_w = 0.2$. We calculate (i) $\max(|g(\hat{x}, \hat{r})|)$, the point where the ratio of $\hat{\psi}_{0,\hat{x},\hat{x}}$ to $\hat{\phi}_0$ is maximum, and we do this for increasing amplitude of vibration α and (ii) the maximum size of wave number ϵ_E such that $E_{\psi,0}$ is within 20%, i.e the $O(1)$ analytical solution is an appropriate approximation.

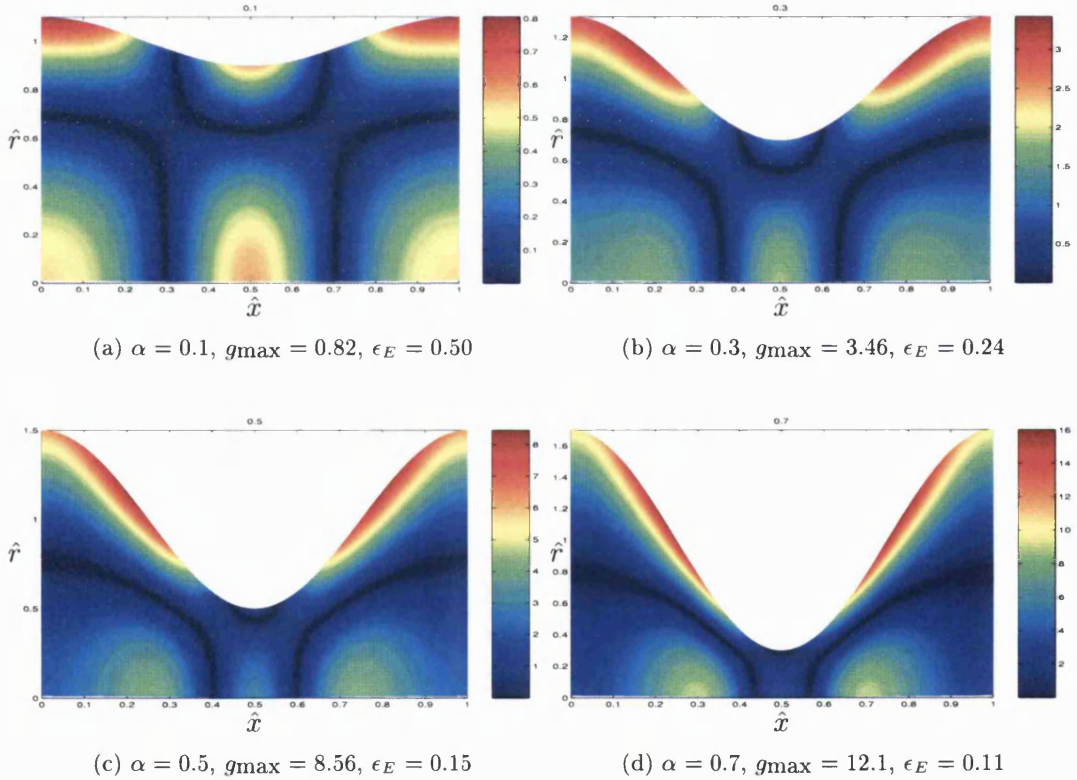


Figure 3-3: Contour Plots of $g(\hat{x}, \hat{r})$ a Measure of the Relative Size of $\hat{\psi}_{0,\hat{x},\hat{x}}$ to $\hat{\phi}_0$ for $\hat{\psi}_w = 0.2$

In Figure 3-3 it is quite clear that as the amplitude of vibration increases the size

of $\hat{\psi}_{0,\hat{x},\hat{x}}$ increases relative to $\hat{\phi}_0$. As a result the size of the wave number, ϵ_E , for which a leading order solution is appropriate decreases to $\epsilon = 0.09$ when $\alpha = 0.9$ to maintain $E_{\psi,0}$ to within 20%. We observe that the greatest ‘error’ occurs when $\hat{f} = 1$ at the boundary of the wall and at the centreline for increasingly large α . Hence, for wave number $\epsilon < 0.2$, the leading order solution for the streamfunction $\hat{\psi}_0$ is a good approximation. We note that as the flux $\hat{\psi}_w$ increases, the maximum moves to the centreline trapped contours, and requires smaller wave number ϵ_E . To recover the higher order term $O(\epsilon^2)$ we introduce the function $E_{\psi,2}$ such that

$$E_{\psi,2} = \epsilon^4 \frac{|\hat{\psi}_{2,\hat{x},\hat{x}}|}{|\hat{\phi}_0 + \epsilon^2 \hat{\phi}_2|},$$

is a measure of the relative size of $\epsilon^4 \hat{\psi}_{2,xx}$ to $\hat{\phi}_0 + \epsilon^2 \hat{\phi}_2$. We expect $\max(E_{\psi,2}) < \max(E_{\psi,0})$ for a given $\epsilon = 0.2$.

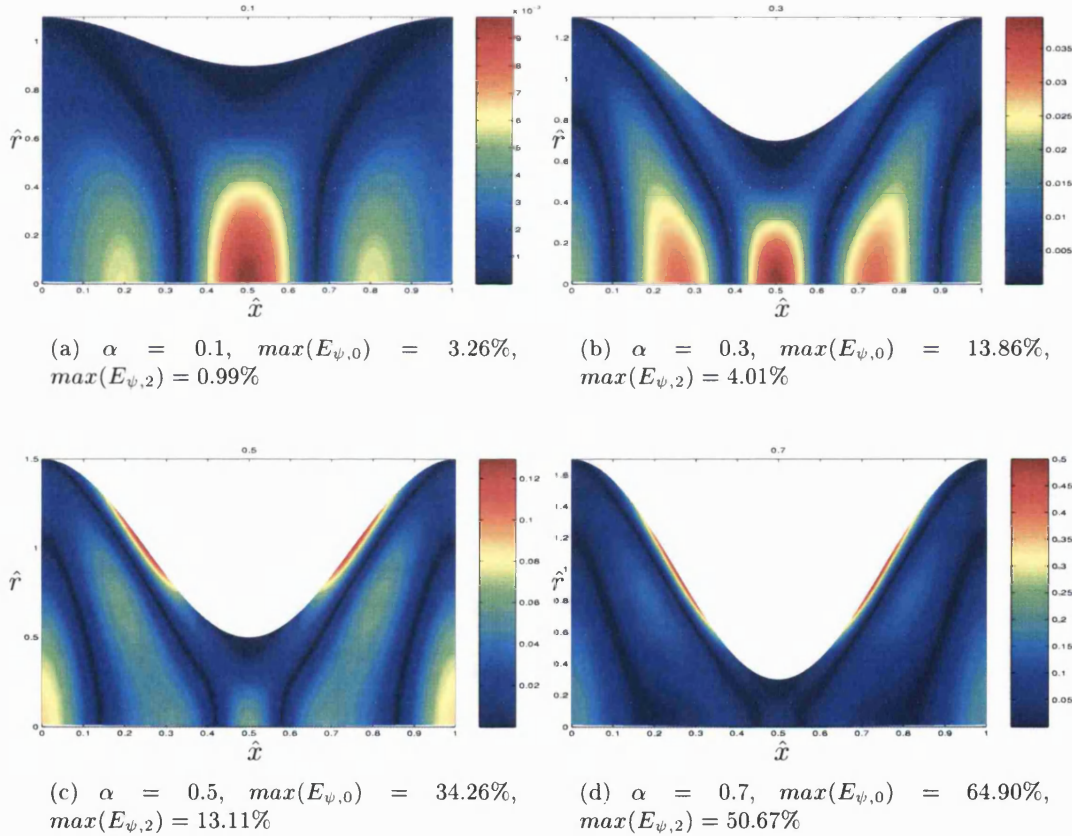


Figure 3-4: Contour Plots of $E_{\psi,2}$ a Measure of the Relative Size of $\epsilon^4 \hat{\psi}_{2,xx}$ to $\hat{\phi}_0 + \epsilon^2 \hat{\phi}_2$ for $\hat{\psi}_w = 0.2$, $\epsilon = 0.2$

In Figure 3-4 we recover curvature in our streamfunction solution by taking the perturbation expansion solution up to $O(\epsilon^2)$ yielding much better results, $\max(E_{\psi,2}) <$

$\max(E_{\psi,0})$ when α is small. We note in all cases only a small proportion of the wave suffers from such ‘errors’. The ‘errors’ do increase as the flow rate increases. The leading order solution is sufficient for $\epsilon < 0.2, \alpha \leq 0.7$ and small flow rates which is in accordance with the anatomical parameters for the intestine [73].

3.4.2 Determining The Semi-Analytic Peristaltic Velocities

The axial and transverse velocities are found by the streamfunction velocity definitions $\hat{u} = (1/r)\hat{\phi}_{\hat{r}}$ and $\hat{v} = -(1/r)\hat{\phi}_{\hat{x}}$. Hence for the power series in ϵ^2 we derive the peristaltic velocities

$$\begin{aligned}\hat{u} &= \hat{u}_0 + \epsilon^2 \hat{u}_2 = 4A\hat{r}^2 + 2B + \epsilon^2 \left(\frac{A''}{2}\hat{r}^4 + \frac{2A''\hat{f}^2}{3}\hat{r}^2 - \frac{A''\hat{f}^4}{6} \right) + O(\epsilon^4), \\ \hat{v} &= \hat{v}_0 + \epsilon^2 \hat{v}_2 = -A'\hat{r}^3 - B'\hat{r} + \epsilon^2 \left(\frac{A'''}{12}\hat{r}^5 + \frac{A'''\hat{f}^2}{6}\hat{r}^3 - \frac{A'''\hat{f}^4}{12}\hat{r} \right) + O(\epsilon^4).\end{aligned}\tag{3.4.7}$$

By dimensionalising \hat{u} , we find the leading order velocities are consistent with those derived by Barton et al. [5]. For very small relative wave amplitude ($\alpha \ll 1$), the peristaltic tube is approximately cylindrical, $\hat{f} \approx 1$. Consequently there is zero vertical motion, $\hat{v} \approx 0$, and horizontal velocity takes the form

$$\hat{u} \approx \left((-4\hat{\psi}_w - 2)\hat{r}^2 + (4\hat{\psi}_w + 1) \right) = \hat{U}(1 - \hat{r}^2) - 1.$$

This is Poiseuille flow in the wave frame with mean axial velocity $\hat{U} = 4\hat{\psi}_w + 2$. Therefore, for any α , the axial velocity is similar to Poiseuille flow, producing a parabolic velocity profile at every axial cross section of the domain.

3.5 Pumping and Copumping: A Consequence of Peristaltic Flow

In the absence of a pressure drop along a tube (i.e. closed ends) there is no flow. A sudden induced peristaltic wave will cause fluid to flow backwards in the contracted regions causing viscous losses, inducing a pressure drop in the opposite direction to the wave or a pressure rise in the direction of the wave. Now if the ends were open and there was a pressure drop across the tube then fluid is pumped by (i) peristalsis and (ii) a driving pressure gradient. So fluid will flow in the direction of the wave in the uncontracted part of the wave, with less fluid flowing backwards in the contracted region if the tube ends were closed. If there is a pressure rise, fluid is driven by *pumping*, and for a pressure drop, fluid is driven by *copumping*, due to the additional flow from a pressure difference. In this section we determine the pressure gradient over one wavelength and show that it is linearly dependent on the flow rate $\Delta\hat{p}_\lambda = c_1\hat{\psi}_w + c_2$.

3.5.1 Determining The Pressure Gradient

Of particular interest is the relationship between pressure and the flow rate. By Stokes equation (3.2.3), the nondimensional pressure gradients are described by

$$\begin{aligned}\frac{\partial \bar{p}}{\partial \hat{x}} &= -\frac{\mu}{\hat{r}} \frac{\partial \bar{\phi}}{\partial \hat{r}} \quad \rightarrow \quad \frac{\partial \hat{p}}{\partial \hat{x}} = -\frac{1}{\hat{r}} \frac{\partial \bar{\phi}}{\partial \hat{r}}, \\ \frac{\partial \bar{p}}{\partial \hat{r}} &= \frac{\mu}{\hat{r}} \frac{\partial \bar{\phi}}{\partial \hat{x}} \quad \rightarrow \quad \frac{\partial \hat{p}}{\partial \hat{r}} = \frac{\epsilon^2}{\hat{r}} \frac{\partial \bar{\phi}}{\partial \hat{x}}.\end{aligned}$$

We consider a perturbation expansion for the pressure gradients to derive

$$\begin{aligned}\hat{p}_{\hat{x}} &= \hat{p}_{0,\hat{x}} + \epsilon^2 \hat{p}_{2,\hat{x}} = 16A + \epsilon^2 \left(-4A''\hat{r}^2 + 2 \left(B'' + \frac{4A''\hat{r}^2}{3} \right) \right), \\ \hat{p}_{\hat{r}} &= \hat{p}_{0,\hat{r}} + \epsilon^2 \hat{p}_{2,\hat{r}} = \epsilon^2 (-8A'\hat{r}).\end{aligned}$$

In the leading order solution the transverse pressure gradient is negligible, which is to be expected as there is no streamline curvature to induce it. Therefore, the pressure gradient is independent of \hat{r} but is also independent of \hat{t} . We assumed there is an integral number of waves moving down the tube, $L_x = n\lambda$, otherwise the volume of the domain, the flow rate and pressure drop between the ends of the tube would be changing with time. Hence, the pressure gradient is only a function of \hat{x} and we can calculate the pressure distribution $p = p(x)$ but more importantly we determine the change in pressure over one wave cycle, $\Delta \hat{p}_\lambda$. The pressure gradient is the same whether it is measured in the fixed frame or in the wave frame. By the Fundamental Theorem of Calculus pressure at any point \hat{x} in the wave frame is given by

$$\hat{p}(\hat{x}) = \hat{p}(0) + \int_0^{\hat{x}} \frac{d\hat{p}}{d\hat{x}} d\hat{x}$$

which can be rearranged for the change in pressure over one wavelength

$$\Delta \hat{p}_\lambda = \int_0^1 \frac{d\hat{p}}{d\hat{x}} d\hat{x}.$$

Using Abramowitz and Stegun [1] we integrate for the pressure gradient

$$\Delta \hat{p}_\lambda = - \int_0^1 \frac{16\hat{\psi}_w d\hat{x}}{(1 + \alpha \cos(2\pi\hat{x}))^4} - \int_0^1 \frac{8d\hat{x}}{(1 + \alpha \cos(2\pi\hat{x}))^2} = -\frac{8\hat{\psi}_w(2 + 3\alpha^2)}{(1 - \alpha^2)^{\frac{7}{2}}} - \frac{8}{(1 - \alpha^2)^{\frac{3}{2}}}.$$

We rearrange the above equation for the flow rate $\hat{\psi}_w$ as a function of the pressure change $\Delta \hat{p}_\lambda$ and amplitude of vibration α ,

$$\hat{\psi}_w = -\frac{(1 - \alpha^2)^{\frac{7}{2}} \Delta \hat{p}_\lambda}{8(2 + 3\alpha^2)} - \frac{(1 - \alpha^2)^2}{(2 + 3\alpha^2)}. \quad (3.5.1)$$

To solve for the peristaltic flow we need to find $\hat{\psi}_w$, this is done by prescribing the pressure change over the domain, $\Delta \hat{p}_{L_x} = n\Delta \hat{p}_\lambda$.

3.5.2 Relating the Fluid Flow Rates to the Pressure Gradient

We have determined that the wave frame flow rate is directly proportional to the pressure drop over a wavelength. For a zero pressure rise (free pumping) we denote the corresponding dimensionless flow rate by $\hat{\psi}_{w0}$, and for a zero flow rate we denote the pressure change by $\Delta\hat{p}_0$. So

$$\hat{\psi}_{w0} = -\frac{(1-\alpha^2)^2}{2+3\alpha^2}, \quad \Delta\hat{p}_0 = -\frac{8}{(1-\alpha^2)^{\frac{3}{2}}}.$$

A zero flow rate corresponds to a pressure drop and in the case of a peristaltic pump, a sufficiently negative flow rate $\hat{\psi} < \hat{\psi}_0$ is required for a pressure rise ($\Delta\hat{p} > 0$). Under certain conditions $\Delta\hat{p}_\lambda$ attains a maximum. First, consider the *instantaneous volume flow rate* Q , the flow rate in fixed frame coordinates. Without introducing further notation for nondimensionalised coordinates in the fixed frame, the dimensionalised instantaneous flow rate in terms of the wave frame flow rate is:

$$Q(x, t) = 2\pi \int_0^f ur dr = 2\pi \int_0^f (\bar{u} + \sigma)r dr = 2\pi \int_0^f \bar{u}\bar{r} d\bar{r} + 2\pi \int_0^f \sigma r dr = \bar{q} + \pi\sigma f^2.$$

The average instantaneous time flow rate over one period \bar{Q} , known as the *time-mean volume flow rate* [64] and its nondimensional equivalent \hat{Q} are:

$$\bar{Q} = \frac{1}{T} \int_0^T Q dt = q + \pi\sigma \left(h^2 + \frac{1}{2}\eta^2 \right), \quad \hat{Q} = \hat{\psi}_w + \frac{1}{2} \left(1 + \frac{1}{2}\alpha^2 \right).$$

Substituting \hat{Q} for $\hat{\psi}_w$ in (3.5.1) yields

$$\frac{\hat{Q}}{2\pi} = \frac{1}{2} \left(1 + \frac{1}{2}\alpha^2 \right) - \frac{(1-\alpha^2)^2}{2+3\alpha^2} - \frac{\Delta\hat{p}_\lambda(1-\alpha^2)^{\frac{7}{2}}}{8(2+3\alpha^2)},$$

an equation for the time mean flow which is directly proportional to the pressure change and takes the form $\hat{Q} = A - B\Delta\hat{p}_\lambda$. In the case of free pumping $\Delta\hat{p}_\lambda = 0$, there exists a flow rate $\hat{Q} = A$ induced by the peristaltic waves. Now, when peristalsis is acting as a pump a positive pressure gradient creates a negative flow $-B\Delta\hat{p}_\lambda$, that represents ‘a back leakage Poiseuille flow’ [41]. Now if we consider a zero time flow rate, then this will produce a maximum pressure rise $\Delta\hat{p}_{\max}$. Similarly a zero pressure rise will correspond to a maximum flow rate \hat{Q}_0 ,

$$\frac{\hat{Q}_0}{2\pi} = \left(1 + \frac{1}{2}\alpha^2 \right) - \frac{(1-\alpha^2)^2}{2+3\alpha^2}, \quad \Delta\hat{p}_{\max} = \frac{4(1+\frac{1}{2}\alpha^2)(2+3\alpha^2)}{(1-\alpha^2)^{\frac{7}{2}}} - \frac{8}{(1-\alpha^2)^{\frac{3}{2}}}.$$

In the literature, [64], the *pumping range* is defined in the region $0 \leq \Delta\hat{p}_\lambda \leq \Delta\hat{p}_{\max}$ and is given correspondingly in terms of the flow rates $0 \leq \hat{Q} \leq \hat{Q}_0$. Hence, a maximum

pressure rise $\Delta\hat{p}_{\max}$ may be attainable if the tube end was closed. However, if there is too great a pressure rise $\Delta\hat{p}_\lambda > \Delta\hat{p}_{\max}$ then there is on average a negative flow rate $\hat{Q} < 0$, a contradiction to the role of peristaltic pumping (an unlikely scenario). Copumping occurs under a pressure drop, $\Delta\hat{p}_\lambda < 0$, which in terms of flow rates satisfies $\hat{Q} > \hat{Q}_0$. One other point to note is that as the wall deformation reaches its maximum, $\alpha \rightarrow 1$, the flow rate tends to $\hat{Q}_0 \rightarrow 3/2\pi$, (agreeing with [5] when dimensionalised) however, this leads to a large pressure gradient tending to negative infinity. We are not concerned with such large amplitude of vibration in the intestine, since in the intestine α is at most 0.6 [5].

3.5.3 The Intestine as a Pump

Peristaltic motion has been studied with the intention to apply the fluid dynamics to machinery in industry biofluids in the human body. Our aim is to understand the fluid dynamics of the small intestine determined by the peristaltic motion and the pressure gradient. The first authors who applied peristalsis were Barton and Raynor [5]. To apply the theory the following anatomical parameters [5] were used² We observe

Anatomical Parameter	Variable	Value	In SI units
Average Length of Intestine [62]	L_x	22.5 feet	675 cm
Average Radius Nondisturbed Tube	h	1.25cm	-
Speed of Peristaltic Wave	σ	2cm/min	0.03cm/s
Peristaltic Wavelength	λ	8.01cm	-
Wave Number	ϵ	0.156	-
Amplitude ratio	α	0.6	-
Time for Chyme to Pass Through SI	T_1	4.5hrs	16200s

Table 3.1: A Table of Anatomical Parameters for the Intestine applied by Barton et al. [5].

the wave number ϵ is sufficiently small (in conjunction with results from Figure 3-3) to justify applying the leading order slowly variant analytical solution (3.4.4). From the anatomical data in Table 3.1, the average chyme velocity can be shown to be $u_c = 2.54$ cm per minute. In [5], Barton et al. applied the time mean volume flow rate \bar{Q} to determine an average velocity $\bar{V} = 1.83$ cm per minute, by assuming there was a *zero pressure gradient* which is a gross assumption. He predicted a negative pressure gradient would make the model realistic. We relate the average velocity to the dimensionless flow rate by

$$\bar{V} = \sigma \times \frac{\hat{Q}}{\pi} = \sigma \left(2\hat{\psi}_w + 1 + \frac{1}{2}\alpha^2 \right),$$

which using (3.5.1), depends on the pressure gradient by

²Parameter values taken from Piersol, Evans, Houssay, Fulton used in Stoll et al. [73]

$$\bar{V} = \sigma \left(2 \left(-\frac{(1-\alpha^2)^{\frac{7}{2}} \Delta \hat{p}_\lambda}{8(2+3\alpha^2)} - \frac{(1-\alpha^2)^2}{(2+3\alpha^2)} \right) + \left(1 + \frac{1}{2}\alpha^2 \right) \right) = \sigma \left(2(c_1 + c_2 \Delta \hat{p}_\lambda) + \left(1 + \frac{1}{2}\alpha^2 \right) \right),$$

for constants c_1, c_2 depending on the amplitude of vibration (see (3.5.1)). Hence the pressure gradient $\Delta \hat{p}_\lambda$ can be determined from the anatomical data by setting $\bar{V} = u_c$ so that

$$\Delta \hat{p}_\lambda = \frac{0.5 (\bar{V} \sigma^{-1} - 1 - 0.5\alpha^2) - c_1}{c_2} = -29.2$$

Hence matching the mean velocity based on Barton's data it appears a negative pressure gradient is present. Unfortunately the results found by Barton depend entirely on his anatomical parameters in table (3.1) being 100% accurate. In fact the length of the intestine estimated to be 22.5 feet by Piersol [62] in 1930 seems a little exaggerated. By further reading we found the value was later remeasured by Vander et al. [75] to be 9 feet, about 270cm. This has paramount implications on the nature of peristaltic flow in the intestine. Originally a pressure drop was calculated but by recalculating we determine a pressure rise $\Delta \hat{p}_\lambda = 21.1$ ($\hat{\psi}_w = -0.31$) is required to attain similar observed and theoretical mean chyme speed. It appears different measurements of the intestine can imply pumping or copumping, and in these measurements we have assumed a constant pressure gradient. An exact measurement of the intraluminal pressure would be key in the development of a model. We discuss the difficulty in achieving such a result.

Since the advent of peristaltic models in the 70s, current literature has progressed and described the different types of intestinal motility that occur in the intestine. However, due to the complex nature of the intestine, no intestine is unique, and so anatomical data varies and are difficult to measure. One such quantity, is the intraluminal pressure. Gastrointestinal manometry studies are tests that measure intraluminal pressure. They also measure the coordination of activity in the muscles of the GI tract.

One such device is the water perfused manometric catheter. They are able to measure pressure over the length of a catheter, not just at a specific point, However, they do not extend much past the entrance to the intestine due to the large length required to go from oesophagus to intestine. Alternatively expanded balloons may be used to measure pressure, but all methods will in some way affect the value they are trying to measure. A further difficulty in understanding pressure in the intestine is that there is no way to measure the pressure gradient over the whole intestine, only intraluminal pressure for portions of the intestine. One such area is the entrance at the duodenum which varies as it is affected by the gastric emptying at the pyloric sphincter [21]. No clear measurement can be given for $\Delta \hat{p}_\lambda$, however, we can roughly estimate it from the observed averaged chyme velocity.

The purpose of the intestine is to pump fluid and the nature of the flow most likely

depends on whether the ileocecal valve (that connects the intestine to the colon) is open or closed. When it is closed, as it is for the majority of the time, peristaltic motion must be of pure pumping ($\Delta\hat{p}_\lambda > 0$) and copumping when the valve opens [47]. Pressure should build up until the valve opens at which point flow should be of pure transport - copumping. Lew et al. [47] proposed that the build up of pressure should promote solute absorption. Another method that promotes absorption through radial mixing of solute is trapping.

3.6 Describing Fluid Particle Motion

In dealing with fluid flow there are two ways to describe the motion kinematically: *Lagrangian* or *Eulerian*. A Lagrangian approach obtains the motion of individual particles specifying the coordinates of the particles' centroids as functions of time, yielding particle path lines. A collection of said path lines are known as *streamlines*. An Eulerian approach describes flow as a velocity vector field where velocities of particles at points in space are determined (as was described in the previous section). The set of vectors representing the velocities describes the motion of the fluid in that space. Therefore the average velocity of individual particles is the mean Lagrangian velocity whereas the mean Eulerian velocity is the average velocity of all particles passing through a fixed point in space. Each approach has its disadvantages; Lagrangian descriptions are difficult to obtain if turbulence exists in the flow whereas an Eulerian description falters in unsteady flow where transport properties such as mixing features and circulation patterns are present. Converting from one approach to another is possible with difficulty depending on the type of flow.

3.6.1 Peristaltic Phenomenon 1: Reflux

An interesting phenomenon occurring in peristaltic flow is *Reflux* and was discovered by Shapiro et al. [64]. It occurs when some fluid particles undergo a net retrograde motion after some period. It is not possible to determine whether a particle moves with or against a wave (a net Lagrangian displacement) from the time mean velocity (the axial velocity averaged over a period, an Eulerian quantity). However, since peristaltic flow is steady in the wave frame fluid particles can be identified by specific wave frame streamlines. It was mentioned in Shapiro et al. [64] that pumping only occurs in the pumping range. This was proved for the channel flow case, and mentioned for the axisymmetric case. We present the proof for the axisymmetric case in Appendix §C.2.

3.6.2 Peristaltic Phenomenon 2: Trapping

Another phenomenon found in peristaltic flows is *Trapping*. For large vibrations and high flow rates streamlines which normally resemble the shape of the wall, split and

in enclosed streamlines encompass a bolus of fluid particles which then undergo recirculation. In general the trapped fluid advances with the mean speed of the wave [64]. Previous literature has focussed on trapping in the pumping range, here we consider trapping for all positive flow rates $\hat{Q} > 0$. As the flow rate increases from pumping to copumping, trapping attached to the centreline disconnects from the centerline and approaches the peristaltic wall with decreasing volume. The various forms trapping takes has strong implications on the amount of mixing occurring in the fluid. Criteria for centerline trapping was the existence of a streamline other than the centreline streamline where $\hat{\psi} = 0$. However this is only when the waves are pumping. Streamlines with $\hat{\psi} = 0$, also exist for copumping where the trapped streamlines will have detached from the centreline. In this case we wish to find the streamlines that surround the bolus. To do this we need to understand fully the properties of the analytical streamfunction $\hat{\psi}$ for different flow rate boundary conditions $\hat{\psi}_w$ and amplitude of vibration α .

3.6.3 The Different Types of Peristaltic Flow

For peristaltic flow we elucidate seven different types of flow for varying $\hat{\psi}_w \in \mathbb{R}$ and $\alpha \in [0, 1]$ in Figure 3-5. We determine the conditions for the different types of flows in the following subsection. From Figure 3-5 there are five flow regions occurring with a purely positive time mean volume flow rate $\hat{Q} \geq 0$, two regions for pumping (as described in Shapiro et al. [64]) and three types of flow for copumping. The results are best viewed in a flow rate $\hat{\psi}_w$ versus amplitude ratio α graph, rather than pressure gradient $\Delta\hat{p}_\lambda$ against α . (See Appendix §C.3 for the alternate visualisations.)

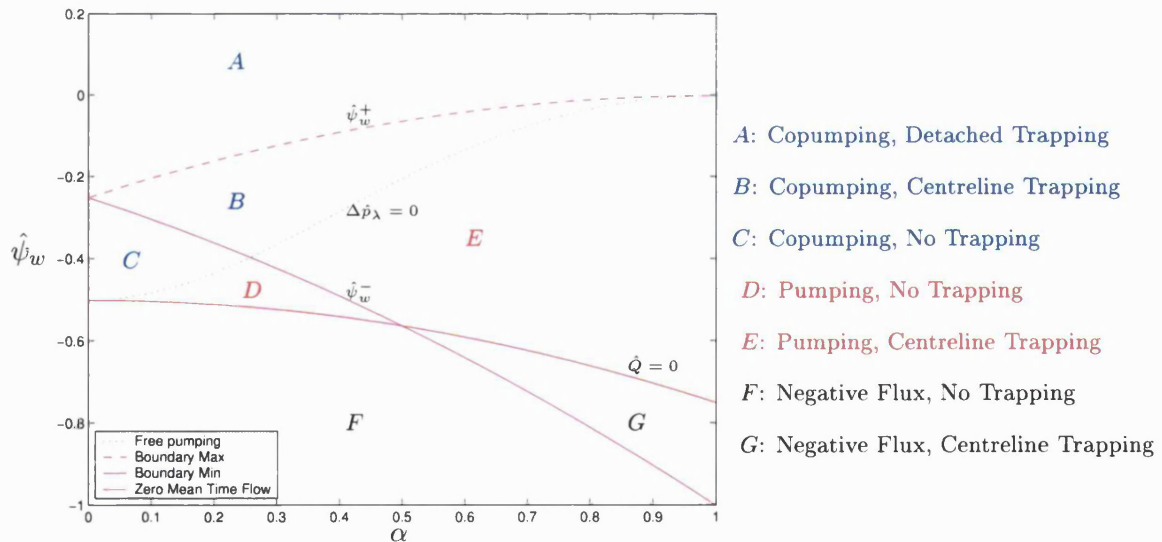


Figure 3-5: A Graph of the Different Flow Regions and Behaviour for Arbitrary Flow Rate $\hat{\psi}_w$ and Amplitude Ratio α

We observe that the different types of flows are linear combinations of (i) either pumping, copumping or negative flux and (ii) no trapping, centreline trapping or detached trapping.

Examples of Streamfunction Behaviour

In figure (3-6) we present the possibility of four different types for fixed amplitude of vibration, $\alpha = 0.1$, and varying flow rates.

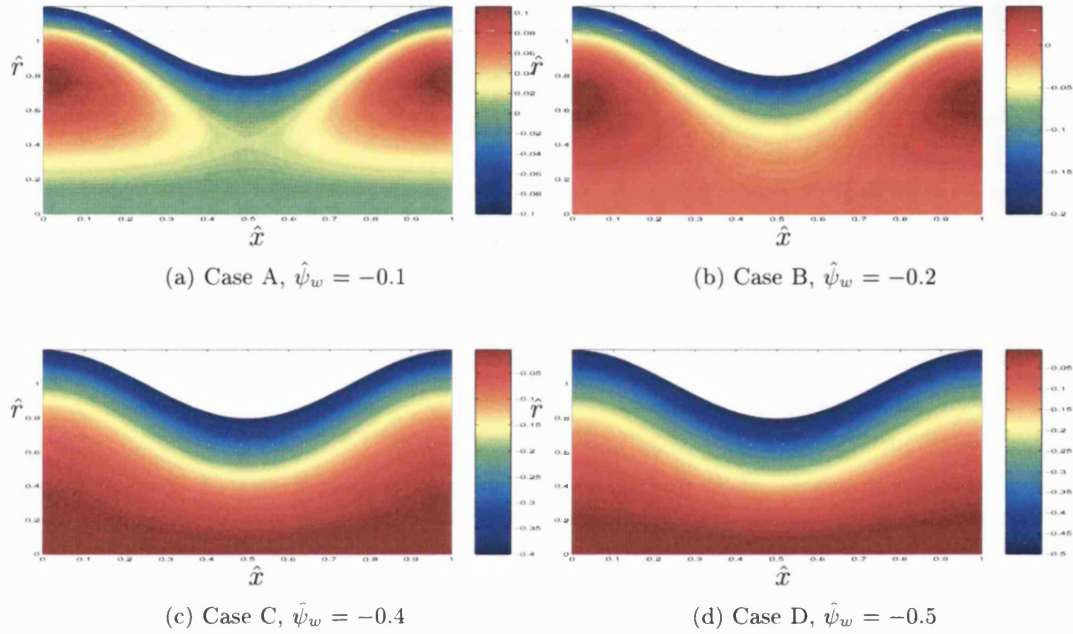


Figure 3-6: Contour Plots of the Streamfunction for Cases A,B,C,D with amplitude of vibration $\alpha = 0.2$

We present results for small flow rates where pumping forces dominate. In case A we observe detached trapping, and centreline trapping in case B. What is not intuitively obvious from the graphs for case C and D is that although solutions of the streamfunction look very similar, fluid particles close to the boundary in case D undergo reflux. We now determine the conditions used in determining the different types of flows seen in Figure 3-5.

3.6.4 Understanding the Behaviour of the Semi-Analytic Streamfunction

We define the peristaltic domain $\Omega \subset \mathbb{R}^2$ by $\Omega = [0, 1] \times [0, \hat{f}(\hat{x})]$. Consider the Stokes streamfunction $\hat{\psi}$ prescribed by (3.4.4) on Ω . At the centreline axisymmetry imposes (i) a zero streamfunction value and (ii) zero symmetry derivatives of the streamfunction

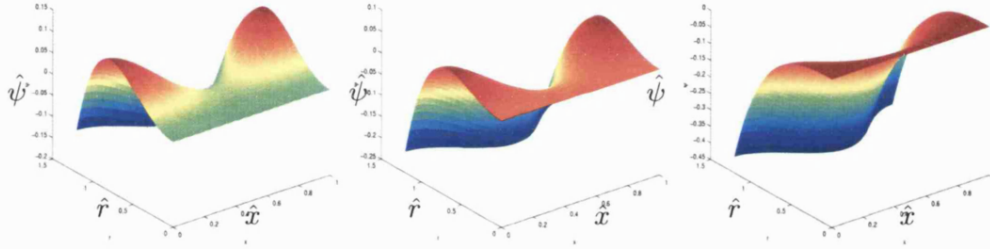
($\hat{\psi}_{\hat{r}} = \hat{\psi}_{\hat{r}\hat{r}} = 0$). Hence, the streamfunction is either increasing or decreasing in \hat{r} away from the centreline, depending on the sign of the second derivative $\hat{\psi}_{\hat{r}\hat{r}}$.

Lemma 3.1. *Streamfunction $\hat{\psi}(\hat{x}, \hat{r})$ is increasing in r if $\hat{\psi}_w > -\frac{1}{4}\hat{f}^2(\hat{x})$ and everywhere increasing for $\hat{\psi}_w > -\frac{1}{4}(1-\alpha)^2 = \hat{\psi}_w^-$ and decreasing for $\hat{\psi}_w < -\frac{1}{4}(1+\alpha)^2 =: \hat{\psi}_w^+$.*

Proof. Differentiating $\hat{\psi}$ in the radial direction yields $\hat{\psi}_{\hat{r}\hat{r}}(x, r) = 12A(\hat{x})r^2 + 2B(\hat{x})$. At the centreline ($\hat{r} = 0$) the second derivative simplifies to $\hat{\psi}_{\hat{r}\hat{r}} = 2B(\hat{x}) = \frac{4\hat{\psi}_w}{\hat{f}^2(\hat{x})} + 1$ which is increasing if $\hat{\psi}_w > -\frac{1}{4}\hat{f}^2(\hat{x})$. The periodic boundary \hat{f} is bounded by its maximum and minimum so that

$$\hat{f}_{\min} = 1 - \alpha \leq \hat{f}(\hat{x}) \leq 1 + \alpha = \hat{f}_{\max}$$

Hence, for $\hat{\psi}_w > -\frac{1}{4}(1 - \alpha)^2$ which we denote $\hat{\psi}_w^-$ the streamfunction is always increasing, and conversely is always decreasing for $\hat{\psi}_w < -\frac{1}{4}(1 + \alpha)^2$, which we denote $\hat{\psi}_w^+$. \square



(a) Case A, $\hat{\psi}_w = -0.1$

(b) Case B, $\hat{\psi}_w = -0.2$

(c) Case C, $\hat{\psi}_w = -0.4$

Figure 3-7: Surface Plots of the Streamfunction for Cases A,B,C with amplitude of vibration $\alpha = 0.2$ to Illustrate Lemma 2

At the peristaltic boundary $\hat{r} = \hat{f}(\hat{x})$, the imposed no slip condition implies the streamfunction gradient satisfies $\hat{\psi}_{\hat{r}} < 0$. Hence the streamfunction achieves a maximum if it is increasing in \hat{r} from the centreline. The critical points of $\hat{\psi}$ then correspond to the location of stagnant fluid particles and regions of enclosed streamlines.

Lemma 3.2. *For $\hat{r} \neq 0$, there are (i) two critical points when $\hat{\psi}_w > -\frac{1}{2}(1 - \alpha)^2$ (ii) one critical point in the range $-\frac{1}{2}(1 - \alpha)^2 > \hat{\psi}_w > -\frac{1}{2}(1 + \alpha)^2$ and (iii) none for $\hat{\psi}_w < -\frac{1}{2}(1 + \alpha)^2$.*

Proof. The point $(\hat{x}_0, \hat{r}_0) \in \Omega$ is a critical point of $\hat{\psi}$ if $\nabla\hat{\psi}(\hat{x}_0, \hat{r}_0) = 0$. The axial derivative condition $\hat{\psi}_{\hat{x}} = A'(\hat{x})r^4 + B'(\hat{x})r^2 = 0$ is satisfied only when $\hat{f}_{\hat{x}} = 0$ which occurs at the points of maximum and minimum of the boundary function $\hat{x} = 0, \frac{1}{2}$.

The radial derivative $\hat{\psi}_r = 4A(\hat{x})r^3 + 2B(\hat{x})r$ has roots when:

$$0 < \hat{r}_0^2 = -\frac{B(\hat{x})}{2A(\hat{x})} = \frac{\hat{f}^2(4\hat{\psi}_w + \hat{f}^2)}{2(2\hat{\psi}_w + \hat{f}^2)} < \hat{f}^2.$$

This inequality is satisfied when both the numerator and the denominator take the same sign:

$$0 < 4\hat{\psi}_w + \hat{f}^2 < 2(2\hat{\psi}_w + \hat{f}^2) \quad \text{or} \quad 0 > 4\hat{\psi}_w + \hat{f}^2 > 2(2\hat{\psi}_w + \hat{f}^2).$$

The rightmost inequality equation can never be satisfied since $\hat{f}^2(\hat{x})$ is always positive. It follows from solving the leftmost that there exists a root when $\hat{\psi}_w > -\frac{1}{4}\hat{f}^2(\hat{x})$. Hence, there exists one critical point when the boundary takes a minimum, $\hat{x} = \frac{1}{2}$, that exists for all $\hat{\psi}_w > \hat{\psi}_w^-$. The second critical point occurs when the boundary takes a maximum, $\hat{x} = 0$, which exists for all $\hat{\psi}_w > \hat{\psi}_w^+$. \square

Lemma 3.3. *The critical point that occurs when the boundary takes its maximum is a relative maximum. The critical point when the boundary takes a minimum is a saddle point.*³

Proof. Evaluating the second derivatives of $\hat{\psi}$ at the critical points (\hat{x}_0, \hat{r}_0) implies

$$\begin{aligned} \hat{\psi}_{\hat{r}\hat{r}}(\hat{x}_0, \hat{r}_0) &= 12A(\hat{x}_0)\hat{r}_0^2 + 2B(\hat{x}_0) = 12A(\hat{x}_0) \left(-\frac{B(\hat{x})}{2A(\hat{x})} \right) + 2B(\hat{x}_0) \\ &= -4B(\hat{x}_0) = -\frac{8\hat{\psi}_2}{\hat{f}^2(\hat{x}_0)} - 2 < 0, \end{aligned}$$

and we obtain a negative second radial derivative term by applying Lemma (3.1). The cross derivative term

$$\hat{\psi}_{\hat{r}\hat{x}}(\hat{x}_0, \hat{r}_0) = 4A'(\hat{x}_0)\hat{r}_0^3 + 2B'(\hat{x})\hat{r}_0 = 0.$$

vanishes since $\hat{f}'_{\hat{x}}(\hat{x}_0) = 0$. The second axial derivative takes the form

$$\hat{\psi}_{\hat{x}\hat{x}}(\hat{x}_0, \hat{x}_0) = A''(\hat{x}_0)\hat{r}_0^4 + B''(\hat{x}_0)\hat{r}_0^2 = \frac{(4\hat{\psi}_w + \hat{f}^2)(\hat{f}''\hat{f}^4)}{8\hat{f}(2\hat{\psi}_w + \hat{f}^2)^2},$$

where $\text{sgn}(\hat{\psi}_{\hat{x}\hat{x}}) = \text{sgn}(\hat{f}'')$ when evaluated at the critical points. The discriminant $\Delta = \hat{\psi}_{\hat{x}\hat{x}}\hat{\psi}_{\hat{r}\hat{r}} - (\hat{\psi}_{\hat{r}\hat{x}}^2)$ determines the nature of the critical point. At $\hat{x} = \frac{1}{2}$, we obtain positive \hat{f}'' , leading to a negative discriminant hence a *saddle point*. By the nature of \hat{f} the other critical point has positive discriminant and is either a *relative maximum* or *minimum* depending on the sign of $\hat{\psi}(0, \hat{r}_0)$ which is positive since $\hat{\psi}_w > \hat{\psi}_w^+$, a *relative maximum*. \square

³A stationary point but not an extremum

Consequently by Lemmas (3.1), (3.2) and (3.3), the saddle point at $\hat{x}_0 = \frac{1}{2}$, and relative maximum at $\hat{x}_0 = 0$, satisfy radial position and streamfunction value

$$\hat{r}_0^2 = -\frac{B(\hat{x})}{2A(\hat{x})} = \frac{\hat{f}^2(\hat{x}_0)(4\hat{\psi}_w + \hat{f}^2(\hat{x}_0))}{2(2\hat{\psi}_w + \hat{f}^2(\hat{x}_0))}, \quad (3.6.1)$$

$$\psi(\hat{x}_0, \hat{r}_0) = -\frac{B^2(\hat{x})}{4A(\hat{x})} = \frac{(4\hat{\psi}_w + \hat{f}^2(\hat{x}_0))^2}{8(2\hat{\psi}_w + \hat{f}^2(\hat{x}_0))}. \quad (3.6.2)$$

Lemma 3.4. *Centerline trapping occurs only when the relative maximum is the only critical point. When both critical points exist there is detached trapping surrounded by a streamfunction whose value is equivalent to that of the saddle point.*

Proof. We consider the case of detached trapping first. When there exists two critical points, there is a relative maximum, and most notably a saddle point. We define the saddle point level set by

$$S^* = S(\hat{\psi}_{sad}) = \left\{ (\hat{x}, \hat{r}) \in \Omega : \hat{\psi}(\hat{x}, \hat{r}) = \hat{\psi}\left(\frac{1}{2}, \hat{r}_0\right) = \hat{\psi}_{sad} \right\}.$$

We denote the set of level sets with streamfunction greater than that of the saddle point by $S^a = \{S(\hat{\psi}) : \hat{\psi}(\hat{x}, \hat{r}) > \hat{\psi}_{sad}\}$ which forms a connected set⁴, with a relative maximum.

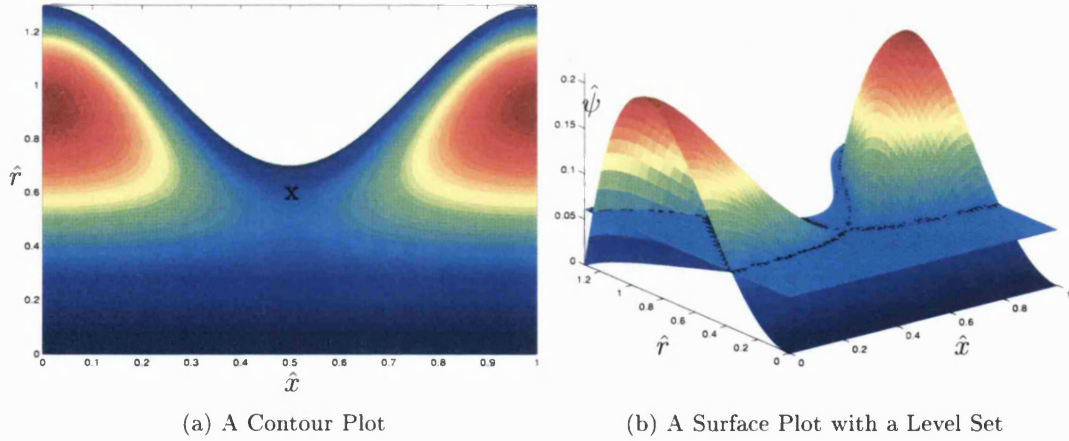


Figure 3-8: An Example Graph to Show Regions of Detached Streamline Trapping ($\alpha = 0.3, \hat{\psi}_w = 0$)

Particle paths correspond to streamlines, hence the relative maximum is a stagnation point surrounded by a trapped bolus of fluid particles in S^a and are confined to

⁴A set which can not be partitioned into two nonempty subsets such that each subset has no points in common with the other

S^a by the separatrix S^{*5} . All level sets below defined by the set $S^b = \{S(\hat{\psi}) : \hat{\psi}(\hat{x}, \hat{r}) < \hat{\psi}_{sad}\}$ form disconnected sets D_1, D_2 where particles in D_i are confined to D_i for all i . Centerline trapping follows the same argument but the separatrix S now occurs at $S_0 = \{(\hat{x}, \hat{r}) \in \Omega : \hat{\psi}(\hat{x}, \hat{r}) = 0\}$ and the set S_b is no longer disconnected. \square

In the pumping range, trapping is always attached to the centreline since $\hat{\psi}_w^- \geq \hat{\psi}_{w0}$. We have shown that detached trapping exists for $\hat{\psi}_w < 0$ but only when the flow rate is sufficiently large and is driven by copumping. However, copumping does not necessarily imply trapping $\hat{\psi}_w^+ \geq \hat{\psi}_{w0}$ for $\alpha \in [0, 0.25]$. From the bounds $\hat{\psi}_w^-, \hat{\psi}_w^+$ on the flow rate $\hat{\psi}_w$, we determine the centerline trapping limits stated by Shapiro [64] when the time mean flow rate \hat{Q} is normalised by \hat{Q}_0 :

$$\hat{Q}^- = \frac{(1 - 2\alpha)(2 + 3\alpha^2)}{\alpha^2(16 - \alpha^2)} < \frac{\hat{Q}}{\hat{Q}_0} < 1 < \frac{(1 + 2\alpha)(2 + 3\alpha^2)}{\alpha^2(16 - \alpha^2)} = \hat{Q}^+. \quad (3.6.3)$$

The graph of time mean flow against α (see Appendix §C.3) confirms our results agree with previous literature and the existence of trapping in the pumping range $0 \leq \hat{Q}/\hat{Q}_0 \leq 1$. We now determine the effects on the behaviour of the flow as the flow rate increases.

3.6.5 High Flow Rate Behaviour of the Fluid Flow

We consider the case of copumping when there are high flow rates. That is, a negative pressure gradient dominates the peristaltic pumping diminishing the effects of peristalsis. We prove that regions of trapping move away from the centerline to the peristaltic boundary with decreasing volume equivalently leading to laminar flow. In all cases we take the limit as $\hat{\psi}_w \rightarrow \infty$, however, this is purely to demonstrate the effects of a high flow rate, we assume the Reynolds number stays sufficiently small and the leading order semi-analytical solution remains valid.

Lemma 3.5. *As flow rate increases, $\hat{\psi}_w \rightarrow \infty$ we observe (i) the saddle point and the relative maximum move away from the centreline to the boundary and (ii) the streamfunction value at the critical points, $\hat{\psi}_c$, tends to $\hat{\psi}_w$.*

Proof. The radial positions of the critical points are given by

$$\hat{r}_0^2 = \frac{\hat{f}^2(\hat{x}_0)(4\hat{\psi}_w + \hat{f}^2(\hat{x}_0))}{2(2\hat{\psi}_w + \hat{f}^2(\hat{x}_0))}.$$

We have shown already that at $\hat{\psi}_w = \hat{\psi}_w^-$ detached trapping occurs, hence as $\hat{\psi}_w \rightarrow \infty$

⁵A separatrix marks the boundary between phase curves with different properties

by taking limits of the radial position of the critical points then

$$\lim_{\hat{\psi}_w \rightarrow \infty} \hat{r}_0^2 = \lim_{\hat{\psi}_w \rightarrow \infty} \frac{\hat{f}^2(\hat{x}_0)(4\hat{\psi}_w + \hat{f}^2(\hat{x}_0))}{2(2\hat{\psi}_w + \hat{f}^2(\hat{x}_0))} = \lim_{\hat{\psi}_w \rightarrow \infty} \frac{\hat{f}^2(\hat{x}_0) \left(4 + \frac{\hat{f}^2(\hat{x}_0)}{\hat{\psi}_w}\right)}{2 \left(2 + \frac{\hat{f}^2(\hat{x}_0)}{\hat{\psi}_w}\right)} = \hat{f}^2(\hat{x}_0).$$

Hence $\hat{r}_0 \rightarrow \hat{f}$ as $\hat{\psi}_w \rightarrow \infty$ and the critical points move to the wall for high flow rates. Now the streamfunction value at the critical point satisfies

$$\psi = -\frac{B^2(\hat{x})}{4A(\hat{x})} = \frac{(4\hat{\psi}_w + \hat{f}^2(\hat{x}_0))^2}{8(2\hat{\psi}_w + \hat{f}^2(\hat{x}_0))},$$

hence, as $\hat{\psi}_w \rightarrow \infty$ the limit of the streamfunction $\hat{\psi}_c$ is

$$\lim_{\hat{\psi}_w \rightarrow \infty} \hat{\psi}_c = \lim_{\hat{\psi}_w \rightarrow \infty} \frac{(4\hat{\psi}_w + \hat{f}^2(\hat{x}_0))^2}{8(2\hat{\psi}_w + \hat{f}^2(\hat{x}_0))} = \lim_{\hat{\psi}_w \rightarrow \infty} \frac{1}{8} \left(\frac{16\hat{\psi}_w + 8\hat{f}^2(\hat{x}_0) + \frac{\hat{f}^4(\hat{x}_0)}{\hat{\psi}_w}}{2 + \frac{\hat{f}^2(\hat{x}_0)}{\hat{\psi}_w}} \right) \rightarrow \hat{\psi}_w.$$

□

Lemma 3.6. *For high flow rates the volume of trapping decreases.*

Proof. The radial positions of the separatrix $\hat{r}_{1,2}$ that encompass detached trapping are the roots of the streamfunction equation

$$\hat{\psi}_{sad} = A(\hat{x})\hat{r}^4 + B(\hat{x})\hat{r}^2.$$

Rearranging we solve the quadratic equation in \hat{r}^2 for the separatrix positions given by

$$\hat{r}_{1,2}^2 = \frac{-B(\hat{x}) \pm \sqrt{B^2(\hat{x}) + 4\hat{\psi}_{sad}A(\hat{x})}}{2A(\hat{x})}, \quad (3.6.4)$$

hence as the flow rate increases

$$\begin{aligned} \lim_{\hat{\psi}_w \rightarrow \infty} \hat{r}_{1,2}^2 &= \lim_{\hat{\psi}_w \rightarrow \infty} \frac{-B(\hat{x}) \pm \sqrt{B^2(\hat{x}) + 4\hat{\psi}_{sad}A(\hat{x})}}{2A(\hat{x})} \\ &= \lim_{\hat{\psi}_w \rightarrow \infty} \frac{\left(\frac{2\hat{\psi}_w}{\hat{f}^2(\hat{x})} + \frac{1}{2}\right) \pm \sqrt{\left(\frac{2\hat{\psi}_w}{\hat{f}^2(\hat{x})} + \frac{1}{2}\right)^2 + 4\hat{\psi}_{sad} \left(-\frac{\hat{\psi}_w}{\hat{f}^2(\hat{x})} - \frac{1}{2\hat{f}^2(\hat{x})}\right)}}{2 \left(\frac{\hat{\psi}_w}{\hat{f}^2(\hat{x})} + \frac{1}{2\hat{f}^2(\hat{x})}\right)} \\ &= \lim_{\hat{\psi}_w \rightarrow \infty} \frac{\left(\frac{2}{\hat{f}^2(\hat{x})} + \frac{1}{2\hat{\psi}_w}\right) \pm \sqrt{\frac{1}{\hat{\psi}_w^2} \left(\frac{2\hat{\psi}_w}{\hat{f}^2(\hat{x})} + \frac{1}{2}\right)^2 + \frac{4\hat{\psi}_{sad}}{\hat{\psi}_w^2} \left(-\frac{\hat{\psi}_w}{\hat{f}^2(\hat{x})} - \frac{1}{2\hat{f}^2(\hat{x})}\right)}}{2 \left(\frac{1}{\hat{f}^2(\hat{x})} + \frac{1}{2\hat{\psi}_w\hat{f}^2(\hat{x})}\right)}. \end{aligned}$$

We know that $\hat{\psi}_{sad} \rightarrow \hat{\psi}_w$ by Lemma (3.5) hence

$$\begin{aligned}
\lim_{\hat{\psi}_w \rightarrow \infty} \hat{r}_{1,2}^2 &= \lim_{\hat{\psi}_w \rightarrow \infty} \frac{\left(\frac{2}{\hat{f}^2(\hat{x})} + \frac{1}{2\hat{\psi}_w}\right) \pm \sqrt{\left(\frac{2}{\hat{f}^2(\hat{x})} + \frac{1}{2\hat{\psi}_w}\right)^2 - 4\left(-\frac{1}{\hat{f}^2(\hat{x})} + \frac{1}{2\hat{\psi}_w\hat{f}^2(\hat{x})}\right)}}{2\left(\frac{1}{\hat{f}^2(\hat{x})} + \frac{1}{2\hat{\psi}_w\hat{f}^2(\hat{x})}\right)} \\
&= \frac{\frac{2}{\hat{f}^2(\hat{x})} \pm \sqrt{\left(\frac{2}{\hat{f}^2(\hat{x})}\right)^2 - \frac{4}{\hat{f}^4(\hat{x})}}}{\frac{2}{\hat{f}^4(\hat{x})}} = \hat{f}^2(\hat{x}).
\end{aligned}$$

Hence the separatrix tends to the wall with decreasing radius, $B^2(\hat{x}) + 4\hat{\psi}_{sad}A(\hat{x}) \rightarrow 0$ as flow rate tends to infinity. \square

Lemma 3.7. *For high flow rates the wave frame velocity is approximately Poiseuille flow in the wave frame.*

Proof. The wave frame velocity equation $\hat{u} = 4A(\hat{x})\hat{r}^2 + 2B(\hat{x})$ may be rewritten in the form

$$\begin{aligned}
\hat{u}(\hat{x}, \hat{r}) &= 4\left(-\frac{\hat{\psi}_w}{\hat{f}^4(\hat{x})} - \frac{1}{2\hat{f}^2(\hat{x})}\right)\hat{r}^2 + 2\left(\frac{\hat{\psi}_w}{\hat{f}^2(\hat{x})} + \frac{1}{2}\right) \\
&= 4\left(-\frac{\hat{\psi}_w}{\hat{f}^2(\hat{x})} - \frac{1}{2}\right)\frac{\hat{r}^2}{\hat{f}^2(\hat{x})} + \left(\frac{4\hat{\psi}_w}{\hat{f}^2(\hat{x})} + 1\right) \\
&= 4\left(\frac{\hat{\psi}_w}{\hat{f}^2(\hat{x})} + \frac{1}{2}\right)\left(1 - \frac{\hat{r}^2}{\hat{f}^2(\hat{x})}\right) - 1.
\end{aligned}$$

Hence for large flow rates, $\hat{\psi}_w$ dominates the reciprocal of the function $\hat{f}(\hat{x})$, so that

$$\hat{u}(\hat{x}, \hat{r}) \approx \left(\frac{4\hat{\psi}_w}{\hat{f}^2(\hat{x})}\right)\left(1 - \frac{\hat{r}^2}{\hat{f}^2(\hat{x})}\right) - 1,$$

which is Poiseuille flow in a non-uniform tube in a frame moving with speed 1. \square

Lemma 3.8. *Axial velocity $\hat{u}(\hat{x}, \hat{r})$ is strictly decreasing in \hat{r} from the centreline at axial point \hat{x} except in the presence of negative velocities $\hat{\psi}_w < \hat{\psi}_w^-$ where it becomes strictly increasing.*

Proof. The longitudinal velocity at \hat{x} is strictly radially decreasing if its radial derivative $\hat{u}_{\hat{r}} = 8A(\hat{x})\hat{r}$ is negative for all \hat{r} . This is true provided $A(\hat{x}) = -\frac{\hat{\psi}_w}{\hat{f}^4(\hat{x})} - \frac{1}{2\hat{f}^2(\hat{x})} < 0$, hence only if $\hat{\psi} > -\frac{1}{2}\hat{f}^2(\hat{x})$. Conversely, the velocity is strictly increasing for $\hat{\psi} < -\frac{1}{2}\hat{f}^2(\hat{x})$. Hence axial velocity is strictly decreasing in the radial direction for all cases of peristaltic flow where $\hat{Q} > 0$. \square

We have shown that high flow rates decrease the amount of trapping which will decrease the amount of mixing of solute. In the following subsection we apply the

results of §3.6.4 to determine the amount of recirculating fluid in the wave frame as a function of $\hat{\psi}_w$ and α .

3.6.6 Determining the Amount of Wave Frame Recirculation

In instances of trapping, a bolus of fluid particles undergo recirculation in the wave frame. As flow and amplitude ratio vary, so too does the volume and location of circulation. This can be used as an indicator of how much radial mixing is occurring. By Lemma 3.7 as the flow rate increases peristaltic flow has been shown to tend to Poiseuille flow where there is no trapping and hence no radial mixing of particles. Hence, peristalsis as a mixing mechanism is optimised for small flow rates. However, decreasing flow rates actually do not maximise trapping volume rather maximum trapping occurs in the copumping range.

Lemma 3.9. *Trapping is maximised at the point where streamlines detach from the centreline.*

Proof. When detached trapping occurs we can find the location of the separatrices $\hat{r}_{1,2}$ (3.6.4). This is maximised in $\hat{\psi}_{sad}$ when the distance between the separatrices given by $\sqrt{B(\hat{x}) + 4A(\hat{x})\hat{\psi}_{sad}}$ is greatest, so when $\hat{\psi}_{sad} = 0$ ie. at the point of detachment. It only remains to show that trapping radius \hat{r}^2 decreases as $\hat{\psi}_w$ decreases for centreline trapping. Now centreline trapping occurs when $\hat{\psi} = A(\hat{x})\hat{r}_c^4 + B(\hat{x})\hat{r}_c^2 = 0$, so that

$$\hat{r}_c^2 = -\frac{B(\hat{x})}{A(\hat{x})} = \frac{\hat{f}^2(\hat{x}_0)(4\hat{\psi}_w + \hat{f}^2(\hat{x}_0))}{2\hat{\psi}_w + \hat{f}^2(\hat{x}_0)}.$$

We denote $g(\hat{\psi}_w) = \hat{r}_c^2(\hat{\psi}_w, \hat{x})$ and determine the rate of change of \hat{r}_c^2 with respect to the flow rate

$$g_{\hat{\psi}_w} = \frac{2\hat{f}^4(\hat{x})}{(2\hat{\psi}_w + \hat{f}^2(\hat{x}))^2} > 0$$

which is always positive for all $\hat{\psi}_w$ hence, $g(\hat{\psi}_w)$ is always increasing in $\hat{\psi}_w$ up to the point of streamline separation. Hence for centreline trapping we have shown that trapping strictly increases as $\hat{\psi}_w$ increases to the point of separation and by Lemma 3.6 we have shown that trapping strictly decreases as $\hat{\psi}_w$ increases. Hence maximum trapping and radial mixing occurs when streamlines split and form trapping. \square

A proof was required for Lemma 3.9 as it was not intuitively obvious that detached trapping was strictly decreasing as the flow rate decreased. We now elucidate graphically in Figure 3-9 the relative sizes of trapping for small flow rates as the amplitude of vibration increases. We calculate for one wavelength the proportion of volume V_p of fluid undergoing trapping to the volume of one wavelength of the tube for various $\hat{\psi}_w$ and α . Hence, V_p is defined by

$$\text{Detached Trapping: } V_p = \frac{\int_0^1 \int_{\hat{r}_1(\hat{x})}^{\hat{r}_2(\hat{x})} \hat{r} d\hat{r} d\hat{x}}{\int_0^1 \int_0^{\hat{f}(\hat{x})} \hat{r} d\hat{r} d\hat{x}}, \quad \text{Centreline Trapping } V_p = \frac{\int_0^1 \int_0^{\hat{r}_c(\hat{x})} \hat{r} d\hat{r} d\hat{x}}{\int_0^1 \int_0^{\hat{f}(\hat{x})} \hat{r} d\hat{r} d\hat{x}}$$

We observe from Figure 3-9 that maximum trapping occurs at the point of streamline detachment from the centreline, for fixed α , corroborating Lemma 3.9.

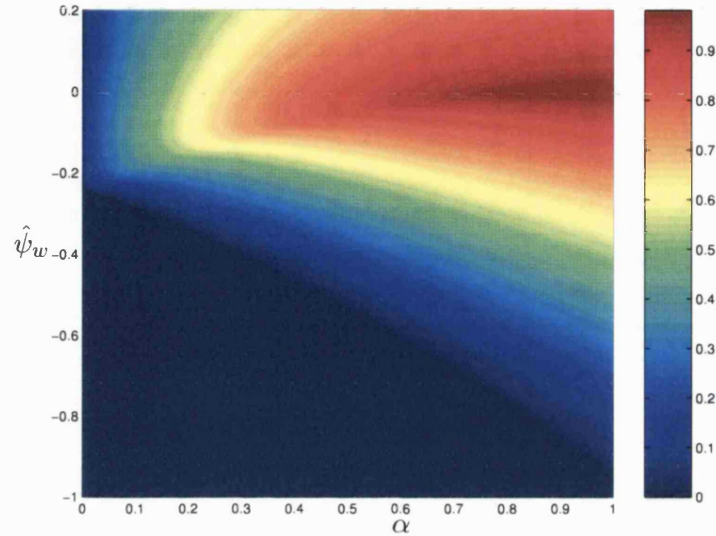


Figure 3-9: A Contour Plot of the Proportion of Volume of 1 Wavelength undergoing Recirculation as the Flow Rate and Amplitude of Vibration Varies.

3.6.7 Particle Paths

In §3.4.2 we determined the peristaltic velocities analytically in the moving frame. By numerically integrating we can obtain the location of a particle, $\check{x}(\check{t}), \check{r}(\check{t})$, in the fixed frame for any time t . Hence plotting the location at all times we can show the particle's path. Let \check{x}, \check{r} be the nondimensionalised fixed frame coordinates, then

$$\begin{aligned} \dot{\check{x}} &= \frac{d\check{x}}{d\check{t}} = u(\check{x}, \check{r}, \check{t}) = \left(-\frac{4\psi_w}{\hat{f}(\check{x}, \check{t})^4} - \frac{1}{2\hat{f}(\check{x}, \check{t})^2} \right) \check{r}^2 + \left(\frac{4\psi_w}{\hat{f}(\check{x}, \check{t})^2} + 1 \right) + 1, \\ \dot{\check{r}} &= \frac{d\check{r}}{d\check{t}} = v(\check{x}, \check{r}, \check{t}) = -\left(\frac{4\psi_w \hat{f}_{\check{x}}(\check{x}, \check{t})}{\hat{f}^5(\check{x}, \check{t})} + \frac{\hat{f}_{\check{x}}(\check{x}, \check{t})}{\hat{f}^3(\check{x}, \check{t})} \right) \check{r}^3 - \frac{4\psi_w \hat{f}_{\check{x}}(\check{x}, \check{t})}{\hat{f}^3(\check{x}, \check{t})} \check{r}. \end{aligned} \quad (3.6.5)$$

Applying a suitable ode solver, we determine the particle paths for particles initially placed at some point in the domain $[x(0), y(0)]$. Particle paths depend upon the initial location of the tracers with respect to the shape of the wave. Fundamental differences are apparent when particles are placed at points of maximum and minimum occlusion for certain $\hat{\psi}_w, \alpha$. In case B (see Figure 3-6) there is centerline trapping and the majority of particles placed at the point of minimum occlusion will undergo recirculation, but no

particles recirculate at the point of maximum occlusion. This is in contrast to case C where axial position of the particles has no effect. However for cases of trapping, there is a greater dependence on the initial positioning of tracers in the particle paths. Hence, it is important to note that taking a uniform spread of particles at just $\tilde{x}(0) = 0$ will omit some important particle paths. We plot the particle paths for case B for 8 particles spread out uniformly in the radial direction and places at the points of maximum and minimum occlusion.

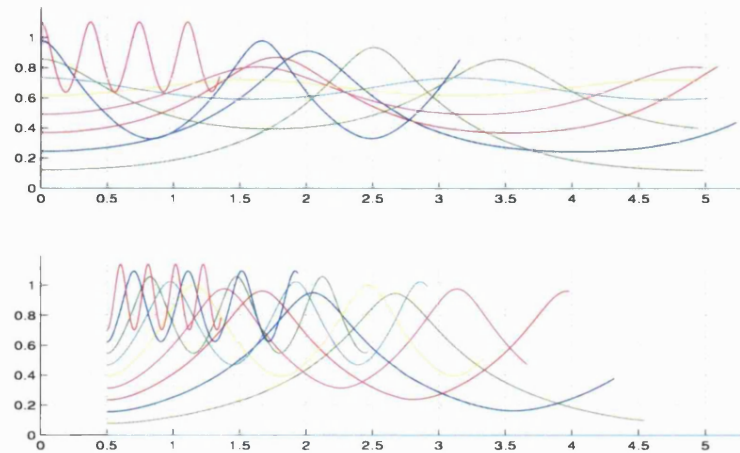


Figure 3-10: Evolution of 9 Particle Paths starting at Maximum and Minimum Points of Occlusion for 5 periods in Case B when $\alpha = 0.2$ and $\hat{\psi}_w = -0.2$.

As predicted we observe very interesting behaviour from the different initial positioning of the tracers. In the top figure most particles encompass a bolus (see Figure 3-6). Such particles exhibit long wavelength oscillations and radial mixing. Of interest is the motion of the particles outside the trapped bolus. In the top figure, there is one such particle and it travels with less speed and with shorter wavelength. This behaviour is shown in the lower figure where more particles are outside the bolus. Normally this is attributed to the slower axial velocities and faster radial velocity the closer the fluid particle is to the moving boundary. We observe trapped particles are moving on average with the speed of the wave by travelling a distance $\tilde{x} = 5$ after times $\tilde{t} = 5$. Consequently, comparing the figures, particles surrounding the bolus are then moving at speeds slower than that of the wave, and would slide backwards over the moving bolus.

Wave frame streamlines correspond to particle paths and an initial glance at the contour plot from Figure 3-6 of case D reveals uninteresting streamline behaviour, there is no radial mixing of fluid and motion would be Poiseuille like. However, reflux occurs in region D, and in Figure 3-11 we observe a proportion of particles close to the boundary move with retrograde motion and that most particles move forward and backwards. At points of maximum occlusion, particles have initial negative longitudinal

velocity and those at minimum occlusion have positive axial velocity.

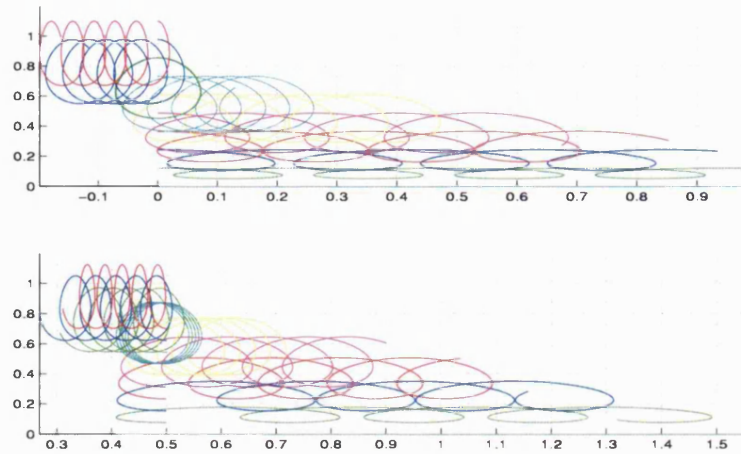


Figure 3-11: Evolution of 9 Particle Paths starting at Maximum and Minimum Points of Occlusion for 5 periods in Case D when $\alpha = 0.2$ and $\hat{\psi}_w = -0.5$.

Though particle paths may cross this is not proof that cross mixing occurs at all. For any two particles placed at the entrance $x(0) = 0$ with initial radial displacement $\check{r}_a > \check{r}_b$ we define radial mixing to occur when $\check{r}_a(\check{t}) < \check{r}_b(\check{t})$ for some time \check{t} . Still for case D, the final displacement of the particles show that the particles maintain radial order at least at the final time step. Running an animation plot of paths shows that the particles do not cross each other at any time, this is seen to happen only in the presence of trapping. In contrast to case D, where there is no trapping, we observe the only difference in behaviour of particles introduced at different points relative to the boundary is a phase difference in their paths.

The remaining particle paths for peristaltic flow cases are shown in Figure 3-12. Just from looking at the paths we can determine the existence of trapping from the presence of radial mixing in cases A, E and G. When there is copumping there is no reflux (cases A,B,C), although some particles do flow backwards at points of maximum occlusion for sufficiently small flow rate (case C). When trapping is present, no matter how small the flow rate the particles in the bolus are seen to advance with the speed of the wave (case G).

3.6.8 Evolution Of an Initial Condition of Passive Particles

For an incompressible fluid, the equations describing particle trajectories form a Hamiltonian system, a dynamical system where volume is preserved. Hence, a slug of tracer particles will then preserve its area under displacement from fluid flow. The dispersion of a slug in peristaltic flow will depend on the initial placement of the particles that form the slug and the time at which they were released into the flow. Hence, for a

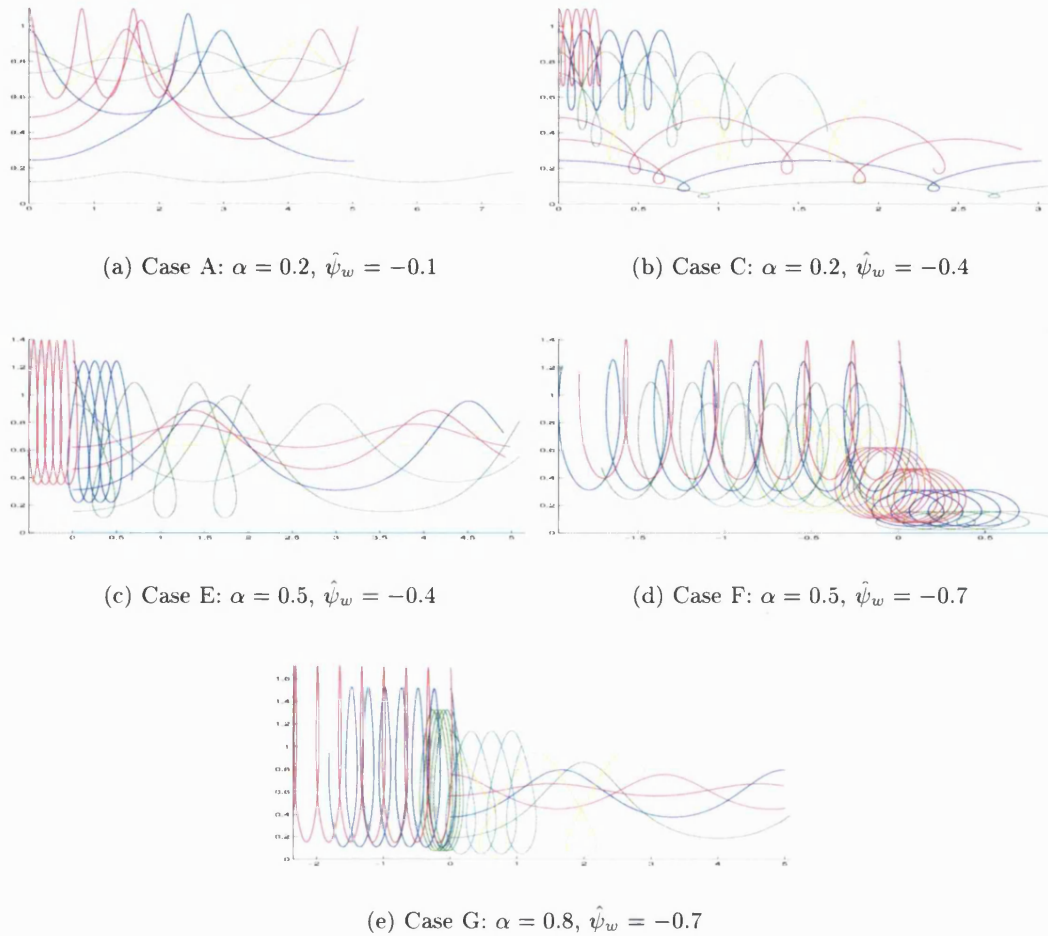


Figure 3-12: Evolution of 9 Particle Paths for 5 seconds in Cases A,C,E,F,G.

sufficiently large number of tracer particles filling one whole wavelength calculate all the particle paths to show the full behaviour of the peristaltic flow. In the following Figures 3-13-3-17, the pink dye represents particles initially placed at the boundary which fades to a black dye for particles at the centreline. We solve for the position $\tilde{x}(\tilde{t}), \tilde{r}(\tilde{t})$ for each particle after four periods and plot the location after each period. Any radial mixing will present itself by a mixing of the dyes.

Case A: Figure 3-13 clearly elucidates the effects of trapping. Black dye at the centreline is propelled forwards with a mixture of pink and black dye above the midline caught in the trapping region. As time progresses the dyes recirculate (see * in the Figure 3-13) around a wave frame stagnation point. We clearly observe here a mixing of the dyes from radial mixing. At the midline there is no trapping and the solute travels undisturbed through the peristaltic tube at speed greater than that of the wave. We note firstly that the initial placement of fluid was in a boundary prescribed by a cosine wave $\tilde{f} = 1 + \alpha \cos(2\pi(\tilde{x} - \tilde{t}))$, where there are two stagnation points (see Figure

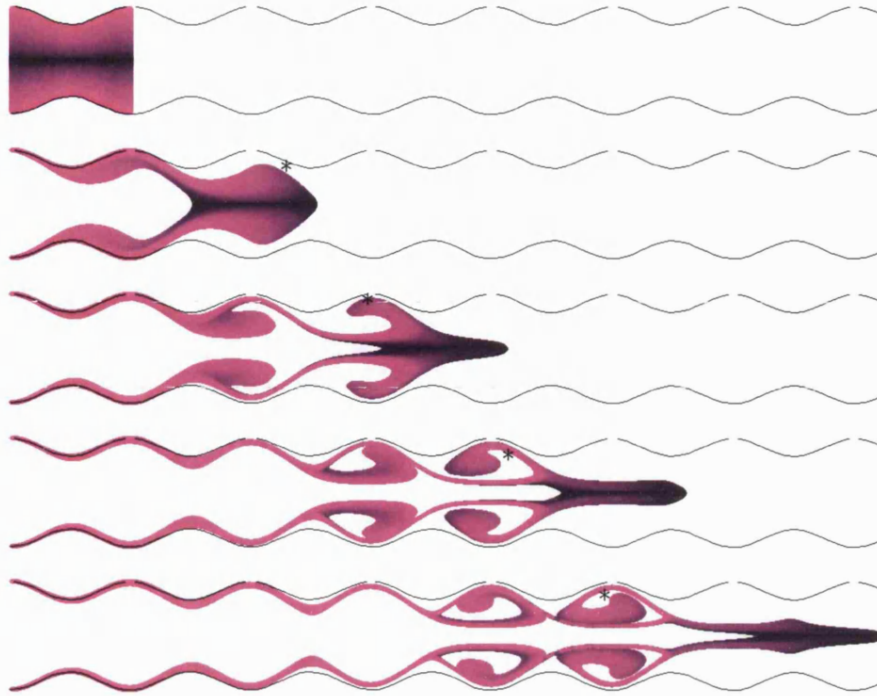


Figure 3-13: Evolution of an Initial Condition consisting of 10^6 passive particles for Case A: $\alpha = 0.2, \hat{\psi}_w = -0.1$. The frames correspond to $T = 0, 1, \dots, 4$ cycles of flow.

3-8) ($\hat{x} = 0, 1$), corresponding to two neighbouring recirculating regions. Secondly the period of the wave is one unit, hence we see that the trapped fluid is indeed moving with the speed of the wave, one wavelength per time unit (as the distance between successive * in Figure 3-13 is one wavelength).

Case B: Figure 3-14 describes peristaltic flow when there is centerline trapping. Here all solute particles from the axis to the top of the trapping region form two wave frame recirculating zones that eventually separate from one another. Generally in the case of centerline trapping solute occupying the point of maximum occlusion lies outside the trapped bolus (Figure 3-6) and travels at a slower speed than that of the wave.

Case C: Figure 3-15 has no trapping and we observe no mixing of dye but the net fluid motion is in the direction of the wave. We also do not observe the negative fluid motion at the points of maximum occlusion as seen in the time dependent particle paths figure (see Figure 3-12(b)). Both illustrations of particle paths are important.

Case D,E: Figure 3-16 describes peristaltic flow when peristalsis is acting as a pump and reflux occurs (highlighted by a †). Just a slight change in flow rate or amplitude ratio and trapping could occur as seen in Figure 3-17. This has a profound affect on solute distribution. Initially there was very little solute movement in Figure 3-16 but now the tracer particles have spread out further in the same amount of time as a result of trapping.

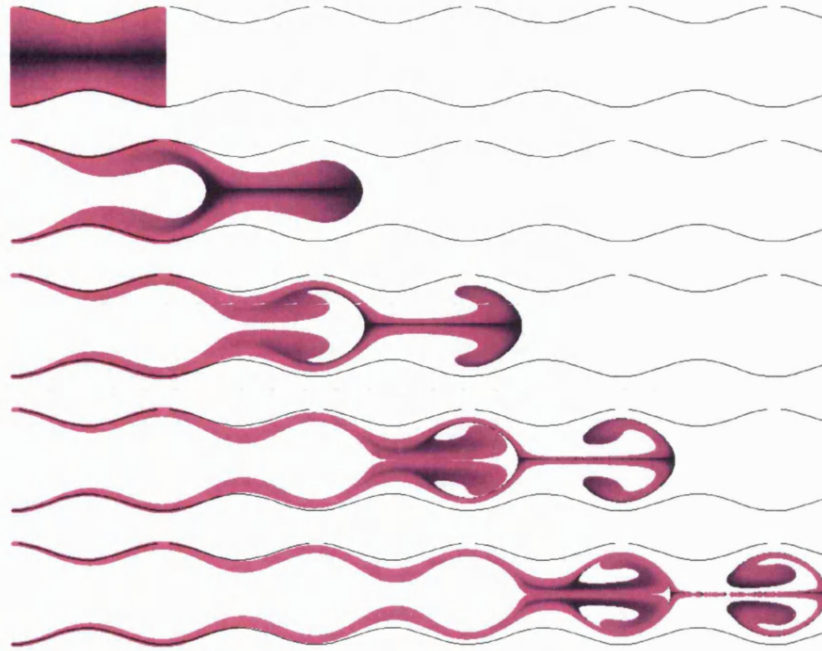


Figure 3-14: Evolution of an Initial Condition consisting of 10^6 passive particles for Case B: $\alpha = 0.2, \hat{\psi}_w = -0.2$. The frames correspond to $T = 0, 1, \dots, 4$ cycles of flow.

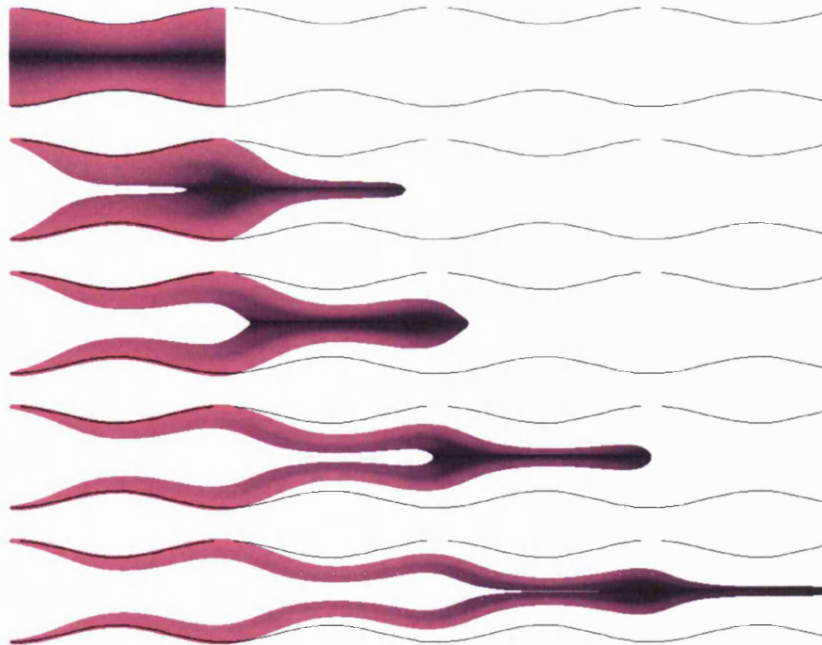


Figure 3-15: Evolution of an Initial Condition consisting of 10^6 passive particles for Case C: $\alpha = 0.2, \hat{\psi}_w = -0.4$. The frames correspond to $T = 0, 1, \dots, 4$ cycles of flow.

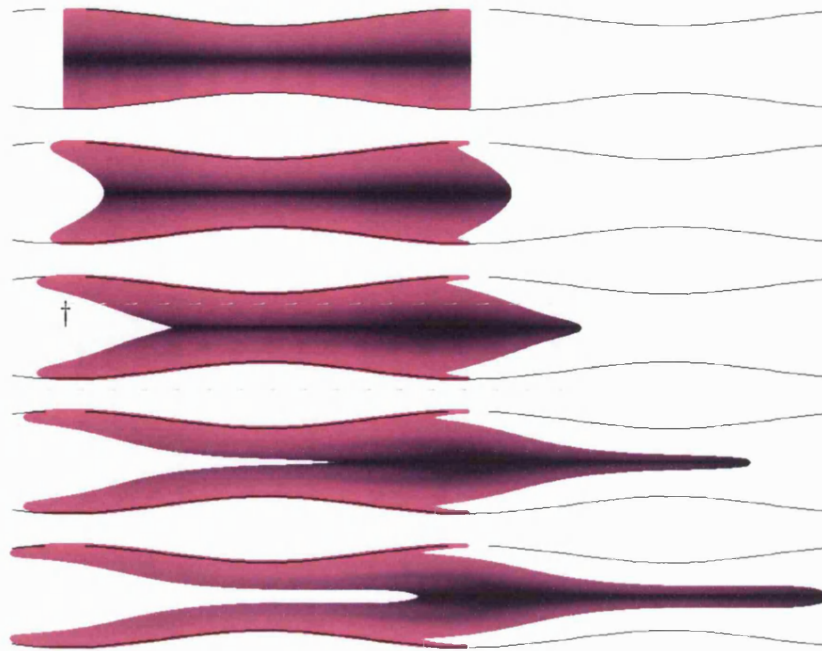


Figure 3-16: Evolution of an Initial Condition consisting of 10^6 passive particles for Case D: $\alpha = 0.2, \hat{\psi}_w = -0.5$. The frames correspond to $T = 0, 1, \dots, 4$ cycles of flow.

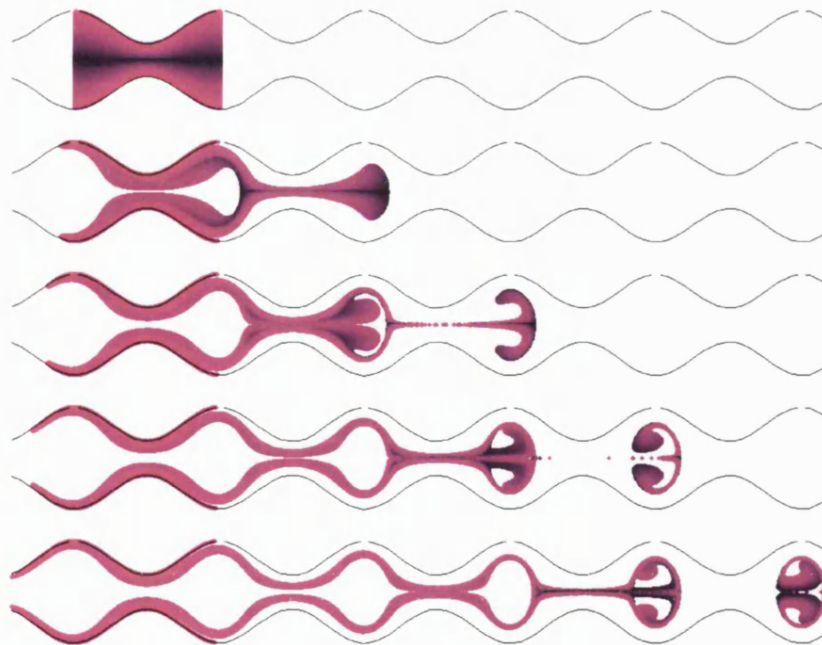


Figure 3-17: Evolution of an Initial Condition consisting of 10^6 passive particles for Case E: $\alpha = 0.5, \hat{\psi}_w = -0.4$. The frames correspond to $T = 0, 1, \dots, 4$ cycles of flow.

3.6.9 A Measure of Peristaltic Induced Convective Dispersion

In the previous subsection we have shown the effects of peristalsis on the convection of non-diffusing *tracer particles* that have been released into fluid undergoing peristaltic flow. In general a *solute* that is introduced into a flow will disperse as a result of (i) diffusion and (ii) convection. (We briefly discussed the latter known as convective dispersion in the background Chapter.) If the solute is non-diffusing then peristaltic convection is solely responsible for the dispersion of the solute. Hence looking at the exotic particle paths we expect peristaltic flow to significantly effect the dispersion of the solute when compared to a much simpler flow like Poiseuille flow.

In the literature there are methods to measure the extent of dispersion for convection alone [69], [37], [38]. In [69] the author studied the convective dispersion of tracer particles for oscillatory flow in furrowed channels in the absence of diffusion. Here, Sobey considered unsteady flow for the full Navier-Stokes equation. By numerically solving the unsteady Navier-Stokes equations in streamfunction-vorticity form, Sobey obtained the particle velocities and subsequently numerically integrated for the particle paths. A measurement of dispersion can be obtained from determining the mean position of the particles in the longitudinal direction \bar{x} and consequently calculating the variance σ^2 .

We determine the position of N particles $[x_i(t), r_i(t)]$ for $i = 1, \dots, N$ at time t with initial condition $[x_i(0), r_i(0)]$. (Note we drop the checks to simplify notation and to standardize it with the literature.) The mean axial position of the particles is given by

$$\bar{x}(t) = \frac{1}{N} \sum_{i=1}^N x_i(t),$$

and the particles are distributed with variance

$$\sigma^2(t) = \frac{1}{N-1} \sum_{i=1}^N (x_i(t) - \bar{x}(t))^2.$$

Now in Hwu et al. [38], the authors measured the instantaneous dispersion coefficient $D(t)$ using the particle variance so that

$$D(t) = \frac{1}{2} \frac{d\sigma^2}{dt}, \quad (3.6.6)$$

and then integrated (3.6.6) over a cycle to obtain K , the cycle dispersion coefficient,

$$K = \int_{\text{cycle}} D(t) dt = \frac{1}{2} \Delta\sigma^2|_{\text{cycle}} = \frac{1}{2} (\sigma^2(t+T) - \sigma^2(t)).$$

It is a requirement that K be constant over a number of cycles to reliably estimate dispersion [38]. We have so far considered measuring convective dispersion in the lon-

gitudinal direction but we are mainly interested in the radial movement of particles towards the boundary, which we expect will enhance absorption. We consider measuring the average movement of particles in the radial direction in time where it is either in the direction of the wall or the centreline. One way would be to calculate the skewness of the particles. This requires knowledge of the mean radial position and the variance of the tracers. However, the domain in the radial direction is fixed and consequently there will be no outliers to affect the radial mean. Hence measuring skewness is only useful in the axial direction and requires knowledge of the axial mean and variance

$$s(t) = \frac{E\left((X - \mu)^3\right)}{\left\{E\left((X - \mu)^2\right)\right\}^{\frac{3}{2}}} = \frac{1}{\sigma^2(t)} \left(\frac{1}{N-1} \sum_{i=1}^N (x_i(t) - \bar{x}(t))^3 \right).$$

To describe the movement of particles in the radial direction we determine the mean radial position of the tracer particles which is given by

$$\bar{r}(t) = \frac{1}{N} \sum_{i=1}^N r_i(t).$$

However, the initial mean changes as a function of the amplitude of vibration α . Hence, we scale the radial positions by the transformation

$$q_i(t) = \frac{r_i(t)}{f(x_i, t)} = \frac{r_i(t)}{1 + \alpha \cos(2\pi(x_i(t) - t))}$$

to obtain a uniform mean for all α . The mean scaled radial position is simply

$$\bar{q}(t) = \frac{1}{N} \sum_{i=1}^N q_i(t).$$

and equals 0.5 if we consider a uniform spread of tracer particles only in the positive radial direction. We denote the radial variance by σ_q^2 so that

$$\sigma_q^2(t) = \frac{1}{N-1} \sum_{i=1}^N (q_i(t) - \bar{q}(t))^2.$$

a measure of the expansion or contraction of the cloud of particles.

Examples of Peristaltic Dispersion

We calculate the particle paths of a slug of passive tracers as in §3.6.8 in a peristaltic flow for the duration of 4 periods. We determine the behaviour of the tracer particles in the peristaltic flow by calculating (i) the mean position of the tracer particles $\bar{x}(t)$, (ii) the variance $\sigma^2(t)$, (iii) the instantaneous dispersion coefficient $D(t)$ and then (iv)

the cycle dispersion coefficient K . We then measure the radial mixing of the particles by (i) the mean radial position $q(t)$ and (ii) the radial variance σ_q^2 .

We measure the particle dispersion quantities for (a) all the particle path cases seen in Figures 3-13 to 3-17 and (b) for varying normalised time mean volume flow rates \hat{Q}/\hat{Q}_0 with amplitudes of vibration $\alpha = 0, 0.1, \dots, 0.5$. In case (b) we solve for (i) a purely pumping case $\hat{Q}/\hat{Q}_0 = 0.5$ (which involves particle paths cases D and E), (ii) a zero pressure gradient case $\hat{Q}/\hat{Q}_0 = 1.5$ and (iii) a copumping case $\hat{Q}/\hat{Q}_0 = 1$ (cases C and B). We also calculate the proportion of particles caught in trapping for all the cases.

Part (a): All Cases: Our results displayed in Figure 3-18 (correspond to analysis of the particle paths Figures 3-13-3-17) show the mean axial particle position \bar{x} moves linearly in the positive x direction. Case A corresponds to the faster flow rate and so tracer particles subsequently spread out the furthest. Consequently the particles exhibit an increasing variance σ which is more pronounced in cases where trapping is present (case D and C show smaller variance). Clearly the instantaneous dispersion coefficient D will be largest for the cases displaying trapping and high flow rates. We note that cases D and E display an oscillatory but overall increasing dispersion coefficient, a result of a momentary slow down in the expansion of the cloud of tracer particles. Hence the cycle dispersion coefficient is always increasing, and unfortunately we are unable to estimate the amount of dispersion.

The mean radial position of the particles in Figure 3-18(d), also display an oscillatory profile, however in general the frequency is shown to increase as the flow rate decreases. We further observe in case B that centreline trapping implies more particles on average move toward the boundary when compared to case A, even though case A has more particles in the trapping region (60% compared to 37%). Both cases have the same amplitude of vibration, however, centreline trapping circulates more particles at the centreline unlike detached trapping influencing \bar{q} . In Figure 3-18(f) we observe the difference between detached and centreline trapping on the radial variance, with fast particles below the detached trapping in case A inducing a positive variance, i.e. a radial spread of the particles. This is in contrast to the remaining cases where we tend to see a decrease in the initial variance as particles group closer towards the boundary.

Part (b): Time Mean Volume Flow Rate Cases: For fixed time mean flow rates in the pumping and weak copumping cases we observe in figures 3-19-3-21 that (i) for high flow rates the mean axial position decreases as trapping increases, suggesting a drop in the mean velocity of particles as they sample the slower wave speed streamline (this is more pronounced as \hat{Q}/\hat{Q}_0 increases), (ii) as the amplitude of vibration increases particles move closer to the boundary observed by an increase in the mean radial position \bar{q} and (iii) trapping is exhibited by fluctuations in the variance σ_q^2 .

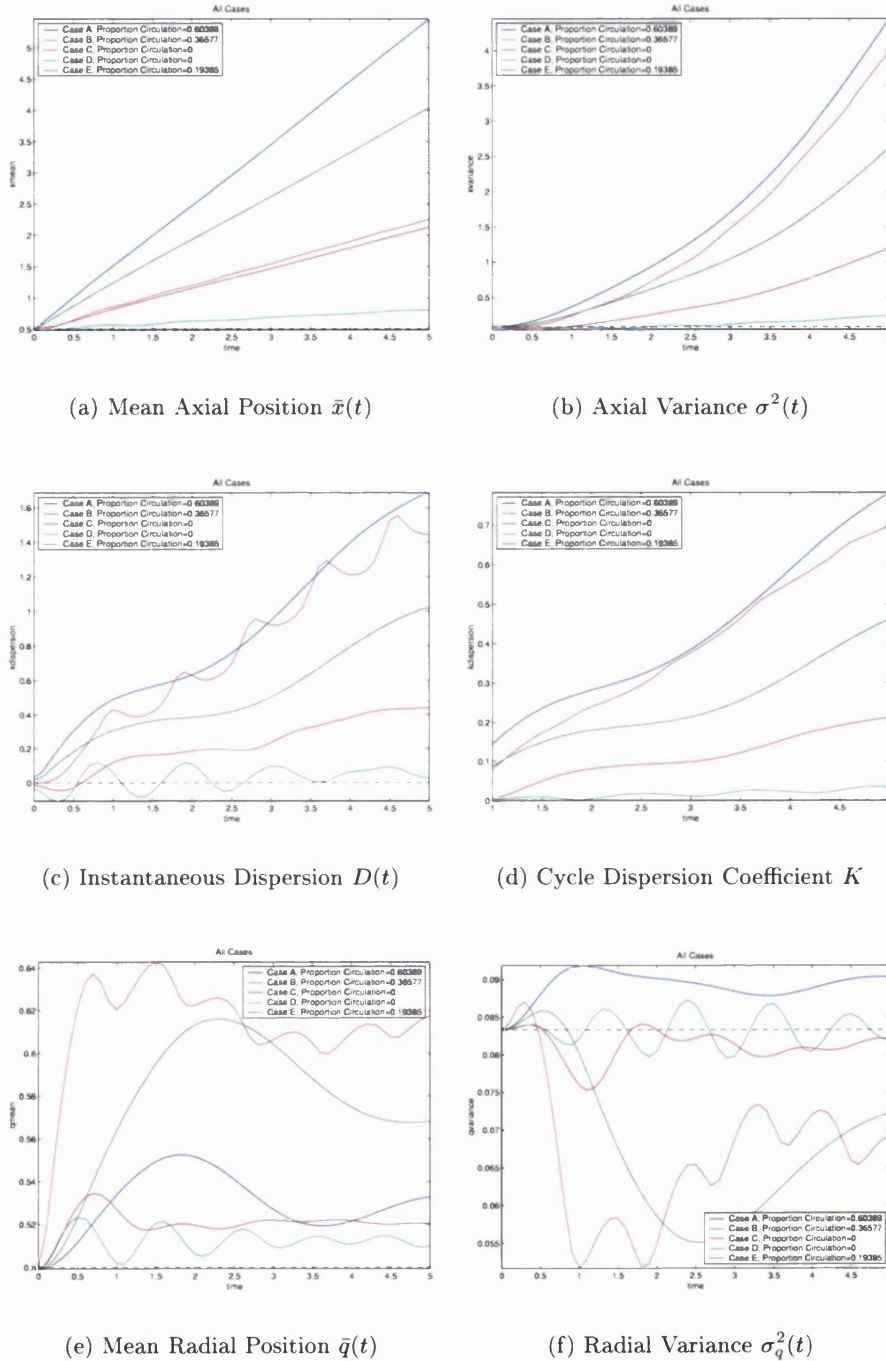
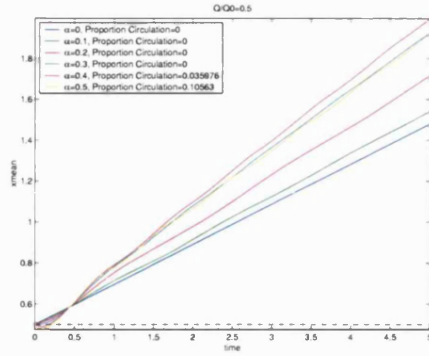
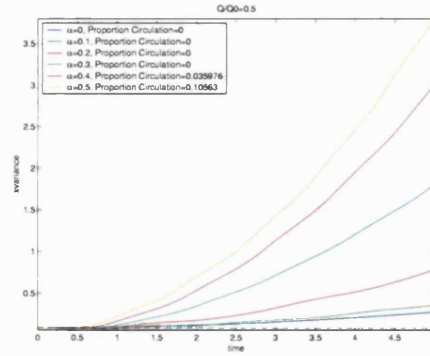


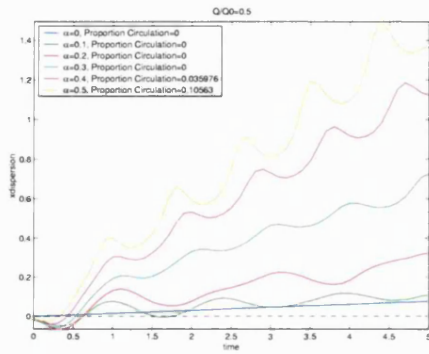
Figure 3-18: Measuring Dispersion and Radial Mixing from Particle Paths for all types of possible Peristaltic Flow Cases.



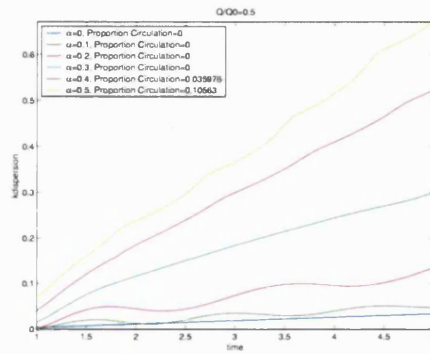
(a) Mean Axial Position $\bar{x}(t)$



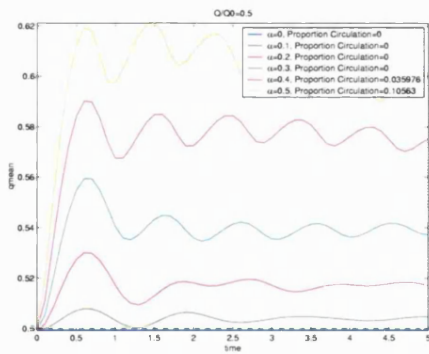
(b) Axial Variance $\sigma^2(t)$



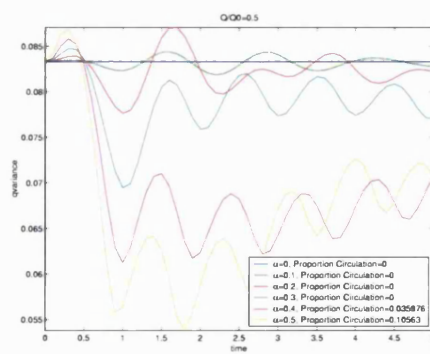
(c) Axial Dispersion $D(t)$



(d) Cycle Dispersion Coefficient K



(e) Mean Radial Position $\bar{q}(t)$



(f) Radial Variance $\sigma_q^2(t)$

Figure 3-19: Measuring Dispersion and Radial Mixing from Particle Paths for Time Mean Flow Rate $Q/Q_0 = 0.5$

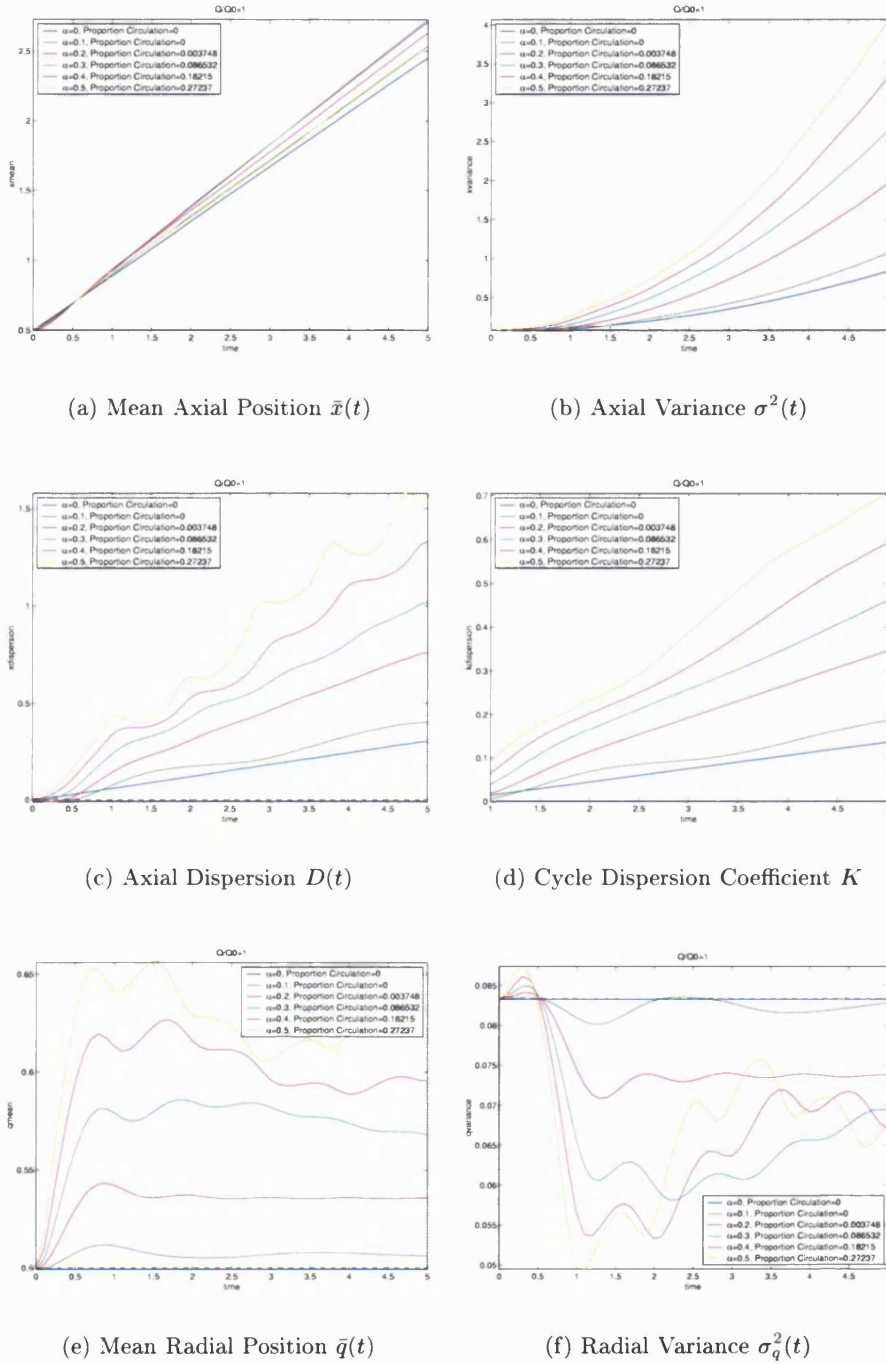
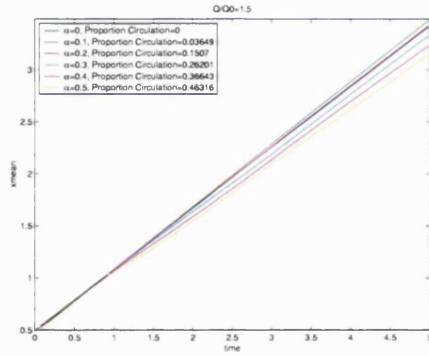
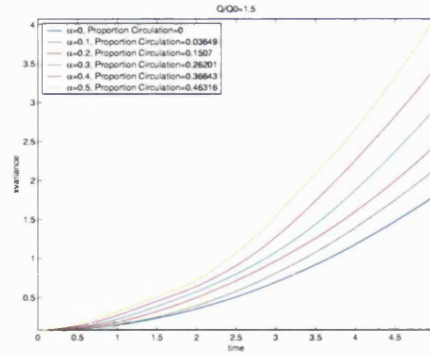


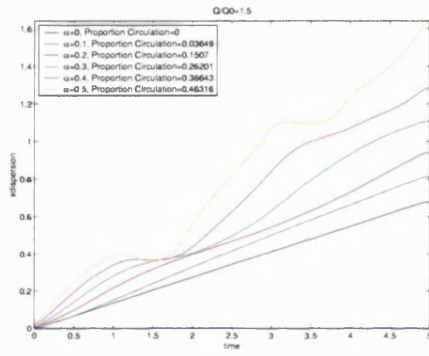
Figure 3-20: Measuring Dispersion and Radial Mixing from Particle Paths for Time Mean Flow Rate $Q/Q_0 = 1$



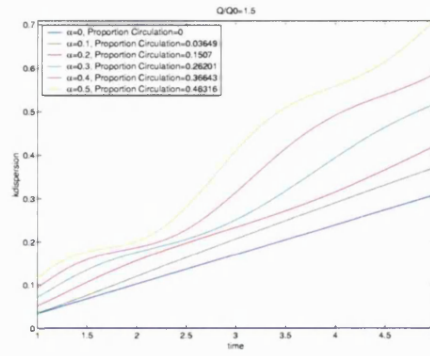
(a) Mean Axial Position $\bar{x}(t)$



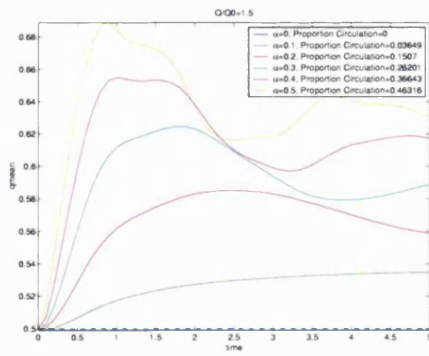
(b) Axial Variance $\sigma^2(t)$



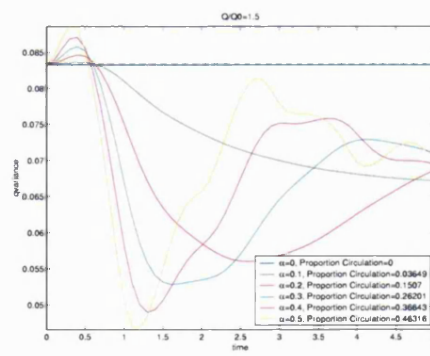
(c) Axial Dispersion $D(t)$



(d) Cycle Dispersion Coefficient K



(e) Mean Radial Position $\bar{q}(t)$



(f) Radial Variance $\sigma_q^2(t)$

Figure 3-21: Measuring Dispersion and Radial Mixing from Particle Paths for Time Mean Flow Rate $Q/Q_0 = 1.5$

3.7 Summary

For viscous fluid flow of chyme in the intestine we simplified the Navier-Stokes equation to Stokes slow flow equations relating pressure and velocity. Consequently using streamfunction-vorticity notation we derived the biharmonic equations for 2D axisymmetric flow. We prescribed a sinusoidal function to describe a standing wave and modelled the Biharmonic problem in the wave frame. Nondimensionalising we introduced the wave number ϵ and through a perturbation expansion in this small parameter we solved the biharmonic equations for the semi-analytic peristaltic velocities. We showed the leading order solution breaks down as the amplitude of vibration α increases as it induces wave curvature. For high flow rates we show the parabolic like peristaltic velocities tend to Poiseuille flow.

From the leading order solution of the peristaltic velocities we have shown there are two states of peristalsis, ‘pumping’ and ‘copumping’. When peristalsis acts as a pump the peristaltic wave induces a pressure rise, this is known as ‘pumping’. However, if there is a pressure drop, then peristalsis is aided by a driving pressure gradient, this is known as ‘copumping’. In these phases peristaltic motion exhibits two phenomena; (i) reflux, where fluid particles near the boundary undergo net retrograde motion after a period (this occurs only in pumping) and (ii) trapping, where fluid particles recirculate in the wave frame. We have further shown that the amount of trapping decreases as the flow rate increases. We elucidated the different flow phenomena using particle paths. From these figures it is clear that trapping is responsible for mixing of solute in the intestine. We studied the convective dispersion of the peristaltic flow in the absence of diffusion. We illustrated the behaviour of this oscillatory flow, namely centreline trapping, which induces large radial mixing. Hence peristaltic flow is very different from Poiseuille flow! We aim to apply the semi-analytic peristaltic velocities $\mathbf{u} = (\check{u}(\check{x}, \check{r}, \check{t}), \check{v}(\check{x}, \check{r}, \check{t}))$ to the 2D dispersion model

$$c_t + \mathbf{u} \cdot \nabla c = D \nabla^2 c,$$

with absorption on the boundary. In the next Chapter we consider the trivial case when $\alpha = 0$, the 2D Poiseuille Dispersion Model.

Chapter 4

Dispersion Models in Cylindrical Flow with Application to the Intestine

In this Chapter we look at the behaviour of the mean concentration of a solute in a cylinder where there is Poiseuille flow. We derive an equation of the form

$$\bar{c}_t + U_e \bar{c}_x = D_e \bar{c}_{xx} - K_e \bar{c}, \quad (4.0.1)$$

a 1D convection dispersion absorption equation for the mean solute concentration \bar{c} which relates the coefficients U_e, D_e, K_e to the overall flow field. The 1D equation is obtained from asymptotic analysis of the full 2D Poiseuille dispersion model for the solute concentration which is governed by

$$c_t + u(r)c_x = D\nabla c^2, \quad \text{in } \Omega \quad (4.0.2)$$

with passive absorption at the boundary modelled by

$$-D\mathbf{n} \cdot \nabla c = K_a c \quad \text{on } \Gamma \quad (4.0.3)$$

The diffusive flux boundary condition is significant, it is a reasonable approximation to modelling the process of absorption in the intestine. We wish to understand how the effective 1D equation (4.0.1) differs from the standard 1D equation for plug flow of a solute in a cylinder by Ho et al. [28],

$$c_t + uc_x = Dc_{xx} - Kc. \quad (4.0.4)$$

In doing so we, (i) build up the standard 1D model as described by (4.0.4), (ii) motivate the 2D Poiseuille dispersion equation (4.0.2) as a better model of solute flow in a

cylinder and (iii) rework the asymptotic analysis that lead to the 1D effective equation (4.0.1) for the impermeable case, $K_a = 0$, and the permeable case $K_a \neq 0$.

We start with the model by Ho et al. (4.0.4) which assumes that a) the solute is transported by plug flow, b) there are no radial inhomogeneities, and c) absorption occurs everywhere in the axisymmetric tube which represents the intestine. We motivate the full 2D Poiseuille flow dispersion model to take into account factors that induce radial inhomogeneities that are not captured by the 1D equation. Specifically we more realistically model a) the viscous no-slip condition of the fluid flow and b) the absorption taking place at the epithelial boundary (4.0.3). This 2D model was the basis of the paper by Stoll et al. entitled ‘A Theory of Molecular Absorption from the Small Intestine’, which is currently the most advance intestinal dispersion model, and upon which this thesis is based. The Poiseuille flow dispersion model was applied to the passage of a therapeutic solute in the intestine where absorption took place on the epithelial boundary.

Stoll et al. applied a macrotransport approach [73] to reduce the full 2D model to (4.0.1). This asymptotic analysis is valid *only* after a significant amount of time has passed $t > t^*$, such that all radial positions have been sampled by the solute particles and then the mean solute profile satisfies (4.0.1). There are two key features in the paper by Stoll et al., (i) it introduces a fictitious initial condition to make the asymptotic equation valid for all time and (ii) models the effects of peristaltic flow as enhanced diffusion by a formula. In applying the model by Stoll et al. we obtained erroneous results and in an effort to understand the model fully we rework the asymptotic analysis that lead to (4.0.1) for (i) the case of an impermeable wall and (ii) the permeable case. For an impermeable wall, it was Taylor [74] who first averaged solute concentration behaviour to

$$\bar{c}_t + U_e \bar{c}_x = D_e \bar{c}_{xx}, \quad (4.0.5)$$

where U_e is the mean Poiseuille velocity and D_e is the dispersion coefficient comprised from the molecular diffusion coefficient and a convective dispersion term arising from molecules diffusing over different speed streamlines from nonuniform flow. Using an alternative nondimensionalisation we derive the 2D equation

$$c_{\tilde{t}} + \ell (1 - \tilde{r}^2) c_{\tilde{x}} = \frac{1}{P_{er}} \left(\ell^2 c_{\tilde{x}\tilde{x}} + c_{\tilde{r}\tilde{r}} + \frac{1}{\tilde{r}} c_{\tilde{r}} \right),$$

and introduce two important parameters: the radial Péclet number P_{er} , and the tube length ratio ℓ . We formulate the dimensionless asymptotic equation as a function of these parameters. Consequently, we compare the numerical solutions for both the full 2D model and its equivalent 1D asymptotic model, highlighting the dependence of applying the asymptotic analysis on the parameter ℓP_{er} which must be small.

We consider the 2D Poiseuille dispersion model with absorption (4.0.2), (4.0.3). The

macrotransport approach applied by Stoll et al. is very complex and is generalised to a range of dispersive phenomena. Hence we rework the analysis by Lungu and Moffatt [52] and show that we can derive the same effective coefficients, U_e, D_e as in Stoll et al. [73]. However our analysis shows that the effective absorption is stated incorrectly yielding unrealistic absorption. We then state the peristalsis formula in its full form and show it is incorrectly applied as it is derived from a perturbation expansion in P_{er} but applied to solute motion with high $P_{er} \gg 1$. This formula is vital to work of Stoll and his co-authors as it yields enhanced diffusion that decreases the Péclet number so that Stoll et al. could then apply a macrotransport approach for solute motion in the intestine. We further show by equating the analysis of Stoll et al. with that of Lungu et al., that the fictitious initial condition, used to compensate \bar{c} for small time $\tilde{t} < t^*$, inappropriately assumes solute motion is effectively represented by

$$c_{\tilde{t}} = \frac{1}{P_{er}} \left(c_{\tilde{r}\tilde{r}} + \frac{1}{\tilde{r}} c_{\tilde{r}} \right), \quad (4.0.6)$$

and is derived from the analytical solution of (4.0.6). We highlight its ineffectiveness with a full 2D numerical solution for four therapeutics used in [73] and solve the equivalent 1D asymptotic equation. Using the 2D solution we approximate the movement of its cross sectional average by a 1D dispersion model using an algorithm to find the effective velocity, the dispersion coefficient and the absorption coefficient and then compare these numerical results to the analytical results found by Stoll et al. We observe a relatively large difference in fraction of mass absorbed when we compare the 1D model by Stoll et al. with its equivalent 2D model.

4.1 Introduction to 1D Dispersion Models

In the background section we discussed the CAT and MMBA model. They were a system of first order odes $y' = f(t, y)$, that described plug flow of a therapeutic solute through a sequence of compartments. However, these models fail to take into account physiological effects, but mainly they only give in a discrete sense the spatial distribution of the solute concentration.

In this section we discuss the formulation of the simple 1D dispersion equation (4.0.4) by Ho et al. [28]. This is a pde which incorporates spatial dependency on the concentration profile of the drug. We build up the model by introducing stepwise: 1) convection, 2) absorption and 3) diffusion, into the governing equation. We nondimensionalise the equation as the model becomes more complicated and introduce important dimensionless variables that elucidate the dominating factors in flow and absorption.

4.1.1 Modelling Solute Transport

We describe the concentration $c = c(x, t)$ of a solute in a 1D domain at any point in space, x , and time, t , by a first order conservation law, $c_t + J_x = 0$ for a flux J . In the presence of a constant flow $u = \text{constant}$, the flux term satisfies $J = uc$ and the governing equation for solute motion is given by

$$c_t + uc_x = 0, \quad (4.1.1)$$

known as the *convection equation*. This models the bulk flow of a substance flowing with constant speed u in the positive x -direction. We have assumed a 1D domain so that any variation in the quantity is restricted to one spatial dimension. We assume an initial concentration in the domain is given by $c(x, 0) = c_0(x)$. The solution of (4.1.1) is a right travelling wave, $c(x, t) = c_0(x - ut)$. As time increases the initial profile of the wave $c_0(x)$ moves with undistorted shape rightwards with speed u .

4.1.2 Modelling Absorption

A solute convecting through a tube may undergo decay (e.g. enzymatic or chemical) or become absorbed, and we can model the solute concentration by the *convection-reaction equation*

$$c_t + uc_x = -Kc.$$

The term $-Kc$ is the reaction term which represents either absorption and or decay of the solute with rate K . As in the previous section, let us consider the initial profile $c_0(x)$ on a domain of length L_x , then we nondimensionalise the variables as follows

$$\tilde{x} = \frac{x}{L_x}, \quad \tilde{t} = \frac{tu}{L_x},$$

and subsequently the dimensionless convection reaction equation takes the form

$$c_{\tilde{t}} + c_{\tilde{x}} = -\bar{D}_a c. \quad (4.1.2)$$

We introduce the *axial Damköhler number*, $\bar{D}_a = KL_x/u$, which describes the rate of drug removal relative to the rate of convection out of the domain [61]. It is an important ratio in determining whether convection or reaction dominates the concentration distribution over the length and time scales of interest. We solve (4.1.2) using the method of characteristics $\xi = \tilde{x} - \tilde{t}$, $\tau = \tilde{t}$ so that (4.1.2) in the wave frame is given by the exponential decay ode, $c_\tau = -\bar{D}_a c$, with solution $c(\xi, \tau) = c_0(\xi)e^{-\bar{D}_a \tau}$. Hence the fixed frame concentration is given by

$$c(\tilde{x}, \tilde{t}) = c_0(\tilde{x} - \tilde{t})e^{-\bar{D}_a \tilde{t}}, \quad (4.1.3)$$

a right travelling exponentially decaying wave. The effect of the Damköhler number is such, when $\bar{D}_a \ll 1$ then convection dominates absorption and the absorption process is known as convection-rate limited. Conversely, if $\bar{D}_a \gg 1$ the process is known as reaction rate limited.

Our main aim is in determining the amount of substance absorbed $M_A(\check{t})$. In doing so we first denote the amount of concentration present in the domain by $M(\check{t})$, and the initial amount present by $M(0) = M_0$. Mass present in the tube is defined by

$$M(\check{t}) = \int_0^1 c(\hat{x}, \check{t}) d\hat{x}, \quad M_0 = \int_0^1 c(\hat{x}, 0) d\hat{x} = \int_0^1 c_0(\hat{x}, 0) d\hat{x}.$$

By integrating the convection decay equation with respect to time and distance, we obtain the mass conservation equation:

$$M(\check{t}) = \underbrace{M_0 e^{-\bar{D}_a \check{t}}}_{\text{absorption}} - \underbrace{e^{-\bar{D}_a \check{t}} \int_0^{\check{t}} e^{\bar{D}_a s} c(1, s) ds}_{\text{outflow}} + \underbrace{e^{-\bar{D}_a \check{t}} \int_0^{\check{t}} e^{\bar{D}_a s} c(0, s) ds}_{\text{inflow}}. \quad (4.1.4)$$

By the above formula we note that solute is lost not only through absorption across the whole domain but also by convection out of the end of the tube. Unless a source is present at the opening of the tube the solute inflow is zero. From (4.1.2) concentration is lost at a rate of $-\bar{D}_a c$, hence the blood stream gains concentration at a rate $+\bar{D}_a c$ so that blood concentration satisfies the time dependent ode $b_{\check{t}} = +\bar{D}_a c$. We integrate with respect to distance to determine the mass absorption equation

$$(M_A)_{\check{t}} = \bar{D}_a M(\check{t}).$$

Hence, by applying the fundamental theorem of calculus in time, the formula for mass absorbed is given by

$$M_A(\check{t}) = M_A(0) + \bar{D}_a \int_0^{\check{t}} M(\check{t}) d\check{t}, \quad (4.1.5)$$

which tells us that the fraction dose absorbed satisfies $F_A(\check{t}) = M_A(\check{t})/M_0$.

4.1.3 Modelling Diffusion

Diffusion occurs as a result of randomly moving solute molecules colliding causing solute movement from regions of high concentration to low concentration. The steeper the concentration gradient the greater the flux. Hence the diffusive flux depends on the spatial derivative and by Fick's law satisfies $J^D = -Dc_x$, for diffusion coefficient D . Consider a fluid convecting a dissolved chemical by plug flow with velocity u . If the solute is diffusing according to Fick's law, then the total flux is given by

$$J = uc - Dc_x.$$

Additionally if the chemical is being absorbed then the chemical concentration is governed by the convection diffusion reaction equation (4.0.4). We nondimensionalise as in the previous subsection to obtain

$$c_{\check{t}} + c_{\check{x}} = \frac{1}{P_e} c_{\check{x}\check{x}} - \bar{D}_a c, \quad (4.1.6)$$

where we introduce $P_e = \frac{uL}{D}$, the dimensionless axial Péclet number [10] which measures the relative importance of axial convection compared to diffusion. For $P_e \ll 1$, the movement of the solute is dominated by diffusion and conversely for $P_e \gg 1$, convection dominates solute motion. For a sufficiently slowly diffusing solute, the diffusion term $c_{\check{x}\check{x}}$ can be ignored and the solution approximately satisfies the convection reaction equation. On a bounded domain an analytical solution may be found in terms of an infinite series of sinusoidal functions or we can use Laplace transforms. It is a far more complicated solution than that found for the convection reaction problem (4.1.3).

For the main equation (4.1.6) to be well posed we must apply appropriate initial and boundary conditions that represent the physical problem mathematically to obtain a unique solution. We consider two models, either (i) a constant amount of solute flowing into the channel $c(0, \check{t}) = c_0$, known as a *Dirichlet* boundary condition, and or (ii) we place an initial amount of solute in the channel $c(\check{x}, 0) = c_0(\check{x})$. The amount of solute absorbed is then calculated in a similar manner as before (4.1.5). We simply assume further that convection dominates diffusion at the boundaries so that a zero Neumann boundary condition, $c_{\check{x}} = 0$, can be imposed at the boundaries. Hence, mass present at any time, $M(\check{t})$, is still prescribed by (4.1.4), since the integral of the diffusion term $c_{\check{x}\check{x}}$ with respect to \check{x} is zero [73].

4.2 Modelling Passive Absorption in the Intestine

In the simple 1D model, absorption was represented in the governing equation (4.0.4) by the first order reaction term $-Kc$. This term represented a combination of absorption and degradation throughout the tube. However, for absorption of solute purely at the boundary we can extend the model to 2D and introduce an appropriate boundary condition. For this thesis we are concerned with modelling only passive absorption that is we assume that particles permeate through the boundary by diffusion. Hence there is a diffusive flux at the boundary, such that

$$J^D = -D\mathbf{n} \cdot \nabla c.$$

This flux term depends on two factors, namely (i) the permeability, K_a , of the tube's membrane wall and (ii) the amount of solute concentration at the membrane. Conse-

quently we obtain the absorption equation

$$-D\mathbf{n}\cdot\nabla c = K_a c,$$

This equation is a Robin boundary condition (seen in [73],[10]). If the membrane is impermeable, $K_a = 0$ and there is a zero diffusive flux, so that $\mathbf{n}\cdot\nabla c = 0$, a Neumann boundary condition. Alternatively, if there is no diffusion then solute concentration at the boundary is zero and no mass is absorbed. We consider absorption in a tube of fixed radius, so that (4.0.3) reduces to

$$-Dc_r = K_a c.$$

Nondimensionalising with respect to the radius of the tube R_0 we obtain

$$c_{\bar{r}} = -D_{ar}c. \quad (4.2.1)$$

We introduce the dimensionless parameter $D_{ar} = \frac{K_a R_0}{D}$, the radial Damköhler number which elucidates the ratio between the wall permeability and the rate of diffusion indicating whether the system is diffusion limited or absorption limited respectively.

Now equation (4.2.1) is the most suitable boundary condition provided solute absorption is not limited by the amount of concentration outside the tube's wall. If this were the case the boundary condition would then be given by

$$c_r = -\frac{D_{ar}c}{\varsigma + c}, \quad (4.2.2)$$

the *Michaelis-Menten* boundary condition. In (4.2.2) the rate at which the amount of solute can be absorbed is bounded, where D_{ar} is now the maximum absorption rate and ς is the concentration at which the rate of absorption is half its maximum. However, in the intestine, it is known that blood flow is sufficiently fast that absorbed therapeutic does not stay long enough at the membrane to impede further absorption [57].

In applying equation (4.2.1) to the intestine we have assumed the wall structure to be smooth, that is the villi are sufficiently small so that (i) they do not affect the fluid flow and (ii) they can be modelled through the permeability K_a by amplifying the permeability of the epithelial wall, K_w , by the increase in surface area S_a (a product of the villi and the microvilli surface area), such that $K_a = K_w S_a$.

4.3 Introduction to 2D Dispersion Models

In this section we discuss further motivation for the 2D extension of the 1D model to factor radial inhomogeneities into a therapeutic model. We build up a model to (i) include absorption only at the boundary rather than everywhere as discussed in §4.2 (ii)

extend diffusion to occur radially not just axially, and (iii) replace plug flow with more realistic Poiseuille flow which takes into account viscous effects at the boundary. All three modification will induce radial inhomogeneities in a solute concentration profile.

We nondimensionalise the equations and introduce alternative dimensionless Péclet number P_{er} , that now depends on the radial length scale of the tube. We introduce a simple example, where the solution is known, to understand the importance of the dimensionless parameters.

4.3.1 Introducing Radial Diffusion

Absorption on the boundary is not the only source of radial variation in concentration but also diffusion. We have so far considered axial diffusion but now we introduce into our 2D model radial diffusion. This is the process that governs solute motion across the membrane used in deriving the boundary condition. It is also plays an important role in the solute profile of very small tubes, such as chromatography [74]. We define the 2D diffusive flux by $J^D = -D\mathbf{n}\cdot\nabla c$ and the 2D convection-diffusion model by

$$c_t + \mathbf{u}\cdot\nabla c = \nabla\cdot(D\nabla c). \quad (4.3.1)$$

For axial plug flow of a solute with concentration $c = c(x, r)$, diffusing with constant coefficient, D , we reduce equation (4.3.1) to

$$c_t + uc_x = D\nabla^2 c,$$

for 2D cylindrical coordinate Laplacian (3.2.2). We present the model in Figure 4-1.

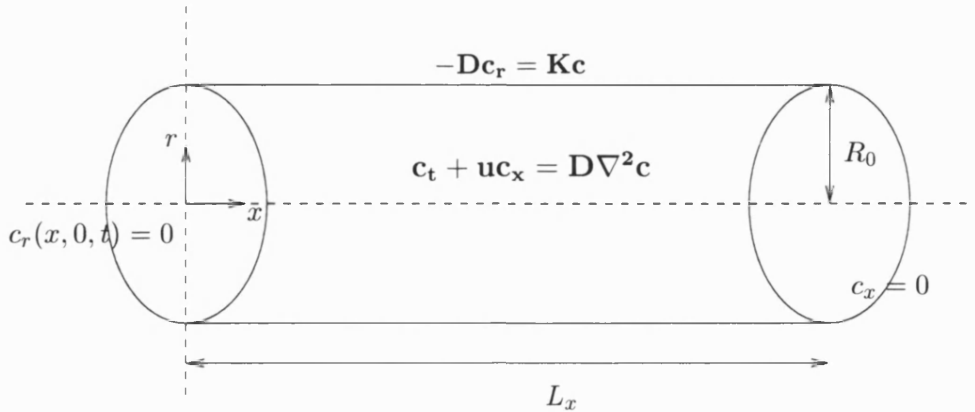


Figure 4-1: A 2D Plug Flow Dispersion Model in a Cylindrical Tube

As opposed to the 1D model (4.1.6), where the axial length L_x is the only appropriate length scale to nondimensionalise the model, the 2D model offers an alternate choice R_0 , the radius of the tube. We are interested in particle residence times and so the

time scale of interest to us is the length of time it takes solute particles to travel to the boundary. Hence we nondimensionalise the time scale with respect to the radius of the tube. In doing so we introduce an important dimensionless parameter, the ratio of the radius and length of the tube $\ell = R_0/L_x$, which satisfies $\ell \ll 1$ for a narrow tube and this is observed throughout the intestine (using anatomical data from [73]). Using the following nondimensionalised variables

$$\tilde{x} = \frac{x}{L_x}, \quad \tilde{r} = \frac{r}{R_0}, \quad \tilde{t} = \frac{tu}{R_0},$$

we derive the dimensionless 2D therapeutic equation

$$\begin{aligned} c_{\tilde{t}} + \ell c_{\tilde{x}} &= \frac{1}{P_{er}} (\ell^2 c_{\tilde{x}\tilde{x}} + c_{\tilde{r}\tilde{r}} + \frac{1}{\tilde{r}} c_{\tilde{r}}), & \text{in } \Omega, \\ c_{\tilde{r}} &= -D_{ar} c, & \text{on } \Gamma. \end{aligned} \quad (4.3.2)$$

We introduce the dimensionless radial Péclet $P_{er} = \frac{uR_0}{D}$. Hence, for a sufficiently long tube $\ell^2 \ll 1$, we see it is quite reasonable to ignore axial diffusion. In general solving this system is possible only by means of a numerical scheme, analytical solutions are fairly hard to come by in higher dimensions. However, applying a few simple assumptions we can obtain an analytical solution for (4.3.2).

4.3.2 A Simple Solvable 2D Problem

Let us consider a solute convecting and diffusing in a tube satisfying the 2D model (4.3.2). In this example we consider the case of a maintained source of solute at the inlet of the tube. It is possible to find an analytical solution if we impose a Bessel function as the Dirichlet boundary condition source term. By considering a specific case of (4.3.2), we can understand the effects of diffusion and absorption on the mean solute concentration profile.

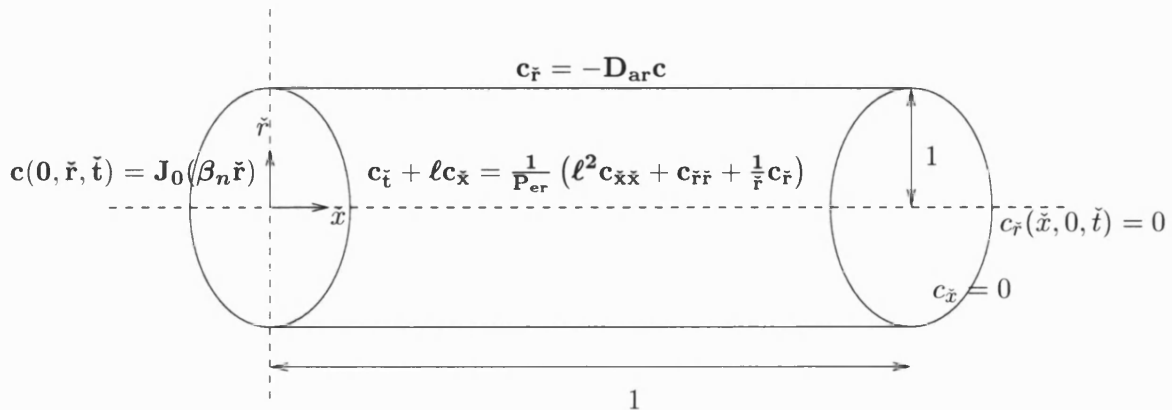


Figure 4-2: A Solvable 2D Plug Flow Dispersion Model in a Cylindrical Tube

For the purposes of understanding this model we neglect the contribution from axial diffusion in this section to obtain a simpler analytical solution. We impose a radially varying Dirichlet boundary condition $c(0, \tilde{r}, \tilde{t}) = J_0(\beta_n \tilde{r})c_0(0)$ where J_0 is a Bessel function of order zero and $c_0(\tilde{x})$ the initial axial concentration profile. An analytical solution may be found through a separation of variables and assuming the solution takes form $c(\tilde{x}, \tilde{r}, \tilde{t}) = J_0(\beta_n \tilde{r})\tilde{c}(\tilde{x}, \tilde{t})$. Substituting in this form of the solution into (4.3.2) (without axial diffusion) yields

$$J_0 \tilde{c}_t + \ell J_0 \tilde{c}_{\tilde{x}} = \frac{1}{P_{er}} \left(\frac{d^2 J_0}{d\tilde{r}^2} + \frac{1}{\tilde{r}} \frac{dJ_0}{d\tilde{r}} \right) \tilde{c}, \quad (4.3.3)$$

The right hand side of (4.3.3) satisfies the zeroth order Bessel equation, and the pde reduces to a simple 1D convection reaction equation seen in (4.1.2):

$$\tilde{c}_t + \ell \tilde{c}_{\tilde{x}} = - \left(\frac{\beta_n^2}{P_{er}} \right) \tilde{c}.$$

An analytical solution for this equation for initial profile $c_0(\tilde{x})$ is given by (4.1.3), hence the concentration c satisfies

$$c(\tilde{x}, \tilde{r}, \tilde{t}) = c_0(\tilde{x} - \ell \tilde{t}) J_0(\beta_n \tilde{r}) e^{-\frac{\beta_n^2}{P_{er}} \tilde{t}}.$$

If the initial axial profile is zero everywhere except at the inlet $c_0(\tilde{x} = 0) = 1$ the solute concentration profile in 2D is given by

$$c(\tilde{x}, \tilde{r}, \tilde{t}) = J_0(\beta_n \tilde{r}) e^{-\frac{\beta_n^2}{P_{er}} \tilde{x}} H(-\ell \tilde{t}). \quad (4.3.4)$$

The eigenvalues β_n are found by substituting the solution (4.3.4) into the absorption boundary condition so that

$$c_{\tilde{r}} = \beta_n J_1(\beta_n) \hat{c} = -D_{ar} J_0(\beta_n) \hat{c} = -D_{ar} c,$$

and consequently they satisfy the transcendental equation

$$\beta_n J_1(\beta_n) = D_{ar} J_0(\beta_n).$$

This equation is seen also in Stoll et al. [73] and Lungu et al. [52] and comes out in the averaging of the concentration in the Poiseuille dispersion model. By [73] and [52] we are only interested in the zeroth eigenvalue β_0 which ranges from 0 to ≈ 2.4 as the Damköhler number varies from a impermeable membrane $D_{ar} = 0$ to an infinitely permeable boundary $D_{ar} \rightarrow \infty$ (see Appendix Figure D-2(c)). Hence, from the solution (4.3.4) as absorption increases the membrane increasingly removes solute at the boundary. From the exponential term we learn that a decreasing P_{er} number decreases

the penetration of the source into the tube, increasing the amount of solute absorbed. This corresponds to an increase in radial diffusion promoting absorption. Similarly, the length ratio ℓ enhances absorption, the smaller the width of the tube becomes the greater the effect of radial diffusion. Consequently penetration of solute into the tube is limited by the dimensionless parameters, ℓ and P_{er} , such that solute concentration drops to $1/e$ after a distance $\tilde{x} \approx \ell P_{er}$.

Though we wish to consider a full 2D model to account for important radial variations, our main interest is the radial cross sectional average of the concentration $\bar{c}(\tilde{x}, \tilde{t})$. This is defined as the *mean solute concentration*, which in dimensional form is given by

$$\bar{c}(x, t) = \langle c \rangle = \frac{1}{A_0} \int \int c(x, r, t) dA = \frac{1}{\int_0^{R_0} \int_0^{2\pi} r dr d\theta} \int_0^{R_0} \int_0^{2\pi} c(x, r, t) r dr d\theta.$$

The nondimensional area average concentration for solution (4.3.4) is then

$$\bar{c}(\tilde{x}, \tilde{t}) = 2 \int_0^1 c(\tilde{x}, \tilde{r}, \tilde{t}) \tilde{r} d\tilde{r} = 2\tilde{c}(\tilde{x}, \tilde{t}) \int_0^1 J_0(\beta_0 \tilde{r}) \tilde{r} d\tilde{r} = \frac{2J_1(\beta_0)}{\beta_0} \tilde{c}(\tilde{x}, \tilde{t}),$$

and decreases as a function of absorption.

4.4 Averaging the Concentration Behaviour for Poiseuille Flow

The 2D plug flow model (4-1) is quite unrealistic. In general fluid moves from regions of high pressure to low pressure but in plug flow there is no pressure difference from the ends of the tube. Secondly the assumption of plug flow neglects the realistic no-slip condition that comes from viscous forces acting on fluid particles at the boundary. Hence incorporating Poiseuille flow instead of plug flow into (4.3.1) is a more physical approach to the way fluid flows. A more realistic pressure drop $\Delta\tilde{p} < 0$ drives the solute with radially varying flow $u(\tilde{r}) \geq 0$, in the positive \tilde{x} direction. The dimensional Poiseuille therapeutic dispersion model is given by

$$c_t + u(r)c_x = D\nabla^2 c. \quad (4.4.1)$$

We note a simple analytical solution is not possible even if we prescribe a Dirichlet boundary condition and we must solve (4.4.1) numerically.

In this section we consider the paper by Stoll et al. [73] who applied the 1D asymptotic equation for the mean solute concentration to model solute transport and absorption in the intestine. The full 2D Poiseuille dispersion model is quite complex to solve numerically and is high in computer cost (cpu time and memory). Hence, a 1D equation is more favourable to solve. Stoll et al. believed that conditions for therapeutic transport in the intestine were sufficient to warrant application of a *macrotransport*

*approach*¹ to obtain an easy numerically soluble 1D equation. However, the asymptotic form is applicable only in the long time, that is only after $\check{t} \gg P_{er}$. In the short time $\check{t} < P_{er}$, the 1D equation (4.4.9) fails to provide an accurate description of the true solute mean's behaviour nor of the amount of solute absorbed. This is where Brenner et al. [10] derived a fictitious initial condition to correct the error in the mean concentration for $\check{t} \ll P_{er}$.

It was hoped that a greater understanding of absorption in the intestine can come from a model that takes into account increased axial diffusion from convective dispersion, unlike a model using plug flow. This understanding would then aid in the design of therapeutic delivery systems. The model by Stoll et al. was designed in the hope that it would be able to factor in the following: molecular properties of the therapeutic and the intestinal anatomy, histology, physiology, and enzymatic activity. The model would then be able to predict the

- mean concentration of therapeutic in the lumen as a function of time and distance
- instantaneous total therapeutic mass; in the lumen, convected out of the ileum, absorbed into the systemic circulation, degraded and the systemic concentration as a function of time following oral administration.

Such detail could then elucidate the amount of drug absorbed and the amount of drug lost in the intestine. The model introduced a bolus of instantaneously dissolvable therapeutic into the duodenum, and applied anatomical data to determine the roles of degradation and permeability on the drug plasma concentration. This data was then compared to experimental therapeutic plasma concentrations following similar intraduodenal injection. However, in reproducing the results in Stoll et al. [73] we obtained erroneous results. Hence we needed to rework their analysis to understand the problem.

We consider two cases of the Poiseuille dispersion model (4.0.2), (4.2.1) when the boundary is (i) impermeable, $D_{ar} = 0$ and (ii) permeable. We break down this section into the following subsections: in §4.4.1 we discuss the results of Taylor's asymptotic analysis for the impermeable case in dimensionless form. We describe the effects of the nondimensional parameters ℓ and P_{er} on the effective coefficients U_e, D_e and the amount of time or distance $d = \ell P_{er}$ until the asymptotic equation (4.0.5) is valid. Then in §4.4.2 we determine the asymptotic conditions for the four therapeutics used in Stoll et al. [73] and show that the asymptotic conditions in the intestine are not met for the impermeable case.

We then consider the permeable case as in Stoll et al. [73]. Application of asymptotic analysis is no longer as straightforward the impermeable membrane case as the conservation of mass no longer applies. It was Sankarasubramanian et al. [4] who were

¹An asymptotic method based on moments

the first to apply analysis to the problem to reduce the 2D model to a 1D equation for the mean concentration. The asymptotic analysis was for unsteady flow $u(r, t)$. However, we focus on the steady Poiseuille flow case that was solved by Lungu and Moffatt [52]. A quite different approach to this problem was taken by Brenner et al. [10], who derived a method known as a ‘macrotransport approach’ to solve a variety of dispersive phenomena problems. Based on this work Stoll et al. applied the 1D asymptotic equation for therapeutic motion in the intestine [73]. Stoll et al. understood the lack of models taking into account complex transport phenomena. They modelled convective dispersion that comes from Poiseuille flow and stated it is responsible for greater mixing of solute particles in the small intestine.

In §4.4.3 we rework the analysis of Lungu et al. [52] and derive the same 1D asymptotic equation derived by Stoll. We highlight an important error in the absorption term seen in all macrotransport work by [6], [10], [73]. Other than this we show that Stoll et al. and Moffatt et al. derived equivalent effective absorption coefficient K_e and effective convection coefficient U_e . However, the effective dispersion term, D_e , in Lungu et al. [52] is in a form quite dissimilar from that by Stoll et al. We manipulate the term in [52] by introducing an asymptotic term used in the macrotransport approach [10], to derive the same D_e found in [73].

We show in §4.4.4 the failings of the fictitious initial condition which is used to apply the long time asymptotic equation for all time. We then discuss in §4.4.5 the application of the enhanced diffusion term meant to describe the effects of peristaltic flow, and how its use contradicts its derivation.

4.4.1 Taylor’s Solute Dispersion for an Impermeable Membrane

Consider the case of an impermeable boundary, $D_{ar} = 0$ where there is no solute flux at the membrane $c_{\bar{r}} = 0$. Dispersion of the solute arises in part from molecular diffusion but also now from radially varying non-uniform axial convection, known as convective dispersion. This convective dispersion is a property of Poiseuille flow, a spatially inhomogeneous velocity field, and comes from Brownian motion of solute molecules moving from one streamline to the next sampling all axial velocities.

Taylor [74] investigated the dependence of the mean solute concentration \bar{c} on Poiseuille flow and diffusion for asymptotically long times. This long time behaviour was based on the following assumptions on the relative sizes of solute convection and molecular diffusion: 1) *axial convection dominates axial diffusion*; the time for changes in concentration to occur from axial diffusion when compared to the time axial convection occurs is sufficiently small that axial diffusion can be ignored, 2) *radial diffusion dominates axial convection*; the radial variations in solute concentration disappear before the onset of the effects of axial convection.

We nondimensionalise (4.4.1) with the same dimensionless quantities used in the

plug flow case so that concentration in the tube satisfies:

$$c_{\check{t}} + \ell(1 - \check{r}^2)c_{\check{x}} = \frac{1}{P_{er}} \left(\ell^2 c_{\check{x}\check{x}} + c_{\check{r}\check{r}} + \frac{1}{\check{r}} c_{\check{r}} \right). \quad (4.4.2)$$

For a sufficiently narrow tube $\ell \ll 1$, the solute concentration distribution is dominated by radial diffusion, seen by the leading order term in ℓ , then by axial convection $O(\ell)$ and finally axial diffusion $O(\ell^2)$. Hence the dimensionless narrow tube model yields terms that satisfy the assumptions of solute motion laid out by Taylor [74]. By using this dimensionless form (4.4.2) the asymptotic assumption that for time $t \geq R_0^2/D$ the mean solute concentration satisfies a 1D equation becomes clearer.

Since $\ell \ll 1$ we seek a perturbation expansion in ℓ for the concentration so that

$$c(\check{x}, \check{r}, \check{t}) = c_0(\check{x}, \check{r}, \check{t}) + \ell c_1(\check{x}, \check{r}, \check{t}) + \ell^2 c_2(\check{x}, \check{r}, \check{t}) + O(\ell^3).$$

The leading order equation corresponds to radial diffusion in a disc and by Fourier analysis and applying separation of variables the analytical solution satisfies

$$c_0(\check{x}, \check{r}, \check{t}) = \sum_{n=0}^{\infty} a_n \exp(-\beta_n^2 P_{er}^{-1} \check{t}) J_0(\beta_n \check{r}), \quad (4.4.3)$$

where β_n are the eigenvalues satisfying the no flux boundary condition $J_1(\beta_n \check{r}) = 0$. Taylor stated that for a radially uniform concentration to occur the radial variations in the initial concentration must have died down to $1/e$.

The smallest eigenvalue β_0 corresponds to the largest exponential term in (4.4.3). Hence radial variation decay occurs after some time τ such that $-\beta_0^2 P_{er}^{-1} \tau = -1$ by (4.4.3), which upon rearranging satisfies

$$\check{t} > P_{er} > P_{er}/\beta_0 = \tau,$$

since $\beta_0 > 1$. This condition is valid for an infinitely long tube where the solute may have convected sufficiently far down the tube before radial variations die down.

A second condition that has been imposed in [10] is that radial diffusion must be much larger than convection so that $1/P_{er} \gg \ell$ (see (4.4.2)) or $\ell P_{er} \ll 1$. We have seen this before in the simple solvable example §4.3.2 where a narrow tube ℓ and a fast diffusing solute P_{er} , promotes solute decay. Hence, Taylor reduced the 2D model to a 1D equation for the cross-sectional average concentration [74], $\bar{c}(\check{x}, \check{t})$, and we can derive it in dimensionless form such that

$$\bar{c}_{\check{t}} + U_e \bar{c}_{\check{x}} = \underbrace{(D^m + D^c)}_{D_e} \bar{c}_{\check{x}\check{x}}, \quad (4.4.4)$$

with effective coefficients

$$U_e = \frac{\ell}{2}, \quad D^m = \frac{\ell^2}{P_{er}}, \quad D^c = \frac{\ell^2 P_{er}}{192}.$$

In (4.4.4) the dimensionless axial dispersion is comprised of (i) the nondimensional axial molecular diffusion D^m and (ii) the dimensionless convective dispersion term D^c which is given in dimensional variables by

$$D^c = \frac{1}{192} \left(\frac{R_0}{L_x} \right)^2 \frac{u R_0}{D},$$

and we note that dispersion from convective forces is inversely dependent on the molecular diffusion. This is from molecules spending shorter times sampling any one fluid streamline when there is large diffusion resulting in a decrease in the axial dispersion of solute due to Poiseuille flow.

We now investigate the importance of the term, ℓP_{er} , on applying Taylor diffusion asymptotics. We solve numerically both the full 2D model and its corresponding asymptotic 1D equation (see Numerics Chapter 6) for the solute mean \bar{c} for varying P_{er} and ℓ . We do this in the case of a slug of instantaneously dissolvable therapeutic being placed at the entrance of the tube. We solve up until time $\tilde{t} = 0.5/\ell$, that is, the time it takes for the mean solute centroid (which moves at speed U_e) to approximately travel a quarter the length of the tube. The results for the mean are a function of d , where $d = \ell P_{er}$ and are shown in Figure 4-3. We label the 2D and 1D numerical solution in blue and red respectively.

As the radial Péclet number decreases solute motion is driven away from convection to diffusion. As a result the problem becomes radially inhomogeneous sooner allowing for a better 1D fit to the 2D model before a significant amount of solute has left the tube. Only in the final case (f) is $\ell P_{er} \ll 1$ satisfied and is shown to be a better fit than the other cases. Given that the mean solute speed is $\ell/2$, the other cases will show a better 1D fit but only after $\tilde{t} \gg P_{er}$, i.e. after the mean solute centroid has travelled a distance $\ell P_{er}/2$ which lies outside the unit tube. We conclude that Taylor's 1D asymptotic equation (4.0.5) is a good approximation only if $\ell P_{er} < 0.1$.

4.4.2 Applying Taylor's 1D Averaged Equation to the Intestine In the Absence of Absorption

The Gastro-Intestinal tract is very long and quite narrow and it is reasonable to postulate that Taylor diffusion could be applied to solute motion in the intestine. We investigate the suitability of applying Taylor asymptotic analysis. We test the conditions in its application to four diffusing therapeutics in the intestine using the anatomical parameters for three mammals described in Stoll et al. [73].

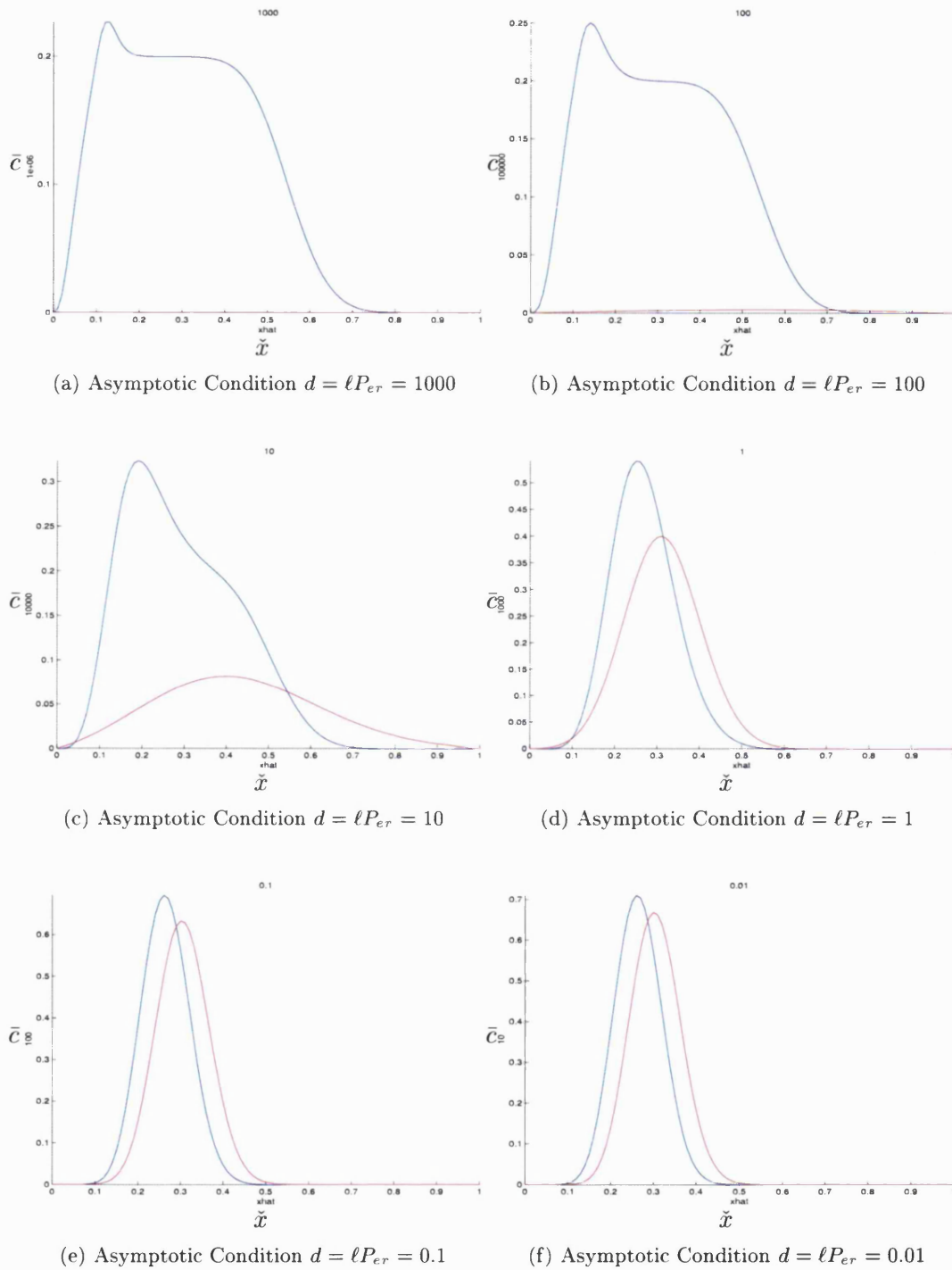


Figure 4-3: A Comparison of the Numerical Solution of the Mean Solute Concentration from the full 2D Poiseuille Dispersion Model (Blue) with the Numerical Solution of the Mean Solute Concentration from the 1D Taylor Dispersion equation (Red).

Therapeutic Parameters		Human		Primate		Rat	
Length of Small Intestine (cm)		285		285		100	
Mean Time Avg Lumen Radius (cm)		1.8		0.8		0.375	
Mean Axial Velocity (cm/s)		1.7e-2		1.7e-2		8.0e-3	
Amplitude Ratio ℓ		6.32e-3		2.81e-3		3.75e-3	
Model Parameters							
Therapeutic	Diffusion D_m (cm ² /s)	P_{er}	ℓP_{er}	P_{er}	ℓP_{er}	P_{er}	ℓP_{er}
Ibuprofen	2.5e-5	2.45e3	1.55e1	1.09e3	3.05e0	2.40e2	6.74e-1
GHRP-1	4.4e-6	1.39e4	8.78e1	6.18e3	1.74e1	1.36e3	3.83e0
Calcitonin	2.7e-6	2.27e4	1.43e2	1.01e4	2.83e1	2.22e3	6.24e0
Insulin	2.2e-6	2.78e4	1.76e2	1.24e4	3.47e1	2.73e3	7.66e0

Table 4.1: A Table of Anatomical and Therapeutic Parameters

In Table 4.1 we observe the amplitude ratios in the intestine of the three mammals are all approximately of the order $O(10^{-3})$. Hence for Péclet numbers between $O(10^3)$ and $O(10^4)$, we determine the asymptotic distance condition $d = \ell P_{er}$ for humans is greater than one. Across the species $d > 1$ for most of the therapeutics. Hence anatomical conditions do not warrant applying asymptotic analysis. For conditions to improve for the 1D equation to be a better approximation of the 2D model in the intestine, the membrane Péclet number must decrease, either by (i) a decrease in fluid velocity in the intestine (e.g. increased viscosity), or (ii) a faster diffusing therapeutic.

4.4.3 Solute Dispersion for a Permeable Membrane

We now derive the dispersion equation by Stoll et al. using Lungu and Moffatt's analysis [52] using alternative scaling. In the case by Lungu et al., the Poiseuille dispersion model was for an infinitely long tube and as such had no characteristic axial length scale. Hence they used an alternative dimensionless form to ours seen in (4.4.2). Their analysis still applies for a finite length tube, however, as seen in (4.4.2) it is not always possible that the mean solute concentration achieves asymptotic form before solute exits the cylinder $d > 1$.

Consider the solute concentration $c(\tilde{x}, \tilde{r}, \tilde{t})$ satisfying (4.4.2), to be a Fourier transform of some function $\hat{c}(k, \tilde{r}, \tilde{t})$ whereby

$$c(\tilde{x}, \tilde{r}, \tilde{t}) = \int_{-\infty}^{\infty} \hat{c}(k, \tilde{r}, \tilde{t}) e^{ik\tilde{x}} dk.$$

Then we can rewrite equation (4.4.2) in terms of the fourier function and transforming all the partial derivatives in \tilde{x} , into multiplication operations in the transform domain k . Let $\tilde{u}(\tilde{r}) = 1 - \tilde{r}^2$, then the pde can then be written as

$$\begin{aligned} \hat{c}_{\tilde{t}} + (i\ell k)\tilde{u}(\tilde{r})\hat{c} &= P_{er}^{-1}(\hat{\nabla}^2 - \ell^2 k^2)\hat{c}, \quad \text{in } \Omega, \\ \frac{\partial \hat{c}}{\partial \tilde{r}} + D_{ar}\hat{c} &= 0, \quad \text{on } \Gamma, \end{aligned}$$

for purely radial gradient operator $\hat{\nabla} = \partial_{\tilde{r}\tilde{r}} + (1/\tilde{r})\partial_{\tilde{r}}$. It was assumed that through separation of variables the general solution has the form

$$\hat{c} = \sum_n A_n F_n(k, \ell, \tilde{r}) e^{-p_n(k, \ell)\tilde{t}},$$

of a sum of exponentially decaying Fourier waves. They then satisfy the time independent eigenfunction problem in space

$$\begin{aligned} -pF + (ik\ell)\tilde{u}F &= P_{er}^{-1}(\hat{\nabla}^2 - \ell^2 k^2)F, & \text{in } \Omega, \\ F_{\tilde{r}} + D_{ar}F &= 0, & \text{on } \Gamma, \end{aligned} \quad (4.4.5)$$

for eigenvalues p_n and corresponding eigenfunction F_n . Multiplying (4.4.5) by \bar{F} and integrating by parts implies the problem satisfies:

$$(p - P_{er}^{-1}\ell^2 k^2) \int_{\Omega} |F|^2 d\Omega = P_{er}^{-1} \int_{\Omega} |\nabla F|^2 \Omega + P_{er}^{-1} D_{ar} \int_{\Gamma} |F|^2 d\Gamma + ik\ell \int_{\Omega} \tilde{u} |F|^2 d\Omega. \quad (4.4.6)$$

Separating (4.4.6) into real and imaginary parts one observes that the real parts of the eigenvalues p_n are greater than k^2 and consequently can be rearranged such that

$$k^2 < Re(p_0) \leq Re(p_1) \leq Re(p_2) \leq \dots$$

With any eigenvalue problem the general solution is given by an infinite sum of the solutions for each n , but for suitably large time \tilde{t} , and $Re(p_0) < Re(p_1)$, the general solution for the Fourier solution \hat{c} and the solute concentration c is dominated by the zeroth eigenvalue solution for sufficiently large \tilde{t} ,

$$\hat{c} \approx A_0 F_0(k, \ell, \tilde{r}) e^{-p_0(k, \ell)\tilde{t}} \quad \Rightarrow \quad c \approx \int_{-\infty}^{\infty} A_0 F_0(k, \ell, \tilde{r}) e^{-p_0(k, \ell)\tilde{t}} e^{ikx} dk \quad (4.4.7)$$

For a narrow tube, if $k\ell \ll 1$, a perturbation expansion in $ik\ell$ can be found for p_0 such that

$$p_0 = p_{00} + (ik\ell)p_{01} + (ik\ell)^2 p_{02} + \dots \quad (4.4.8)$$

Hence, we can substitute (4.4.8) into (4.4.7) such that

$$\begin{aligned} c &\approx \int_{-\infty}^{\infty} A_0 F_0 e^{-(p_{00} + (ik\ell)p_{01} + (ik\ell)^2 p_{02} + \dots)\tilde{t}} e^{ikx} dk \\ &\approx \int_{-\infty}^{\infty} A_0 F_0 e^{-p_{00}\tilde{t}} (1 + (ik\ell)p_{01}\tilde{t} + O(k^2 \ell^2 \tilde{t}^2)) e^{ikx} dk \\ &\approx c_0 + o(1) \end{aligned}$$

By a similar method we can show

$$\frac{\partial c}{\partial \tilde{x}} = \frac{\partial c_0}{\partial \tilde{x}} + o(1)$$

It follows from differentiating the asymptotic form (4.4.7) with respect to time that

$$\begin{aligned} \frac{\partial c}{\partial \tilde{t}} &= \frac{\partial}{\partial \tilde{t}} \int_{-\infty}^{\infty} A_0 F_0 e^{-p_0 \tilde{t}} e^{ikx} dk = \int_{-\infty}^{\infty} -p_0 A_0 F_0 e^{-p_0 \tilde{t}} e^{ikx} dk \\ &= \int_{-\infty}^{\infty} -(p_{00} + (ik\ell)p_{01} + (ik\ell)^2 p_{02} + \dots) A_0 F_0 e^{-p_{00} \tilde{t}} (1 + (ik\ell)p_{01} \tilde{t} + O(k^2 \ell^2 \tilde{t}^2)) e^{ikx} dk \\ &= -p_{00} \int_{-\infty}^{\infty} A_0 F_0 e^{-p_{00} \tilde{t}} e^{ikx} dk - p_{01} \ell \int_{-\infty}^{\infty} (ik) A_0 F_0 e^{-p_{00} \tilde{t}} e^{ikx} dk \\ &\quad - p_{02} \ell^2 \int_{-\infty}^{\infty} (ik)^2 A_0 F_0 e^{-p_{00} \tilde{t}} e^{ikx} dk + o(1) \end{aligned}$$

Hence, the 1D asymptotic equation governing the solute concentration is given by

$$\frac{\partial c_0}{\partial \tilde{t}} = -p_{00} c_0 - p_{01} \ell \frac{\partial c_0}{\partial \tilde{x}} - p_{02} \ell^2 \frac{\partial^2 c_0}{\partial \tilde{x}^2} - O(\ell^3), \quad (4.4.9)$$

a 1D convection diffusion reaction equation (from hereon we drop the subscript 0). The coefficients of the pde represent an effective absorption $K_e = p_{00}$, an effective convection $U_e = p_{01} \ell$ and an effective diffusion $D_e = p_{02} \ell^2$. The expansion coefficients of p_0 are found by substituting the power series of p_0 into (4.4.5) under the assumption that F_0 can also be expressed by a similar perturbation expansion,

$$F_0 = F_{00} + (ik\ell)F_{01} + (ik\ell)^2 F_{02} + \dots$$

Hence comparing powers of $ik\ell$, the coefficients satisfy

$$\begin{aligned} O(1) \quad & (P_{er}^{-1} \hat{\nabla}^2 + p_{00}) F_{00} = 0, \\ O(k\ell) \quad & (P_{er}^{-1} \hat{\nabla}^2 + p_{00}) F_{01} = (\hat{u} - p_{01}) F_{00}, \\ O((k\ell)^2) \quad & (P_{er}^{-1} \hat{\nabla}^2 + p_{00}) F_{02} = (\hat{u} - p_{01}) F_{01} - (p_{02} + P_{er}^{-1}) F_{00}. \end{aligned} \quad (4.4.10)$$

Lungu et al. stated that F_{00} can be normalised so that its square integral is unity,

$$\int |F_{00}|^2 d\Omega = 1. \quad (4.4.11)$$

Hence, multiplying the $O(1)$ equation by F_{00} and using Green's Identity with the Robin boundary condition, we find p_{00} satisfies

$$p_{00} = P_{er}^{-1} \left(\int |\hat{\nabla} F_{00}|^2 d\Omega + D_a \int_{\Gamma} |F_{00}|^2 d\Gamma \right) = \frac{\beta_0^2}{P_{er}}.$$

The solution to the $O(1)$ equation is then given by $F_{00} = \Phi J_0(\beta_0)$, where Φ was found

through normalising the solution,

$$\Phi = \left[2\pi \int_0^1 J_0^2(\beta_0 \tilde{r}) \tilde{r} d\tilde{r} \right]^{-1/2} = [\pi(J_0^2(\beta_0) + J_1^2(\beta_0))]^{-1/2}.$$

Most important is that the eigenvalue β must satisfy the dimensionless transcendental equation

$$\beta_0 J_1(\beta_0) = D_a J_0(\beta_0). \quad (4.4.12)$$

Hence, upon rearranging (4.4.12), the effective absorption coefficient can be found so that

$$K_e = p_{00} = \frac{\beta_0^2}{P_{er}} = \frac{D_{ar}}{P_{er}} \left(\frac{\beta_0 J_0(\beta_0)}{J_1(\beta_0)} \right) = \frac{D_{ar}}{P_{er}} \frac{\alpha^*}{2}.$$

The above asymptotic form for α^* differs from the work by [73], [10], [6] where they have inverted the Bessel functions. We plot α^* as a function of the Damköhler number in Appendix Figure D.1 and it is the same as seen in [10], [6] for α^* match, which suggests a transcript error. This has a profound effect on the fraction dose absorbed if it were applied incorrectly. Moving on to solve $O(\ell k)$ equation for F_{01} , we apply a similar method and multiply by F_{00} so that

$$P_{er}^{-1} \int F_{00} \hat{\nabla} F_{01} d\Omega + P_{er}^{-1} p_{01} \int F_{01} F_{00} = \int (\hat{u} - p_{01}) |F_{00}|^2.$$

This above problem can only be solved under the assumption that the left hand side of the equation was zero [52], so that

$$p_{01}(\beta_0) = \int \hat{u} |F_{00}|^2 d\Omega = \frac{\int_0^1 \hat{u}(\tilde{r}) (J_0(\beta_0 \tilde{r}))^2 \tilde{r} d\tilde{r}}{\int_0^1 (J_0(\beta_0 \tilde{r}))^2 \tilde{r} d\tilde{r}} = \frac{1}{2} \left(1 + \frac{J_1^2(\beta_0) + [2\beta_0^{-1} J_1(\beta_0) - J_0(\beta_0)]^2}{3 [J_0^2(\beta_0) + J_1^2(\beta_0)]} \right)$$

We plot U_e/\bar{V} as a function of the Damköhler number in Appendix Figure D.1, this is in agreement with the asymptotic convection term found in Brenner et al. [10]. Simply multiplying $\gamma^* = 2p_{01}$ by ℓ and we obtain the corresponding dimensionless effective velocity term found in [73]. It is only left to show the equivalence of the effective diffusion term D_e . Lungu et al. applied a similar solvability condition to derive the following

$$\begin{aligned} (p_{02} + P_{er}^{-1}) F_{00} &= \int (\hat{u} - p_{01}) F_{00} F_{01} d\Omega = \int ((P_{er}^{-1} \hat{\nabla} + p_{00}) F_{01}) F_{01} d\Omega \\ &= p_{00} \int_{\Omega} |F_{01}|^2 d\Omega - P_{er}^{-1} \int_{\Omega} |\hat{\nabla} F_{01}|^2 d\Omega - P_{er}^{-1} D_a \int_{\Gamma} |F_{01}|^2 d\Omega \\ &= -M(D_{ar}) \end{aligned} \quad (4.4.13)$$

where F_{01} is found solving $O(\ell k)$. We manipulate (4.4.13) to reduce it to an asymptotic form found in [73].

Deriving the Effective Dispersion Coefficient

In showing that the effective dispersion coefficient by derived by Stoll et al. [73] and Lungu et al. [52] are one and the same we need not solve for F_{01} , but rather we define a dimensionless function B that is proportional to the ratio of F_{01} and F_{00} so that

$$B(\hat{r}) = -\frac{F_{01}(\hat{r})}{F_{00}(\hat{r})}.$$

We substitute $F_{01} = -BF_{00}$ into (4.4.13) and obtain

$$(P_{er}^{-1}\hat{\nabla}^2 + p_{00})(BF_{00}) = (p_{01} - \hat{u})F_{00},$$

Expanding the laplacian operator yields and denoting $' \equiv d/d\hat{r}$

$$P_{er}^{-1}F_{00}\hat{\nabla}^2 B + 2P_{er}^{-1}B'F_{00}' + BP_{er}^{-1}\hat{\nabla}^2 F_{00} + p_{00}BF_{00} = (p_{01} - \hat{u})F_{00},$$

Rearranging we obtain

$$P_{er}^{-1}F_{00}\hat{\nabla}^2 B + 2P_{er}^{-1}B'F_{00}' + \underbrace{B(P_{er}^{-1}\hat{\nabla}^2 F_{00} + p_{00}F_{00})}_{=0 \text{ by } O(1)} = (p_{01} - \hat{u})F_{00}, \quad (4.4.14)$$

Consequently we determine the second order ode

$$\frac{d^2 B}{d\hat{r}^2} + \frac{1}{\hat{r}} \frac{dB}{d\hat{r}} + \frac{2F_{00}'}{F_{00}} \frac{dB}{d\hat{r}} = P_{er}(p_{01} - \hat{u}), \quad (4.4.15)$$

The boundary condition for B obtained from (4.4.5) so that

$$\frac{dB}{d\hat{r}} = \frac{1}{F_{00}^2} (F_{00}'F_{01} - F_{00}F_{01}').$$

But on the boundary we have $F_{0i}' + D_a F_{0i} = 0$, so

$$\frac{dB}{d\hat{r}} = \frac{1}{F_{00}^2} (F_{00}'F_{01} - F_{00}D_a F_{01}) = \frac{F_{01}}{F_{00}^2} (F_{00}' + D_a F_{00}) = 0. \quad (4.4.16)$$

Hence a zero derivative boundary condition for B and so we have proved B satisfies the field equation mentioned in [6], [10]. Consequently the effective diffusion component $M(D_{ar})$ can be rewritten using (4.4.14) as

$$\begin{aligned} M(D_{ar}) &= \int_{\Omega} (p_{01} - \hat{u})F_{00}F_{01} = -P_{er}^{-1} \int_{\Omega} (F_{00}\hat{\nabla}^2 B + 2\hat{\nabla}B\hat{\nabla}F_{00})(BF_{00}) \\ &= -P_{er}^{-1} \int_{\Omega} F_{00}^2 B\hat{\nabla}^2 B + 2BF_{00}\hat{\nabla}B\hat{\nabla}F_{00} \end{aligned}$$

Hence,

$$\begin{aligned} M(D_{ar}) &= P_{er}^{-1} \int_{\Omega} \hat{\nabla} B \hat{\nabla} (F_{00}^2 B) - \underbrace{\int_{\Gamma} F_{00}^2 B \hat{\nabla} B}_{=0 \text{ by (4.4.16)}} - \int_{\Omega} 2BF_{00} \hat{\nabla} B \hat{\nabla} F_{00} \\ &= P_{er}^{-1} \int_{\Omega} F_{00}^2 (\hat{\nabla} B)^2 \end{aligned} \quad (4.4.17)$$

As in [10], we apply an integrating factor to (4.4.15) to find the derivative of B

$$\frac{dB}{d\tilde{r}} = \frac{P_{er}\tilde{r}}{2} \left(1 + \frac{J_1^2(\beta_0\tilde{r})}{J_0^2(\beta_0\tilde{r})} \right) \left((\ell p_{01}(\beta_0) - \ell) - \tilde{r}^2 (\epsilon p_{01}(\beta_0\tilde{r}) - \ell) \right). \quad (4.4.18)$$

Now the effective dispersion coefficient is given by

$$D_e = -p_{02}\ell^2 = \ell^2 (M(D_{ar}) + P_{er}^{-1}) = \frac{\ell^2}{P_{er}} \left(1 + \int F_{00}^2 |\hat{\nabla} B|^2 \right).$$

Hence by substituting (4.4.18) in (4.4.17) we obtain

$$\begin{aligned} D_e &= \frac{\ell^2}{P_{er}} \left(1 + \int \Phi^2 J_0^2(\beta_0\tilde{r}) \left(\frac{P_{er}\tilde{r}}{2} \right)^2 \dots \right. \\ &\quad \left. \left(1 + \frac{J_1^2(\beta_0\tilde{r})}{J_0^2(\beta_0\tilde{r})} \right)^2 (\ell(p_{01}(\beta_0) - 1) - \ell\tilde{r}^2(p_{01}(\beta_0\tilde{r}) - 1))^2 \tilde{r} d\tilde{r} \right) \\ &= \frac{\ell^2}{P_{er}} \left(1 + \frac{P_{er}^2}{4} \frac{\Omega}{48} \right), \end{aligned}$$

where Ω is the diffusion factor described in [73]. We plot Ω as a function of the Damköhler number in Appendix Figure D.1. Hence we have derived the 1D asymptotic equation to the 2D Poiseuille dispersion model

$$c_t + \left(\frac{\gamma^*}{2} \ell \right) c_{\tilde{x}} = \frac{\ell^2}{P_{er}} \left(1 + \frac{\Omega}{192} P_{er}^2 \right) c_{\tilde{x}\tilde{x}} - \frac{\alpha^* D_{ar}}{2P_{er}} c \quad (4.4.19)$$

The coefficients γ^*, α^* and Ω are functions of the Damköhler number (see Appendix Figure D-2). For zero absorption the coefficients equal unity and (4.4.19) reduces to the 1D Taylor asymptotic equation. From the asymptotic coefficient we see that as absorption increases the effective velocity increases corresponding to slower streamlines being eroded. Similarly, the contribution to dispersion from convection decreases as molecules are no longer able to diffuse into the slower streamlines and spread out further axially. In the next subsection we consider the macrotransport approach by Stoll et al. for solute dispersion in the intestine.

4.4.4 Compensating for Long Time Behaviour: Deriving The Fictitious Initial Condition

Brenner et al. [10] state that for the long time asymptotics 1D equation (4.4.9) to be valid for short time, then the mean solute concentration must satisfy

$$\bar{c}_{\text{fic}}(\check{x}, 0) = \int_0^1 A(\check{r})c(\check{x}, \check{r}, 0)\check{r}d\check{r}.$$

where the true initial mean at $\check{t} = 0$ was defined as

$$\bar{c}_{\text{true}}(\check{x}, 0) = \int_0^1 c(\check{x}, \check{r}, 0)\hat{r}d\check{r}.$$

It was assumed that the initial cross-sectional average satisfies $\bar{c}(\check{x}, 0) = \phi(\check{x})$, and so

$$\bar{c}_{\text{fic}}(\check{x}, 0) = \bar{A}^* \bar{c}_{\text{true}}(\hat{x}, 0), \quad \text{such that} \quad \bar{A}^* = \int_0^1 A(\check{r})\check{r}d\check{r},$$

and the fictitious and true initial mean concentration are not identical. Now the fictitious function $A(\hat{r})$ was chosen by Brenner to be the solution of a boundary value problem which in our dimensionless coordinates is

$$\nabla_{\hat{r}}^2 A(\hat{r}) + P_{er} \bar{K}_A^* = 0, \quad (4.4.20)$$

with absorption boundary condition $\mathbf{n} \cdot \nabla_{\hat{r}} A(\hat{r}) = -D_{ar} A(\hat{r})$. This is known as the adjoint eigenvalue problem for $A(\hat{r})$ [10]. We observe that $A(\hat{r})$ satisfies the leading order equation of Moffat's long time asymptotic analysis (4.4.10) for p_{00} .

$$(P_{er}^{-1} \nabla^2 + p_{00}) F_{00} = 0. \quad (4.4.21)$$

However, F_{00} and A are not the same, their equations are self adjoint so that their solutions differ by a multiplicative constant and this depends on the normalisation condition applied to F_{00} and A . The macrotransport approach by Brenner et al. applies conditional probability densities based on the Brownian behaviour of a single molecule. One of the main variables introduced was P_0^∞ , the long time zero order local moment. This is very similar to F_{00} which was also uniquely defined such that its square integral was unity (4.4.11). However, P_0^∞ satisfies (4.4.20) known as the characteristic eigenvalue problem, but also a second unique normalisation conditions

$$(i) \quad \int P_0^\infty d\Omega = 1, \quad (4.4.22)$$

$$(ii) \quad \int P_0^\infty A(\hat{r}) d\Omega = 1. \quad (4.4.23)$$

Hence, the fictitious term $A(\tilde{r})$, local moment P_0^∞ and our perturbation expansion term F_{00} are related by:

$$P_0^\infty A(\tilde{r}) = F_{00}^2 = \Phi^2 J_0^2(\beta_0 \tilde{r}), \quad P_0^\infty = c_P J_0(\beta_0 \tilde{r}), \quad A(\tilde{r}) = c_A J_0(\beta_0 \tilde{r}), \quad (4.4.24)$$

where the multiplicative constants c_P, c_A are found through the normalisation condition (4.4.23) such that

$$c_P = \left(\frac{\beta_0^2}{2\pi D_{ar} J_0(\beta_0)} \right), \quad c_A = \left(\frac{2D_{ar}}{2J_0(\beta_0) (\beta_0^2 + D_{ar}^2)} \right). \quad (4.4.25)$$

Batycky et al. have shown that there is significance in the value of the fictitious constant c_A [6]. Consider the Poiseuille dispersion model (4.4.2) to leading order term in ℓ , that is

$$c_{\tilde{t}} = \frac{1}{P_{er}} \left(c_{\tilde{r}\tilde{r}} + \frac{1}{\tilde{r}} c_{\tilde{r}} \right) + O(\ell), \quad (4.4.26)$$

with the appropriate absorption boundary condition (4.2.1). The corresponding asymptotic equation to leading order is then

$$\bar{c}_{\tilde{t}} = -p_{00} \bar{c} + O(\ell). \quad (4.4.27)$$

We are basically considering radial diffusion in a disc with absorption at the boundary, since convective fluxes $O(\ell)$ are assumed to be negligible. For an initial condition $c(\tilde{r}, 0) = f(\tilde{r})$, the analytical solution is given by

$$c(\tilde{r}, \tilde{t}) = \sum_{n=0}^{\infty} \alpha_n J_0(\beta_n \tilde{r}) e^{-\frac{\beta_n^2 \tilde{t}}{P_{er}}}, \quad \alpha_n = \frac{2\beta_n^2}{J_0^2(\beta_n) (\beta_n^2 + D_{ar}^2)} \int_0^1 f(\tilde{r}) J(\beta_n \tilde{r}) \tilde{r} d\tilde{r},$$

(see [10]). The cross-sectional average is subsequently given by

$$\bar{c}(\tilde{t}) = \sum_{n=0}^{\infty} \frac{2D_{ar} J_0(\beta_n)}{\beta_n^2} \alpha_n e^{-\frac{\beta_n^2 \tilde{t}}{P_{er}}},$$

Arranging the eigenvalues in increasing size order such that β_0 is the smallest, then the leading order term of the exact solution is found to be

$$\bar{c}(\tilde{x}, \tilde{t}) \approx \left\{ \left(\frac{2D_{ar}}{J_0(\beta_0) (\beta_0^2 + D_{ar}^2)} \right) 2 \int_0^1 f(\tilde{r}) J_0(\beta_0 \tilde{r}) \tilde{r} d\tilde{r} \right\} e^{-\frac{\beta_0^2 \tilde{t}}{P_{er}}} = \bar{c}_{\text{true}}(0) e^{-\frac{\beta_0^2 \tilde{t}}{P_{er}}}.$$

Now the solution for the asymptotic equation can easily be solved for

$$\bar{c}(\tilde{t}) = \bar{c}_{\text{fic}}(0) e^{-p_{00} \tilde{t}} = \bar{c}_{\text{fic}}(0) e^{-\frac{\beta_0^2 \tilde{t}}{P_{er}}} = \left(2 \int_0^1 f(\tilde{r}) A(\tilde{r}) \tilde{r} d\tilde{r} \right) e^{-\frac{\beta_0^2 \tilde{t}}{P_{er}}}. \quad (4.4.28)$$

For initial condition $c(\hat{x}, \tilde{r}, 0) = f(\tilde{r})$ we substitute $A(\tilde{r})$ (4.4.24) and c_A (4.4.25) into (4.4.28) to obtain the asymptotic solution

$$\bar{c}(\hat{t}) = \left\{ c_A 2 \int_0^1 f(\tilde{r}) J_0(\beta_0 \tilde{r}) \tilde{r} d\tilde{r} \right\} e^{-\frac{\beta_0^2 \hat{t}}{P_{er}}}.$$

We have shown that the mean concentration solution to the purely radially diffusive part of the Poiseuille problem (4.4.26) matches the equivalent solution of the asymptotic equation (4.4.27) to leading order eigenvalue β_0 . We clearly see the motivation for a fictitious initial condition by Batycky et al. However, we also see the limits to which the fictitious term was applied, and that is of a purely radially diffusing solute. If convection plays a larger role in the dispersion of the solute then we do not expect to see the fictitious initial term to compensate effectively for short time.

Application of a Fictitious Initial Condition

Consider the case where the initial condition is constant in the radial direction $\bar{c}(\hat{x}, 0) = c_0(x)$. Then using (4.4.24) and (4.4.25) we derive the fictitious condition used in the model by Stoll et al. [73]:

$$\bar{A}^* = 2 \int_0^1 A(\tilde{r}) \tilde{r} d\tilde{r} = \frac{4D_{ar}^2}{\beta_0^2 (\beta_0^2 + D_{ar}^2)}, \quad (4.4.29)$$

so that $\bar{c}_{\text{fic}} = \bar{A}^* \bar{c}_{\text{true}}$. As the boundary membrane becomes increasingly impermeable, $D_{ar} \rightarrow 0$, the fictitious term tends to unity, $\bar{A}^* \rightarrow 1$. Conversely, as the membrane becomes more permeable, $D_{ar} \rightarrow \infty$, then $\bar{A}^* \rightarrow 0.692$ [6]. See Appendix Figure D.1 for the graph of \bar{A}^* versus the Damköhler number. Hence, all long time asymptotic coefficients of the permeable membrane reduce to those of Taylor when $D_{ar} = 0$, for an impermeable membrane.

Here lies the ambiguity of the macrotransport approach applied by Stoll, Baycky and Brenner. They have suggested that a fictitious term compensates long time asymptotics over the short time to justify the use of the asymptotic equation for a physical problem rather than for theoretical purposes only. However, we know this fictitious term is one in the impermeable case and the asymptotic equation reduces to that of Taylor's which has been shown to be valid only for $d = \ell P_{er} \ll 1$. Hence, following the argument by Stoll et al., the 1D asymptotic mean concentrations of an impermeable membrane are a valid representation of the full two-dimensional mean for all time (see Figures 4-3(a) and 4-3(b)). We have clearly shown it is not possible to compensate for short time for an impermeable membrane, leaving open the question whether the fictitious initial condition do so for an increasingly permeable wall. We satisfy this argument later by solving numerically the full 2D model (4.4.2), (4.2.1) and the 1D asymptotic equation (4.4.19) with the fictitious term (4.4.29). Now Stoll et al. made

one amendment to the macrotransport approach laid out by Brenner et al. [10]. That is peristalsis can be modelled by enhanced diffusion making the time for the asymptotic equation to become valid shorter. We review this in the next subsection.

4.4.5 Modelling Peristalsis by Enhanced Diffusion

In the intestine, fluid undergoes peristaltic motion, the body's natural adaption to enhance mixing and increased absorption. This process is very complex and quite difficult to model. It was simplified by Stoll et al. [73] to be a macrotransport process yielding enhanced diffusion. Consider in 2D tracer particles in an incompressible fluid trapped in closed streamlines such that they undergo Taylor vortex-like flow [10] with velocities

$$\begin{aligned} u(x, y, t) &= A(t) \cos\left(\frac{\pi x}{d_1}\right) \sin\left(\frac{\pi y}{d_2}\right), \\ v(x, y, t) &= -A(t) \sin\left(\frac{\pi x}{d_1}\right) \cos\left(\frac{\pi y}{d_2}\right), \end{aligned}$$

and time dependent field strength

$$A(t) = A_0 \exp(-\pi \nu t (d_1^{-2} + d_2^{-2})).$$

An enhanced diffusion coefficient is found by applying a perturbation expansion for small Péclet number (large diffusion). Using a macrotransport approach Brenner [10] derived the enhanced dispersion coefficient:

$$D_{en} = D + \left(\frac{A(d_1 d_2)^2}{4\pi^2 D}\right) \left(1 + \left(\frac{d_1}{d_2}\right)^2\right) + O(D^{-2}).$$

Hence for circular trapped streamlines and constant field strength $A = \Gamma$, Stoll et al. formulated the enhanced dispersion term

$$D_{en} = D_m + \frac{(\Gamma d^*)^2}{8\pi^2 D_m}. \quad (4.4.30)$$

Without this diffusion enhancement, the therapeutic P_{er} number would be too high to even consider applying a macrotransport approach.

We determine $d = \ell P_{er}$, for the four therapeutics applied to Humans (seen earlier), as a function of 1) molecular diffusion and 2) enhanced diffusion from peristalsis. We tabulate the results, see Table 4.2, and observe two facts (i) the Péclet numbers for the therapeutics are too large to apply a perturbation expansion, invalidating the use of the peristaltic diffusion formula (4.4.30), and (ii) even applying the formula the condition $d = \ell P_{er}(De)$ does not sufficiently decrease to warrant applying the 1D asymptotic equation (4.4.9).

We also note the results for $P_{er}(De)$ are inconsistent with those obtained from Stoll

Therapeutic Parameter	Ibuprofen	GHRP-1	Calcitonin	Insulin
Molecular Diffusion D_m	2.5e-05	4.4e-6	2.7e-6	5.2e-4
Enhanced Diffusion D_e	7.1e-5	2.7e-4	4.3e-4	5.2e-4
$P_{er}(D_m)$	2.4e3	1.4e4	2.3e4	2.8e4
$P_{er}(D_{en})$	8.6e2	2.3e2	1.4e2	1.2e2
$\ell P_{er}(D_m)$	15.4	87.8	1.4e2	1.8e2
$\ell P_{er}(D_{en})$	5.4	1.4	0.90	0.73

Table 4.2: A Table of Therapeutic Péclet Numbers and their Corresponding Asymptotic Condition Value (main asymptotic conditions are shown in bold).

et al., 10 orders of magnitude lower are seen for Calcitonin and Insulin in [73]. This is sufficient cause for concern when viewing the work by Stoll et al., especially when they calculated that the initial bolus of tracer particles will only have travelled 5-10cm ($d \approx 0.02 - 0.04$) into the small intestine by the time $t \gg R_0^2/D$. This justified the use of the fictitious initial condition by Stoll et al. as it need only compensate for a very short distance. However, from the above table we see that $\ell P_{er}(D_e) > 0.7 \gg 0.04$ so that the tracers will have travelled well over 70% of the intestine before the mean solute concentration would attain asymptotic form. Now using the anatomical and therapeutic parameters in [73] we investigate the results obtained for the mean using (i) the asymptotic approach and (ii) numerically solving the full 2D model.

4.5 Comparing the Numerical Solution of the Full 2D model with the Numerical Solution of the 1D Asymptotic Equation

We now test the validity of the model by Stoll et al., particularly on the effectiveness of the fictitious initial condition, by numerically solving the full 2D Poiseuille dispersion model (4.4.2), (4.2.1) and compare the mean solute concentration \bar{c}_2 with \bar{c}_1 , the numerical solution of the 1D model (4.4.19). Given the four therapeutic Ibuprofen, GHRP-1, Calcitonin and Insulin, and anatomical parameters in humans [73], we determine ℓ , P_{er} and D_{ar} . We solve the full 2D Poiseuille dispersion model (4.4.2) using finite difference operators on a discretised domain for solute concentration $c(\tilde{x}_j, \tilde{t}_n, \tilde{r}_k)$ (see Numerics Chapter 6). We solve up to time $\tilde{t} = 1/2\ell$, where the peak of the centroid concentration will on average have travelled one quarter of the distance of the intestine, we then find the cross-sectional average concentration $\bar{c}_2(\tilde{x}_j, \tilde{t}_n)$ using trapezium rule. We stipulate the time condition to ensure that little mass will have been lost by convection out of the intestine. Subsequently we solve the 1D asymptotic equation (4.4.9) for the mean concentration $\bar{c}_1(\tilde{x}_j, \tilde{t}_n)$.

We compare the mean solute concentration of the two models, and determine whether (i) the full Poiseuille model can be approximated by a 1D dispersion equa-

tion, if so (ii) what are the effective coefficients and (iii) how do these numerically obtained coefficients compare with those obtained asymptotically by Stoll. We require an algorithm to determine the first two conditions.

4.5.1 Approximating the Numerically Obtained Mean Solute Concentration of the 2D Dispersion Model by a 1D Dispersion Equation

Having solved for the 2D Poiseuille dispersion mean concentration for a discretised set of time and spatial steps $\bar{c}_2(\tilde{x}_j, \tilde{t}_n)$, we assume that the cross-sectional average of the numerical solution can be represented by a 1D dispersion equation

$$\frac{\partial \bar{c}_2}{\partial \tilde{t}} + U_h \frac{\partial \bar{c}_2}{\partial \tilde{x}} = D_h \frac{\partial^2 \bar{c}_2}{\partial \tilde{x}^2} - K_h \bar{c}_2, \quad (4.5.1)$$

for unknown effective convection, diffusion and absorption coefficients U_h, D_h, K_h respectively. It is these constants that we will use to check against the asymptotic coefficients U_e, D_e, K_e . The unknown coefficients may be found by the following algorithm.

Step 1: Determining the Absorption Coefficient

We may determine K_h from one of two similar ways. This allows us to verify we are coding our algorithm correctly for K_h . The first approach is based on the total amount of drug present based on (4.1.4). We assume that negligible mass has been lost by convection out of the tube, and that there is no inflow either, hence equation (4.1.4) reduces to a simple exponential equation

$$M(\hat{t}) = M_0 e^{-K_h \hat{t}},$$

which we can rearrange to solve for K_h . Hence the absorption coefficient of the numerically obtained 2D mean concentration is found by

$$K_h = \frac{1}{\hat{t}} \ln \left(\frac{M_0}{M(\hat{t}_n)} \right) = \frac{1}{\hat{t}} \ln \left(\frac{\int_0^1 \bar{c}_2(\tilde{x}_j, 0) d\tilde{x}}{\int_0^1 \bar{c}_2(\tilde{x}_j, \tilde{t}_n) d\tilde{x}} \right),$$

which should be true for all times $\hat{t}_n, n = 1, \dots, N$. The alternative method which we can use to corroborate our above result is based on taking the Laplace transform of equation (4.5.1) so that

$$\hat{c}_{\tilde{t}} + U_h (s\hat{c} - \bar{c}_2(0, \tilde{t})) = D_h (s^2 - s\hat{c}_{\tilde{x}}(0, \tilde{t}) - \hat{c}(0, \tilde{t})) - K_h \hat{c}, \quad \hat{c}(s, \tilde{t}) = \int_0^\infty \bar{c}_2(\tilde{x}, \tilde{t}) e^{-s\tilde{x}} d\tilde{x}$$

We must apply a zero Dirichlet boundary condition at the inlet (this is not unreasonable see Numerics Chapter 6) and taking $s = 0$ the above formulation reduces to

$$K_h = \frac{\hat{c}_{\tilde{t}}}{\hat{c}} = \frac{\int_0^\infty \bar{c}_{\tilde{t}} d\tilde{x}}{\int_0^\infty \bar{c} d\tilde{x}} = \frac{\int_0^1 \bar{c}_{\tilde{t}}(\tilde{x}, \tilde{t}) d\tilde{x}}{\int_0^1 \bar{c}(\tilde{x}, \tilde{t}) d\tilde{x}}.$$

Using backwards finite difference on the time derivative term with a time step interval of $\Delta\check{t}$, we may approximate for K_h using the numerical solution to find

$$K_h = \frac{\left(\int_0^1 \bar{c}(\check{x}, \check{t}_n) d\check{x} - \int_0^1 \bar{c}(\check{x}, \check{t}_{n-1}) d\check{x} \right)}{\Delta\check{t} \int_0^1 \bar{c}(\check{x}, \check{t}_n) d\check{x}} = \frac{M(\check{t}_n) - M(\check{t}_{n-1})}{\Delta\check{t} M(\check{t}_n)},$$

where $\check{t}_n = 1/(2\ell)$, and \check{t}_{n-1} is the penultimate finite difference step in time. Hence, for greater accuracy we take very small time steps. The first method is the simpler of the two, however, it is always useful to find means to corroborate our results with an alternative method.

Step 2: Determining the Effective Velocity

The effective convection of the mean concentration is found by tracking the peak of the mean solute concentration, $\max_j(\bar{c}_2(\check{x}_j, \check{t}_n))$, which corresponds to the centroid of a 1D dispersion model. For simple plug flow the centroid moves approximately with speed U_h . Hence, for any time \check{t} , we can find the axial distance \check{x}_j that corresponds to the peak so that $\bar{c}_2(\check{x}_j, \check{t}_n) \geq \bar{c}_2(\check{x}_j, \check{t}_n) \forall \check{x}_j = 0, \dots, N$. We denote the peak axial position by $\check{x}^* = \check{x}_j$ and assume the peak moves with constant velocity so that the effective velocity is simply given by $U_h \approx \check{x}^*/\check{t}_n$.

Step 3: Determining the Effective Dispersion

Finding the effective dispersion is more difficult and we approximate D_e by a least squares fit. We apply the effective absorption and convection term found in steps 1 and 2 to the dispersion equation

$$\frac{\partial \tilde{c}}{\partial \check{t}} + U_h \frac{\partial \tilde{c}}{\partial \check{x}} = D_h \frac{\partial^2 \tilde{c}}{\partial \check{x}^2} - K_h \tilde{c}, \quad (4.5.2)$$

for mean solute concentration \tilde{c} . We apply the mean concentration of the 2D initial concentration to be the initial condition for (4.5.2) and apply the same Neumann boundary conditions at the ends of the tube. We wish to solve for D_h as accurately as possible and this involves applying a diffusion transformation (see §6.1.3) to (4.5.2) and solve the resulting diffusion equation

$$\frac{\partial w}{\partial \check{t}} = D_h \frac{\partial^2 w}{\partial \check{x}^2}. \quad (4.5.3)$$

Hence we convert the mean solute concentration \bar{c}_2 to the decreasing Fourier wave. We solve (4.5.3) numerically for w and we minimise the function F given by

$$F(D_h) = \sum_{j=0}^J \sum_{n=1}^N (w(\check{x}_j, \check{t}_n) - w_2(\check{x}_j, \check{t}_n))^2,$$

to find the effective dispersion D_h .

4.5.2 Comparing the Numerical Solutions of the Models

For the four therapeutics we solve the 2D model (4.4.2) and approximate the mean solute concentration with a 1D dispersion model. We compare the effective coefficients and the mean concentration $[\bar{c}_2, U_h, D_h, K_h]$ with those from the model by Stoll et al. $[\bar{c}_1, U_e, D_e, K_e]$ but most importantly we compare the mass fraction absorbed in both models. In the 1D case, (4.4.9), the mass fraction absorbed, F_a , is given by (4.1.5) so that:

$$F_a^1 = \frac{M_A(\tilde{t})}{M_0} = \frac{K_e \int_0^{\tilde{t}} M(\tilde{t}) d\tilde{t}}{M_0}.$$

In 2D the amount of therapeutic absorbed is determined by the flux boundary condition $c_{\tilde{r}} = -D_a c$, where at any time \tilde{t} the mass absorbed is given by

$$M_A(\tilde{t}) = \int_0^{\tilde{t}} \int_0^1 \int_0^{2\pi} -c_{\tilde{r}}(\tilde{x}, \tilde{t}, \phi, R_0) d\phi d\tilde{x} d\tilde{t} = 2\pi \int_0^{\tilde{t}} \int_0^1 \frac{D_{ar}}{P_{er}} c(\tilde{x}, \tilde{t}, 1) d\tilde{x} d\tilde{t}.$$

Hence, mass fraction absorbed depends on the mass on the boundary $M_{\Gamma}(\tilde{t}) = \int_0^1 c(\tilde{x}, \tilde{t}, 1) d\tilde{x}$ at any time such that

$$F_a^2 = \frac{M_A(\tilde{t})}{M_0} = \frac{D_{ar} \int_0^{\tilde{t}} M_{\Gamma} d\tilde{t}}{M_0}. \quad (4.5.4)$$

We numerically solve the full 2D model and then numerically solve the asymptotic equation (4.4.9) with and without the fictitious initial condition. This corresponds to the analysis by Stoll et al. and by Moffatt et al. respectively. We do this to see if the fictitious term effectively compensates for short time. We also solve the full 2D model and its asymptotic equivalent when there are no peristaltic effects, $D_{en} = D_m$.

Discussion

Comparing Figures 4-4(a)-(d) with Figures 4-4(e)-(h) we see just how important enhanced diffusion through peristalsis is in applying the macrotransport approach to the Poiseuille dispersion model. As predicted in §4.4.5, without enhanced diffusion, the model (4.3.2) is convection dominant and the the mean can not be represented by a dispersive process $\ell P_{er} > 10$, see Figures 4-4(e)-(h). Even with enhanced diffusion, Figures 4-4(a)-(d), the sizes of $d = \ell P_{er}$ for the four therapeutics lie in the range $0.5 < \ell P_{er} < 5$ and we clearly observe a bad fit to the 2D process.

The fictitious initial condition implemented by Stoll et al. [73] was meant to resolve the issue of applying an asymptotic equation for all time. We observe in Figures (4-4)(a)-(d), the fictitious condition only serves to increase or decrease \bar{c}_1 however we obtain different effective velocity and diffusion values, see Table 4.3.

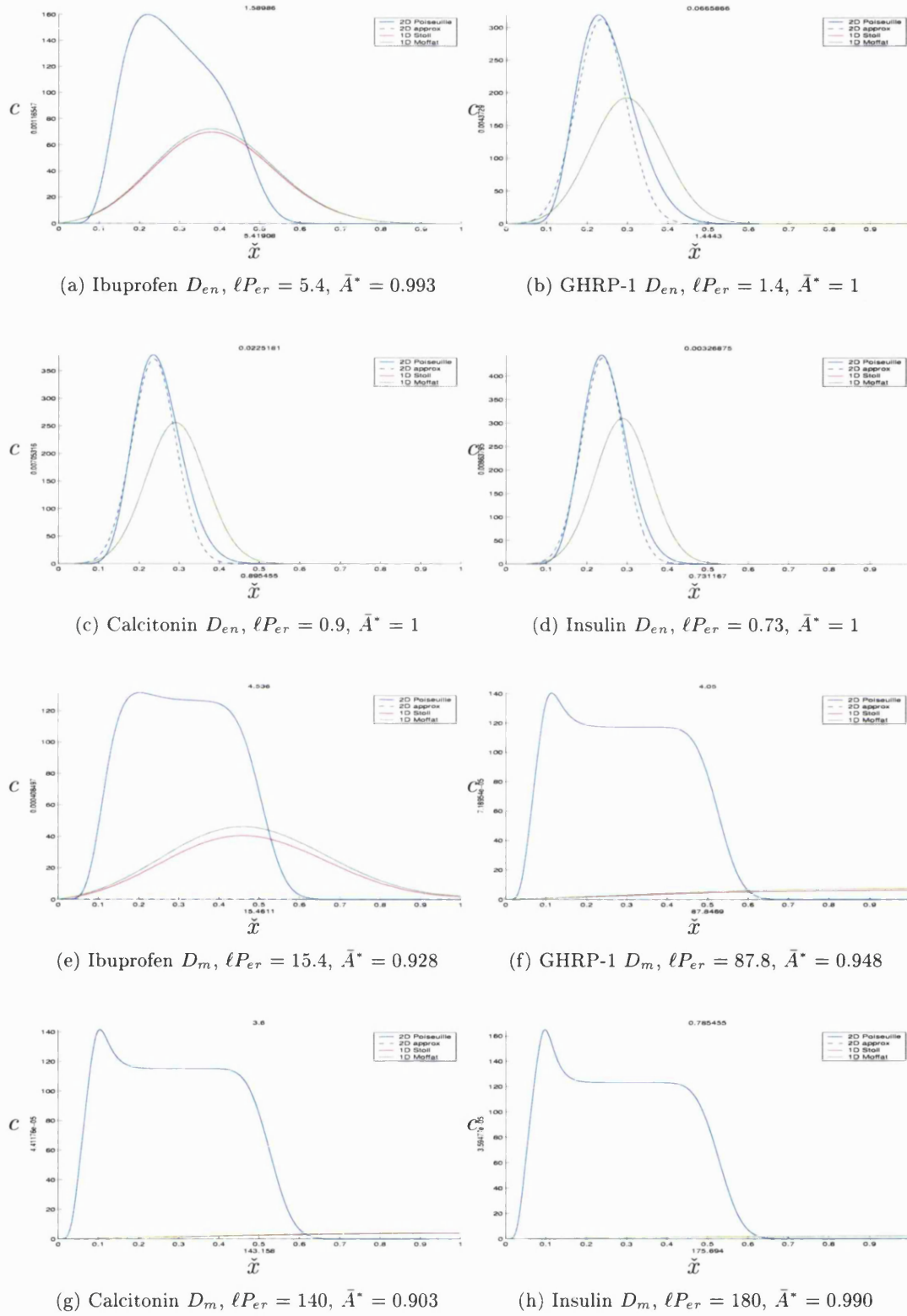


Figure 4-4: A Comparison of the Numerical Solution of the full 2D Poiseuille Dispersion Model with the Numerical Solution of the 1D Macrotransport Dispersion equation.

Therapeutic	\bar{K}^*	K_h	\bar{U}^*	U_h	\bar{D}^*	D_h
Ibuprofen	2.584e-03	3.977e-03	3.815e-03	2.358e-03	1.586e-04	3.401e-02
GHRP-1	1.553e-03	1.856e-03	3.193e-03	2.484e-03	4.777e-05	1.897e-05
Calcitonin	1.516e-03	1.682e-03	3.170e-03	2.526e-03	2.976e-05	1.328e-05
Insulin	4.064e-04	4.361e-04	3.160e-03	2.568e-03	2.440e-05	1.113e-05

Table 4.3: A Table of Asymptotic Coefficients Compared Against the Determined Numerical Effective Coefficients

From Table 4.3 we observe that the absorption coefficient is a very good guess, $\bar{K}^* \approx K_h$, and is within 10% for the better approximated therapeutics. We hypothesise this is due to the fact that the effective absorption constant is the leading order term in the perturbation expansion. From Figure 4-4 and the above table we observe $\bar{U}^* > U_h$, effective velocity predicted by the asymptotics is faster than the actual velocity. The same effect is seen in Figure 4-3, the better the asymptotic fit $\ell P_{er} \ll 1$ the more $\bar{U}^* \rightarrow U_h$. The algorithm fails to converge for the first therapeutic for the diffusion coefficients as the process is convection dominant. However, for the remaining therapeutics the effective diffusion coefficients are found to be of the same order 10^{-5} but the asymptotic values are slightly larger. Hence inappropriately applying asymptotic analysis results in larger convection and dispersion coefficients resulting in more mass loss by convection out of the tube than what would occur in reality. We calculate the fraction dose absorbed in the 2D and 1D case.

Therapeutic	ℓP_{er}	F_a^2	F_a^1	D_{ar}
Ibuprofen	5.4	9.72%	9.99%	1.6e+00
GHRP-1	1.4	2.11%	9.08%	6.7e-02
Calcitonin	0.9	1.17%	9.73%	2.3e-02
Insulin	0.73	0.22%	2.80%	3.3e-03

Table 4.4: A Table of Fraction Dose of Therapeutic Absorbed from the 2D Model Compared with the 1D Model

Looking at Table 4.4 the mass fraction absorbed varies quite significantly for the better fitting therapeutics, Figures 4-4(b-d). Less mass is absorbed in the 2D case than in the 1D, this occurs for two reasons 1) the fictitious term does not compensate sufficiently and 2) the 1D asymptotic equation assumes radial diffusion is dominant and that solute is absorbed quicker, but in reality for slowly diffusing solutes it takes time for the solute to move to the boundary.

4.6 Summary

In this Chapter we have started with the basics by building up the 1D dispersion model introducing the convection, diffusion and reaction terms. Consequently nondimension-

alising has introduced important dimensionless parameters, the Péclet number and the Damköhler number. They determine whether solute motion is dominated by convection, diffusion or absorption. Finally we showed in the 1D dispersion model how to calculate the fraction of solute absorbed. We then extended the 1D model to a 2D dispersion model. We moved absorption to the boundary which was represented by the diffusive flux term; $-Dc_r = Kc$. This equation is fundamental to this thesis and describes passive diffusion through a permeable membrane. We further introduced radial diffusion and discussed a simple 2D plug flow dispersion model to understand the solute motion and absorption process.

We removed plug flow as the basis of fluid motion and replaced it with Poiseuille flow. We discussed Taylor diffusion when the tube membrane is impermeable. The 2D Poiseuille dispersion model can be simplified to a 1D asymptotic dispersion equation for the mean solute concentration after a long time (a time by which the radial inhomogeneities have died down). The 1D equation depended on an effective dispersion coefficient and an effective convection coefficient. The asymptotic analysis introduced convective-dispersion, this is where solute diffusion is enhanced by nonuniform convection such as Poiseuille flow. We showed how the application of the analysis depends on two dimensionless parameters, the radial Péclet number P_{er} and ℓ , the ratio of the tube radius to length. There are two conditions for the asymptotic equation, namely (i) $t \gg P_{er}$, a sufficient amount of time must have passed and (ii) if in a finite length tube $d = \ell P_{er} \ll 1$, the 1D equation is applicable after a distance d which must be before solute leaves the tube. We then showed that the conditions for applying the asymptotic equation are not met in the intestine.

We reworked analysis by Moffatt et al. and derived the 1D asymptotic equation for the 2D Poiseuille dispersion model in the case of a permeable membrane. We introduced the absorption dependent effective convection coefficient, the effective dispersion coefficient and the effective absorption coefficient. The analysis showed that as absorption increases, slow streamlines at the boundary are eroded increasing the effective convection speed of the solute centroid, whilst decreasing convective dispersion and consequently decreasing the effective dispersion term. We show that Stoll et al. applied this 1D asymptotic equation inappropriately to the intestine in that (i) he applied the equation for all time using a fictitious initial condition which we have shown to be valid only for diffusive dominant systems and (ii) he assumed peristalsis could be modelled by enhanced diffusion, however, we showed that the conditions used in deriving the formula were violated by Stoll et al.

We solved the full 2D Poiseuille dispersion model and its effective 1D equation numerically, and we conclusively showed (i) the fictitious initial condition does not work, (ii) even with enhanced diffusion from peristalsis the condition to apply the asymptotic equation $d = \ell P_{er}$ are not met at all, (iii) when comparing the 2D and 1D mean solute concentration it is apparent the 1D equation overcompensates the

effective convection and diffusion term but even worse is the fraction dose absorbed in the 1D case is significantly higher than the 2D case. We now wish to model the effect of peristalsis on solute dispersion and determine whether peristalsis can really be modelled by enhanced diffusion as suggested by Stoll et al.

Chapter 5

The Peristaltic Dispersion Model

In this Chapter we look at the behaviour of the mean concentration of a solute in a vibrating tube where the flow is peristaltic and apply this to the intestine. We discuss whether the mean solute concentration can be represented by

$$\bar{c}_t + U_e \bar{c}_x = D_e \bar{c}_{xx} - K_e \bar{c} \quad (5.0.1)$$

the 1D dispersion equation which relates the coefficients U_e, D_e, K_e to the peristaltic flow field. We showed that this was possible in the trivial case of peristaltic flow when the amplitude of vibration, α , was zero, yielding Poiseuille flow. The full 2D peristaltic dispersion model for the solute concentration is governed by

$$c_t + \mathbf{u} \cdot \nabla c = D \nabla^2 c, \quad (5.0.2)$$

where $\mathbf{u} = (\dot{u}, \dot{v})$ are the steady-periodic peristaltic velocities derived from Stokes slow flow equations in Chapter 3. This is a moving boundary problem where we prescribe the location of the vibrating wall by the sinusoidal function

$$\tilde{r} = \check{f}(\check{x}, \check{t}) = 1 + \alpha \cos(2\pi(\check{x} - \check{t})), \quad (5.0.3)$$

where α is the amplitude of vibration. We assume further that the boundary is permeable and the solute is subject to passive absorption which satisfies

$$-D \mathbf{n} \cdot \nabla c = K_a c. \quad (5.0.4)$$

It was suggested by Stoll et al. [73] that peristaltic motion of a solute can be modelled by Poiseuille flow with an enhanced diffusion term D_{en} such that the solute concentration satisfies

$$c_t + u(r)c_x = D_{en} \nabla^2 c. \quad (5.0.5)$$

From equation (5.0.5), Stoll et al. modelled solute motion in the intestine by the average concentration satisfying equation (5.0.1).

In this Chapter we wish to validate the hypothesis by Stoll et al. by (i) solving the 2D peristaltic dispersion equation, (5.0.2), numerically and determining the mean solute concentration denoted \bar{c}_{pe} , (ii) determining whether \bar{c} can be modelled by the 1D effective equation, (5.0.1), by applying the 1D dispersion model algorithm in §4.5.1, (iii) solving the 2D Poiseuille dispersion equation with enhanced diffusion (5.0.5) numerically and determining the mean solute concentration denoted \bar{c}_{po} , (iv) determining whether the mean peristaltic concentration \bar{c}_{pe} can be approximated by \bar{c}_{po} as diffusion is increased.

To solve the peristaltic dispersion model numerically we apply a suitable transformation from the peristaltic ‘physical’ domain to a rectangular ‘computational’ domain and use finite differences to discretise the equation into a system of odes by the method of lines and solve using a suitable DAE solver (see Chapter 6). We solve the model for the five¹ different flow regions found from the leading order semi-analytic velocities in Chapter 3. There are five key parameters of the peristaltic dispersion model in total. We have introduced three from peristaltic flow; α the amplitude of vibration, $\hat{\psi}_w$ the dimensionless flow rate and ϵ the wave curvature. There are a further two parameters from modelling solute motion; the solute Péclet number P_{eh} and that Damköhler number D_{ar} .

We show that for a small radial Péclet number, P_{eh} , the mean concentration \bar{c}_{po} satisfies a 1D dispersion model (5.0.1) with a very slight oscillatory component to it. The fast diffusion (small P_{eh}) removes the radial inhomogeneities in the solute concentration imposed by the peristaltic velocities, however, unless P_{eh} is very small there will remain slight inhomogeneities in the axial component which are responsible for the observed oscillation. We can apply a low pass filter to remove the noisy high frequency component to the mean concentration to obtain a smoother Gaussian profile. As the Péclet number increases, the peristaltic convective forces dominate diffusion and the mean solute concentration suffers increasingly from an overlapping oscillatory term. We can again apply the low pass filter and we observe the mean concentration profile looks similar to Poiseuille dispersion of a solute but only in the cases where there is little trapping. In case C of peristaltic flow there is no reflux or trapping, just mild retrograde motion of fluid at the point of the wave’s contraction. We clearly observe that solute motion exhibits characteristics shown in Poiseuille dispersion of a solute. In cases D and E we notice that solute motion is increasingly retarded from reflux and \bar{c}_{po} and \bar{c}_{pe} are very dissimilar.

We now compare the dimensionless form of the peristaltic dispersion model (5.0.2) with the dimensionless form of the Poiseuille dispersion model (5.0.5) for the same solute parameters, P_{eh}, D_{ar} and for the same instantaneous mean volume flow rate \hat{Q} .

¹From Figure 3-5 there are 5 regions with a strictly positive instantaneous mean volume flow rate.

We compare the filtered mean solute concentration from the peristaltic model \bar{c}_{pe}^f with the mean concentration from the Poiseuille model \bar{c}_{po} . We then artificially increase the diffusion D_{en} , decreasing P_{eh} , for the Poiseuille dispersion model and compare the mean solute concentration \bar{c}_{po}^e with \bar{c}_{pe}^f . The mean solute concentrations look very dissimilar, hence we show that peristalsis is too complex to be modelled simply by enhanced diffusion as believed by Stoll et al. We further show by solving for a radially nonuniform initial condition, that peristalsis increases absorption as trapping and the deformation of the tube brings solute closer to the boundary unlike Poiseuille flow.

These results show that peristalsis is a great means to (i) mix food, (ii) bring food closer to the boundary and (iii) retard food movement and thus maximise absorption in the duodenum where nutrients are mainly absorbed and the villi are largest.

5.1 Deriving the 2D Peristaltic Dispersion Model

We consider the behaviour of a therapeutic in solute form² placed in a fluid undergoing peristaltic flow induced by the vibrating wall. The boundary of the tube is permeable and the solute is subject to passive absorption. The profile of the solute concentration depends on (i) the molecular diffusion D of the drug, (ii) the permeability of the membrane K_a and (iii) the nature of the peristaltic flow. We define the 2D peristaltic dispersion equation governing the solute's distribution in expanded form by

$$c_t + u(x, r, t)c_x + v(x, r, t)c_r = D \left(c_{xx} + c_{rr} + \frac{1}{r}c_r \right), \quad (5.1.1)$$

where (u, v) are the velocities from peristaltic flow. We prescribe the boundary to be a periodic time dependent function of the form $f(x, t)$, which exhibits passive absorption of the solute modelled by

$$-D\mathbf{n} \cdot \nabla c = K_a c. \quad (5.1.2)$$

Describing the Peristaltic Flow

We now derive the nature of the peristaltic flow. We assume that the fluid is viscous and the flow has been fully established to yield a steady periodic flow by the time the drug has been introduced. In Chapter 3 we obtained the biharmonic equations for Stokes' slow flow which were solved³ by a perturbation expansion in the small wave curvature, $\epsilon < 1$. We determined the leading order semi-analytic peristaltic velocities in dimensionless form which are given in the fixed frame by

$$\begin{aligned} \tilde{u}(\tilde{x}, \tilde{t}; \hat{\psi}_w) &= 4A(\tilde{x}, \tilde{t}; \hat{\psi}_w)\tilde{r}^2 + 2B(\tilde{x}, \tilde{t}; \hat{\psi}_w) + 1 + O(\epsilon^2), \\ \tilde{v}(\tilde{x}, \tilde{t}; \hat{\psi}_w) &= -A'(\tilde{x}, \tilde{t}; \hat{\psi}_w)\tilde{r}^3 - B'(\tilde{x}, \tilde{t}; \hat{\psi}_w) + O(\epsilon^2). \end{aligned} \quad (5.1.3)$$

²We assume the complete instantaneous dissolution of the therapeutic in the flowing fluid.

³Alternatively we could solve for the peristaltic velocities numerically see Chapter 6

The velocities are periodic and depend on the flow rate $\hat{\psi}_w$. In deriving the velocities we made the following assumptions (i) the curvature of the wave ϵ is sufficiently small that we can ignore higher order terms from the power series (3.4.7), (ii) by taking the leading order term we obtain a formula for the pressure gradient over a wavelength, $\Delta\hat{p}_\lambda$ as a function of the flow rate $\hat{\psi}_w$, (iii) the domain is an integral number of wavelengths so that the pressure gradient over the whole domain, $\Delta\hat{p}$ is constant.

Following these assumptions we have shown in Chapter 3 the existence of five different types peristaltic flow depending on the flow rate $\hat{\psi}_w$ (or pressure gradient $\Delta\hat{p}_\lambda$) and the amplitude of vibration α . The type of flow affects directly the numerical scheme (see §6.3.2) we can implement to solve the model and also the boundary condition we can impose at the inlet (see §5.1.1). We also define the velocities as a function of the flow rate $\hat{\psi}_w$ rather than the pressure gradient since it is easier to distinguish the different flow regions on the flow rate versus amplitude ratio graph, see Figure 5-2, than on the pressure gradient versus amplitude ratio graph (see Appendix Figure C-1).

Scaling the Dispersion Model

We now proceed to nondimensionalise the peristaltic dispersion model (5.1.1), (5.1.2) for which there is more than one choice of scaling for time \check{t} and space \check{x} . We first introduce the following dimensionless quantities which are independent of our choice of scaling

$$\check{r} = \frac{r}{h}, \quad \check{f} = \frac{f}{h}, \quad \check{u} = \frac{u}{\sigma}, \quad \check{v} = \frac{\lambda v}{h\sigma}, \quad \check{\mu} = \frac{\mu}{\mu_0}, \quad P_{eh} = \frac{\sigma h}{D}.$$

We now consider scaling the axial length x and the time t . In the Poiseuille dispersion model, x was scaled by the length of the tube, $L_x = n\lambda$, and t by the radius of the tube⁴, $R_0 = h$. Hence, we introduced the tube length ratio $\ell = R_0/L_x$ into the model. In nondimensionalising the peristaltic velocities we scaled x and t by the wavelength of the tube, λ , and consequently introduced the wave curvature $\epsilon = R_0/\lambda$, a ratio of the height of the wave to the length of the wave. The dimensionless quantities ℓ and ϵ are related by

$$\epsilon = \frac{h}{\lambda} = \frac{R_0 n}{L_x} = n\ell. \quad (5.1.4)$$

We mentioned in Chapter 4 that an appropriate choice of nondimensionalising time is with respect to the radial length scale. Hence we rescale the peristaltic time scale \check{t} with respect to the radius of the nondisturbed tube such that

$$\check{t}_1 = \frac{t\sigma}{h} = \frac{1}{\epsilon} \frac{t\sigma}{\lambda} = \frac{1}{\epsilon} \check{t},$$

⁴We also scaled by a characteristic speed, however, that is not factor in our choice of scale seen later.

and keeping the peristaltic length scale \check{x} we obtain the nondimensionalised peristaltic dispersion model

$$c_{\check{t}} + \check{u}(\check{x}, \check{r}, \check{t})c_{\check{x}} + \check{v}(\check{x}, \check{r}, \check{t})c_{\check{r}} = \frac{\epsilon}{P_{eh}}c_{\check{x}\check{x}} + \frac{1}{\epsilon P_{eh}} \left(c_{\check{r}\check{r}} + \frac{1}{\check{r}}c_{\check{r}} \right). \quad (5.1.5)$$

This is in a similar form to the Poiseuille dispersion model which was given by

$$c_{\check{t}} + \ell(1 - \check{r}^2) = \frac{1}{P_{er}} \left(\ell^2 c_{\check{x}\check{x}} + c_{\check{r}\check{r}} + \frac{1}{\check{r}}c_{\check{r}} \right). \quad (5.1.6)$$

The standing peristaltic waves are now described by

$$\check{r} = \check{f}(\check{x}, \check{t}_1) = 1 + \alpha \cos(2\pi(\check{x} - \epsilon \check{t}_1)).$$

From here on we drop the subscript on the time variable. We observe in equation (5.1.5) that when the Péclet number is sufficiently small the diffusion terms may be ignored, and flow is convection dominant. In this case the solute profile should be similar to the evolution of the particle paths seen in §3.6.8. All that is required now is to scale the boundary condition, hence

$$\frac{c_r - f'c_x}{\sqrt{1 + (f')^2}} = \frac{K}{D}c \quad \mapsto \quad \frac{c_{\check{r}} - \epsilon^2 \hat{f}'c_{\check{x}}}{\sqrt{1 + \epsilon^2(\hat{f}')^2}} = -D_{ar}c, \quad (5.1.7)$$

which simplifies to a purely radial boundary condition when curvature is sufficiently small ($\epsilon \ll 1$), e.g. $\check{c}_{\check{r}} = -D_{ar}\check{c}$. Hence the 2D peristaltic dispersion model is shown in the following figure

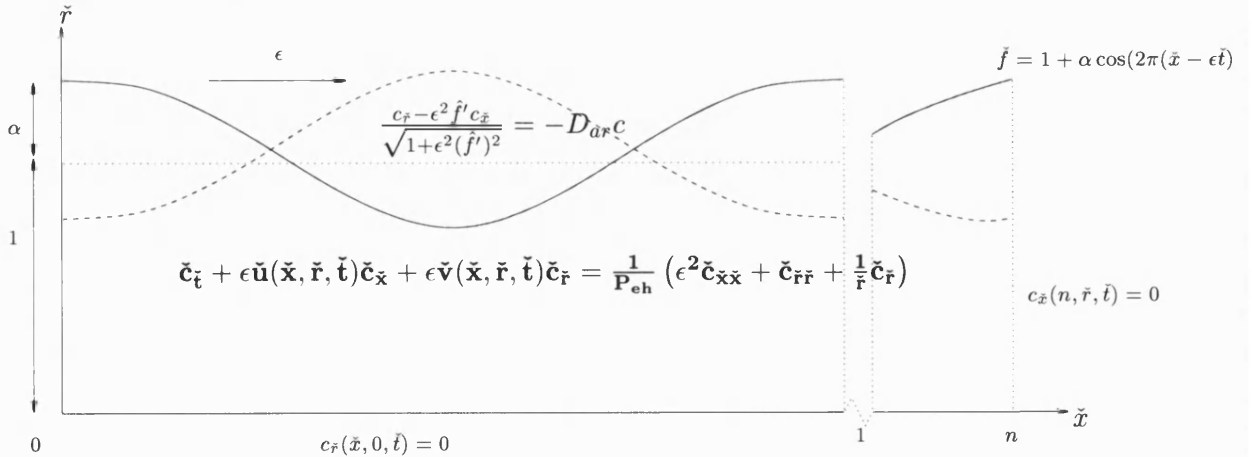


Figure 5-1: The Peristaltic Dispersion Model

We have prescribed a symmetry condition along the centreline of the tube and have also prescribed a Neumann boundary condition at the outlet to imply convective fluxes

dominate over diffusion at the boundary. We now discuss the restrictions that the different peristaltic flow regions have on the dispersion model when it comes to (i) its application and (ii) solving the model numerically.

5.1.1 Conditions for a Maintained Source at the Inlet

The peristaltic dispersion model is a moving boundary problem, and as such the inlet boundary is constantly changing in size, but more importantly the peristaltic velocities at the inlet are constantly changing. To model the therapeutic distribution in the presence of a maintained source, a condition for the model would be that fluid flow is purely in the positive direction. However, in peristaltic flow this is not always the case as a small positive instantaneous mean flow rate has been shown to give rise to negative flow (see Appendix Lemma C.2). This is clearly shown in the case of pumping where it has been proved that reflux occurs, which would violate an imposed Dirichlet boundary condition and the model would be ill-posed. Hence, the peristaltic dispersion model should only be solved for a purely pumping case when a slug of solute is placed in the tube. We then require a Neumann boundary condition at the inlet to prevent solute leaving the tube. This is a realistic condition if we apply this model to the intestine since the inlet to the intestine is a valve that closes to prevent chyme moving back into the stomach.

However, not only does peristaltic flow cases in the pumping zone have negative velocities but so too do specific cases of flow in the copumping region. From the particle paths for case C (see Figure 3-12), we observe that fluid particles around the point of maximum occlusion have retrograde motion. We consider the leading order semi-analytic solution for the peristaltic velocities (5.1.3). For horizontal velocity at some point \tilde{x} to be purely positive then

$$\tilde{u}(\tilde{x}, \tilde{r}) = 4A(\tilde{x})\tilde{r}^2 + 2B(\tilde{x}) + 1 > 0,$$

must be satisfied for all radial positions. Hence,

$$\tilde{r}^2 > \frac{2B(\hat{x}) + 1}{2A(\hat{x})} = \frac{4\hat{\psi}_w \hat{f}^2 + 2\hat{f}^4}{4\hat{\psi}_w + 2\hat{f}^2} > 0,$$

Consequently, the horizontal velocity is positive at some point \tilde{x} when $\hat{\psi}_w > -0.5\hat{f}^2(\tilde{x})$. Hence, \tilde{u} is positive $\forall \tilde{x}$ when

$$\hat{\psi}_w > -\frac{1}{2}\hat{f}_{\min}^2 = -\frac{1}{2}(1 - \alpha)^2.$$

We highlight this result on the flow rate versus amplitude ratio in Figure 5-2 by the black line. We observe negative velocities occur not only in case C but in case B where centreline trapping is present. It is important to know when negative velocities occur

as this directly affects our choice of numerical scheme used to solve (5.1.5).

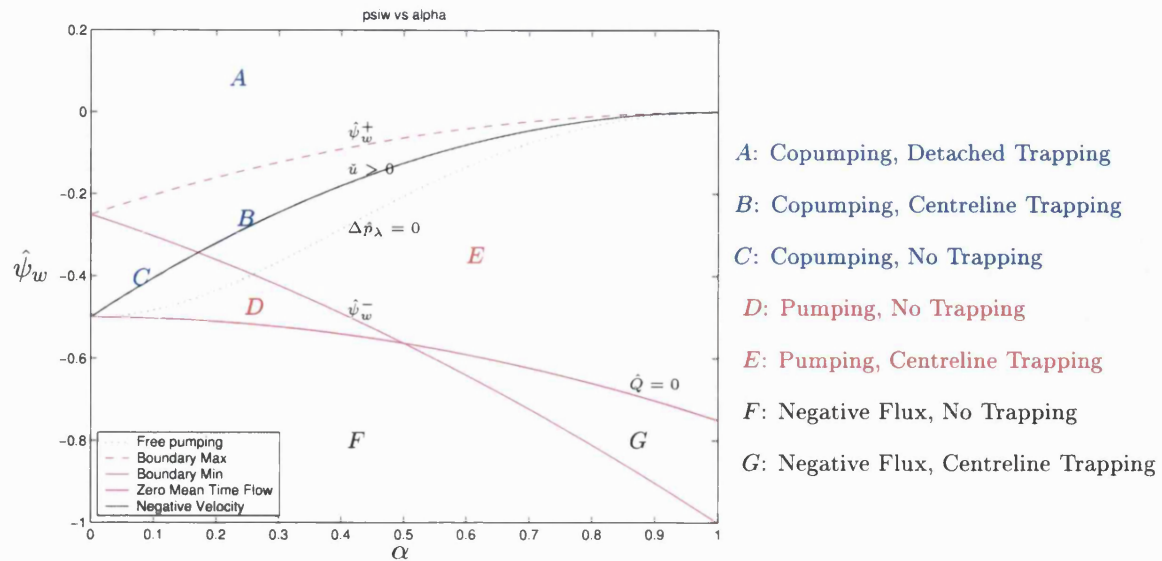


Figure 5-2: A Graph of Flow Rate, $\hat{\psi}_w$, versus Amplitude of Vibration, α , indicating the Region of Purely Positive Horizontal Velocity

5.1.2 Comparing the Peristaltic Dispersion Model with the Poiseuille Dispersion Model

In this section we derive a means to compare the effects of peristaltic flow with Poiseuille flow on the behaviour of solute concentration. We have shown that peristaltic flow tends to Poiseuille flow when (i) the amplitude of vibration tends to zero and (ii) for high flow rate $\hat{\psi}_w$ (see Lemma 3.7). Hence we expect the behaviour of the solute concentration governed by the peristaltic dispersion model to be similar to solute concentration in the Poiseuille dispersion model for these cases. But what happens when peristaltic phenomena occur, such as trapping and reflux. How do they affect the profile of the solute concentration? We wish to compare the peristaltic dispersion model (5.1.5) with the Poiseuille dispersion model (5.1.6), but how do we do so?

According to Poiseuille flow, a zero pressure gradient would result in zero fluid motion. However, for peristaltic flow a zero pressure gradient does not imply the same result, rather we observe Poiseuille like flow, and depending on the amplitude of vibration some trapping (see Figure 5-2). Similarly, a positive pressure gradient does not equate to complete retrograde motion as it does with Poiseuille flow. Hence, we can not compare the two models by imposing the same pressure gradient when deriving the fluid flow.

In the peristalsis Chapter 3 we derived the ‘time mean volume flow rate’, \hat{Q} , that is, the average over one period of the peristaltic wave of the amount of fluid moving. Hence, it is feasible to compare both dispersion models when therapeutic solute is

introduced into peristaltic flow and Poiseuille flow have the same \hat{Q} . The peristaltic and Poiseuille mean volume flow rate satisfy

$$\left. \frac{\hat{Q}}{2\pi} \right|_{\text{peri}} = \hat{\psi}_w + \frac{1}{2} \left(1 + \frac{1}{2} \alpha^2 \right), \quad \left. \frac{\hat{Q}}{2\pi} \right|_{\text{pois}} = \hat{\psi}_{wp}.$$

Hence, we assign Poiseuille flow to have the flow rate

$$\hat{\psi}_{wp} = \hat{\psi}_w + \frac{1}{2} \left(1 + \frac{1}{2} \alpha^2 \right),$$

so that we can describe the laminar flow derived in §3.3 by

$$\tilde{u}(\tilde{r}) = \left(4\hat{\psi}_{wp} \right) (1 - \tilde{r}^2) = \left(4\hat{\psi}_w + 2 + \alpha^2 \right) (1 - \tilde{r}^2).$$

We expect Poiseuille flow to now transport the same amount of fluid as the peristaltic flow after one period. Now when the amplitude of vibration dies down, $\alpha = 0$, the peristaltic dispersion model simplifies to

$$c_{\tilde{t}} + \epsilon \tilde{u}(\tilde{r}) c_{\tilde{x}} = \frac{1}{P_{eh}} \left(\epsilon^2 c_{\tilde{x}\tilde{x}} + c_{\tilde{r}\tilde{r}} + \frac{1}{\tilde{r}} c_{\tilde{r}} \right). \quad (5.1.8)$$

an alternatively scaled version of the Poiseuille dispersion model (5.1.6). Hence we compare the peristaltic dispersion model with a Poiseuille dispersion model by numerically solving equations (5.1.5) and (5.1.8). Ideally one would compare the solutions of the models when $\tilde{t} = \frac{T_n}{\epsilon}$, $T_n \in \mathbb{N}$, at points in time when the same volume of fluid has been transported by peristalsis in the peristaltic tube that would have been transported by laminar flow in an undisturbed tube. However, for high flow rates fluid travels the distances of several wavelengths in just one period, and we are limited in solving (5.1.5) numerically for a small number of wavelengths. Hence, we compare models up to a time \tilde{t}^* that depends on the flow rates.

5.2 Solving the Peristaltic Dispersion Model

We solve numerically the peristaltic dispersion model governed by equation (5.1.5) up to time $\tilde{t} = t^*$ when a slug of solute with radially uniform concentration,

$$\check{c}(\tilde{x}, \tilde{r}, \tilde{t}) = \phi(\tilde{x}) = 1000 (H(\tilde{x}) - H(\tilde{x} - l)),^5$$

is placed at the entrance to the tube at time $\tilde{t} = 0$. The size of the initial slug of solute, l , determines how much therapeutic is released into regions of trapping or reflux. We expect slightly different solutions for different values of l when the Péclet number falls

⁵ $H(\tilde{x})$ denotes the heaviside function.

and solute motion is dominated by peristaltic convection.

In the peristaltic dispersion model there are 5 key parameters. From peristalsis we obtained the amplitude of vibration α , the flow rate $\hat{\psi}_w$, and the wave curvature ϵ . In deriving a dispersion model we introduced the Péclet number P_{eh} and the Damköhler number D_{ar} . However, an important factor that also plays a role in the dispersion model is n , the number of wavelengths that make up the domain. We are interested in parameter ranges similar to those observed in the small intestine for the various therapeutics considered by Stoll et al. [73]. We discuss the choice of parameter values as follows.

Amplitude of Vibration, α

The peristaltic vibrations vary depending on the strength of the segmentation contractions, from a slight deviation $\alpha = 0.1$ to $\alpha = 0.4$. Any longer and the solver takes a significantly larger time to solve the problem, and due to limited resources this becomes counterproductive. It is also unnecessary as we have shown in Figure 3-9 that large trapping also occurs at small wavelengths, and we can still observe large mixing for small amplitude of vibrations.

Wave Curvature Number, ϵ

The wave number can be estimated to be ≈ 0.1 using anatomical data [5], [73].

Flow Rate, $\hat{\psi}_w$

The movement of chyme in the small intestine is very slow [73]. We have estimated that the flow rate is about $\hat{\psi}_w = -0.31$ in §3.5.3 and this falls in the pumping range when we observe Figure 5-2. However, as the illeocecal sphincter opens, the pressure gradient is likely to move from a positive value to a negative value [47], so flow rate moves from the pumping range to the copumping range. The exact value at any particular time is unknown and so we solve (5.1.5) for various values of small flow rate $\hat{\psi}_w$ in the pumping and copumping zones to illustrate the effects of peristalsis on the solute concentration profile.

Number of Wavelengths, n

From literature the wavelength λ ranges from 8 – 10 cm and the average length of the intestine is 285 cm [73]. Consequently, there are approximately $n = 30$ wavelengths across the length of the intestine. In fact we do not need to consider solving the model for so many wavelengths as 90% of most solute is absorbed in the first portion of the intestine, the duodenum [73] and very little ‘absorbable’ solute enters the ileum.

Péclet Number, Pe_h

Both physical and physicochemical properties of the therapeutic determine the solute Péclet number. We vary the Péclet number to similar fast and slow diffusing drugs, as we did in Chapter 4. From this we can examine the effects of the solute profile when it is driven by (i) peristalsis or (ii) diffusion.

Damköhler Number, Da_r

Again the physicochemical properties of the therapeutic and the permeability of the tubes wall affect the amount of absorption and the Damköhler number. As the Damköhler number increases, an increasing number of streamlines away from the wall containing solute are eroded. Hence by Lemma 3.8, as axial velocity is strictly decreasing in the radial direction, we can say that the effective velocity of the mean solute concentration will always increase for all cases of peristaltic flow with $\hat{Q} > 0$. We do not consider varying the Damköhler number in this Chapter as we are already varying a number of parameters and we already know the effect of its variation on the mean solute concentration. We maintain $Da_r = 1$ for all cases based on the therapeutic values observed in [73].

Unfortunately, we can not solve for just any range of parameter values. There are limits imposed not just by the numerical scheme but by the cpu. We are solving a DAE, using the method of lines to obtain the system of odes $M\dot{c} = Ac$. The matrices have size $JK \times JK$ for $J = 200$ grid points in the axial direction and $K = 50$ in the radial direction. There are two factors that decide how large we can take JK , (i) the cpu's memory and (ii) the cpu solve time. We solve the system using DASSL, a DAE solver for FORTRAN 90 on a unix machine.⁶

We require a sufficient number of grid points per wavelength to compute the peristaltic flow accurately, $\lambda_n = K/n$. Hence we solve the model for just $n = 10$ wavelengths. Although this falls short of the number of wavelengths in the intestine (≈ 30), we are interested in qualitative results rather than quantitative. The results of peristaltic convection of a solute over 10 wavelengths are sufficient to elucidate the behaviour of the solute.

Unfortunately the problem becomes increasingly stiff as the amplitude of vibration increases and the DAE solver is no longer able to solve the model effectively. Hence, with our current numerical scheme and solver we are limited so solving (5.1.5) for $\alpha < 0.5$. Similarly we restrict how long we solve the model for, and generally stop the computation long before solute exits the tube. We solve for just enough time to explain the observed behaviour of the solute concentration.

⁶The machine runs Redhat 9, and has an Intel 2.5 Pentium 4 processor with 1 gigabyte of RAM.

5.3 Results of the 2D Peristaltic Dispersion Model

In this section we numerically solve the 2D peristaltic dispersion model (5.1.5) with the 2D Poiseuille dispersion model (5.1.8) for the five different types of peristaltic flow (see Figure 5-2) and compare the effects of peristaltic motion to Poiseuille flow on solute motion and absorption. We then vary the Péclet number to simulate solute motion driven by (i) diffusion ($P_{er} = 100$ small) and (ii) peristaltic convection ($P_{er} = 1000$ large). In the case of a highly diffusive drug, the mean solute concentration has a Gaussian profile and we apply our 1D dispersion model algorithm to determine the effects of increased absorption on the mean velocity U_e for the different peristaltic flows. For each calculation we present the following,

1. A plot of the mean solute concentration along the tube for the peristaltic case \bar{c}_{pe} (blue), its noise free case \bar{c}_{pe}^f (green) and the Poiseuille case \bar{c}_{po} (red), at various times with their corresponding 1D dispersion model approximation \bar{c}_{pe} (dashed blue lines), \bar{c}_{pe}^f (dashed red lines) respectively.
2. Contour plots of the solute concentration for the peristaltic and Poiseuille model at various times.
3. A plot of the cumulative amount of mass absorbed in time for the peristaltic model (blue) and Poiseuille model (red).

We note that the low pass filter (see §E.2 for description) is employed automatically as we need to solve for many examples. To do so we wrote a small program to find the oscillations in the fast Fourier transform of the mean solute concentration and to remove them. This program is not perfect at finding the oscillations and as such we obtain slight oscillations in the noise free solution at the inlet and outlet. However, it is where the concentration is nonzero that the filter works sufficiently to remove the noise. We further note that we output solutions at times that vary between cases, this is to elucidate peristaltic behaviour with the best three plots, e.g. every 2, 4, 8 periods for case B, but every 8, 12, 16 periods for case E.

5.3.1 Case A - Slow Flow

We solve the peristaltic dispersion model (5.1.5) for slow flow in case A when there is detached trapping and no reflux. We implement a small amplitude of vibration $\alpha = 0.1$ and numerically solve for two cases of a slow and fast diffusing solute, when the flow rate is $\hat{\psi}_w = 0$, which exhibits large trapping, 40.7%.

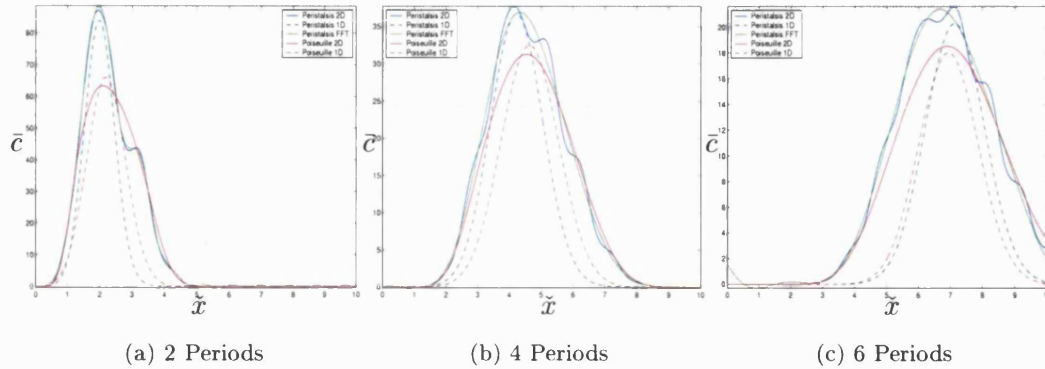


Figure 5-3: Mean Solute Concentration for the Peristaltic Dispersion Model and the Poiseuille Dispersion Model, and their 1D Dispersion Approximation with the the FFT of the Peristaltic Solution, for a Fast Diffusing Solute, $P_{er} = 100$, when $\alpha = 0.1$, $\hat{\psi}_w = 0$ and $D_{ar} = 1$.

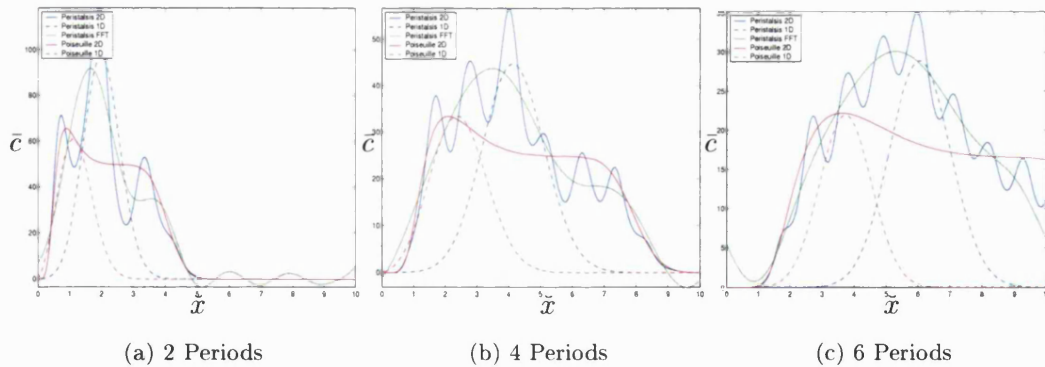


Figure 5-4: Mean Solute Concentration for the Peristaltic Dispersion Model and the Poiseuille Dispersion Model, and their 1D Dispersion Approximation with the the FFT of the Peristaltic Solution, for A Slow Diffusing Solute, $P_{er} = 1000$, when $\alpha = 0.1$, $\hat{\psi}_w = 0$ and $D_{ar} = 1$

In Figure 5-3, we clearly observe that for the fast diffusing solute the mean solute concentration of the peristaltic dispersion model \bar{c}_{pe} is essentially that of the Poiseuille dispersion model \bar{c}_{po} plus some oscillatory term. The two means move approximately with the same effective velocity and exhibit the same effective dispersion. We confirm this with contour plots of the solute concentration profiles in Figures 5-7 and 5-8.

As the level of diffusion decreases and convective fluxes dominate solute motion, we observe in Figure 5-4 that the amplitude of oscillations have increased in \bar{c}_{pe} and the frequency of oscillations increases with time. It is clear that both means no longer move with a 1D Gaussian profile. The head and rear of the solute profile for both models move essentially with the same speed, approximately the same amount of convective dispersion occurs but the convective speed of the slow diffusing drug is clearly much slower than of the fast diffusing drug.

In both cases of the diffusing solute, the amount of mass absorbed by peristalsis is much more than that of Poiseuille (see Figures 5-5, 5-6). We observe (i) most solute is absorbed at the entrance to the tube (ii) the amount of mass absorbed levels off with time, $M(t) = t^\gamma$ for smaller Péclet number, e.g. γ is smaller for smaller P_{er} .

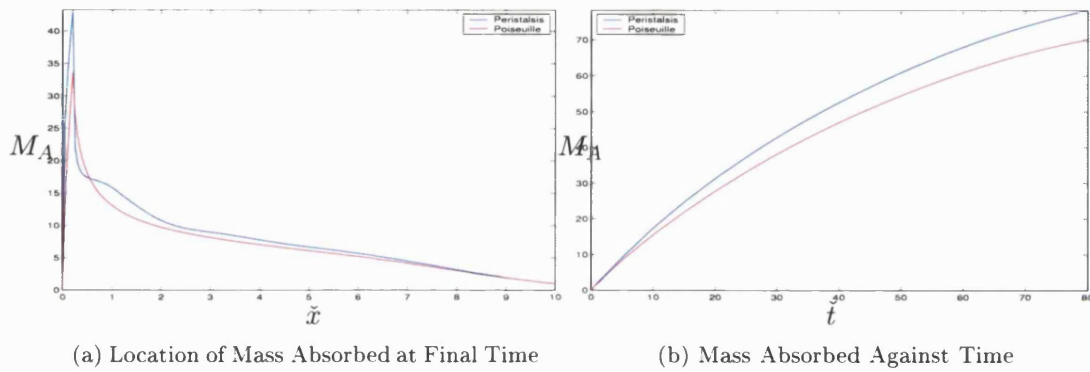


Figure 5-5: Mass Absorbed for the Peristaltic and Poiseuille Dispersion Models for a Fast Diffusing Solute, $P_{er} = 100$, when $\alpha = 0.1$, $\hat{\psi}_w = 0$ and $P_{er} = 1000$, $D_{ar} = 1$

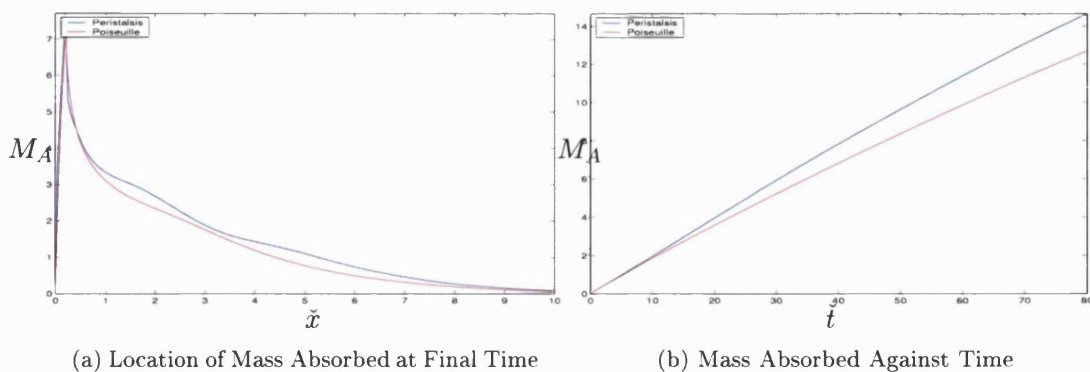
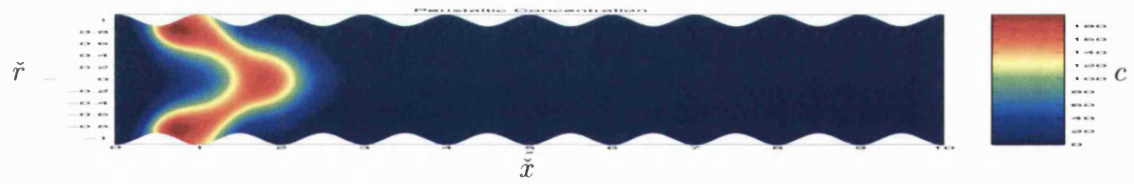
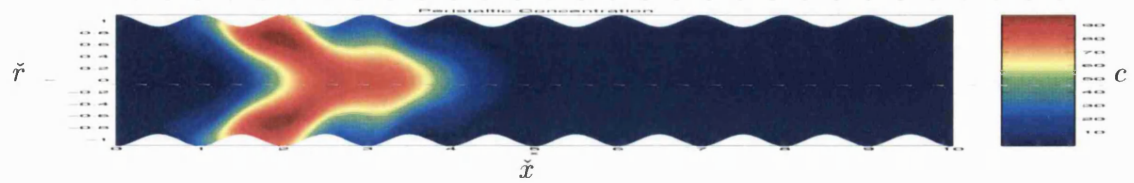


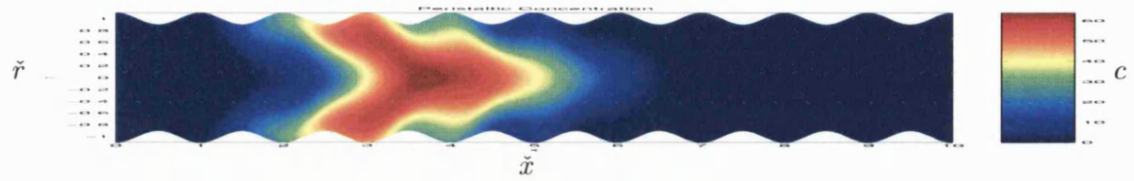
Figure 5-6: Mass Absorbed for the Peristaltic and Poiseuille Dispersion Models for a Slow Diffusing Solute, $P_{er} = 1000$, when $\alpha = 0.1$, $\hat{\psi}_w = 0$ and $P_{er} = 1000$, $D_{ar} = 1$



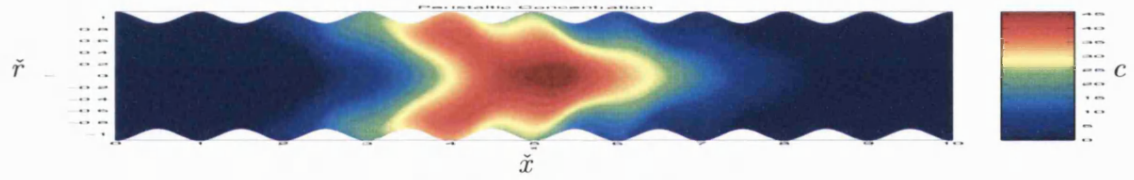
(a) Peristaltic Contour Profile After 1 Period



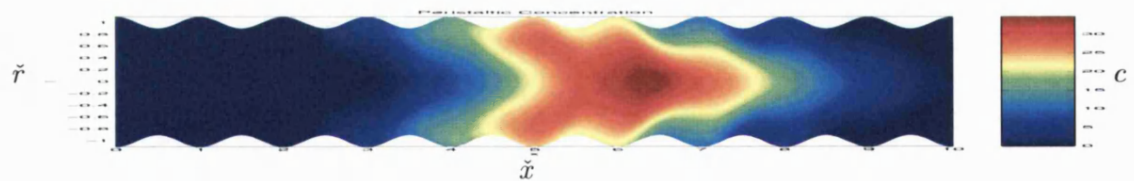
(b) Peristaltic Contour Profile After 2 Periods



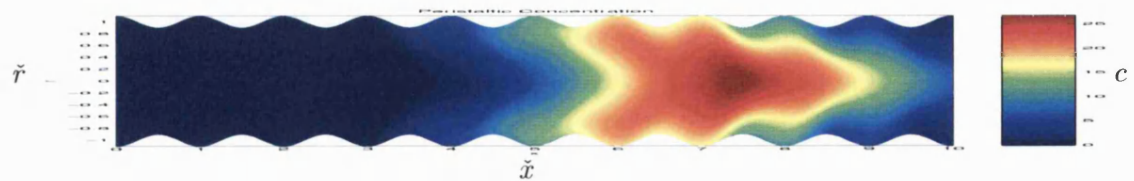
(c) Peristaltic Contour Profile After 3 Periods



(d) Peristaltic Contour Profile After 4 Periods

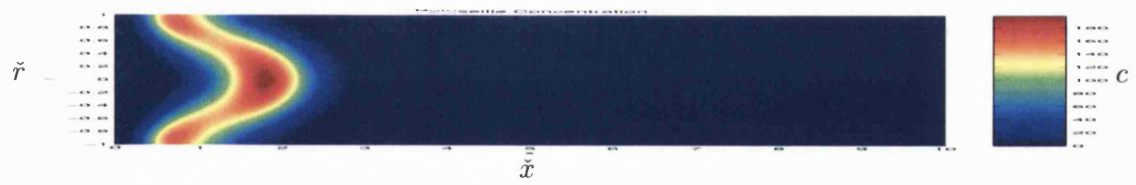


(e) Peristaltic Contour Profile After 5 Periods

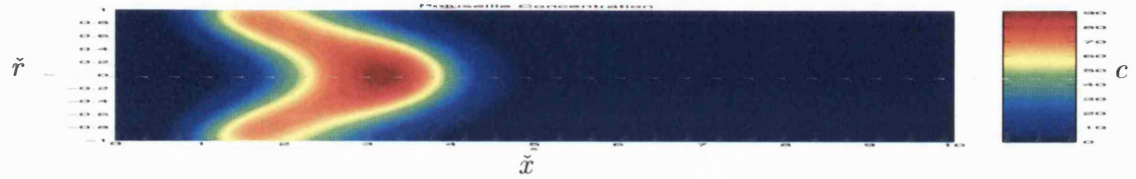


(f) Peristaltic Contour Profile After 6 Periods

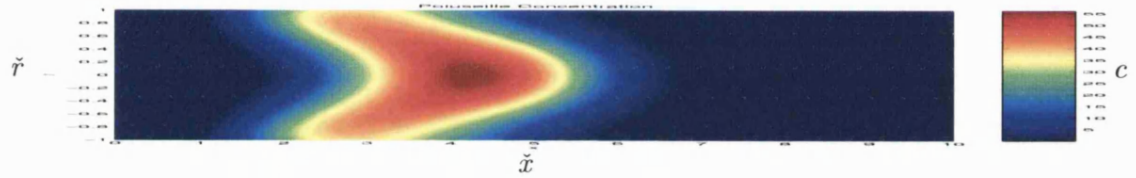
Figure 5-7: Peristaltic Contour Plots when $\hat{\psi}_w = 0$, $P_{er} = 100$, $\alpha = 0.1$, $D_{ar} = 1$



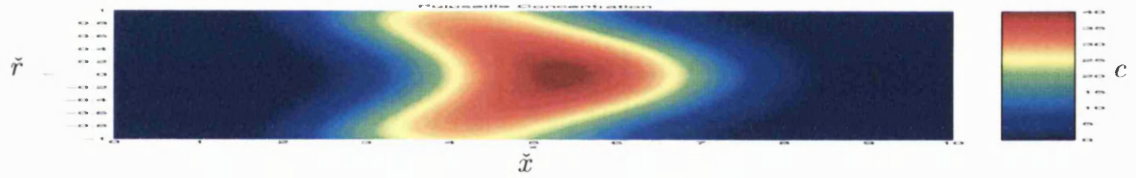
(a) Poiseuille Contour Profile After 1 Period



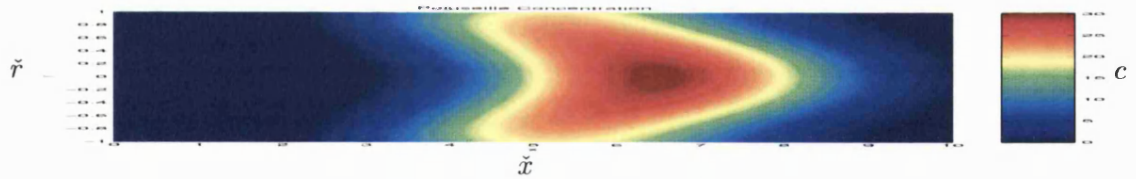
(b) Poiseuille Contour Profile After 2 Periods



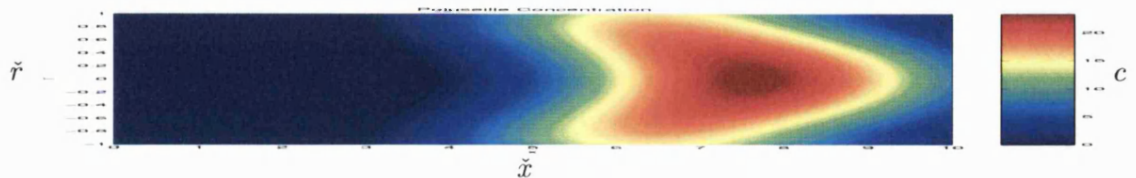
(c) Poiseuille Contour Profile After 3 Periods



(d) Poiseuille Contour Profile After 4 Periods

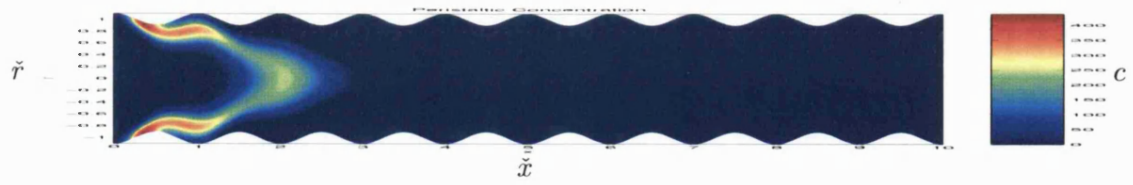


(e) Poiseuille Contour Profile After 5 Periods

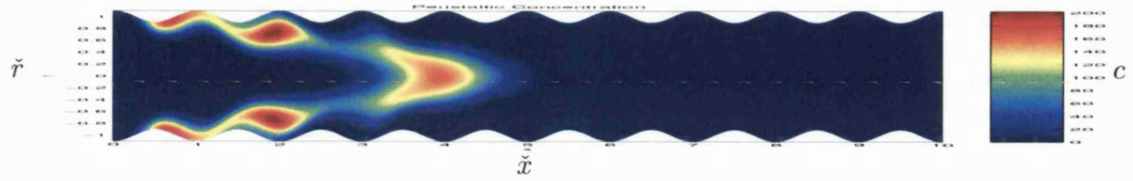


(f) Poiseuille Contour Profile After 6 Periods

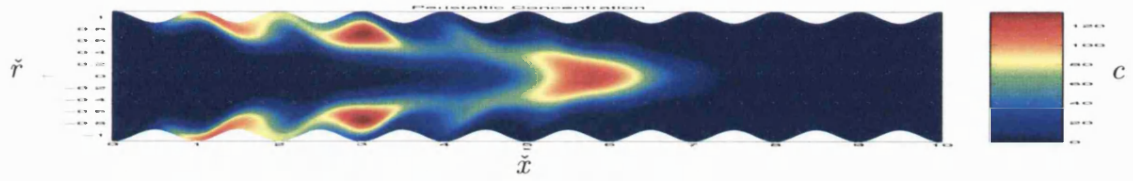
Figure 5-8: Poiseuille Contour Plots when $\hat{\psi}_w = 0$, $P_{er} = 100$, $\alpha = 0.1$, $D_{ar} = 1$



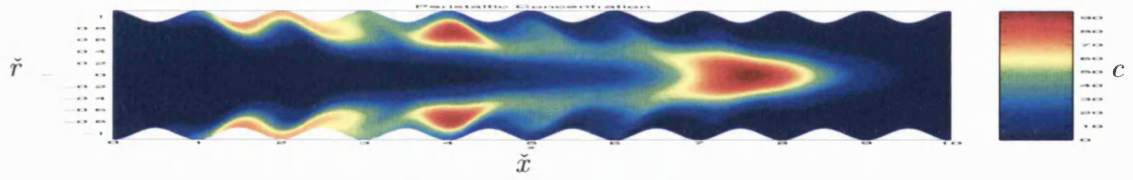
(a) Peristaltic Contour Profile After 1 Period



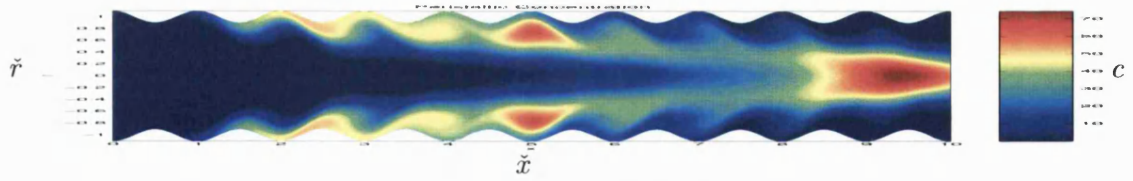
(b) Peristaltic Contour Profile After 2 Periods



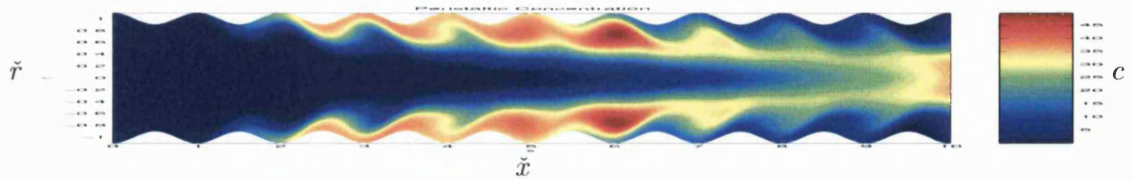
(c) Peristaltic Contour Profile After 3 Periods



(d) Peristaltic Contour Profile After 4 Periods

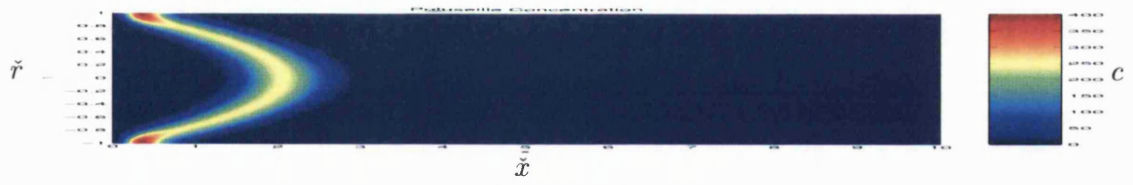


(e) Peristaltic Contour Profile After 5 Periods

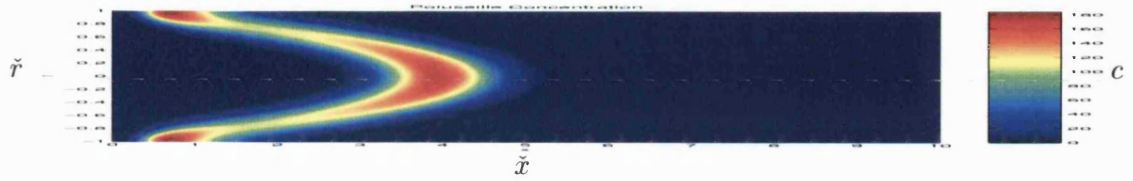


(f) Peristaltic Contour Profile After 6 Periods

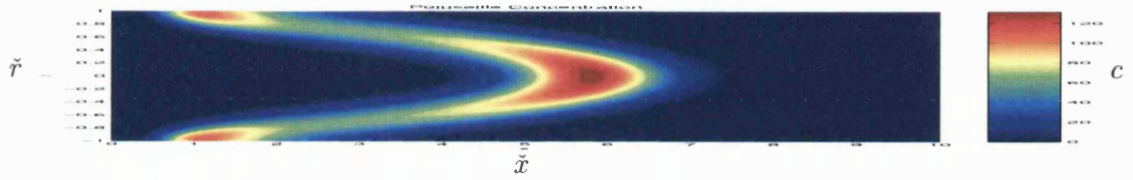
Figure 5-9: Peristaltic Contour Plots when $\hat{\psi}_w = 0$, $P_{er} = 1000$, $\alpha = 0.1$, $D_{ar} = 1$



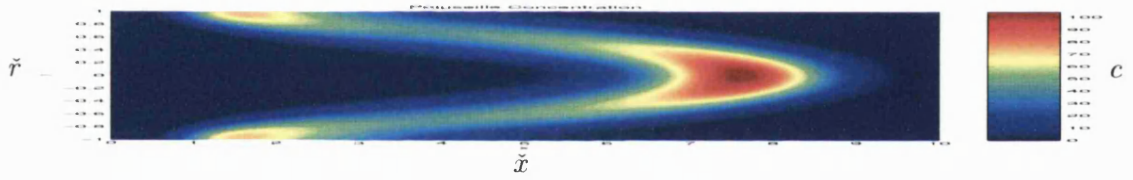
(a) Poiseuille Contour Profile After 1 Period



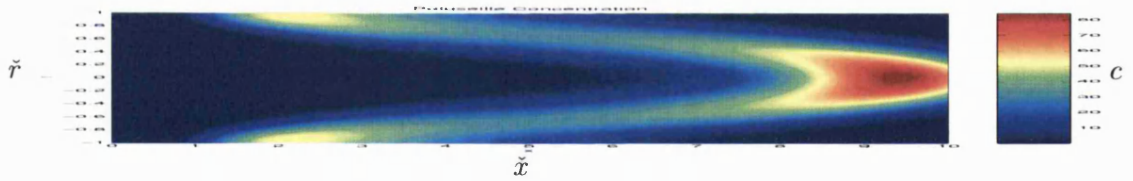
(b) Poiseuille Contour Profile After 2 Periods



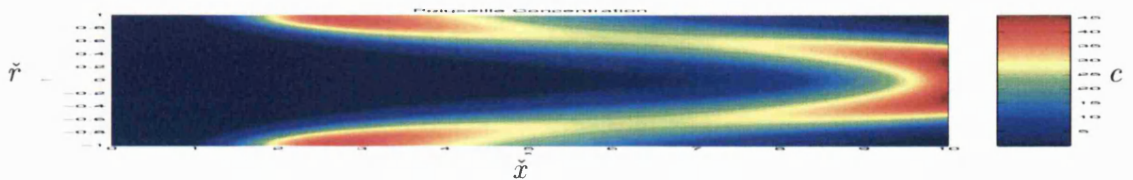
(c) Poiseuille Contour Profile After 3 Periods



(d) Poiseuille Contour Profile After 4 Periods



(e) Poiseuille Contour Profile After 5 Periods



(f) Poiseuille Contour Profile After 6 Periods

Figure 5-10: Poiseuille Contour Plots when $\hat{\psi}_w = 0$, $P_{er} = 1000$, $\alpha = 0.1$, $D_{ar} = 1$

5.3.2 Case A - Fast Flow

We solve the peristaltic dispersion model (5.1.5) for fast flow in case A when there is detached trapping and no reflux. We implement a small amplitude of vibration $\alpha = 0.1$ and numerically solve for two cases of a slow and fast diffusing solute, when the flow rate is $\hat{\psi}_w = 1$ which exhibits less trapping, namely 17.6%, than that of the slow flow case (40.7% in §5.3.1).

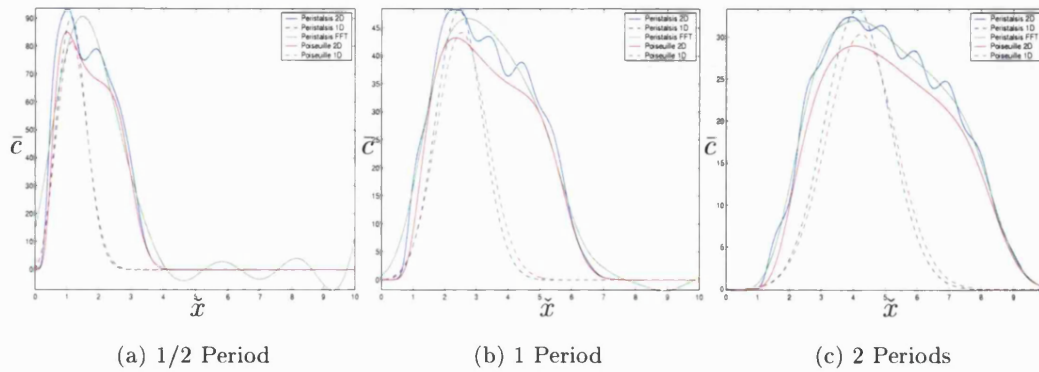


Figure 5-11: Mean Solute Concentration for the Peristaltic Dispersion Model and the Poiseuille Dispersion Model, and their 1D Dispersion Approximation with the the FFT of the Peristaltic Solution, for a Fast Diffusing Solute in Case A, $P_{er} = 100$, when $\alpha = 0.1$, $\hat{\psi}_w = 1$ and $D_{ar} = 1$.

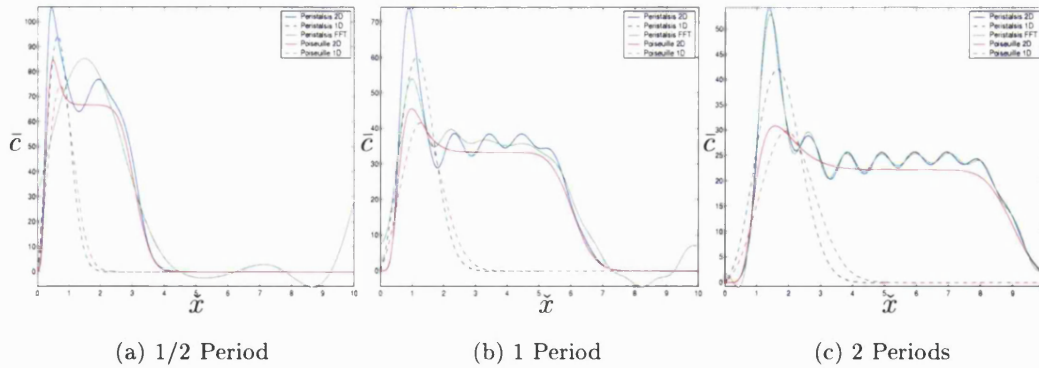


Figure 5-12: Mean Solute Concentration for the Peristaltic Dispersion Model and the Poiseuille Dispersion Model, and their 1D Dispersion Approximation with the the FFT of the Peristaltic Solution, for A Slow Diffusing Solute in Case A, $P_{er} = 1000$, when $\alpha = 0.1$, $\hat{\psi}_w = 1$ and $D_{ar} = 1$

In Figure 5-11, we observe the same results as in the slow flow case for the fast diffusing solute. The mean solute concentration of the peristaltic dispersion model \bar{c}_{pe} is essentially that of the Poiseuille dispersion model \bar{c}_{po} plus some oscillatory term. See Figures 5-15 and 5-16 for contour plots.

Again, as the level of diffusion decreases and convective forces dominate solute motion, we observe in Figure 5-12 that the amplitude of oscillations have increased in \bar{c}_{pe} and the frequency of oscillations increases with time. However, this differs from that of the slow flow case as the amount of trapping has decreased, and the amplitude of oscillations is not so pronounced. We observe that \bar{c}_{pe} is approximately \bar{c}_{po} plus some oscillatory term. See Figures 5-17 and 5-18 for contour plots.

Similar to the slow flow case, $\hat{\psi}_w = 0$, the amount of mass absorbed by peristalsis is much more than that of Poiseuille for the fast and slow diffusing solute, see Figures 5-13 and 5-14.

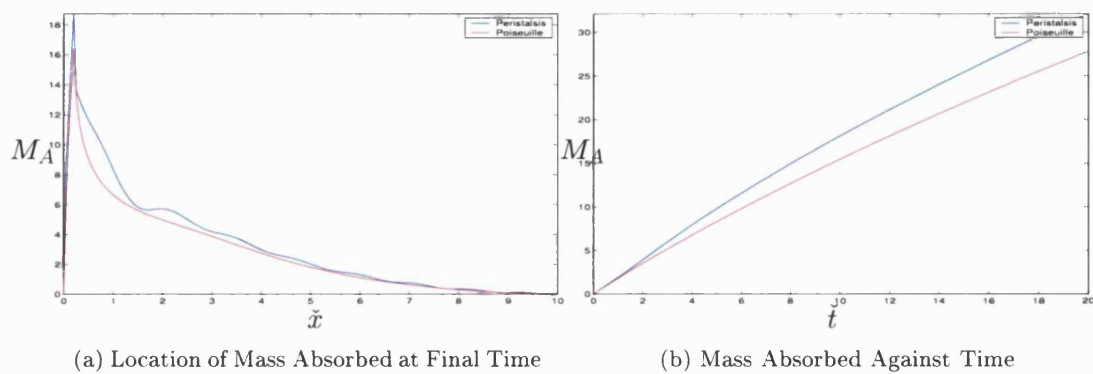


Figure 5-13: Mass Absorbed for the Peristaltic and Poiseuille Dispersion Models for a Fast Diffusing Solute, $P_{er} = 100$, when $\alpha = 0.1$, $\hat{\psi}_w = 1$ and $P_{er} = 1000$, $D_{ar} = 1$

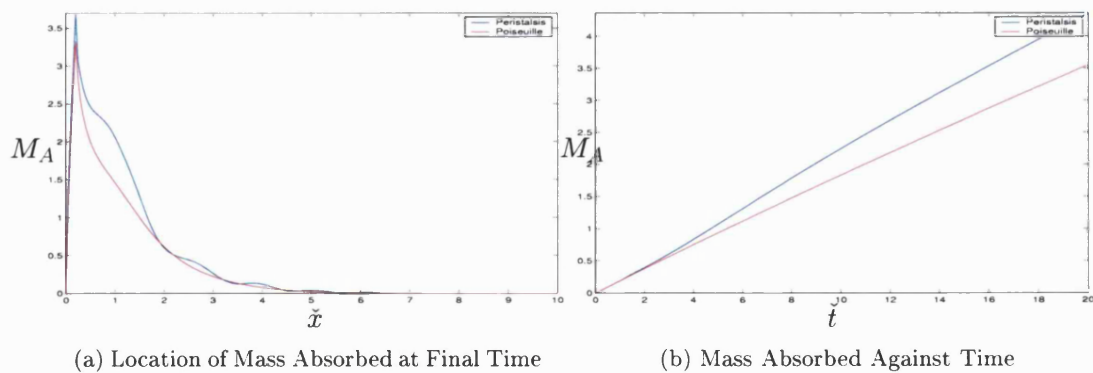
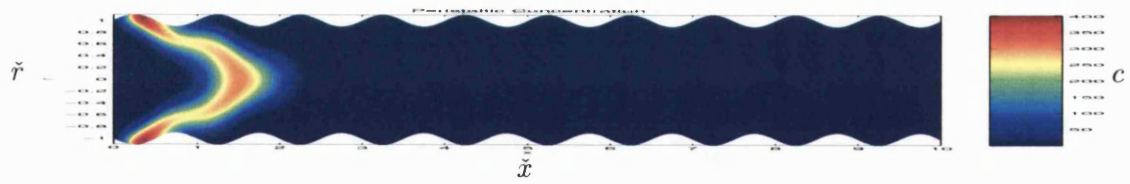
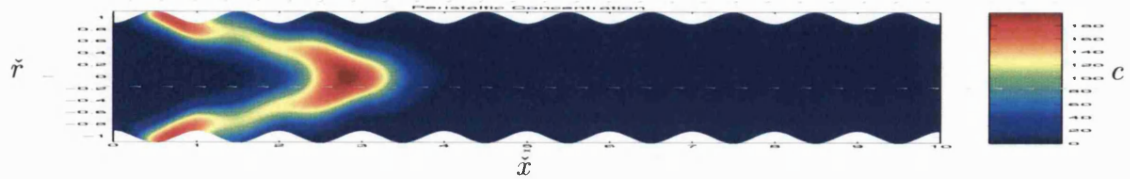


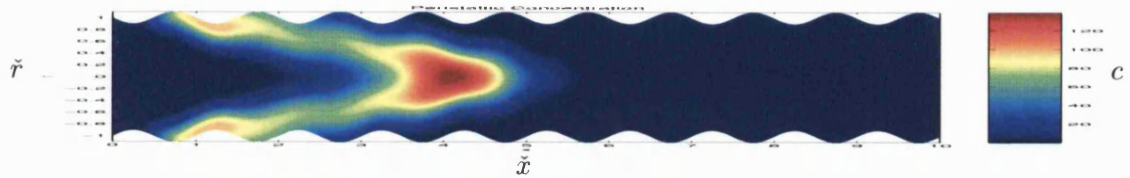
Figure 5-14: Mass Absorbed for the Peristaltic and Poiseuille Dispersion Models for a Slow Diffusing Solute, $P_{er} = 1000$, when $\alpha = 0.1$, $\hat{\psi}_w = 1$ and $P_{er} = 1000$, $D_{ar} = 1$



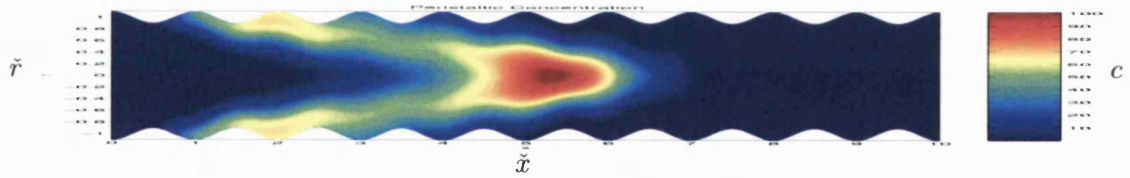
(a) Peristaltic Contour Profile After 0.25 Periods



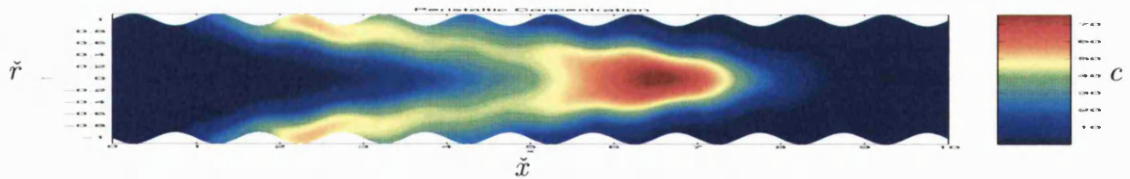
(b) Peristaltic Contour Profile After 0.5 Periods



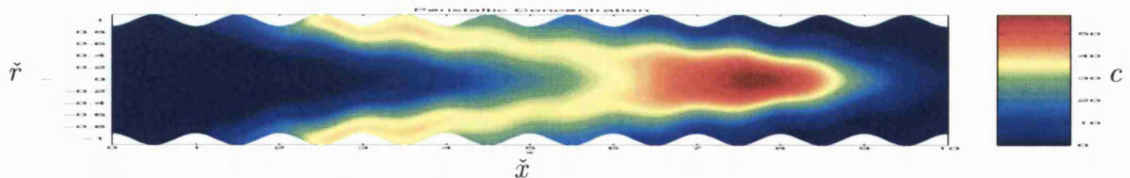
(c) Peristaltic Contour Profile After 0.75 Periods



(d) Peristaltic Contour Profile After 1 Period

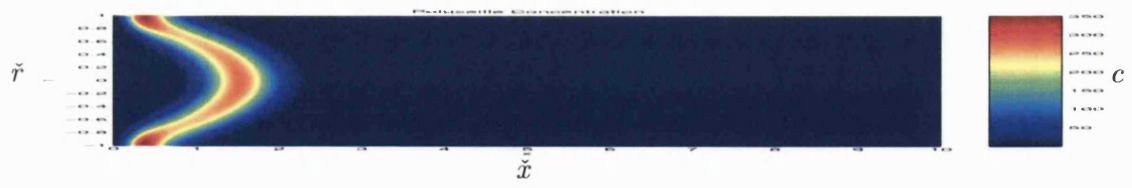


(e) Peristaltic Contour Profile After 1.25 Periods

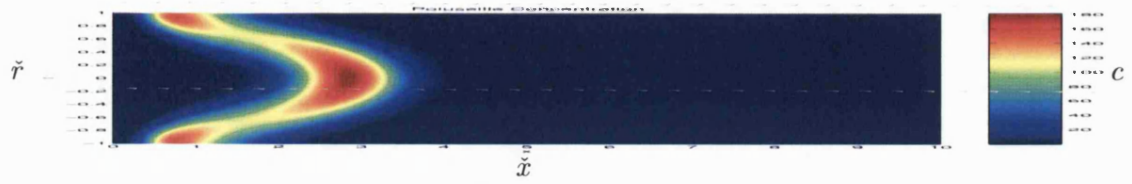


(f) Peristaltic Contour Profile After 1.5 Periods

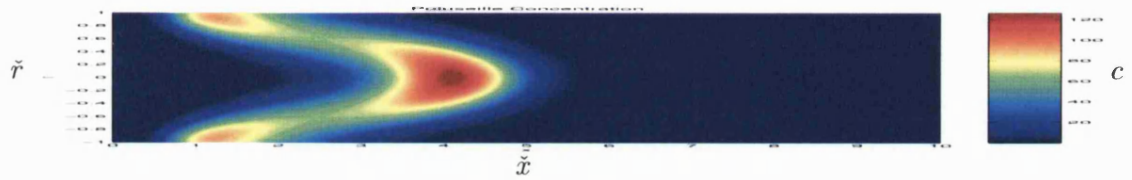
Figure 5-15: Peristaltic Contour Plots for Case A when $\hat{\psi}_w = 1$, $P_{er} = 100$, $\alpha = 0.1$, $D_{ar} = 1$



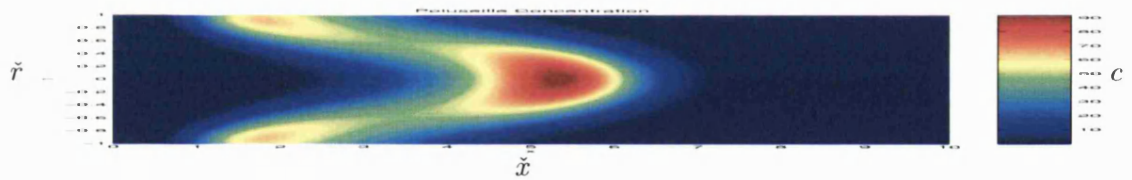
(a) Poiseuille Contour Profile After 0.25 Periods



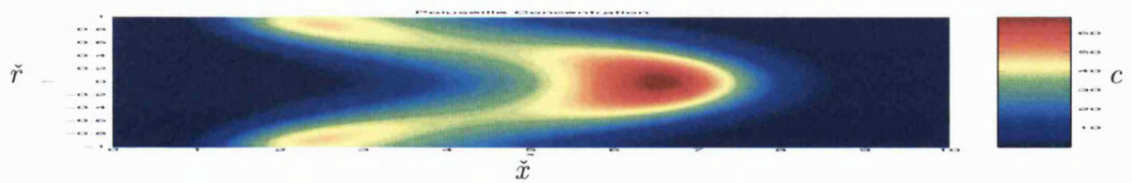
(b) Poiseuille Contour Profile After 0.5 Periods



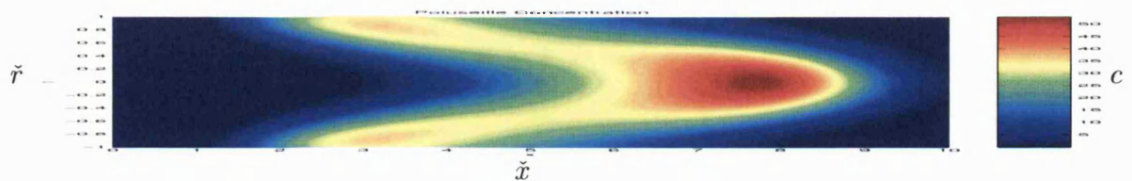
(c) Poiseuille Contour Profile After 0.75 Periods



(d) Poiseuille Contour Profile After 1 Period

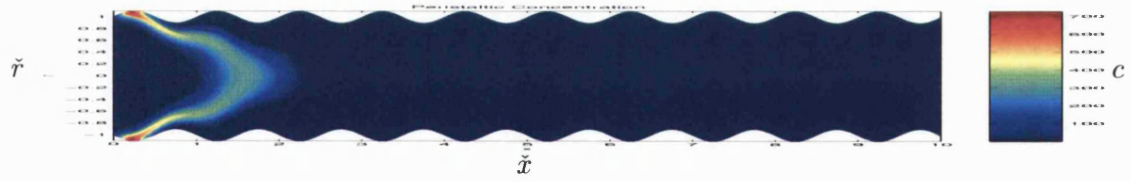


(e) Poiseuille Contour Profile After 1.25 Periods

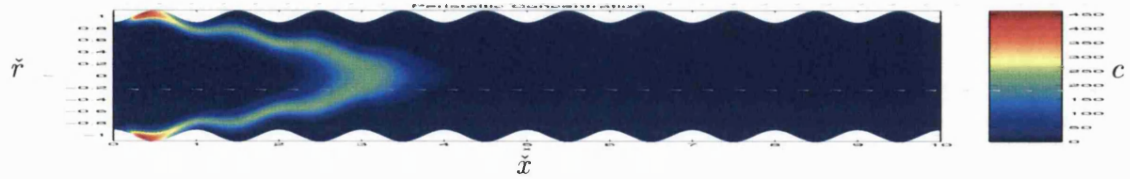


(f) Poiseuille Contour Profile After 1.5 Periods

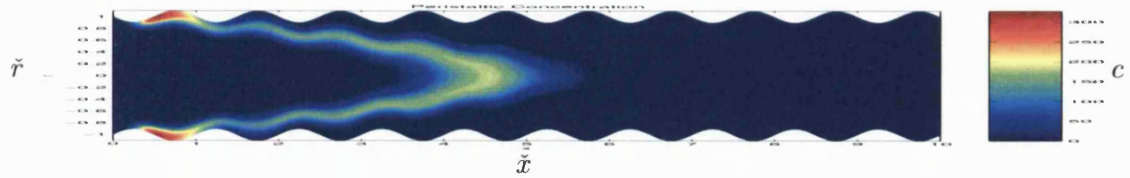
Figure 5-16: Poiseuille Contour Plots for Case A when $\hat{\psi}_w = 1$, $P_{er} = 100$, $\alpha = 0.1$, $D_{ar} = 1$



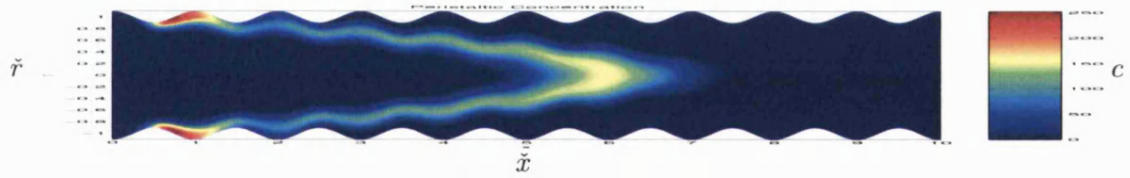
(a) Peristaltic Contour Profile After 0.25 Periods



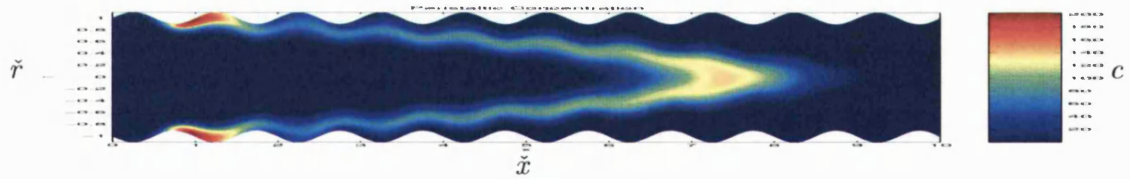
(b) Peristaltic Contour Profile After 0.5 Periods



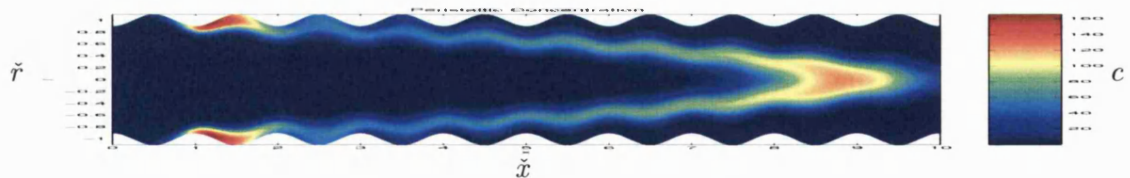
(c) Peristaltic Contour Profile After 0.75 Periods



(d) Peristaltic Contour Profile After 1 Period

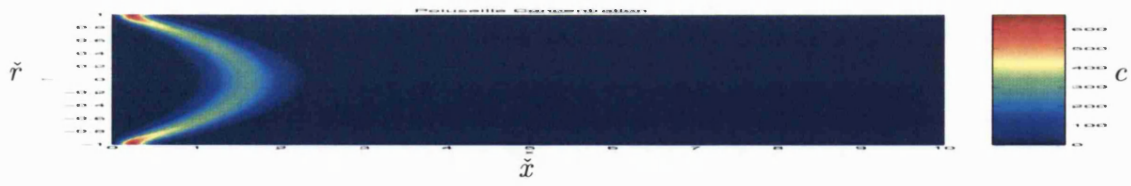


(e) Peristaltic Contour Profile After 1.25 Periods

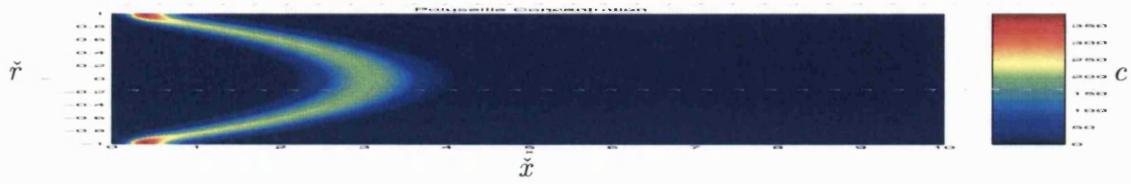


(f) Peristaltic Contour Profile After 1.5 Periods

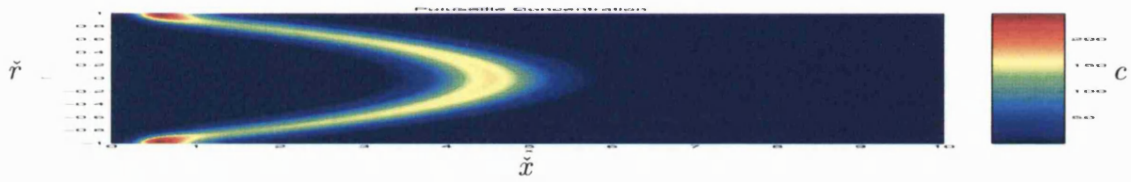
Figure 5-17: Peristaltic Contour Plots for Case A when $\hat{\psi}_w = 1$, $P_{er} = 1000$, $\alpha = 0.1$, $D_{ar} = 1$



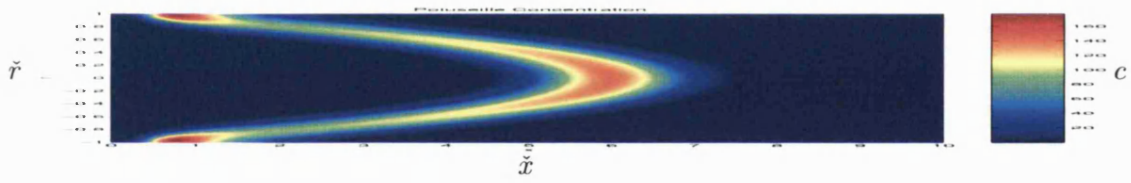
(a) Poiseuille Contour Profile After 0.25 Periods



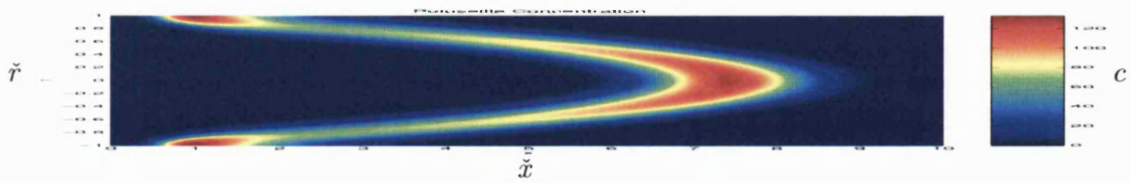
(b) Poiseuille Contour Profile After 0.5 Periods



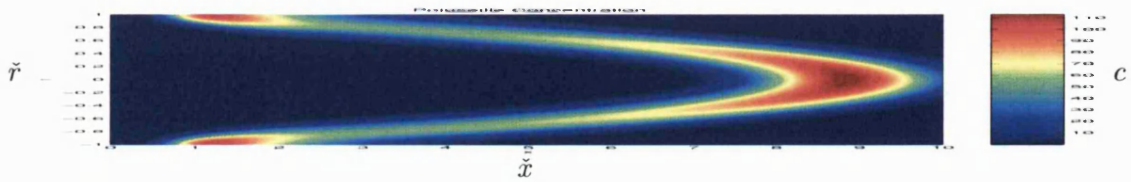
(c) Poiseuille Contour Profile After 0.75 Periods



(d) Poiseuille Contour Profile After 1 Period



(e) Poiseuille Contour Profile After 1.25 Periods



(f) Poiseuille Contour Profile After 1.5 Periods

Figure 5-18: Poiseuille Contour Plots for Case A when $\hat{\psi}_w = 1$, $P_{er} = 1000$, $\alpha = 0.1$, $D_{ar} = 1$

5.3.3 Case B - Centreline Trapping

We solve the peristaltic dispersion model (5.1.5) for case B of peristaltic flow, when there is centreline trapping, 36.6%, and no reflux. We implement a small amplitude of vibration $\alpha = 0.2$ and numerically solve for two cases of a slow and fast diffusing solute.

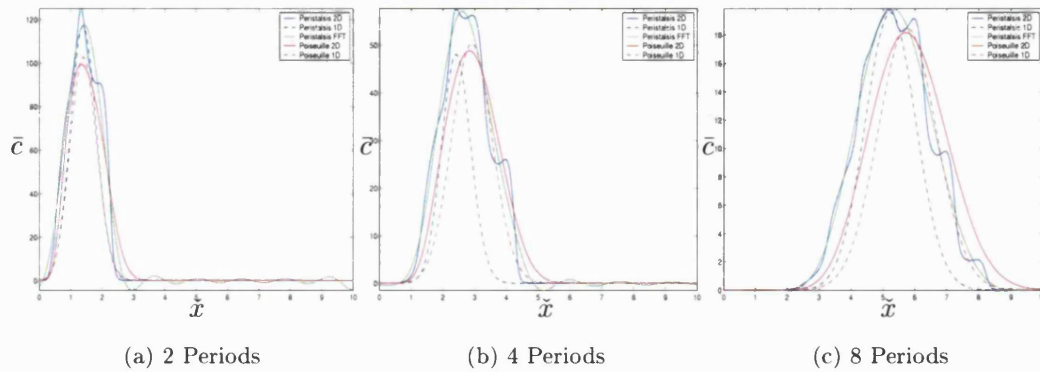


Figure 5-19: Mean Solute Concentration for the Peristaltic Dispersion Model and the Poiseuille Dispersion Model, and their 1D Dispersion Approximation with the the FFT of the Peristaltic Solution, for a Fast Diffusing Solute in Case B, $P_{er} = 100$, when $\alpha = 0.2$, $\hat{\psi}_w = -0.2$ and $D_{ar} = 1$.

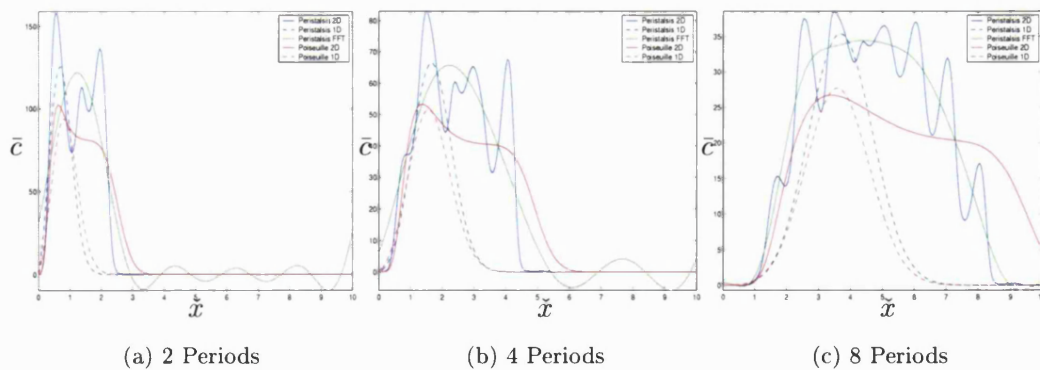


Figure 5-20: Mean Solute Concentration for the Peristaltic Dispersion Model and the Poiseuille Dispersion Model, and their 1D Dispersion Approximation with the the FFT of the Peristaltic Solution, for A Slow Diffusing Solute in Case B, $P_{er} = 1000$, when $\alpha = 0.2$, $\hat{\psi}_w = -0.2$ and $D_{ar} = 1$.

In Figures 5-19 5-20, we observe quite different results from that of the detached trapping case. Most striking is the advancement of the wave of the solute. Previously the head of the peristaltic wave has always coincided with Poiseuille wave. However, that is no longer the case in centreline trapping. This is more pronounced in the case of a slow diffusing solute. The head of the Poiseuille wave should move approximately with

speed $U_0 = 2\epsilon\bar{V} = \epsilon(4\hat{\psi}_w + 1 + \alpha^2)$, which after 6 periods should occur just after $\tilde{x} = 7.2$ if there were no diffusion. However, the head of the peristaltic wave is trapping which moves with speed of the wave which is one wavelength per period. Hence, we observe the head of the solute occurs around $\tilde{x} = 6$. What is interesting is that in both the fast and slow diffusing solute the head of the peristaltic wave is very steep, and that diffusion does not appear to axially spread the solute forward of the waves head, as it did for the detached trapping case. Hence peristaltic centreline trapping retards solute motion.

Again in the fast diffusing case the mean solute concentration of the peristaltic dispersion model \bar{c}_{pe} is similar to that of the Poiseuille dispersion model \bar{c}_{po} plus some oscillatory term. Now for the case of the slow diffusing solute we observe a large oscillatory term but more importantly we notice the large amplitude of the wave at the head of the solute profile is decreasing in size with time with respect to the size of the other waves, suggesting that not all solute in further most trapped regions is advancing with the wave, and that it is in fact moving into circulating regions behind the leading wave (see Figures 5-26 5-25). We still observe enhanced absorption from peristalsis.

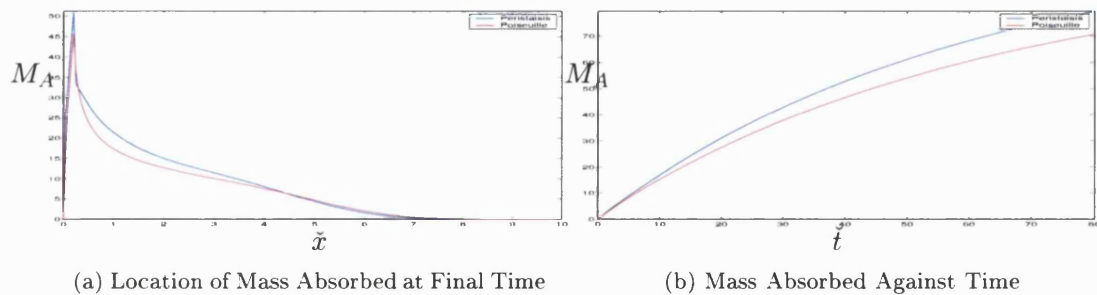


Figure 5-21: Mass Absorbed for the Peristaltic and Poiseuille Dispersion Models for a Fast Diffusing Solute, $P_{er} = 100$, when $\alpha = 0.2$, $\hat{\psi}_w = -0.2$ and $P_{er} = 1000$, $D_{ar} = 1$

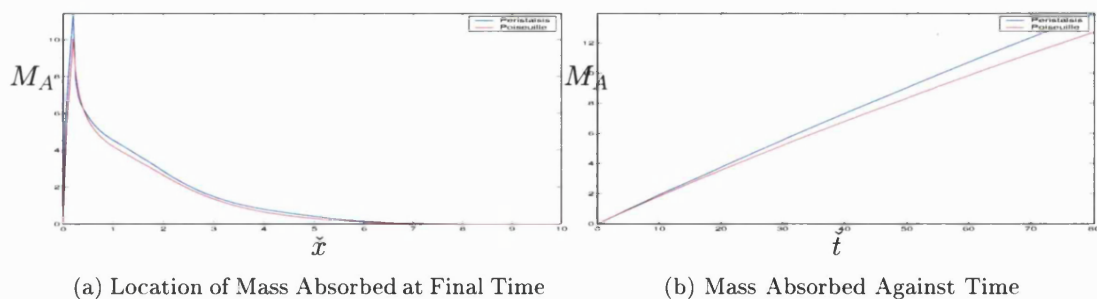
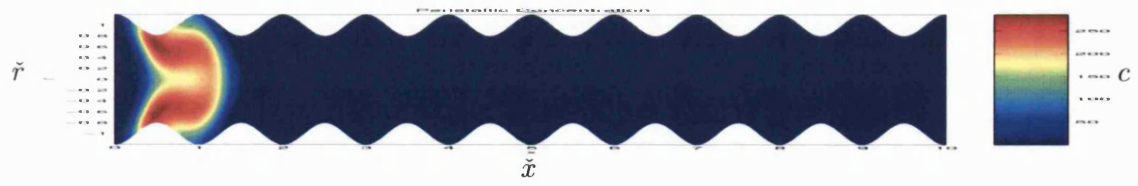
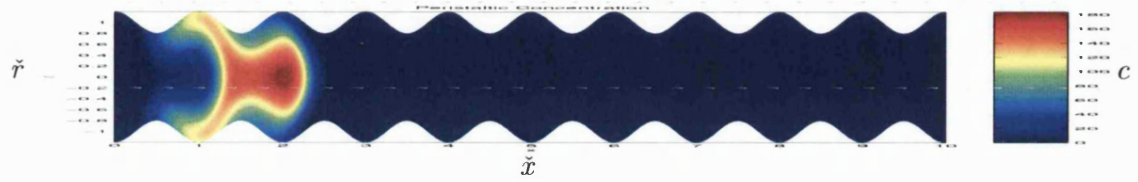


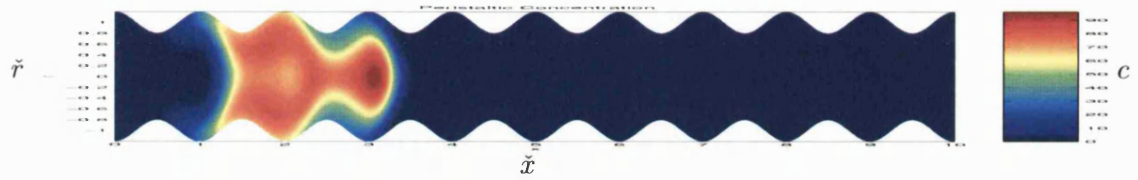
Figure 5-22: Mass Absorbed for the Peristaltic and Poiseuille Dispersion Models for a Slow Diffusing Solute, $P_{er} = 1000$, when $\alpha = 0.2$, $\hat{\psi}_w = -0.2$ and $P_{er} = 1000$, $D_{ar} = 1$



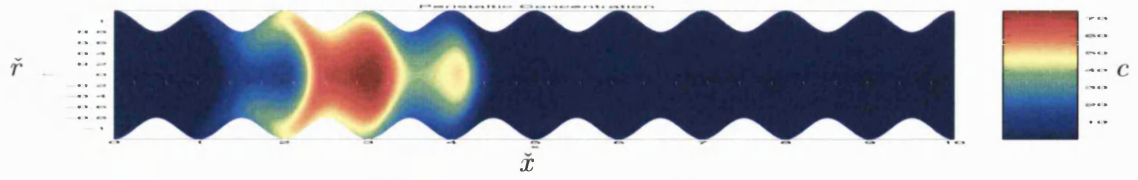
(a) Peristaltic Contour Profile After 1 Period



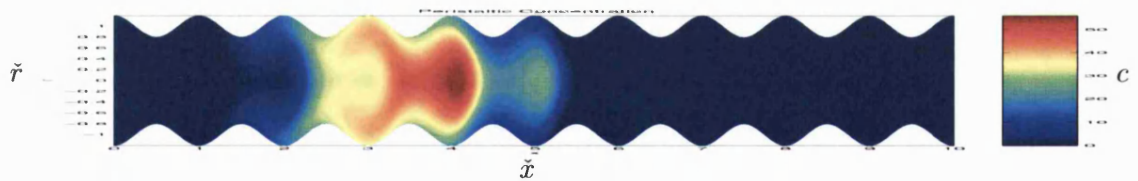
(b) Peristaltic Contour Profile After 2 Periods



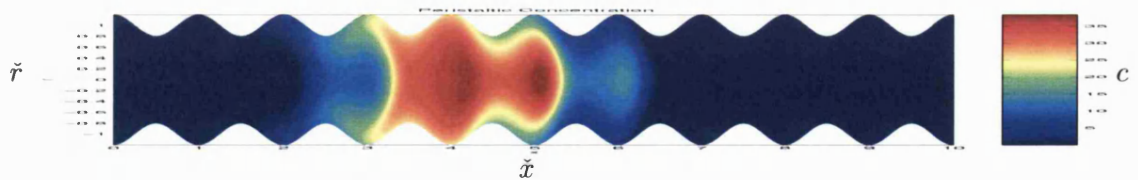
(c) Peristaltic Contour Profile After 3 Periods



(d) Peristaltic Contour Profile After 4 Periods

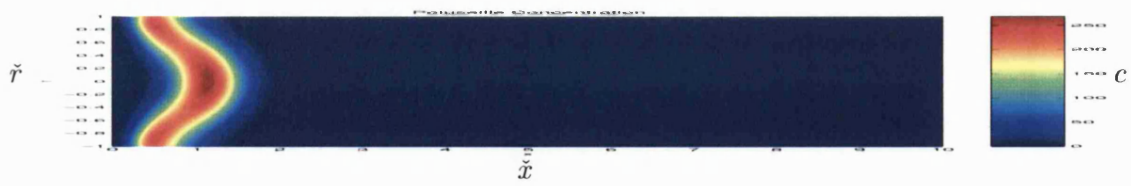


(e) Peristaltic Contour Profile After 5 Periods

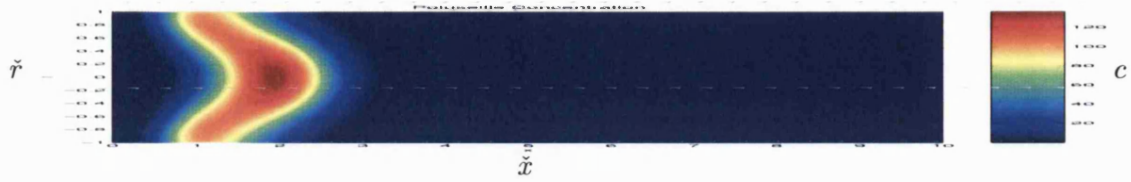


(f) Peristaltic Contour Profile After 6 Periods

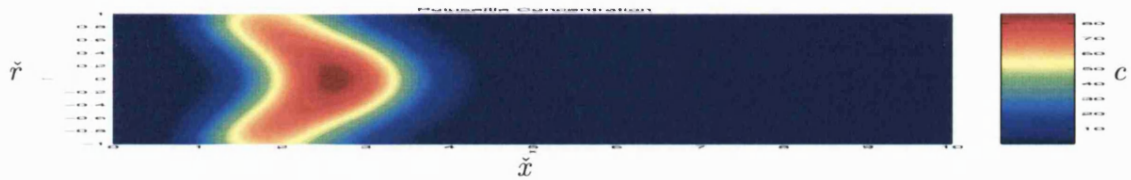
Figure 5-23: Peristaltic Contour Plots for Case B when $\hat{\psi}_w = -0.2$, $P_{er} = 100$, $\alpha = 0.2$, $D_{ar} = 1$



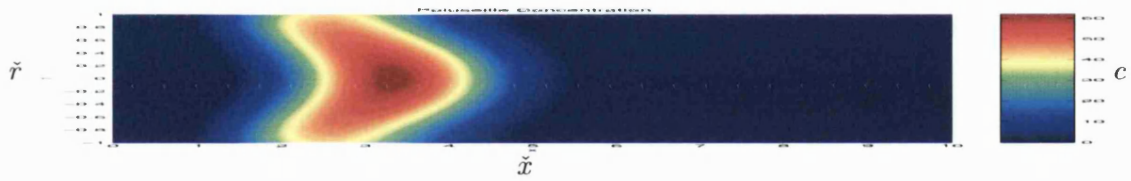
(a) Poiseuille Contour Profile After 1 Period



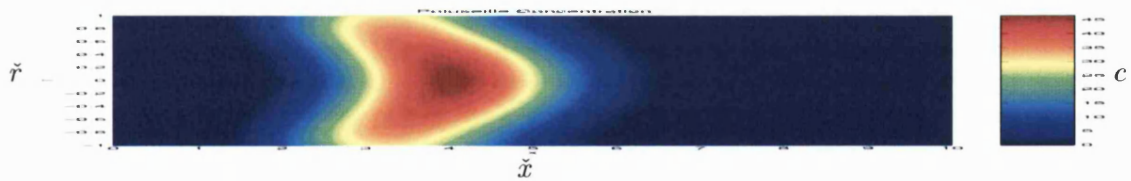
(b) Poiseuille Contour Profile After 2 Periods



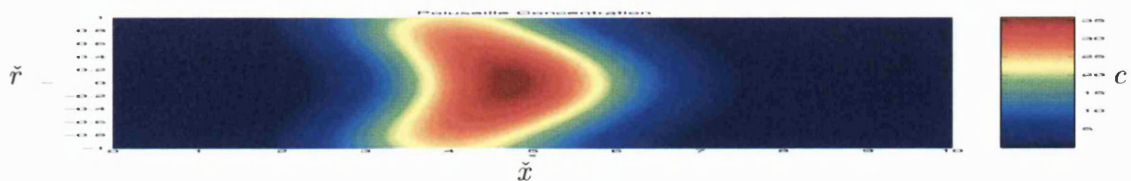
(c) Poiseuille Contour Profile After 3 Periods



(d) Poiseuille Contour Profile After 4 Periods

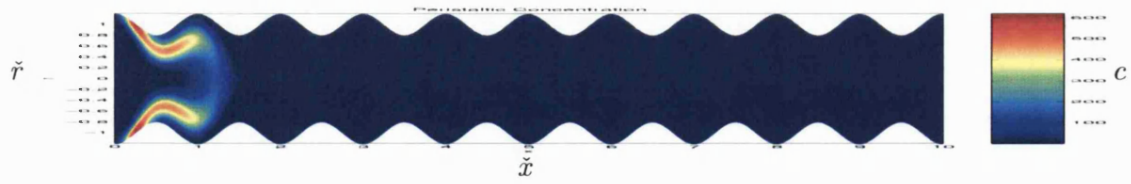


(e) Poiseuille Contour Profile After 5 Periods

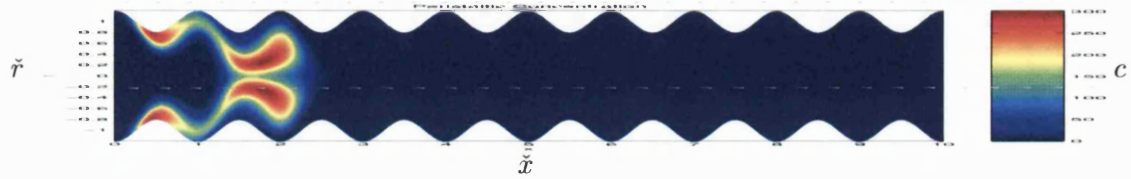


(f) Poiseuille Contour Profile After 6 Periods

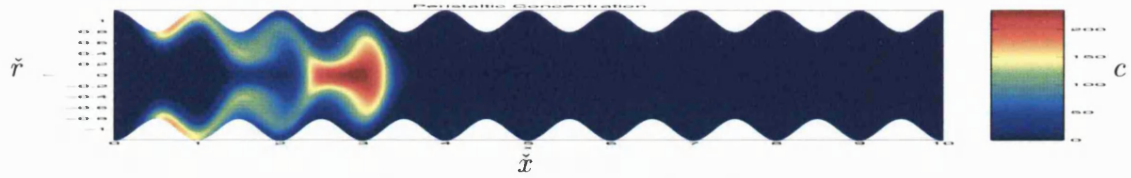
Figure 5-24: Poiseuille Contour Plots for Case B when $\hat{\psi}_w = -0.2$, $P_{er} = 100$, $\alpha = 0.2$, $D_{ar} = 1$



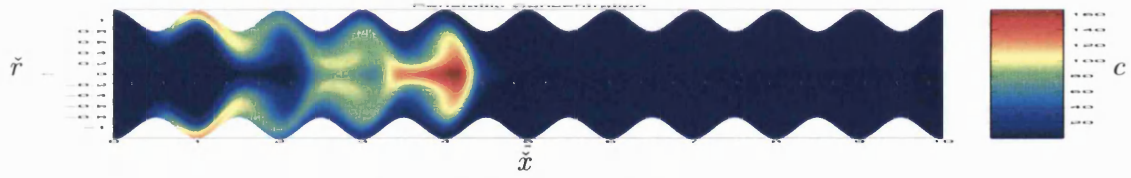
(a) Peristaltic Contour Profile After 1 Period



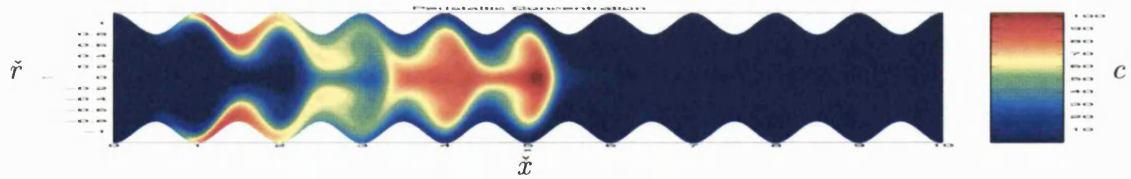
(b) Peristaltic Contour Profile After 2 Periods



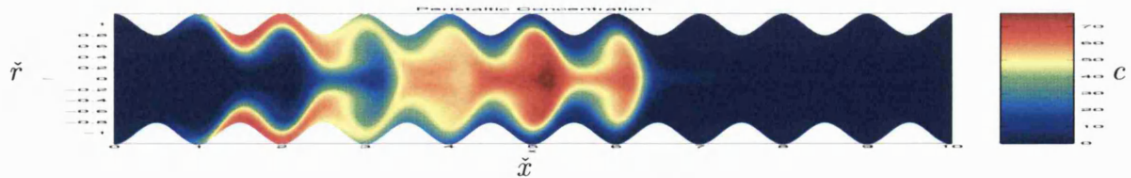
(c) Peristaltic Contour Profile After 3 Periods



(d) Peristaltic Contour Profile After 4 Periods

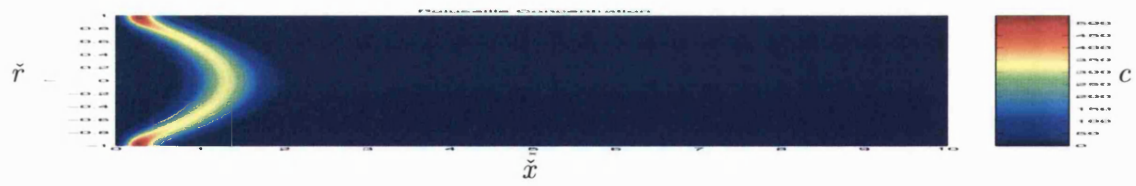


(e) Peristaltic Contour Profile After 5 Periods

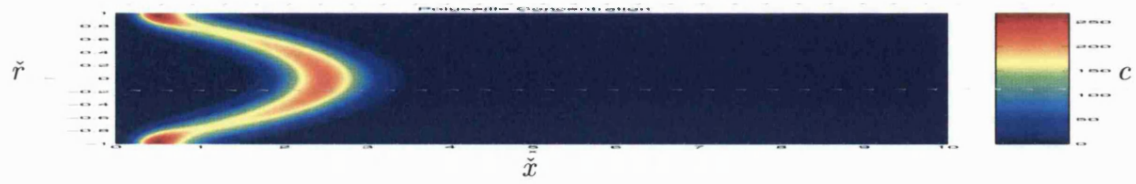


(f) Peristaltic Contour Profile After 6 Periods

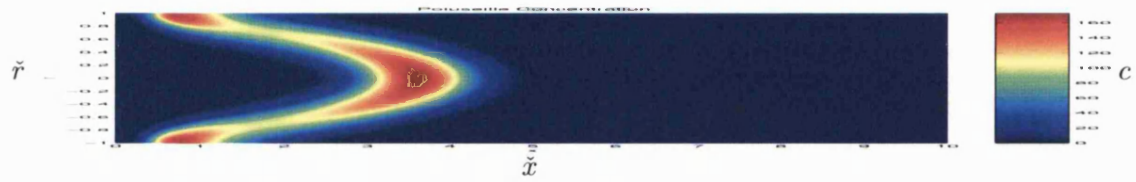
Figure 5-25: Peristaltic Contour Plots for Case B when $\hat{\psi}_w = -0.2$, $P_{er} = 1000$, $\alpha = 0.2$, $D_{ar} = 1$



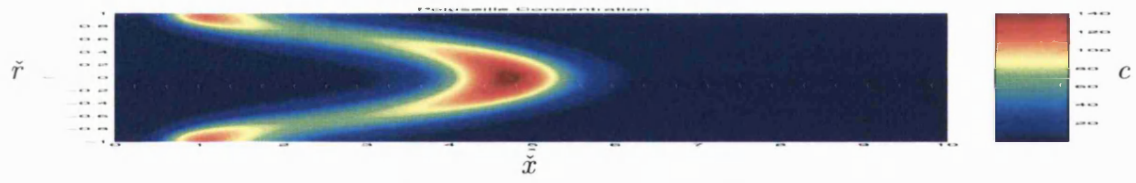
(a) Poiseuille Contour Profile After 1 Period



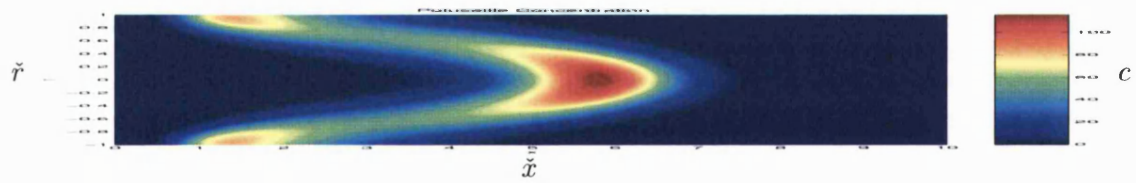
(b) Poiseuille Contour Profile After 2 Periods



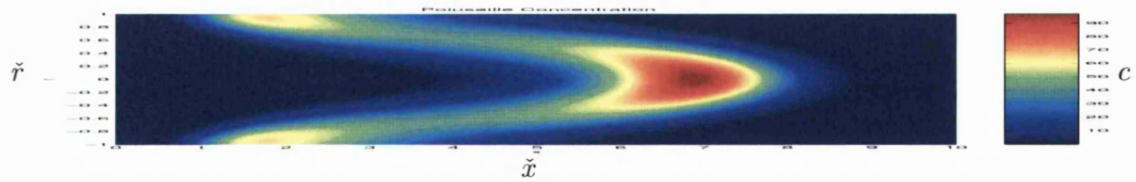
(c) Poiseuille Contour Profile After 3 Periods



(d) Poiseuille Contour Profile After 4 Periods



(e) Poiseuille Contour Profile After 5 Periods



(f) Poiseuille Contour Profile After 6 Periods

Figure 5-26: Poiseuille Contour Plots for Case B when $\hat{\psi}_w = -0.2$, $P_{er} = 1000$, $\alpha = 0.2$, $D_{ar} = 1$

5.3.4 Case C - No Trapping

We solve the peristaltic dispersion model (5.1.5) for case C of peristaltic flow where there are no peristaltic phenomena. We implement a small amplitude of vibration $\alpha = 0.2$ and numerically solve for two cases of a slow and fast diffusing solute.

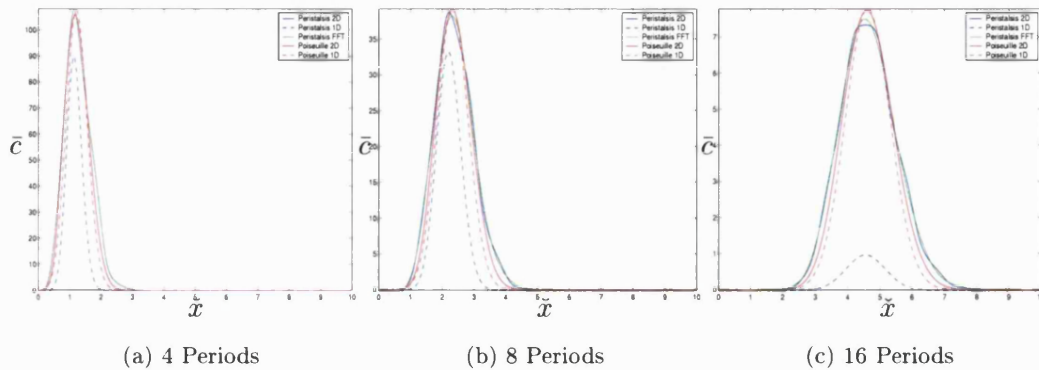


Figure 5-27: Mean Solute Concentration for the Peristaltic Dispersion Model and the Poiseuille Dispersion Model, and their 1D Dispersion Approximation with the the FFT of the Peristaltic Solution, for a Fast Diffusing Solute in Case C, $P_{er} = 100$, when $\alpha = 0.1$, $\hat{\psi}_w = -0.38$ and $D_{ar} = 1$.

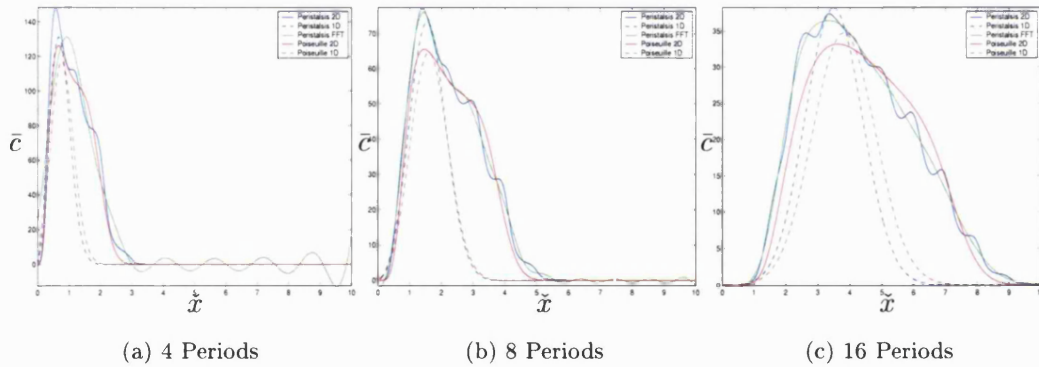


Figure 5-28: Mean Solute Concentration for the Peristaltic Dispersion Model and the Poiseuille Dispersion Model, and their 1D Dispersion Approximation with the the FFT of the Peristaltic Solution, for A Slow Diffusing Solute in Case C, $P_{er} = 1000$, when $\alpha = 0.1$, $\hat{\psi}_w = -0.38$ and $D_{ar} = 1$

In case C there is no trapping and as such we do not observe a large oscillatory component on the mean solute concentration for the slow diffusing solute (see Figure 5-28). The oscillations occur as a result of the nonuniform axial velocity profile induced by peristalsis. The weak oscillatory term is removed for small Péclet number (see Figure 5-27) and the mean solute profiles for the two models, \bar{c}_{pe} and \bar{c}_{po} , are almost identical.

We continue to observe peristalsis is responsible for more absorption of solute when

compared to Poiseuille flow. This is because solute need not travel as far to the boundary at points of contraction. Consequently, peristalsis at any amplitude of vibration will always result in increased absorption.

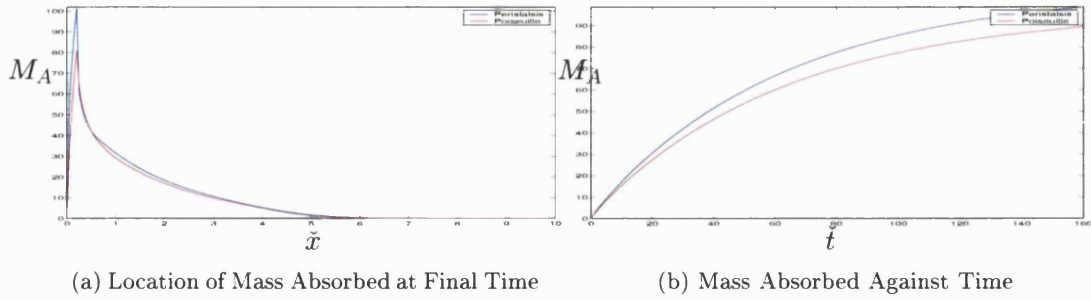


Figure 5-29: Mass Absorbed for the Peristaltic and Poiseuille Dispersion Models for a Fast Diffusing Solute, $P_{er} = 100$, when $\alpha = 0.1$, $\hat{\psi}_w = -0.38$ and $P_{er} = 1000$, $D_{ar} = 1$

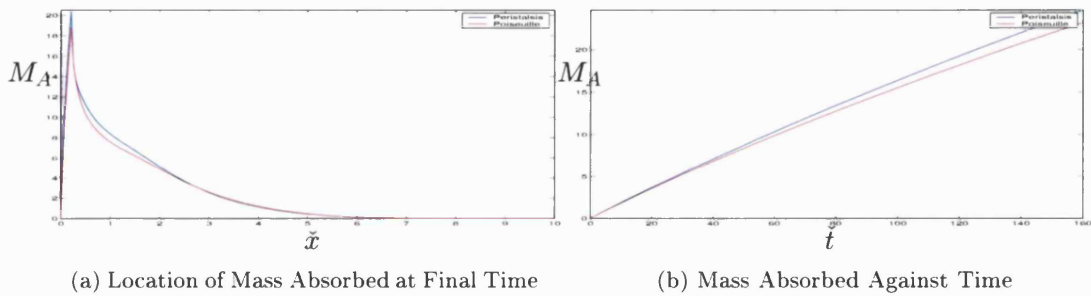
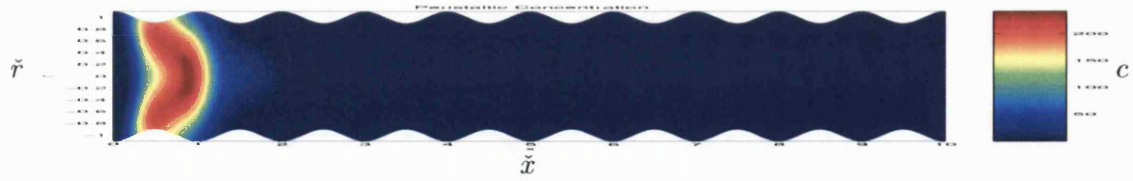
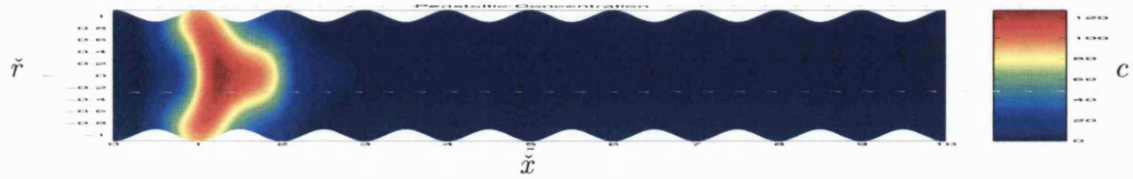


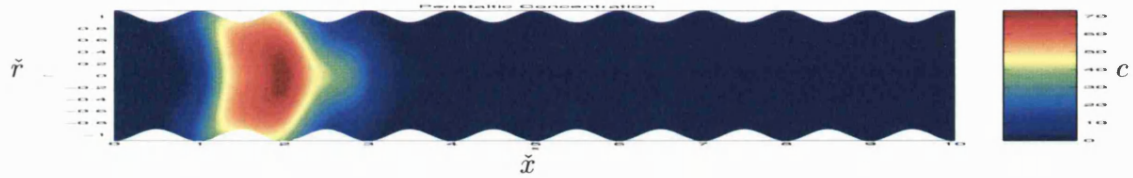
Figure 5-30: Mass Absorbed for the Peristaltic and Poiseuille Dispersion Models for a Slow Diffusing Solute, $P_{er} = 1000$, when $\alpha = 0.1$, $\hat{\psi}_w = -0.38$ and $P_{er} = 1000$, $D_{ar} = 1$



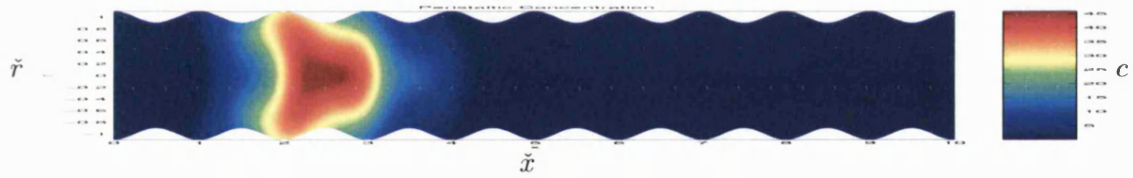
(a) Peristaltic Contour Profile After 2 Period



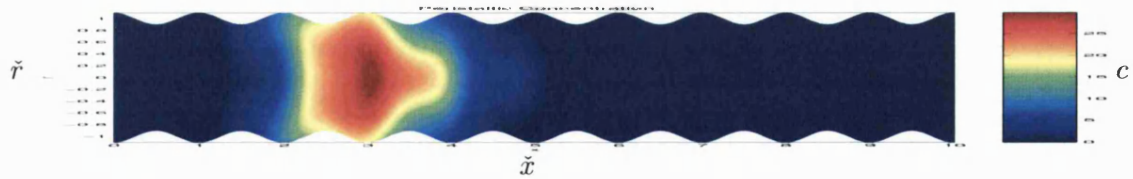
(b) Peristaltic Contour Profile After 4 Periods



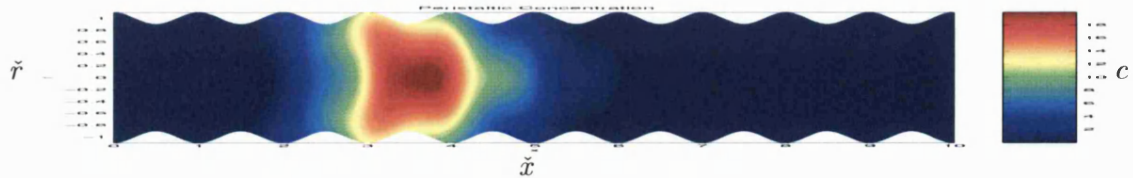
(c) Peristaltic Contour Profile After 6 Periods



(d) Peristaltic Contour Profile After 8 Periods

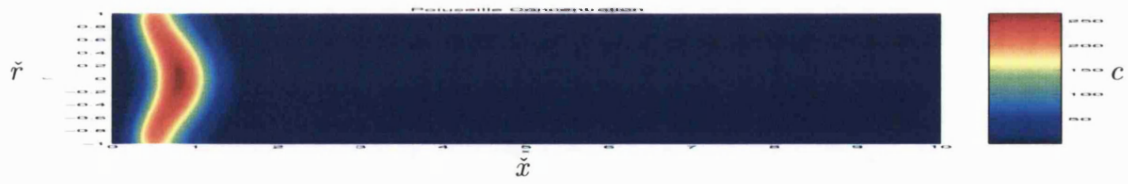


(e) Peristaltic Contour Profile After 10 Periods

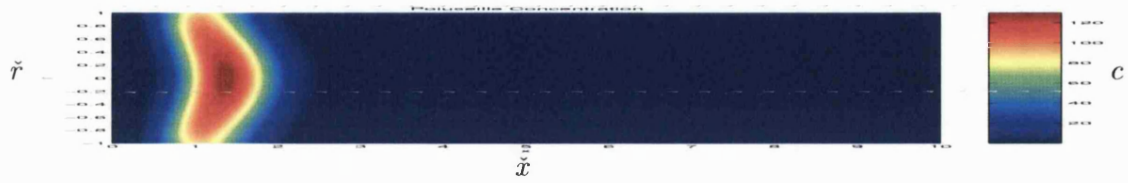


(f) Peristaltic Contour Profile After 12 Periods

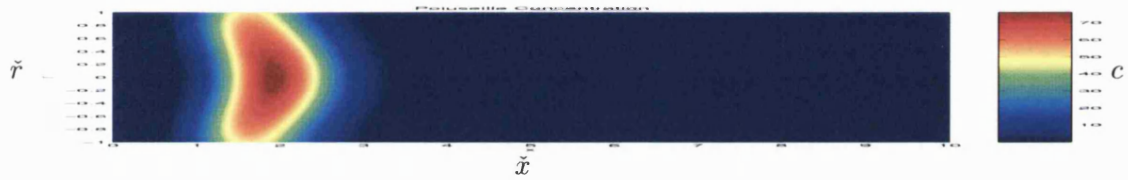
Figure 5-31: Peristaltic Contour Plots for Case C when $\hat{\psi}_w = -0.38$, $Pe_r = 100$, $\alpha = 0.1$, $D_{ar} = 1$



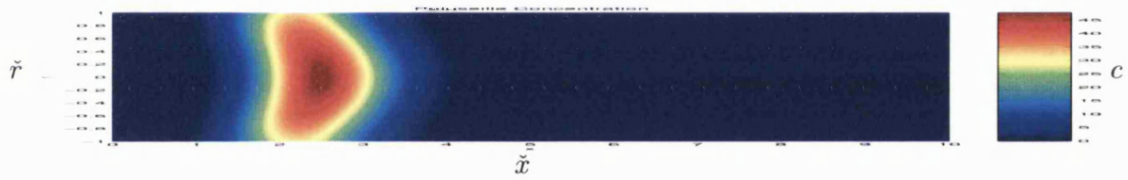
(a) Poiseuille Contour Profile After 2 Period



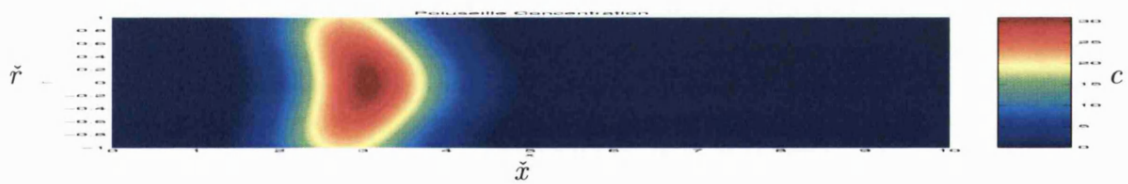
(b) Poiseuille Contour Profile After 4 Periods



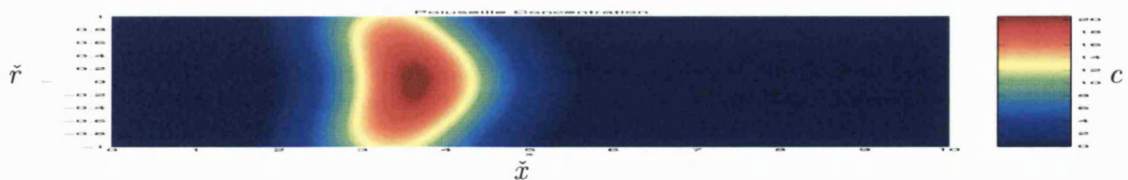
(c) Poiseuille Contour Profile After 6 Periods



(d) Poiseuille Contour Profile After 8 Periods

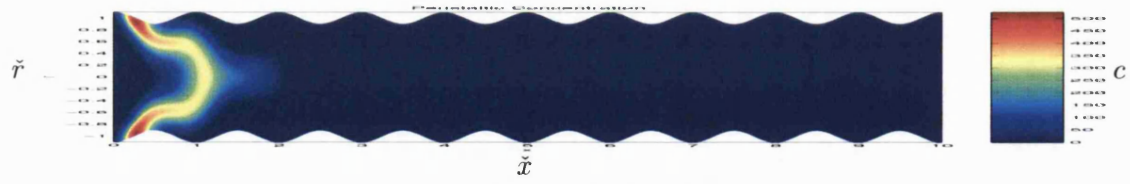


(e) Poiseuille Contour Profile After 10 Periods

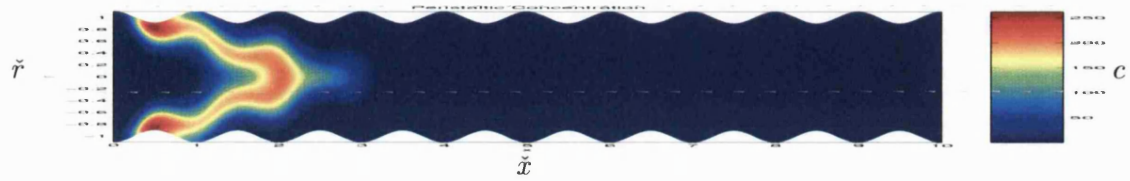


(f) Poiseuille Contour Profile After 12 Periods

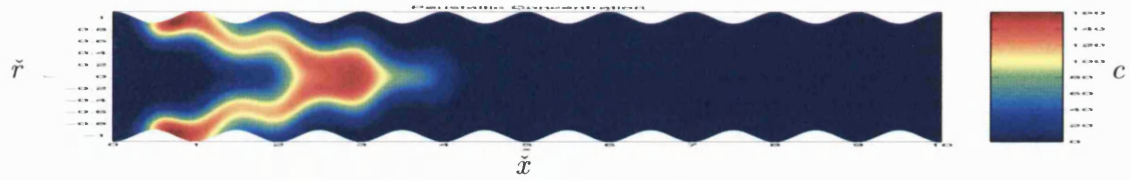
Figure 5-32: Poiseuille Contour Plots for Case C when $\hat{\psi}_w = -0.38$, $P_{er} = 100$, $\alpha = 0.1$, $D_{ar} = 1$



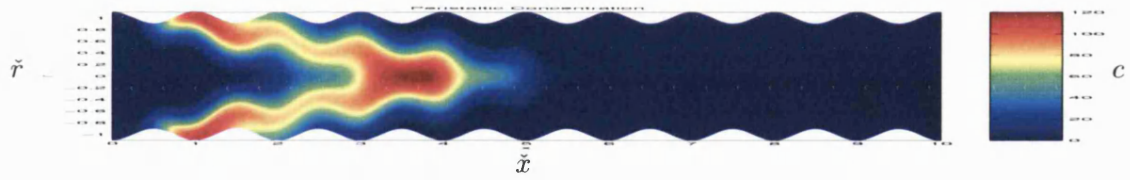
(a) Peristaltic Contour Profile After 2 Period



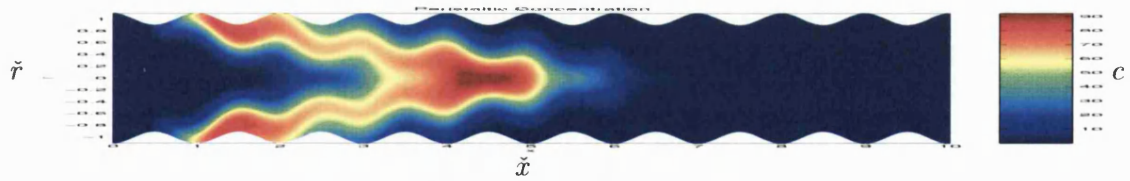
(b) Peristaltic Contour Profile After 4 Periods



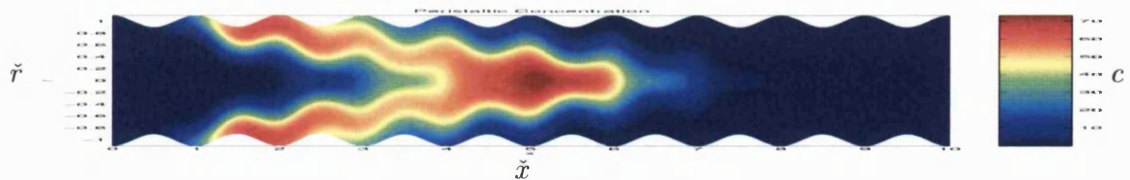
(c) Peristaltic Contour Profile After 6 Periods



(d) Peristaltic Contour Profile After 8 Periods

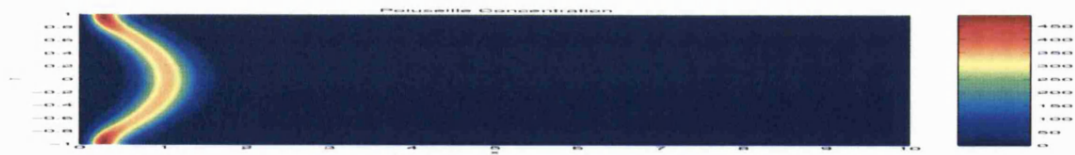


(e) Peristaltic Contour Profile After 10 Periods

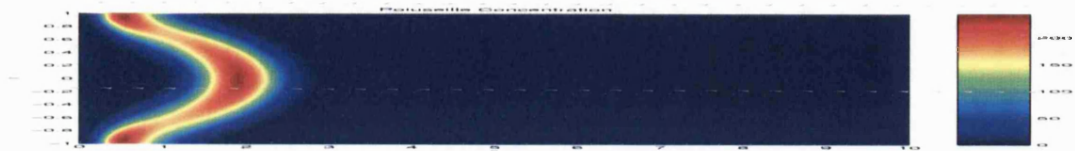


(f) Peristaltic Contour Profile After 12 Periods

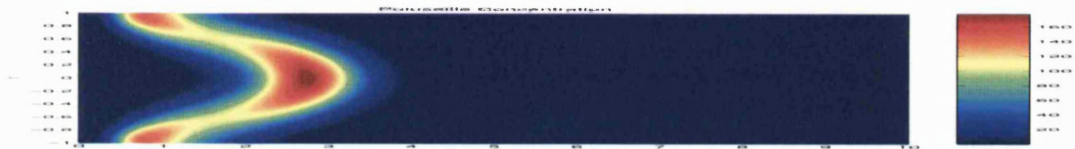
Figure 5-33: Peristaltic Contour Plots for Case C when $\hat{\psi}_w = -0.38$, $Pe_r = 1000$, $\alpha = 0.1$, $D_{ar} = 1$



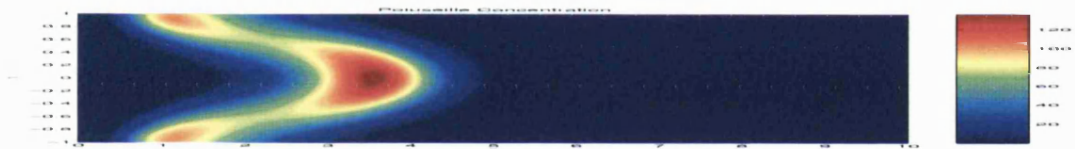
(a) Poiseuille Contour Profile After 2 Period



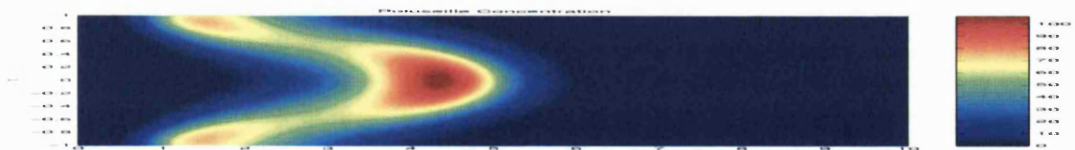
(b) Poiseuille Contour Profile After 4 Periods



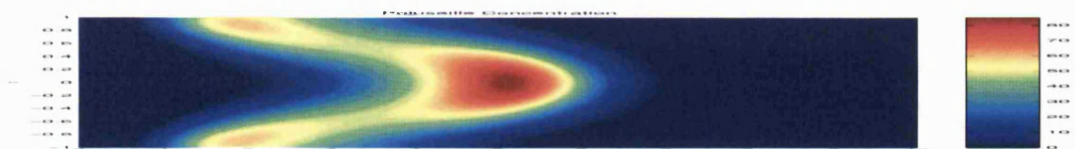
(c) Poiseuille Contour Profile After 6 Periods



(d) Poiseuille Contour Profile After 8 Periods



(e) Poiseuille Contour Profile After 10 Periods



(f) Poiseuille Contour Profile After 12 Periods

Figure 5-34: Poiseuille Contour Plots for Case C when $\hat{\psi}_w = -0.38$, $P_{er} = 1000$, $\alpha = 0.1$, $D_{ar} = 1$

5.3.5 Case D - No Trapping, Reflux

We solve the peristaltic dispersion model (5.1.5) for case D of peristaltic flow where there is mild reflux. We implement an amplitude of vibration $\alpha = 0.3$ and a flow rate $\hat{\psi}_w = -0.43$ and numerically solve for two cases of a slow and fast diffusing solute when the solute is initially placed one wavelength into the domain. This is so that we can observe the effects of reflux.

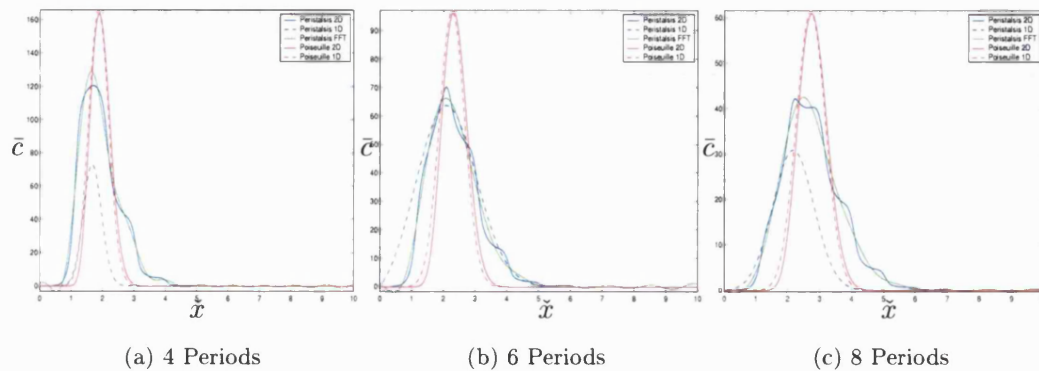


Figure 5-35: Mean Solute Concentration for the Peristaltic Dispersion Model and the Poiseuille Dispersion Model, and their 1D Dispersion Approximation with the the FFT of the Peristaltic Solution, for a Fast Diffusing Solute in Case D, $P_{er} = 100$, when $\alpha = 0.3$, $\hat{\psi}_w = -0.43$ and $D_{ar} = 1$.

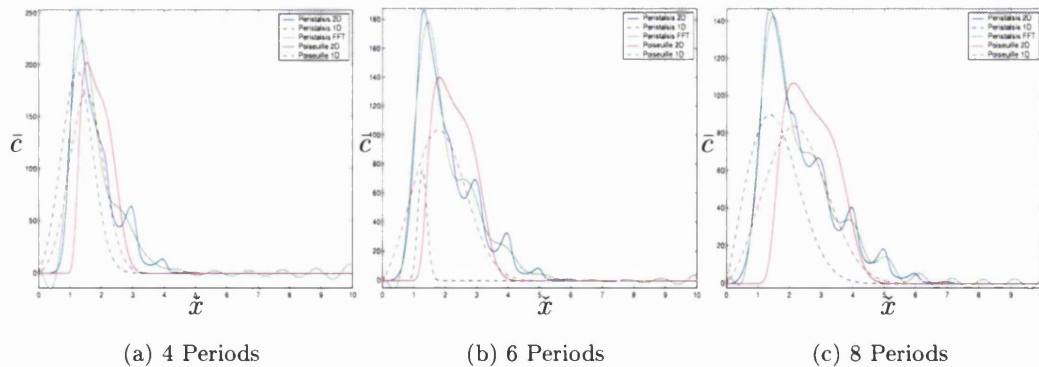


Figure 5-36: Mean Solute Concentration for the Peristaltic Dispersion Model and the Poiseuille Dispersion Model, and their 1D Dispersion Approximation with the the FFT of the Peristaltic Solution, for A Slow Diffusing Solute in Case D, $P_{er} = 1000$, when $\alpha = 0.3$, $\hat{\psi}_w = -0.43$ and $D_{ar} = 1$

In case D we have reflux and as such we expect some solute to make its way back towards the inlet. In Figure 5-35, the fast diffusing solute, we observe the effect of reflux in the peristaltic mean concentration \bar{c}_{pe} which has a larger effective dispersion when compared to that from Poiseuille flow \bar{c}_{po} , and a slower effective convection speed.

For the slow diffusing solute, see Figure 5-36, the effects of reflux are even more apparent as convection forces dominate. We observe the Poiseuille mean \bar{c}_{po} convects solute only forwards, there is negligible solute at $\tilde{x} < 1$. However, solute in the peristaltic flow slowly creeps backwards and suffers from an oscillatory component. As a result of this particular peristaltic flow, the noise free mean \bar{c}_{pe}^f , looks very dissimilar to the Poiseuille mean independent of the Péclet number.

What is most interesting is the greater absorption of solute from the peristaltic flow than observed in the Poiseuille flow. Case C only exhibited a mild increase in absorption from peristalsis. The only difference between the two cases is that case D exhibits reflux, which is responsible for solute absorption at $\tilde{x} < 1$, see Figure 5-38(a). However, the fact is that the amplitude of vibration in case D, $\alpha = 0.3$, when compared to case C, $\alpha = 0.1$, is responsible for the large increase in absorption as solute need travel less to move to the boundary (see §3.6.9 where we observed a greater radial mean \bar{q} for tracer particles as α increases). Solving for case D takes a long time and requires a large number of time steps. This is why we have only solved for 8 periods.

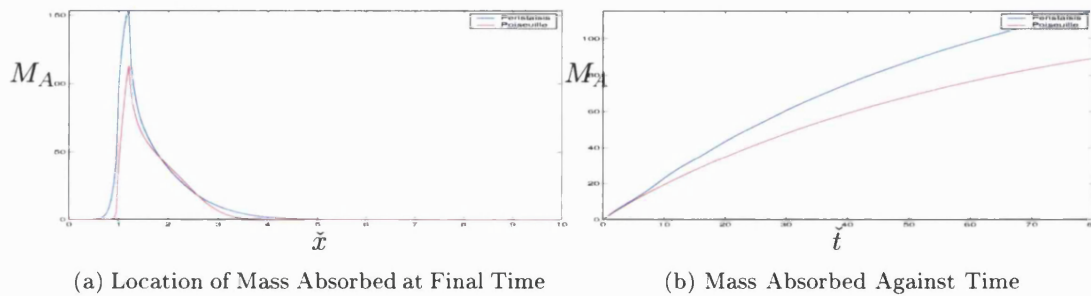


Figure 5-37: Mass Absorbed for the Peristaltic and Poiseuille Dispersion Models for a Fast Diffusing Solute, $P_{er} = 100$, when $\alpha = 0.3$, $\hat{\psi}_w = -0.43$ and $P_{er} = 1000$, $D_{ar} = 1$

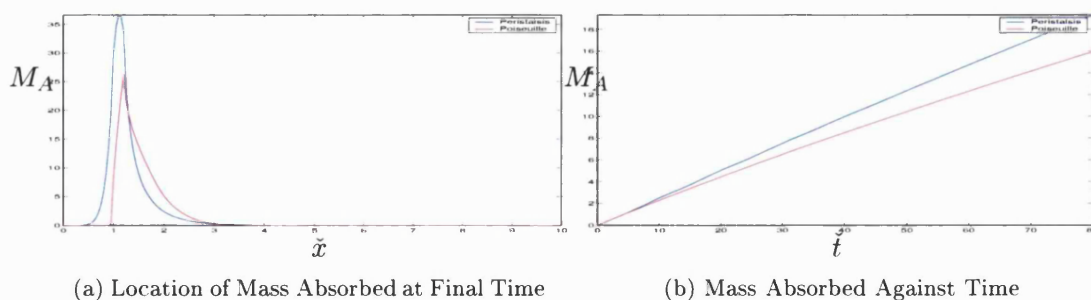
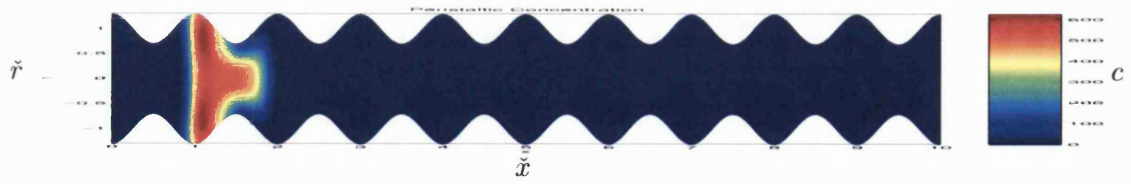
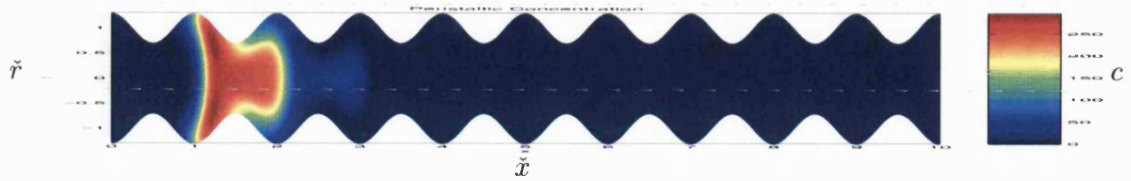


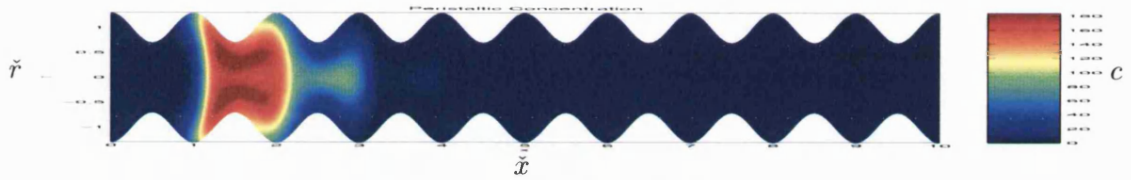
Figure 5-38: Mass Absorbed for the Peristaltic and Poiseuille Dispersion Models for a Slow Diffusing Solute, $P_{er} = 1000$, when $\alpha = 0.3$, $\hat{\psi}_w = -0.43$ and $P_{er} = 1000$, $D_{ar} = 1$



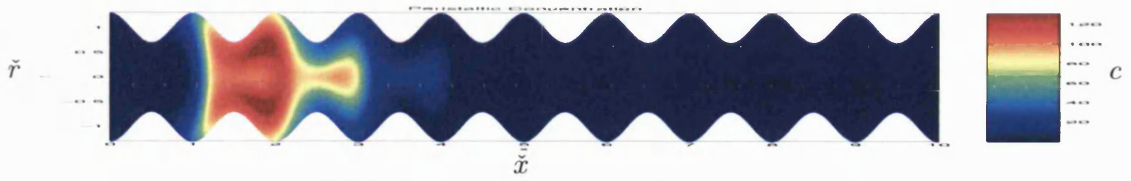
(a) Peristaltic Contour Profile After 1 Period



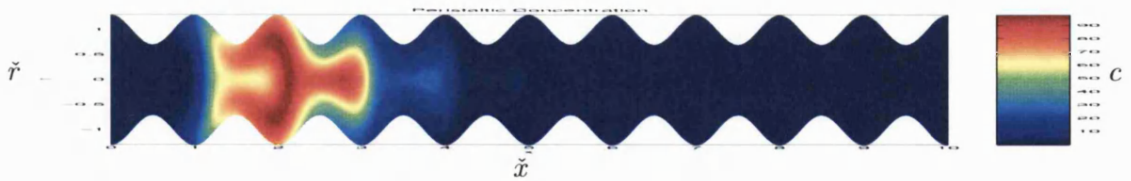
(b) Peristaltic Contour Profile After 2 Periods



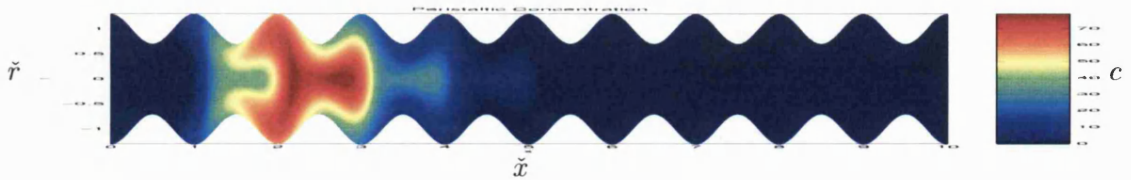
(c) Peristaltic Contour Profile After 3 Periods



(d) Peristaltic Contour Profile After 4 Periods

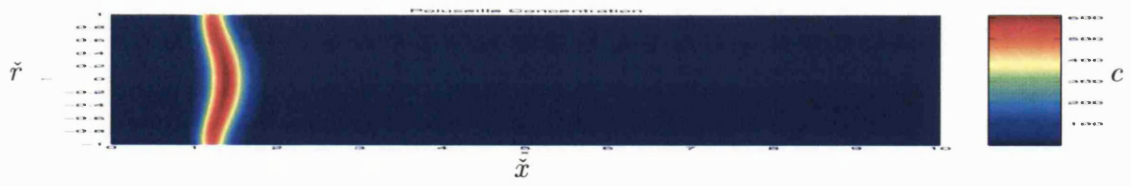


(e) Peristaltic Contour Profile After 5 Periods

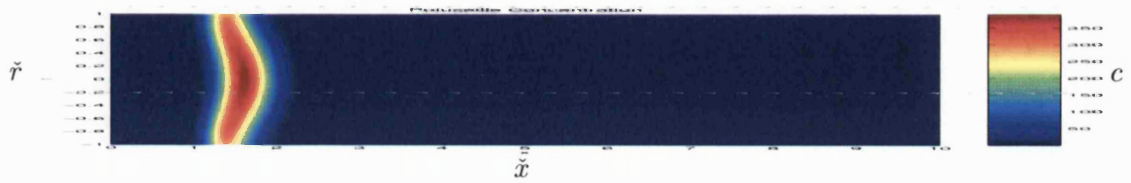


(f) Peristaltic Contour Profile After 6 Periods

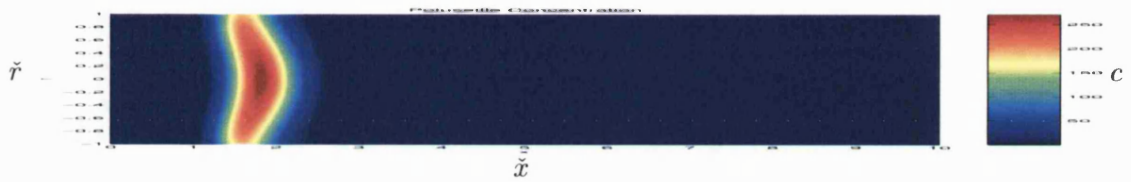
Figure 5-39: Peristaltic Contour Plots for Case D when $\hat{\psi}_w = -0.43$, $P_{er} = 100$, $\alpha = 0.3$, $D_{ar} = 1$



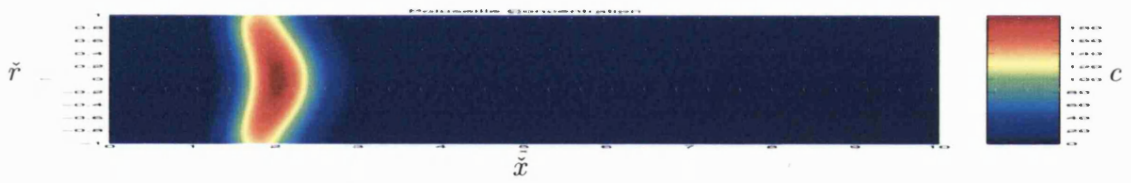
(a) Poiseuille Contour Profile After 1 Period



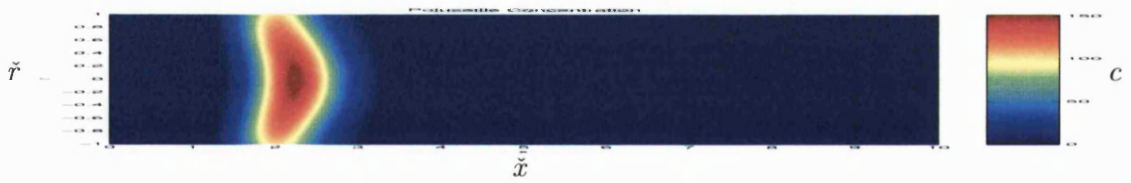
(b) Poiseuille Contour Profile After 2 Periods



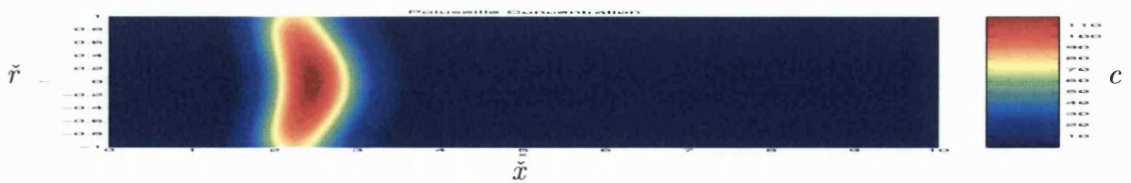
(c) Poiseuille Contour Profile After 3 Periods



(d) Poiseuille Contour Profile After 4 Periods

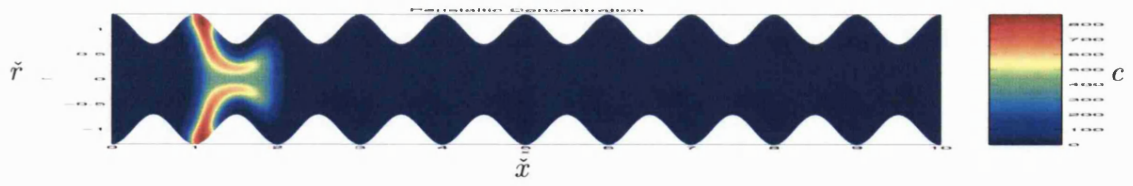


(e) Poiseuille Contour Profile After 5 Periods

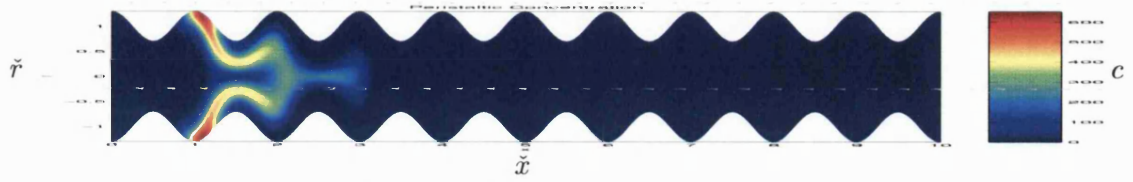


(f) Poiseuille Contour Profile After 6 Periods

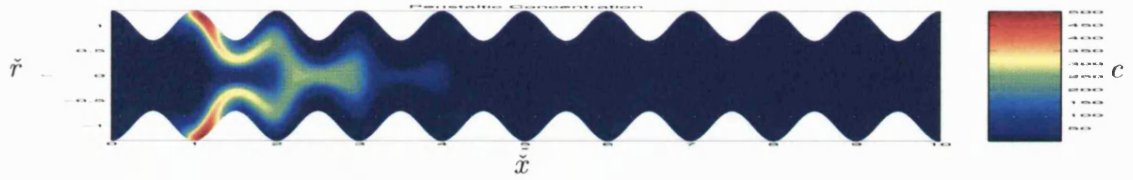
Figure 5-40: Poiseuille Contour Plots for Case D when $\hat{\psi}_w = -0.43$, $P_{er} = 100$, $\alpha = 0.3$, $D_{ar} = 1$



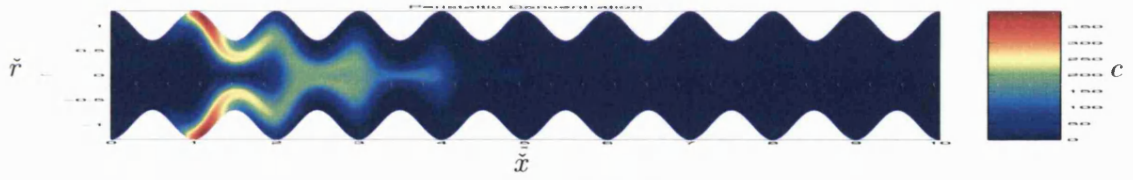
(a) Peristaltic Contour Profile After 1 Period



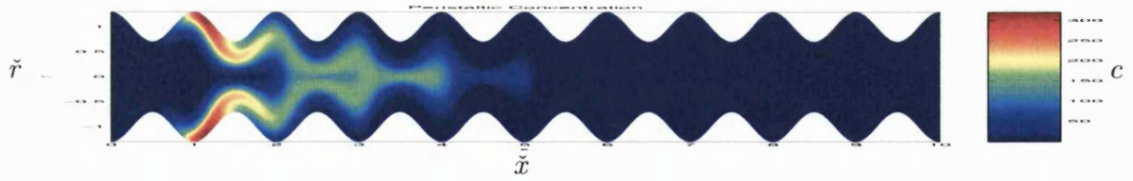
(b) Peristaltic Contour Profile After 2 Periods



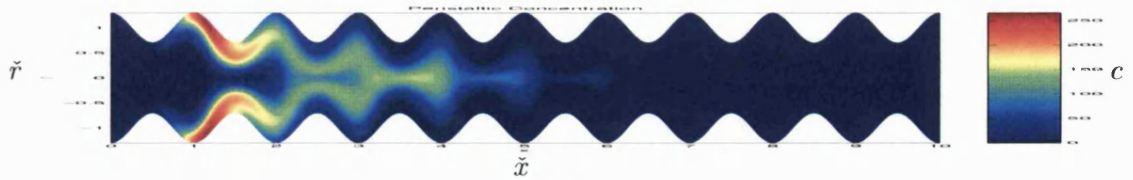
(c) Peristaltic Contour Profile After 3 Periods



(d) Peristaltic Contour Profile After 4 Periods

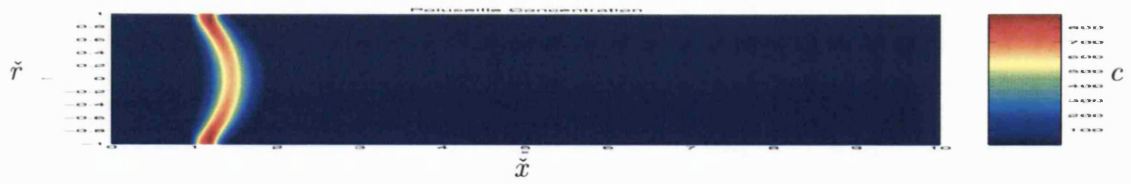


(e) Peristaltic Contour Profile After 5 Periods

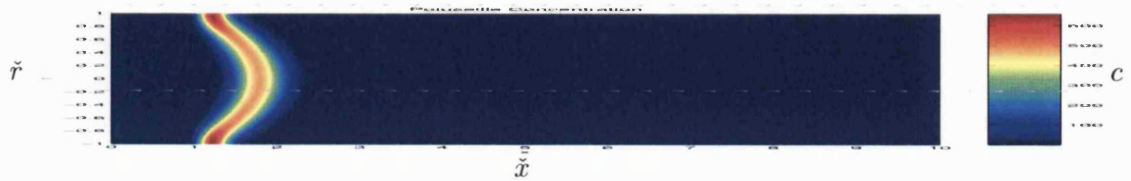


(f) Peristaltic Contour Profile After 6 Periods

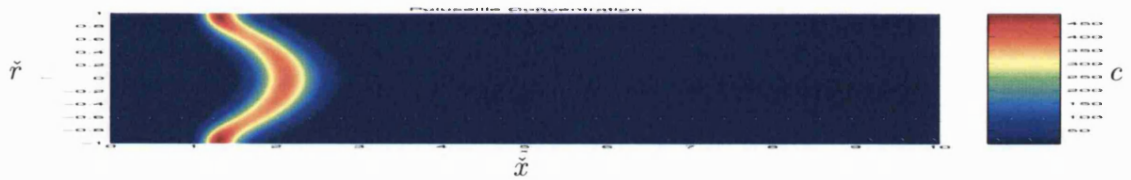
Figure 5-41: Peristaltic Contour Plots for Case D when $\hat{\psi}_w = -0.43$, $Pe_r = 1000$, $\alpha = 0.3$, $D_{ar} = 1$



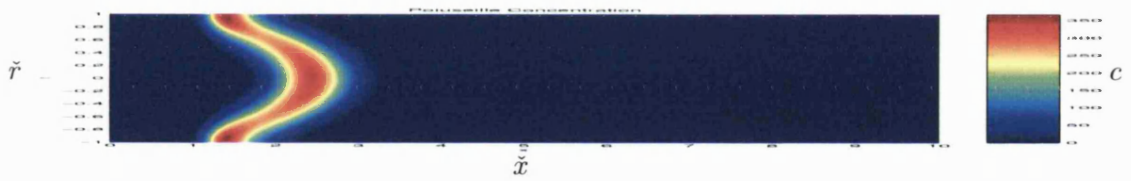
(a) Poiseuille Contour Profile After 1 Period



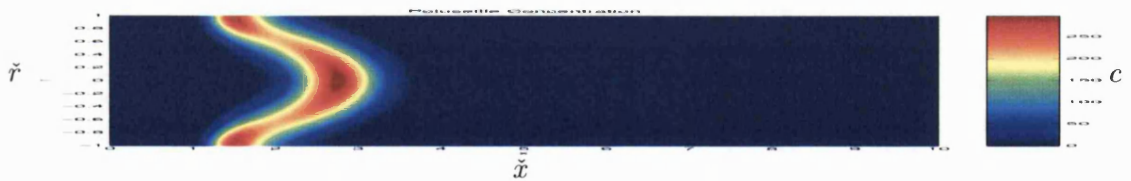
(b) Poiseuille Contour Profile After 2 Periods



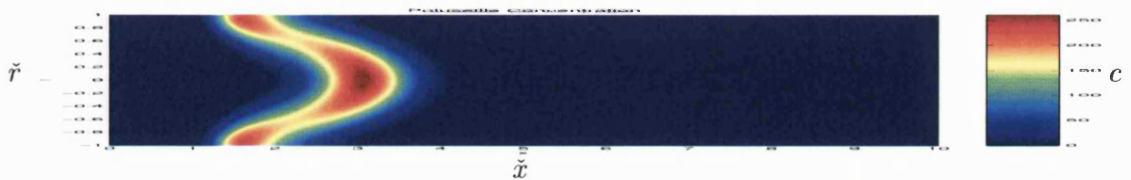
(c) Poiseuille Contour Profile After 3 Periods



(d) Poiseuille Contour Profile After 4 Periods



(e) Poiseuille Contour Profile After 5 Periods



(f) Poiseuille Contour Profile After 6 Periods

Figure 5-42: Poiseuille Contour Plots for Case D when $\hat{\psi}_w = -0.43$, $P_{er} = 1000$, $\alpha = 0.3$, $D_{ar} = 1$

5.3.6 Case E - Trapping and Reflux

We solve the peristaltic dispersion model (5.1.5) for case E of peristaltic flow where there is reflux and trapping, 24%. We implement an amplitude of vibration $\alpha = 0.4$ and a flow rate $\hat{\psi}_w = -0.3$ and numerically solve for two cases of a slow and fast diffusing solute when the solute is initially placed one wavelength into the domain, again to observe the effects of reflux.

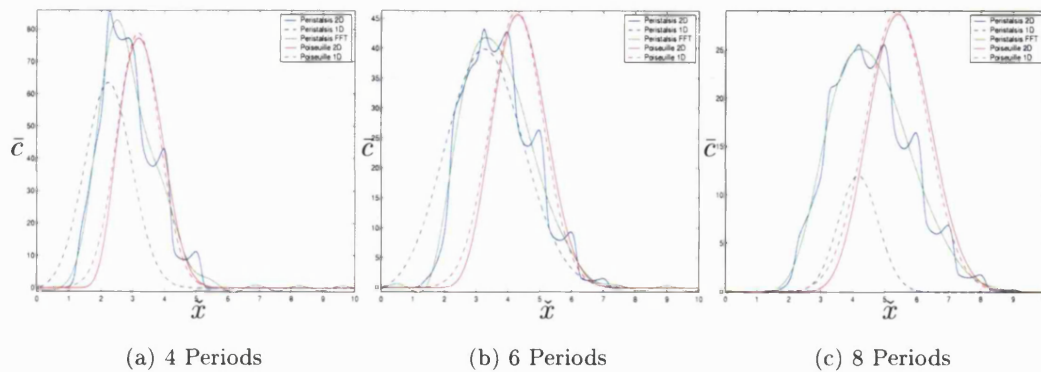


Figure 5-43: Mean Solute Concentration for the Peristaltic Dispersion Model and the Poiseuille Dispersion Model, and their 1D Dispersion Approximation with the the FFT of the Peristaltic Solution, for a Fast Diffusing Solute in Case E, $P_{er} = 100$, when $\alpha = 0.4$, $\hat{\psi}_w = -0.3$ and $D_{ar} = 1$.

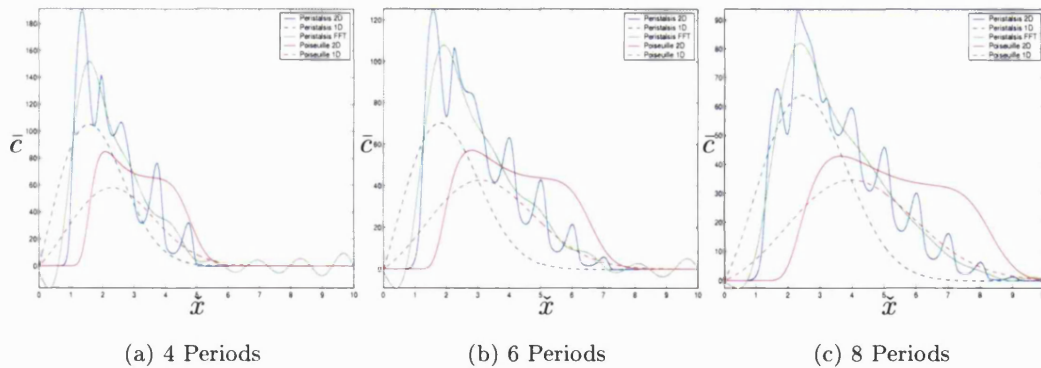


Figure 5-44: Mean Solute Concentration for the Peristaltic Dispersion Model and the Poiseuille Dispersion Model, and their 1D Dispersion Approximation with the the FFT of the Peristaltic Solution, for A Slow Diffusing Solute in Case E, $P_{er} = 1000$, when $\alpha = 0.4$, $\hat{\psi}_w = -0.3$ and $D_{ar} = 1$

Our results of case E are very interesting. The mean solute concentrations are very dissimilar. This case exhibits centreline trapping which we have shown is responsible for retarding solute motion. We observe the same effects here. Poiseuille flow is convecting solute faster than peristalsis, see Figures 5-43–5-44. This is perhaps even

more pronounced because reflux is also occurring. However, as the solute is able to diffuse it appears trapping dominates reflux and we observe very little solute convecting backwards to $\tilde{x} < 1$ (this is very different from the particle paths see Figure 3-17).

For the fast diffusing solute, the filter reveals a Gaussian like profile but the oscillations in the mean \bar{c}_{pe} have prevented the 1D dispersion algorithm from applying a best fit curve. When convection forces dominate, $P_{er} = 1000$, the shape of the mean solute concentrations are extremely different. Peristaltic flow in case E is not at all Poiseuille like. Again we observe more solute is absorbed in the peristaltic flow, see Figures 5-45, 5-46. We note the slightly larger concentration in \bar{c}_{pe} when compared to \bar{c}_{po} , this may be a result of numerical error where the solver needed more time steps to yield an accurate solution. However, the effects of peristalsis are non the less still observed.

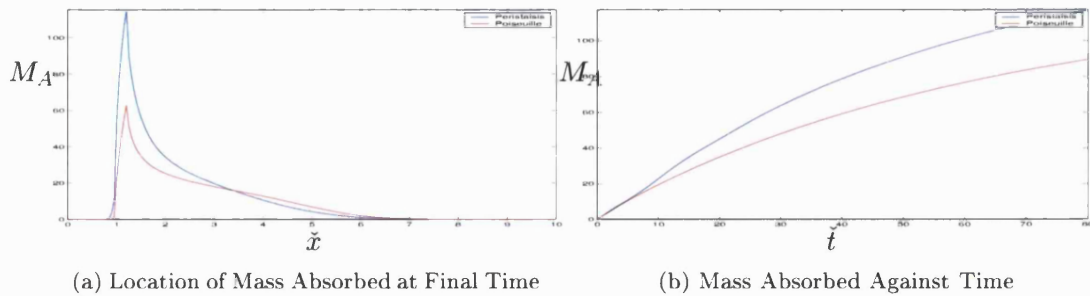


Figure 5-45: Mass Absorbed for the Peristaltic and Poiseuille Dispersion Models for a Fast Diffusing Solute, $P_{er} = 100$, when $\alpha = 0.4$, $\hat{\psi}_w = -0.3$ and $P_{er} = 1000$, $D_{ar} = 1$

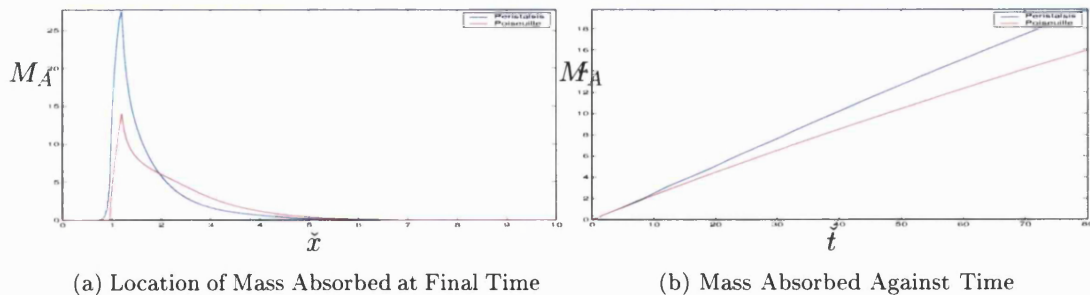
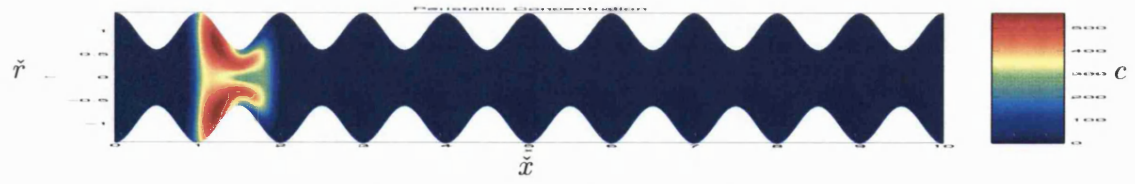
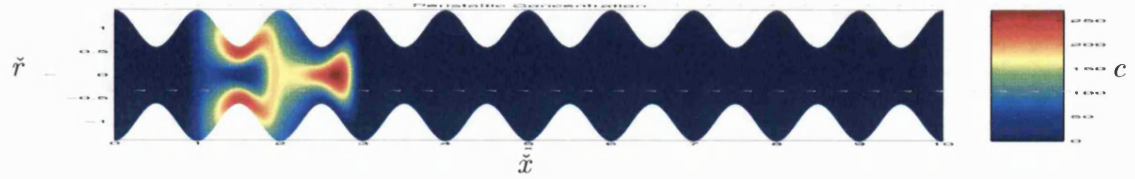


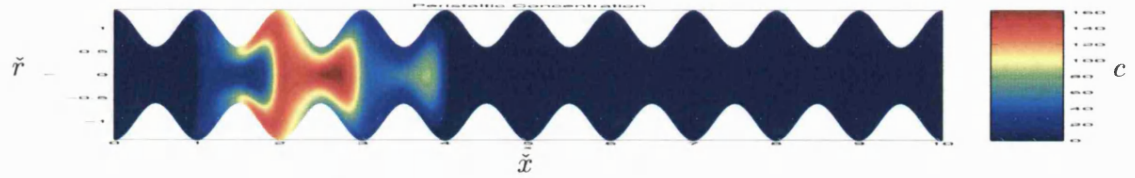
Figure 5-46: Mass Absorbed for the Peristaltic and Poiseuille Dispersion Models for a Slow Diffusing Solute, $P_{er} = 1000$, when $\alpha = 0.4$, $\hat{\psi}_w = -0.3$ and $P_{er} = 1000$, $D_{ar} = 1$



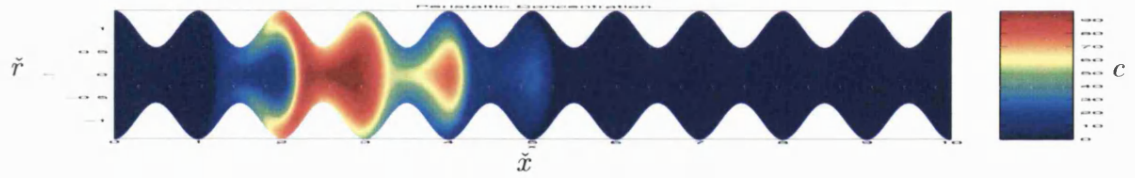
(a) Peristaltic Contour Profile After 1 Period



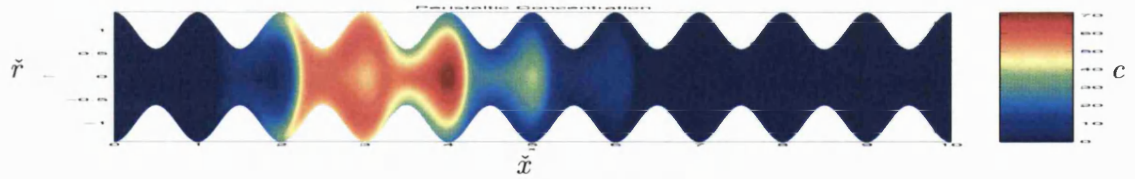
(b) Peristaltic Contour Profile After 2 Periods



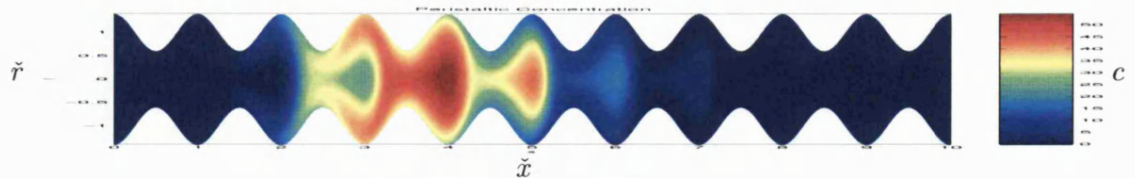
(c) Peristaltic Contour Profile After 3 Periods



(d) Peristaltic Contour Profile After 4 Periods

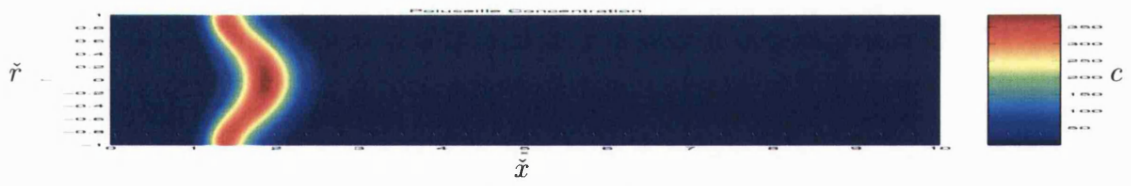


(e) Peristaltic Contour Profile After 5 Periods

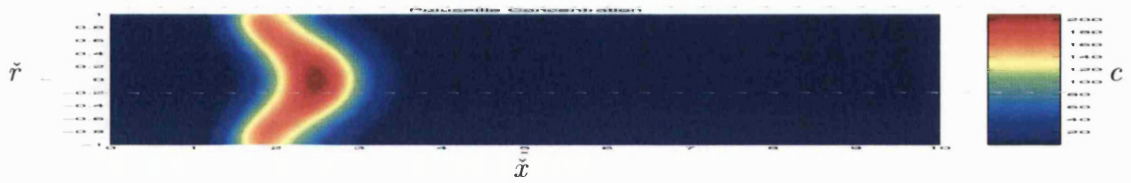


(f) Peristaltic Contour Profile After 6 Periods

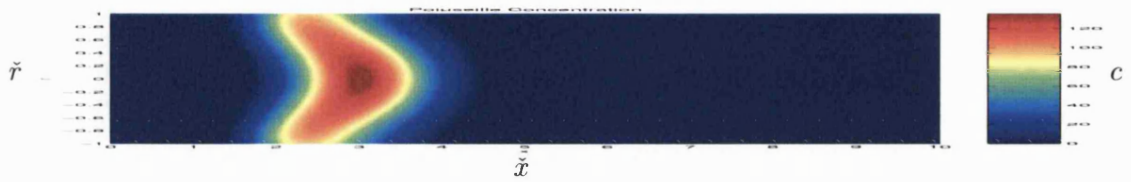
Figure 5-47: Peristaltic Contour Plots for Case E when $\hat{\psi}_w = -0.3$, $P_{er} = 100$, $\alpha = 0.4$, $D_{ar} = 1$



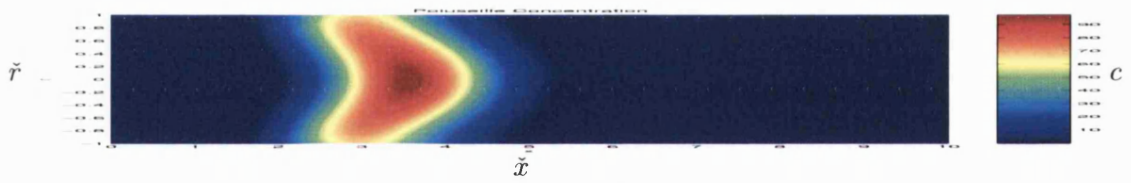
(a) Poiseuille Contour Profile After 1 Period



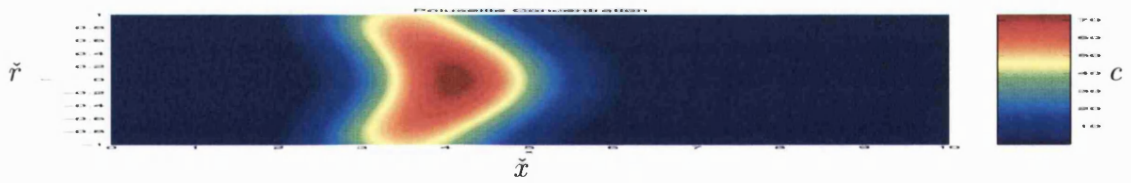
(b) Poiseuille Contour Profile After 2 Periods



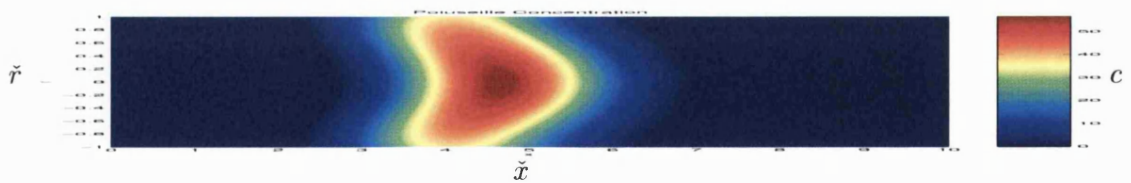
(c) Poiseuille Contour Profile After 3 Periods



(d) Poiseuille Contour Profile After 4 Periods

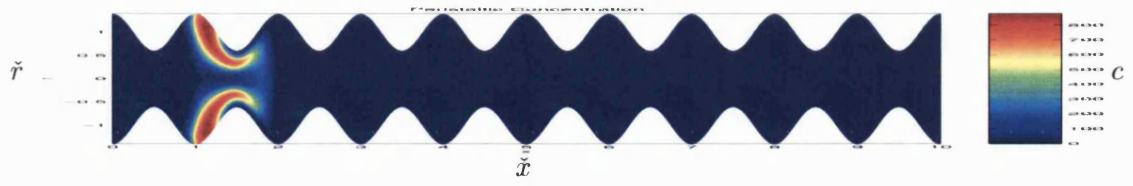


(e) Poiseuille Contour Profile After 5 Periods

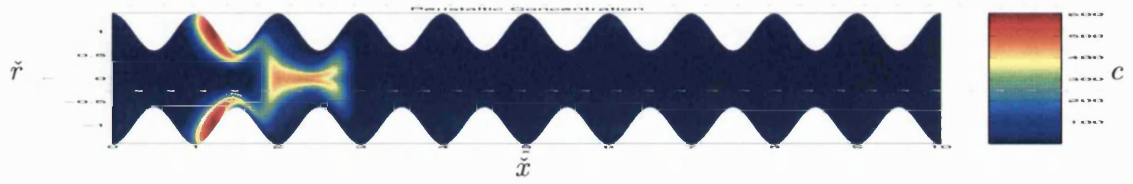


(f) Poiseuille Contour Profile After 6 Periods

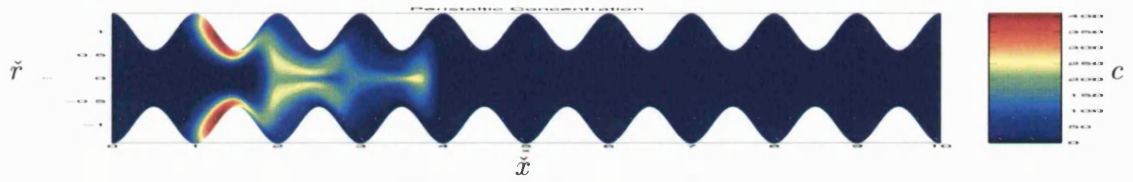
Figure 5-48: Poiseuille Contour Plots for Case E when $\hat{\psi}_w = -0.3$, $P_{er} = 100$, $\alpha = 0.4$, $D_{ar} = 1$



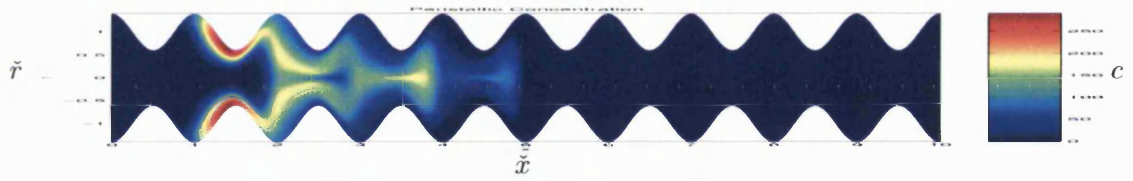
(a) Peristaltic Contour Profile After 1 Period



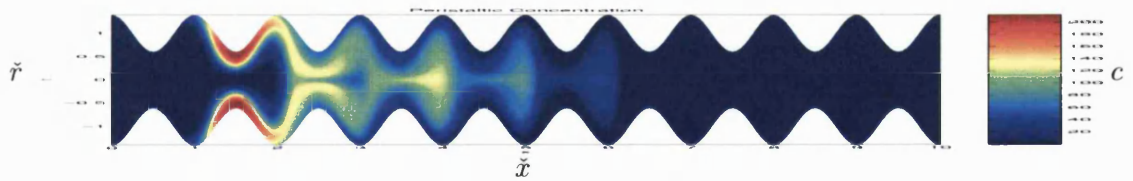
(b) Peristaltic Contour Profile After 2 Periods



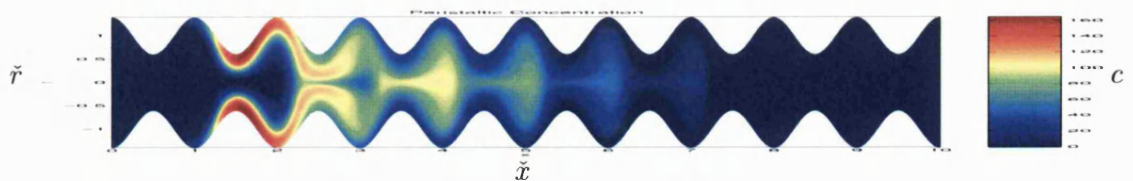
(c) Peristaltic Contour Profile After 3 Periods



(d) Peristaltic Contour Profile After 4 Periods

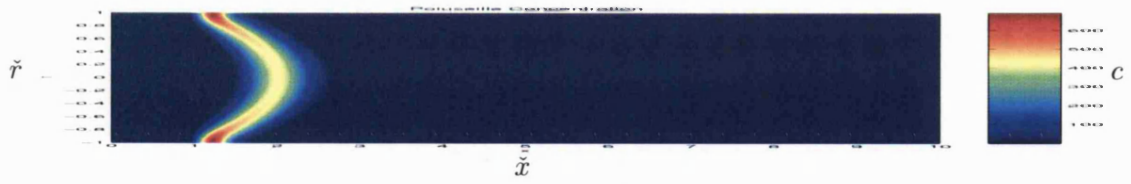


(e) Peristaltic Contour Profile After 5 Periods

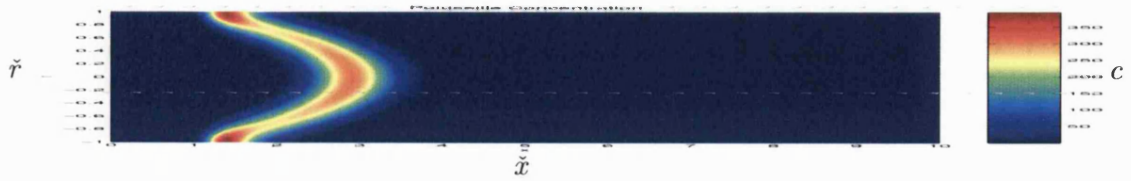


(f) Peristaltic Contour Profile After 6 Periods

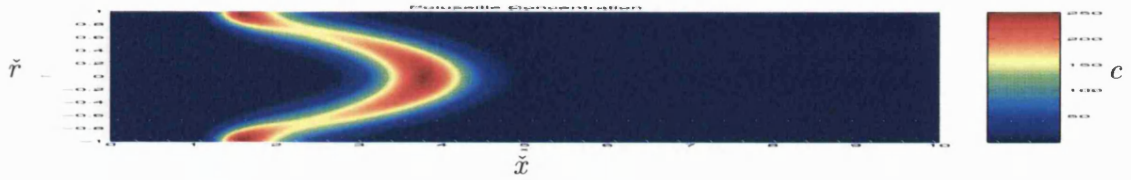
Figure 5-49: Peristaltic Contour Plots for Case E when $\hat{\psi}_w = -0.3$, $P_{er} = 1000$, $\alpha = 0.4$, $D_{ar} = 1$



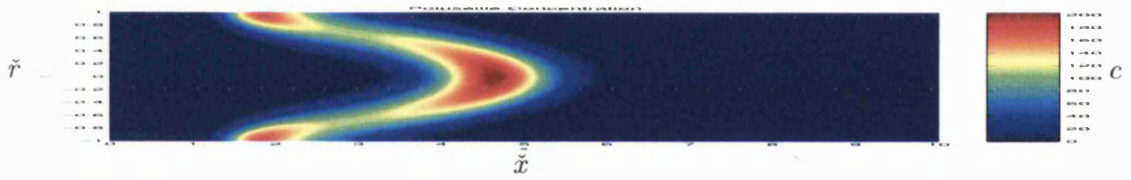
(a) Poiseuille Contour Profile After 1 Period



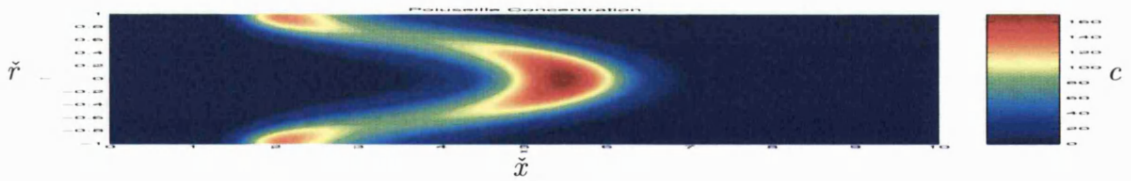
(b) Poiseuille Contour Profile After 2 Periods



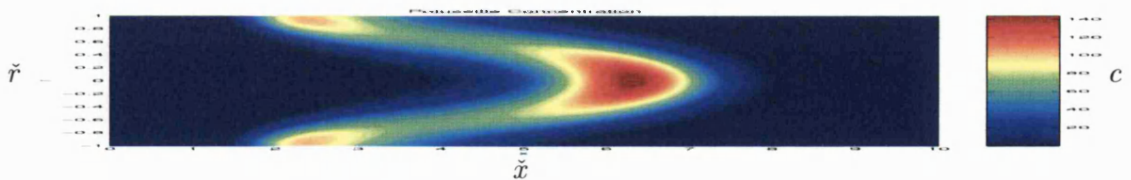
(c) Poiseuille Contour Profile After 3 Periods



(d) Poiseuille Contour Profile After 4 Periods



(e) Poiseuille Contour Profile After 5 Periods



(f) Poiseuille Contour Profile After 6 Periods

Figure 5-50: Poiseuille Contour Plots for Case E when $\hat{\psi}_w = -0.3$, $P_{er} = 1000$, $\alpha = 0.4$, $D_{ar} = 1$

5.4 Discussion of the Behaviour of Solute Motion under Peristaltic Flow with Application to the Intestine

The effects of peristalsis on solute motion have been studied and compared to that of Poiseuille flow and the effects are fascinating. Our first observation is the oscillations on the peristalsis mean solute profile \bar{c}_{pe} . These oscillations are dampened for faster diffusing solutes (low Péclet number) as the radial inhomogeneities are removed by faster radial motion from diffusion. We also observe the effect of the Péclet number on the mass of solute in the domain. The smaller the diffusion the more solute is convected out of the tube from the fast streamlines at the centre of the tube. This is not the case for a fast diffusing solute which remains in the tube for longer as the solute samples fast and slow streamlines and moves as a whole with an effective velocity less than that of the fast moving streamlines at the centreline.

In general, for small Péclet number the mean solute concentration for peristaltic model and the Poiseuille model are (i) approximately the same, $\bar{c}_{pe} \approx \bar{c}_{po}$, and (ii) have a Gaussian profile that is effectively captured by the 1D dispersion model algorithm. This is not the case for larger Péclet number where both models do not take Gaussian shape. However, the mean solute concentrations can be shown to be similar for specific cases of peristaltic flow.

When trapping is negligible, as seen in case A for high flow rates (as predicted by our analysis in the Peristalsis Chapter 3), then

$$\bar{c}_{pe} \approx \bar{c}_{po} + \text{oscillatory term},$$

where the oscillatory term can be removed using a low pass filter (see Appendix §E.2) so that

$$\bar{c}_{pe}^f \approx \bar{c}_{po}.$$

When trapping is prominent, the noise free solution of the peristaltic mean solute concentration does not look like that from Poiseuille flow

$$\bar{c}_{pe} \neq \bar{c}_{po},$$

as trapping has greatly distorted the flow of the solute.

We observe that centreline trapping is responsible for retarding the overall motion of the solute when compared to Poiseuille flow and appears to convect solute motion backwards into circulating regions behind the leading wave. We believe that solute in trapping is circulated around and is brought closer to the slow streamlines surrounding the bolus. At this point the solute diffuses into the slower streamlines and it eventually diffuses back into the fast streamlines at a later time where it enters a circulating region behind the leading wave. Not only does peristalsis aid absorption by bringing solute

closer to the membrane, but also in retarding the advance of the solute, keeping solute in the tube for longer when compared to Poiseuille flow.

In the intestine, enzymes are released at the membrane to break down the chyme for absorption [75]. Hence peristalsis is an efficient means to (i) mix the enzymes with the chyme, (ii) bring solute closer to the membrane to be absorbed and (iii) retard the advance of the solute to allow the enzymes sufficient time to work and then bring solute to the wall where absorption is site specific.

5.5 Weak Peristaltic Forces: A Superimposed Oscillatory Profile in the Mean Solute Concentration

It has been shown that oscillations in the mean solute profile are a byproduct of the peristaltic flow. Solute is convected by either i) trapping or ii) parabolic flow. The former is a key feature of peristalsis suggesting that the cross-sectional average is dominated by convection through trapping and peristalsis presents itself at leading order in the mean concentration $\bar{c} = \bar{c}_{pe}$. However, in copumping where there are regions of small trapping from high flow rates, flow is dominated by parabolic velocities seen in laminar flow and less by the effects of peristalsis (Lemma 3.6). Hence we hypothesised the peristaltic mean solute concentration profile is the mean solute concentration profile from Poiseuille flow plus some contribution from peristalsis.

Let us consider the peristaltic velocities \hat{u}, \hat{v} . For small amplitude of vibration we can simplify the reciprocal of the boundary function \hat{f}^{-n} for small n , so that

$$\frac{1}{\hat{f}^n(\hat{x})} = \frac{1}{(1 + \alpha \cos(2\pi\hat{x}))^n} \approx 1 - n\alpha \cos(2\pi\hat{x}) + O(\alpha^2)$$

using a binomial series. Hence we can reduce the peristaltic velocities \hat{u}, \hat{v} to Poiseuille flow at leading order plus a peristaltic term at $O(\alpha)$:

$$\begin{aligned} \hat{u} &= 4A(\hat{x})\hat{r}^2 + 2B(\hat{x}) \\ &= 4\left(-\frac{\hat{\psi}_w}{\hat{f}^4} - \frac{1}{2\hat{f}^2}\right)\hat{r}^2 + 2\left(\frac{2\hat{\psi}_w}{\hat{f}^2} + \frac{1}{2}\right) \\ &\approx 4\left(-\hat{\psi}_w(1 - 4\alpha \cos(2\pi\hat{x})) - \frac{1}{2}(1 - 2\alpha \cos(2\pi\hat{x}))\right)\hat{r}^2 + 2\left(2\hat{\psi}_w(1 - 2\alpha \cos(2\pi\hat{x})) + \frac{1}{2}\right) \\ &\approx \left(4\left(-\hat{\psi}_w - \frac{1}{2}\right)\hat{r}^2 + (4\hat{\psi}_w + 1)\right) + \alpha \cos(2\pi\hat{x})\left(4(4\hat{\psi}_w + 1)\hat{r}^2 - 8\right) \\ &\approx \hat{u}_{po}(\hat{r}) + \alpha \cos(2\pi\hat{x})\hat{u}_{pe}(\hat{r}), \end{aligned} \tag{5.5.1}$$

$$\begin{aligned}
\hat{v} &= -A'(\hat{x})\hat{r}^3 - B'(\hat{x})\hat{r} \\
&\approx -\left(\frac{4\hat{\psi}_w\hat{f}'}{\hat{f}^5} + \frac{\hat{f}'}{\hat{f}^3}\right)\hat{r}^3 + \left(\frac{4\hat{\psi}_w\hat{f}'}{\hat{f}^3}\right)\hat{r} \\
&\approx \alpha \sin(2\pi\hat{x}) \left(2\pi \left(-\left(4\hat{\psi}_w - 1\right)\hat{r}^3 + 4\hat{\psi}_w\hat{r}\right)\right) \\
&\approx \alpha \sin(2\pi\hat{x})\hat{v}_{\text{pe}}(\hat{r}) + O(\alpha^2).
\end{aligned}$$

Hence, the 2D ‘simplified peristaltic’ dispersion model is given by

$$c_{\tilde{t}+\epsilon} \left(\check{u}_{\text{po}} + \alpha \cos(2\pi\hat{x})\hat{u}_{\text{pe}}(\hat{r}) \right) c_{\tilde{x}+\epsilon} \left(\alpha \sin(2\pi\hat{x})\hat{v}_{\text{pe}}(\hat{r}) \right) c_{\tilde{r}} = \frac{1}{P_{eh}} \left(\epsilon^2 c_{\tilde{x}\tilde{x}} + c_{\tilde{r}\tilde{r}} + \frac{1}{\tilde{r}} c_{\tilde{r}} \right),$$

up to $O(\alpha^2)$ for small peristaltic amplitude of vibration α . The peristaltic dispersion model has been simplified and now neglects the effects of trapping from the simplification of the peristaltic velocities. When $\alpha = 0$, it is quite clear that this problem reduces to the 2D Poiseuille dispersion model.

This model is similar to the spreading of heat or soluble surfactant along a thin liquid film seen in Jensen et al. [43]. In this paper, Jensen et al. applied asymptotic analysis to reduce a 2D channel dispersion model in a domain bounded by a function $h(x, t)$ like ours and showed the concentration profile can be written in terms of a mean solute concentration plus a small fluctuation term. In our case the solute concentration takes the form

$$c(\tilde{x}, \tilde{r}, \tilde{t}) = \bar{c}_{\text{po}}(\tilde{x}, \tilde{t}) + \alpha c_1(\tilde{x}, \tilde{r}, \tilde{t}),$$

where the cross sectional average of the fluctuation is zero

$$\bar{c}_1 = \frac{2}{\tilde{f}^2(\tilde{x}, \tilde{t})} \int_0^{\tilde{f}^2(\tilde{x}, \tilde{t})} \check{c}_1(\tilde{x}, \tilde{r}, \tilde{t}) \tilde{r} d\tilde{r} = 0.$$

Ideally we would like to use the analysis from Jensen et al. to find the asymptotic form for the peristaltic model. This is beyond the scope of this thesis and would be a useful subject for further investigation.

5.6 Comparing Peristaltic Dispersion with Poiseuille Flow with Enhanced Diffusion

In the previous section we have shown that for high flow rates peristalsis appears as an oscillatory component that can be removed by applying a high pass filter to obtain a cleaner mean solute concentration profile similar to that of the Poiseuille dispersion model. In this section we test the validity of the claim by Stoll et al. that peristaltic motion of a solute can be effectively represented by Poiseuille flow plus some enhanced

diffusion.

We take an arbitrary case where peristalsis exhibits circulating regions much like the recirculating regions suggested by Stoll et al. [73] in his derivation of the enhanced diffusion formula (§4.4.5). We consider a slow diffusing solute $P_{eh} = 1000$ in peristaltic flow case B where there is centreline trapping, the flow conditions of which given by $\alpha = 0.2, \hat{\psi}_w = -0.2$. We solve the peristaltic dispersion model for the mean solute concentration and clear up the noise to obtain \bar{c}_{pe}^f . We then solve the Poiseuille dispersion model for $P_{eh} = 1000$ and subsequently for $P_{eh} = 100, 10$ to represent increased diffusion. We obtain the following solution.

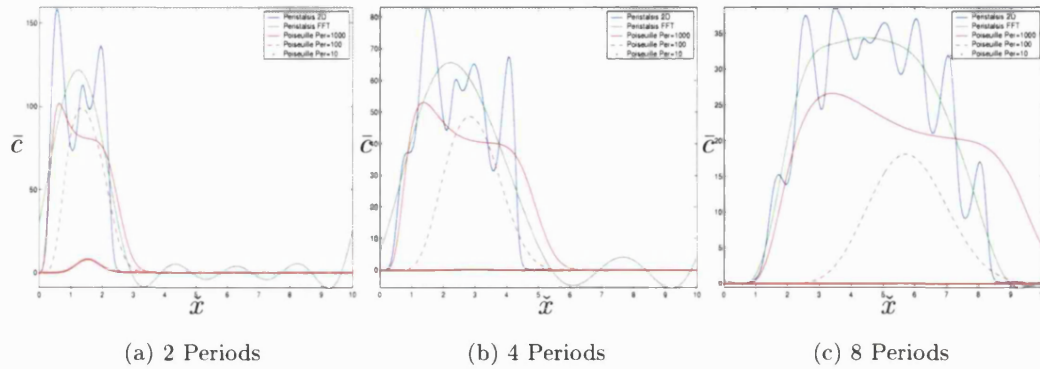


Figure 5-51: The Mean Solute Concentration for the Peristaltic Dispersion Model and the Poiseuille Dispersion Model with Enhanced Diffusion.

It has become quite clear that from increasing diffusion, we have only helped to enhance axial diffusion and make the Poiseuille solute profile take Gaussian profile which looks nothing like the cleaner peristaltic profile. Tests have shown that this is true for other cases of peristaltic flow. Peristaltic flow is just too complex to model it by only enhanced diffusion. The effects of trapping slow the effective convection of the mean concentration but enhanced diffusion acts to increase it. In most examples we have shown peristalsis increases absorption but the amounts are quite similar. In the next section we consider the effects of peristalsis on a more realistic radially nonuniform initial condition.

5.6.1 Enhanced Absorption by Peristalsis

In all our examples of the 2D dispersion models we have placed an initial amount of solute at the entrance of the domain, that occupies a very thin region. In reality the initial conditions are not so uniform. We experiment with the case of a radially nonuniform slug initial condition modelled by

$$\check{c}(\check{x}, \check{r}, 0) = 1000 (H(\check{x}) - H(\check{x} - l)) \left(H(\check{r}) - H\left(\frac{\check{r}(\check{x}, 0)}{2}\right) \right).$$

This initial condition is a step function in the radial direction of the original initial condition. It represents a solute placed at the centre of entrance to the tube. As a result we obtain very different mean solute concentration profiles for both the peristalsis and Poiseuille model when for the slow diffusing drug $P_{eh} = 1000$. We observe the effects of

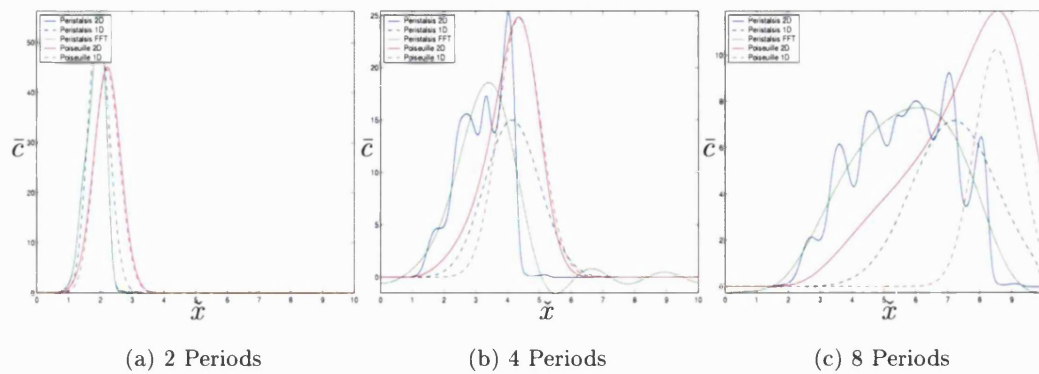


Figure 5-52: Solute Mean Concentration for the Peristaltic and Poiseuille Diffusion Model for a Radially Nonuniform Initial Condition.

retardation on the peristalsis mean solute concentration (see also Figures 5-55, 5-54). We now look at the amount of mass absorbed and its location.

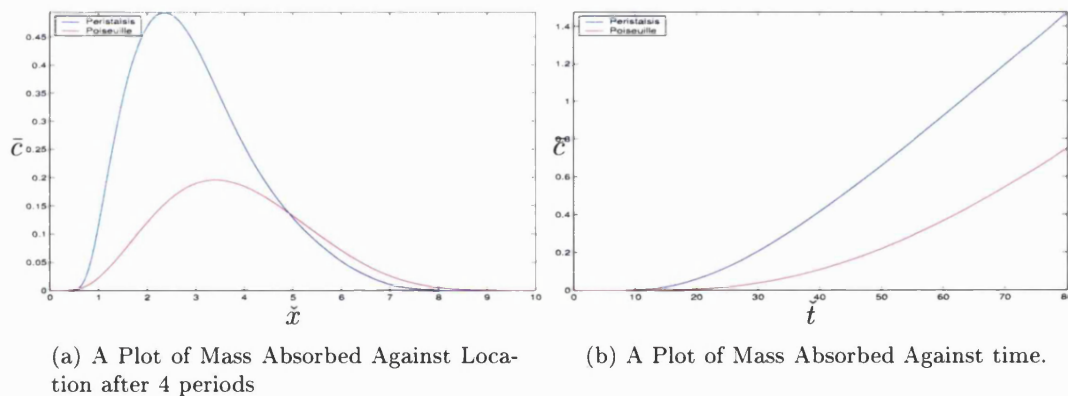


Figure 5-53: Mass Absorbed for the Peristaltic and Poiseuille Diffusion Model for a Radially Nonuniform Initial Condition.

In Figure (5-53) it is quite obvious more mass has been absorbed in the peristaltic case, and much of it is located towards the entrance of the tube as opposed to the Poiseuille model. This shows that trapping enhances mixing, increases absorption and slows solute flow down. Hence more solute is absorbed at the entrance to the tube corresponding our initial findings.

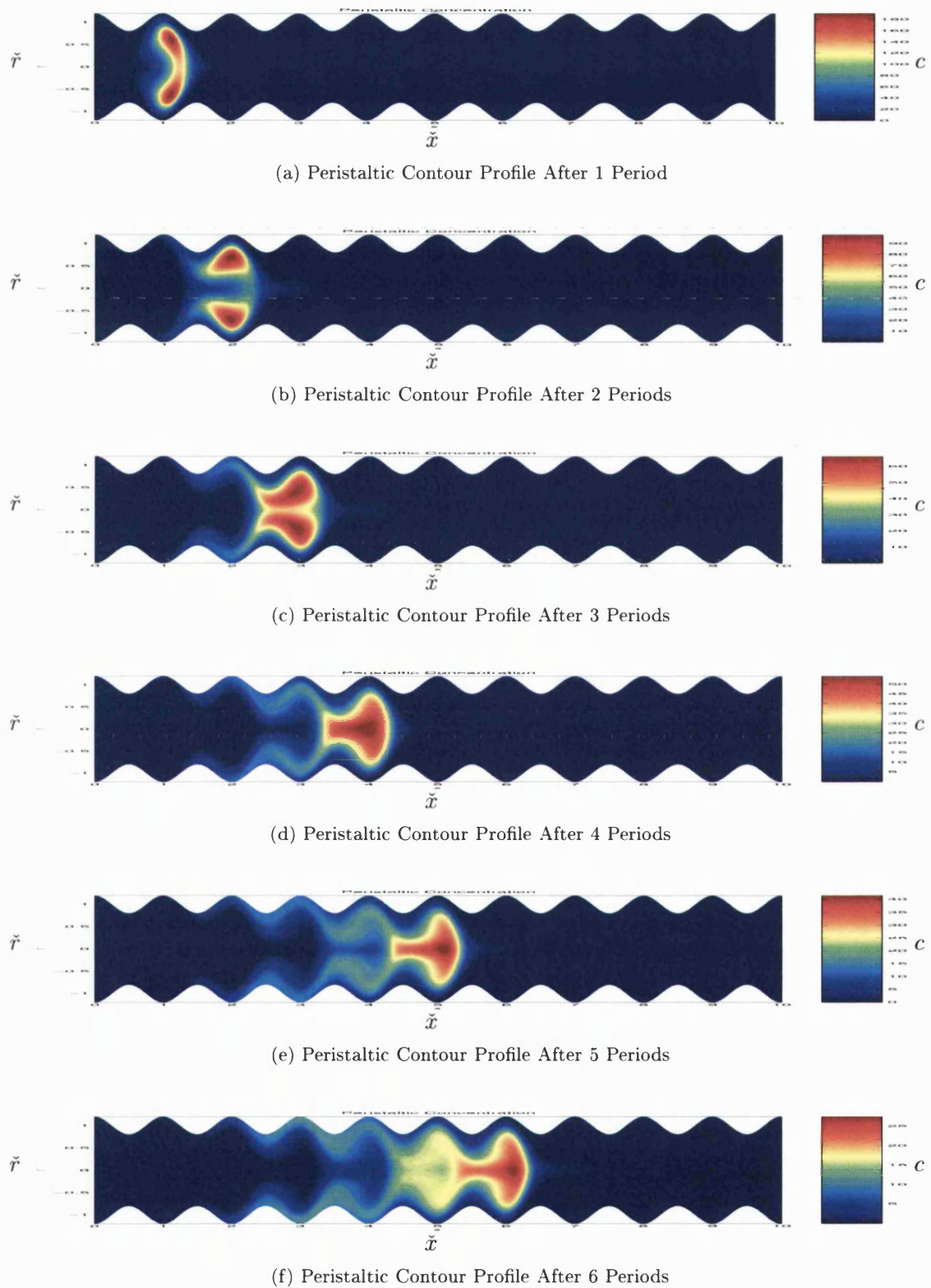
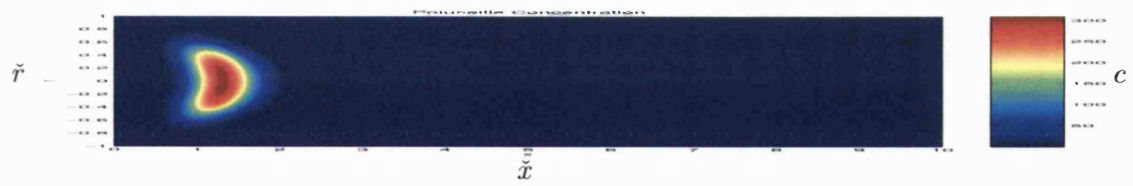
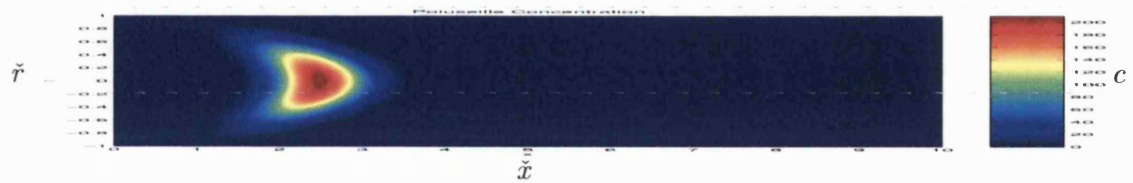


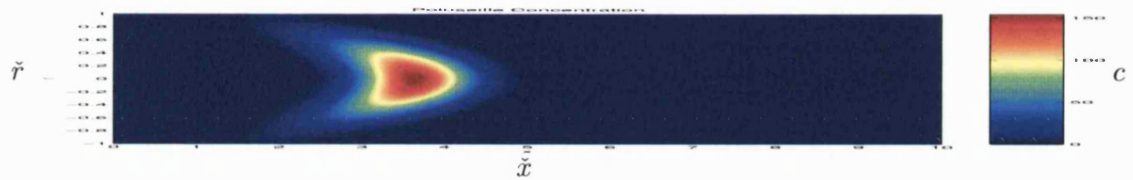
Figure 5-54: Peristaltic Contour Plots for Radially Non-Uniform Initial Condition for Case B when $\hat{\psi}_w = -0.2$, $P_{er} = 100$, $\alpha = 0.2$, $D_{ar} = 1$



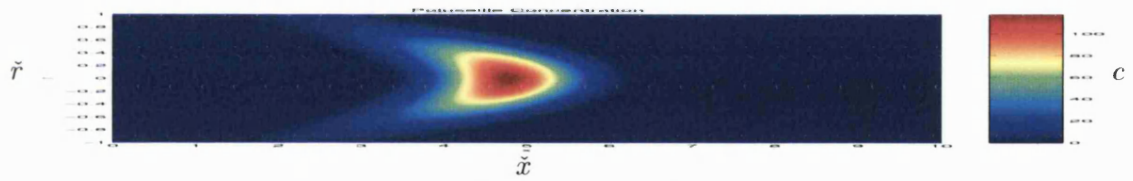
(a) Poiseuille Contour Profile After 1 Period



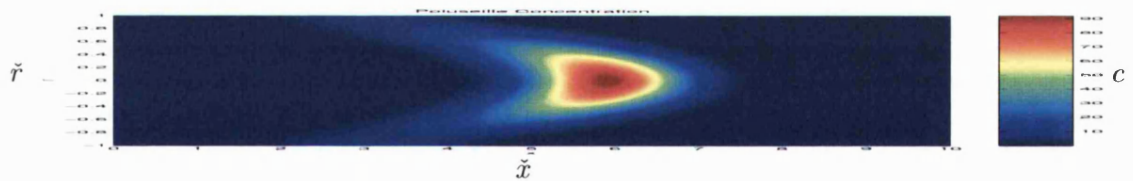
(b) Poiseuille Contour Profile After 2 Periods



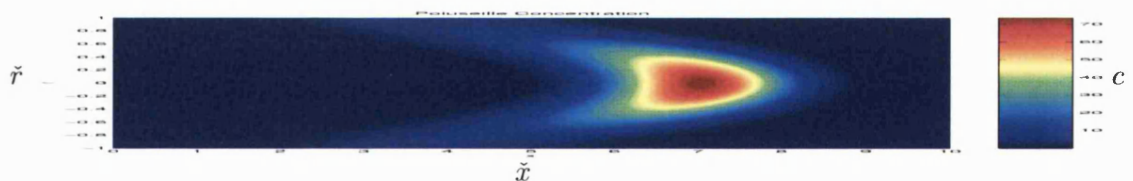
(c) Poiseuille Contour Profile After 3 Periods



(d) Poiseuille Contour Profile After 4 Periods



(e) Poiseuille Contour Profile After 5 Periods



(f) Poiseuille Contour Profile After 6 Periods

Figure 5-55: Poiseuille Contour Plots for Radially Non-Uniform Initial Condition for Case B when $\hat{\psi}_w = -0.2$, $P_{er} = 100$, $\alpha = 0.2$, $D_{ar} = 1$

5.7 Summary

In this Chapter we have applied the derived semi-analytic peristaltic velocities to leading order into a 2D dispersion model, to model solute in a tube with flow induced by the pressure gradient and the peristaltic waves. The complex nature of this model meant we had to solve the solute concentration profile numerically. Unlike the Poiseuille model the peristaltic model has a number of restrictions imposed by the peristaltic velocities, (i) the wave curvature must be small $\epsilon < 0.2$ for the leading order peristaltic velocities to be a suitable representation of the flow, (ii) the domain size must be an integral number of wavelengths and (iii) peristalsis induces negative velocities which means the numerical scheme must be altered (see numerics Chapter). As a result of computing time, memory and the stiffness of the model we can only solve the peristaltic dispersion model for (i) small amplitude ratios $\alpha < 0.5$ and (ii) a limited number of wavelengths $n = 10$ to optimise mesh size.

We solved the peristaltic dispersion model and the Poiseuille dispersion model simultaneously for the same flow and solute parameters for the different types of peristaltic flow. We showed for slow diffusing therapeutics the peristaltic convective forces dominate and the mean solute concentration exhibits an oscillatory component. These oscillations die down for faster diffusing solutes and $\bar{c}_{pe} \approx \bar{c}_{po}$ tend to a Gaussian profile, which can be modelled numerically by a 1D dispersion model.

When there is little trapping we show that the peristaltic mean concentration is approximately that of the Poiseuille model plus some oscillatory component which can be removed by a high pass filter to show that $\bar{c}_{pe}^f \approx \bar{c}_{po}$. Some analysis was applied by Jensen et al. [43] on a similar problem to show thin film motion exhibited an oscillatory component. We derived a simpler peristaltic model on which the analysis of Jensen et al. could be applied to derive the oscillatory component explicitly for future work. However, when trapping is significant it is not possible to filter the \bar{c}_{pe} for \bar{c}_{po} as trapping alters the flow so that fluid motion is no longer mostly Poiseuille-like.

We showed that for centreline trapping the flow of the solute is retarded and it ‘appears’ that solute moves into circulating regions behind the leading wave. This is responsible for (i) greater absorption as solute is left in the tube for longer and moved closer to the boundary and also for (ii) the large amount of absorption occurring earlier in the tube not seen in the Poiseuille model.

We tested the theory from Stoll et al. that peristalsis could be modelled by the Poiseuille dispersion model plus some enhanced diffusion. We compared the mean solute concentration of the noise free peristaltic dispersion model, \bar{c}_{pe}^f with the mean concentration from the Poiseuille model for decreasing Péclet number to simulate enhanced diffusion \bar{c}_{po}^e . Observations of the effects of enhanced diffusion were (i) the mean solute concentration \bar{c}_{po} looked increasingly like a Gaussian profile which \bar{c}_{pe}^f does not and (ii) the mean speed of \bar{c}_{po} was increased, convecting solute further down the tube

than seen in \bar{c}_{pe}^f .

Finally for a radially varying initial condition, we showed more clearly that more solute is absorbed in a peristaltic flow than in a Poiseuille flow as trapping convects solute to the boundary and that more absorption occurs in peristalsis at the entrance to the tube than in the Poiseuille model.

Essentially peristalsis is an efficient means to mix the enzymes from the membrane and enhance absorption. The effects of which are too complicated to be modelled simply by an averaged formula.

Chapter 6

Numerical Methods for the Fluid Flow and for the Dispersion Models

In this Chapter we set up the numerical methods used to solve the 1D and 2D dispersion models derived in the previous Chapters. We discretise these differential algebraic equations in space using finite difference operators on a non-uniform mesh and apply the method of lines to solve the resulting system of odes $M(c)c' = g(t, x, c, \dots)$. This uses the stiff solvers *ode15s* in Matlab or *dassl* in Fortran. In order to compare the full 2D Poiseuille dispersion model (4.4.2) and its 1D asymptotic equation (4.4.9) it is very important that the numerical results we obtain are accurate. Hence, we test the general accuracy of our finite difference numerical schemes for similar equations with known solutions.

For the 1D therapeutic model we try to reduce numerical dispersion that arises from applying upwinding on the convection term. We compare the known solution of the model with the numerical solution when applying the following schemes a) standard upwinding, b) diffusion transformation and c) a moving mesh pde. We show that the diffusion transformation is the most accurate but is only applicable for uniform absorption. However, in the intestine absorption is nonuniform and the transformation is not possible. Hence a moving mesh approach is likely to provide the greatest accuracy in this case.

When considering the full 2D Poiseuille model (4.4.2) we solve the system of odes using Fortran 95 which integrates the DAEs at a fraction of time compared to Matlab. For slowly diffusing compounds there is a steep concentration gradient at the peristaltic boundary and for increased accuracy we locate more grid points at the membrane to capture the boundary layer. This is important as the measurement of mass absorbed is taken directly from the solute concentration at the boundary which must be solved

for as accurate as possible with our chosen numerical scheme.

In the peristaltic dispersion model (5.1.5) the peristaltic velocity profiles can be found 1) analytically from the perturbation expansion (3.4.1) or 2) from solving the biharmonic equations numerically (see Appendix §E). We then transform the peristaltic solute model to a rectangular domain and discretise the equations with finite difference operators. We subsequently input the rectangular domain velocities into the dispersion model (5.1.5) and solve it numerically in Fortran. It is necessary to apply an alternating upwind/downwind method for the axial convection term that depends on the sign of the peristaltic velocities.

6.1 Numerically Solving the 1D Dispersion Model

We consider the 1D asymptotic convection diffusion reaction (4.4.9), introduced by Stoll et al. [73], for the asymptotic long time reduction of the 2D Poiseuille dispersion model (4.4.2). After a sufficient amount of time, solute concentration $c(\tilde{x}, \tilde{t})$ in a tube in the axial direction \tilde{x} may be modelled by the dimensionless equation

$$c_{\tilde{t}} + U_e c_{\tilde{x}} = D_e c_{\tilde{x}\tilde{x}} - K_e c, \quad \tilde{t} > 0, \quad 0 < \tilde{x} \leq 1, \quad (6.1.1)$$

where it is assumed the solute moves with effective velocity U_e , an effective dispersion D_e and is removed from the tube at an effective absorption rate K_e (see Chapter 4). This pde may be solved for two cases of drug transport where the case determines the type of initial and boundary conditions we must apply. We consider:

- **An Initial Amount of Solute is Placed in the Tube.**

$$\begin{aligned} \text{Initial Condition:} \quad & c(\tilde{x}, 0) = \phi(\tilde{x}), & 0 \leq \tilde{x} \leq 1, \\ \text{Boundary Conditions:} \quad & c(0, \tilde{t})_{\tilde{x}} = c(1, \tilde{t})_{\tilde{x}} = 0, & \tilde{t} \geq 0. \end{aligned}$$

The Neumann boundary conditions imply that the convection forces dominate over diffusion at the boundaries [73]. For the problem to be well posed in our numerical scheme (6.1.1), it is necessary to additionally prescribe a zero Dirichlet boundary condition at the inlet, $c(0, \tilde{t}) = 0$ for $\tilde{t} \geq 0$ to prevent numerical scheme errors at the boundary (6.1.2).

- **A maintained source of therapeutic at the entrance.**

$$\begin{aligned} \text{Initial Condition:} \quad & c(\tilde{x}, 0) = 0 & 0 < \tilde{x} \leq 1 \\ \text{Boundary conditions:} \quad & c(0, \tilde{t}) = c_0, c(1, \tilde{t})_{\tilde{x}} = 0, & \tilde{t} \geq 0 \end{aligned}$$

In this case a constant amount of solute is being released into an initially solute free tube.

Analytical solutions may be found for the case where a slug of solute is introduced, in terms of an infinite Fourier series. However, for simplicity we test our numerical scheme for a simpler known solution in the case of a maintained source.

6.1.1 Discretising the 1D Dispersion Equation on a Uniform Mesh

We discretise (6.1.1) on a uniform mesh by using finite difference operations. Let $0 \leq \check{t} \leq T$ and $0 \leq \hat{x} \leq 1$ and consider a uniform spatial step $\Delta\check{x} = 1/J$ for given J . We denote the numerical approximation of the concentration $c(\check{x}_j, \check{t}_n)$ at a meshpoint by c_j^n where $(\check{x}_j, \check{t}_n) = (j\Delta\check{x}, n\Delta\check{t})$ for $j = 0, 1, \dots, J$, $n = 0, 1, \dots, N$. We define the following notation for the finite difference operators as in [58]:

$$\begin{aligned} \text{Upwinding:} \quad & \Delta_{-x}c(\check{x}, \check{t}) &:= c(\check{x}, \check{t}) - c(\check{x} - \Delta\check{x}, \check{t}), \\ \text{Downwinding:} \quad & \Delta_{+x}c(\check{x}, \check{t}) &:= c(\check{x} + \Delta\check{x}, \check{t}) - c(\check{x}, \check{t}), \\ \text{Central Difference:} \quad & \Delta_{0x}c(\check{x}, \check{t}) &:= \frac{1}{2} (c(\check{x} + \Delta\check{x}, \check{t}) - c(\check{x} - \Delta\check{x}, \check{t})), \\ \text{2nd Order Central Difference:} \quad & \delta_x^2c(\check{x}, \check{t}) &:= c(\check{x} + \Delta\check{x}, \check{t}) - 2c(\check{x}, \check{t}) + c(\check{x} - \Delta\check{x}, \check{t}). \end{aligned}$$

Since flow is constant in the positive direction we apply upwinding on the convection term to prevent spurious oscillations in the numerical solution [58]. We also apply the second order centered difference operator to the diffusive term. Hence equation (6.1.1) is reduced to a discretised system of J odes:

$$c_{i,j} = -U_e \frac{\Delta_{-x}c_j}{\Delta\check{x}} + D_e \frac{\delta_x^2c_j}{\Delta\check{x}^2} - K_e c_j, \quad \forall j = 1, \dots, J, \quad (6.1.2)$$

that satisfy the linear system $\mathbf{c}_{\check{t}} = \mathbf{A}\mathbf{c}$ for column vectors $\mathbf{c}_{\check{t}}, \mathbf{c} \in \mathbb{R}^{(J+1) \times 1}$ and tridiagonal matrix $\mathbf{A} \in \mathbb{R}^{(J+1) \times (J+1)}$. The interior tridiagonal entries of \mathbf{A} correspond to interior grid points

$$[A_i, A_{i-1,i}, A_{i,i+1}] = \left[\frac{U_e}{\Delta\check{x}} + \frac{D_e}{\Delta\check{x}^2}, -\frac{U_e}{\Delta\check{x}} - \frac{2D_e}{\Delta\check{x}^2} - K_e, \frac{D_e}{\Delta\check{x}^2} \right], \quad \forall i = 1, \dots, J-1.$$

At the outlet, we introduce a fictitious grid point c_{J+2} outside the grid, known as a ghost point, so that the prescribed Neumann boundary condition can be given in discretised form by

$$c_{\check{x}}(1, \check{t}) \approx \frac{\delta_{0,\check{x}}c_{J+1}}{\Delta\check{x}} = \frac{c_{J+2} - c_J}{2\Delta\check{x}} = 0. \quad (6.1.3)$$

The ghost point satisfies $c_{J+2} = c_J$ so that (6.1.2) at the outlet satisfies

$$[A_{J+1,J}, A_{J+1,J+1}] = \left[\frac{2D_e}{\Delta\check{x}^2}, -\frac{2D_e}{\Delta\check{x}^2} - K_e \right].$$

It is only left to prescribe (6.1.2) at the inlet, however, depending on the choice of finite difference we may obtain an ill posed problem. We discuss this issue in §6.1.2.

For the moment we have derived the standard finite difference approach to solving a convective dispersive equation by the method of lines. However, for sharp wave fronts seen in convective dominating systems, e.g. in slowly diffusing therapeutics, the numerical solution suffers increasing error through artificial numerical dispersion due to the upwinding term. We seek alternative methods to reduce such errors such as a pde transformation §6.1.3 and a moving mesh approach §6.1.4. For simplicity we limit our research to just the two schemes mentioned, however, we note there are other methods such as the Lax Wendroff scheme and Total Variation Diminishing scheme that can be applied to the 1D dispersion model [58], [46].

6.1.2 Determining a Well-Posed Numerical Scheme

Consider the case where an initial amount of solute occupies the tube, so that $c(\tilde{x}, 0) = \phi(\tilde{x})$. In general a Neumann boundary condition $c_{\tilde{x}} = 0$ can be applied to represent an insulated boundary. However, we show that it can also represent a maintained source at the inlet $c(0, \tilde{t}) = \phi(0)$ if the Neumann condition is applied inappropriately. Let us consider equation (6.1.1) with the Neumann boundary condition, then as in (6.1.3) we apply a ghost point to be applied on the dispersion term so that

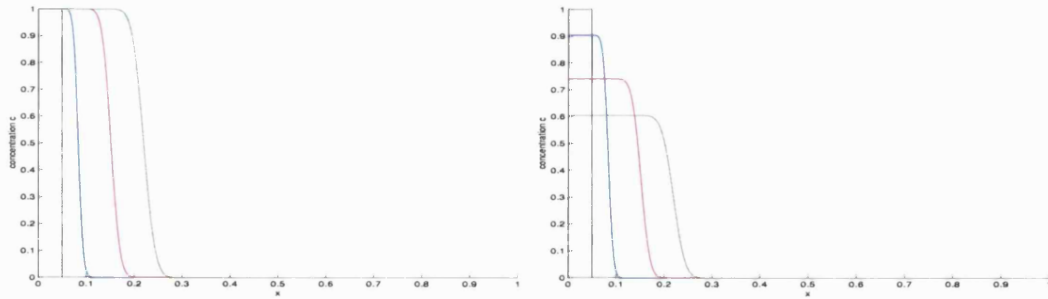
$$[A_{1,1}, A_{1,2}] = \left[-\frac{2D_e}{\Delta\tilde{x}^2} - K_e, \frac{2D_e}{\Delta\tilde{x}^2} \right], \quad (6.1.4)$$

Hence, the concentration at the inlet boundary condition satisfies

$$c_{\tilde{t},0} = \left(-\frac{2D_e}{\Delta\tilde{x}^2} - K_e \right) c_0 + \frac{2D_e}{\Delta\tilde{x}^2} c_1. \quad (6.1.5)$$

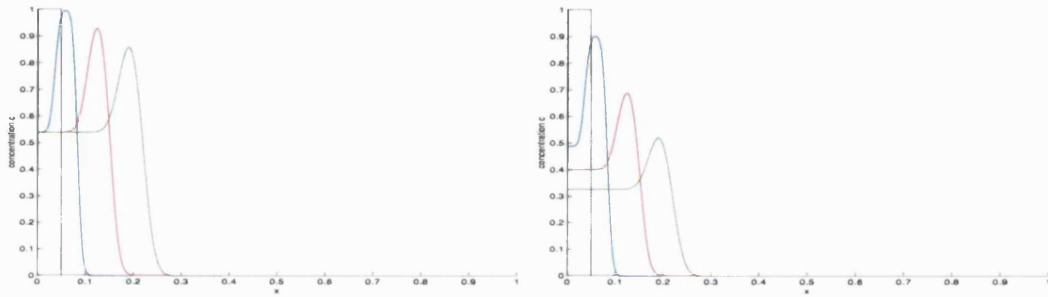
Consider the case where there is no absorption, then for an applied constant initial concentration $\phi(\tilde{x}) = \phi_0$ yields a constant concentration $c(0, \tilde{t}) = \phi_0$ (see Figure 6-1(a)). A similar argument for non-zero absorption yields a decaying inlet concentration $c(0, \tilde{t}) = e^{-K_e\tilde{t}}\phi_0$ (see Figure 6-1(b)). This maintained source arises from applying upwinding, $\Delta_{-\tilde{x}}$, to the convection term resulting in a constant (or decaying) amount of solute being produced at the inlet [58]. Even applying a zero initial inlet boundary condition $\phi(0) = 0$, the inlet concentration increases in time due to diffusion of the initial slug. This then feeds back into the system as if it were a slowly increasing maintained source (Figure 6-1(c), (d)).

We solve (6.1.1) for the different boundary conditions with and without absorption to show the inappropriateness of some numerical schemes in dealing with upwinding on the convection term.⁷ To correct the numerical scheme we prescribe a zero Dirchlet boundary condition $c_{\tilde{t},1} = 0$, to prevent an inlet source from occurring (see Figure 6-1(e)). This results in a Gaussian profile for the concentration solution, which is what we expect.



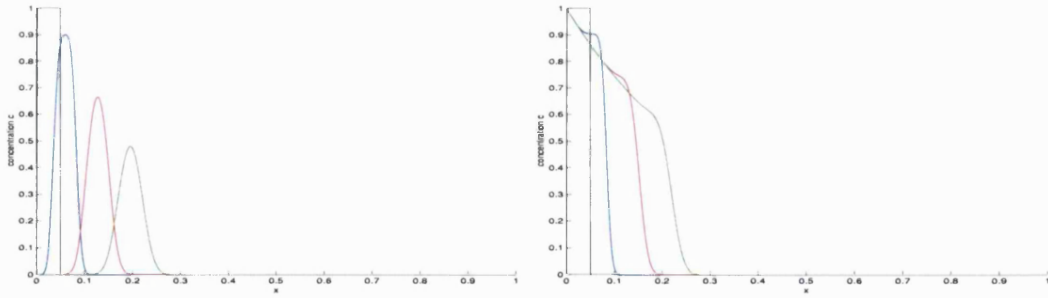
(a) Unwanted Maintained Source $c(0, \bar{x}_0) = 1, K_e = 0$

(b) Unwanted Decaying Source $c(0, \bar{x}_0) = 1, K_e > 0$



(c) Feeding Back Source at Inlet $c(0, \bar{x}_0) = 0, K_e = 0$

(d) Feeding Back Source at Inlet $c(0, \bar{x}_0) = 0, K_e = 0$



(e) Proper zero Dirichlet Boundary Condition $c(0, \bar{x}_0) = 0, K_e > 0$

(f) Actual Maintained Source $c(0, \bar{x}_0) = 1, K_e > 0$

Figure 6-1: The Effects of an Inappropriate Inlet Boundary Condition in the Numerical Scheme on the Solute Concentration Profile at time $\check{t} = 10$ when $U_e = 1e - 2, D_e = 1e - 4$.

6.1.3 A Diffusion Transformation of the 1D Dispersion Equation

In general applying a first order upwinding scheme, $\Delta_{-\tilde{x}}$, leads to unwanted numerical diffusion as the difference method is only accurate up to $O(h)$ [58]. A useful pde transformation, $c(\tilde{x}, \tilde{t}) = w(\tilde{x}, \tilde{t})e^{\alpha\tilde{x} - \beta\tilde{t}}$, can reduce the convection diffusion reaction pde (6.1.1) to a pure diffusion equation $w_{\tilde{t}} = D_e w_{\tilde{x}\tilde{x}}$.

Proof. Defining $\hat{e} = e^{(\alpha\tilde{x} - \beta\tilde{t})}$, then substituting $c(\tilde{x}, \tilde{t}) = w(\tilde{x}, \tilde{t})e^{(\alpha\tilde{x} - \beta\tilde{t})}$ into (6.1.1) yields:

$$\begin{aligned} (w\hat{e})_{\tilde{t}} + U_e(w\hat{e})_{\tilde{x}} &= D_e(w\hat{e})_{\tilde{x}\tilde{x}} - K_e(w\hat{e}) \\ w_{\tilde{t}}\hat{e} - \beta w\hat{e} + U_e w_{\tilde{x}}\hat{e} + U_e\alpha w\hat{e} &= D_e(w_{\tilde{x}}\hat{e} + \alpha w\hat{e})_{\tilde{x}} - K_e w\hat{e} \\ w_{\tilde{t}}\hat{e} + U_e w_{\tilde{x}}\hat{e} + (U_e\alpha - \beta)w\hat{e} &= D_e(w_{\tilde{x}\tilde{x}}\hat{e} + 2\alpha w_{\tilde{x}}\hat{e} + \alpha^2 w\hat{e}) - K_e w\hat{e} \\ w_{\tilde{t}} + U_e w_{\tilde{x}} + (U_e\alpha - \beta)w &= D_e w_{\tilde{x}\tilde{x}} + 2\alpha D_e w_{\tilde{x}} + (\alpha^2 D_e - K_e)w \\ w_{\tilde{t}} &= D_e w_{\tilde{x}\tilde{x}} + (2\alpha D_e - U_e)w_{\tilde{x}} + (\alpha^2 D_e - K_e - U_e\alpha + \beta)w. \end{aligned}$$

The last two terms in the brackets can be set to zero by an appropriate choice of α and β . Hence (6.1.1) transforms to $w_{\tilde{t}} = D_e w_{\tilde{x}\tilde{x}}$ a purely diffusion pde provided U_e is constant. \square

By applying the diffusion transformation we have removed the convection term, the source of numerical diffusion from upwinding. To apply this method the initial condition and boundary conditions must suitably be transformed for w . We then simply discretise with finite difference as seen earlier but without convection and diffusion to solve the linear system $w_{\tilde{t}} = Aw$. Having found the numerical solution of w we simply transform back for the concentration profile c .

6.1.4 Refinement Techniques of 1D Partial Differential Equations

In general very little has been done to design more accurate and efficient methods for solving dispersion models with application to therapeutic drugs. In 1D the dispersion equation is very common with applications to ground water transport [36]. There have been many adaptive schemes designed to reduce numerical dispersion and oscillations coming from sharp wave fronts [36]. Generally numerical methods use fixed spatially uniform grids to solve the time dependent pde. In Numerical Analysis there are various techniques for improving accuracy in any numerical scheme, which include

- *p-refinement*; which involves using higher order schemes.
- *h-refinement*; that subdivides elements or nodes.
- *r-refinement*; that relocates existing grid points without adding any new nodes.

The advantage of *h-refinement* is that it is simple and robust, however as it is a static regriding method it requires interpolation and is not smooth in time. In contrast, *r-refinement*, is continuous in time and requires no interpolation but becomes increasingly difficult, and in higher dimensions becomes highly nonlinear and suffers from distorted meshes.

As in Huang et al. [36], we apply a moving mesh partial differential equation known as an MMPDE (an r-refinement mesh adaptation), which has been shown to reduce errors in the numerical solution of (6.1.1) when compared to standard techniques [36]. This involves moving the mesh around in an orderly way where the solution varies significantly, by applying the *equidistribution principle*. This is where mesh points are selected by equalising the monitor function, $M(\tilde{x}, \tilde{t})$, which measures a property of the physical solution or its error, over each element. However, we differ from Huang et al. by testing the solution of equation (6.1.1) with the more spatially smooth MMPDE which we now explain in detail.

6.1.5 Formulation of a Moving Mesh Partial Differential Equation

At the forefront of adaptive mesh movement are Russell and Huang who have unified and developed the class of moving mesh algorithms based on their MMPDE (see review [33]). We formulate our moving mesh equation based on their work [30], [35], [55], [72], [31], particularly on [36]. We define a coordinate transformation by mapping from a computational domain $\Omega^c \subset \mathbb{R}$ to a physical domain $\Omega \subset \mathbb{R}$. A similar coordinate transformation is used in solving the peristaltic biharmonic problem numerically where the peristaltic domain is our physical domain and the rectangular domain is our computational domain. We denote \tilde{x} as the physical coordinate and ξ as the computational coordinate, however since our problem is dimensionless the physical coordinate is also defined as the computational coordinate on the unit interval $[0, 1] = \Omega = \Omega^c$. The MMPDE generates meshes on Ω as images of a fixed uniform computational mesh on Ω^c by a one-to-one time dependent coordinate transformation $\tilde{x} = \tilde{x}(\xi, \tilde{t})$ with fixed boundary nodes $\tilde{x}(0, \tilde{t}) = 0$ and $\tilde{x}(1, \tilde{t}) = 1$.

We define a uniform mesh on the computational domain, $\Omega^c = \xi_j$ where $\xi_j = j/J$ for $j = 0, \dots, J$. The domain Ω^c is mapped to a corresponding physical mesh $\Omega = x_j$. There are two methods to derive the mesh equation of the map $\tilde{x}(\xi)$ which are interrelated by the equidistribution principle. They are 1) a variational approach, that is the map that minimises a functional depending on the properties of the physical solution and the mesh captured by the monitor function used in [36] or 2) direct manipulation of the equidistribution principle. Both methods obtain similar results, although the latter generates more choices for the mesh equation [33].

In [36] the functional was given by

$$I[\xi] = \frac{1}{2} \int_0^1 \frac{1}{M} \left(\frac{\partial \xi}{\partial \tilde{x}} \right)^2 d\tilde{x},$$

which when minimised produces equidistribution. This mesh adaptation functional is formulated by the inverse mapping $\xi = \xi(\tilde{x})$ rather than $\tilde{x} = \tilde{x}(\xi)$ to prevent mesh crossings. The MMPDE is then defined as the modified heat flow equation for the functional $I[\xi]$, such that

$$\frac{\partial \xi}{\partial \tilde{t}} = \frac{1}{\tau M} \frac{\partial}{\partial \tilde{x}} \left(\frac{1}{M} \frac{\partial \xi}{\partial \tilde{x}} \right),$$

for a user prescribed parameter $\tau > 0$, that is the timescale that moves the mesh towards equidistribution. Hence rewriting in terms of the physical coordinate $\tilde{x} = \tilde{x}(\xi(\tilde{x}, \tilde{t}), \tilde{t})$, then

$$\alpha \frac{\partial \tilde{x}}{\partial \tilde{t}} = \frac{\partial}{\partial \xi} \left(M \frac{\partial \tilde{x}}{\partial \xi} \right),$$

as derived in [36] for time scaling parameter $\alpha = \tau M^3 \tilde{x}_\xi^2$. Alternatively in Huang et al. [33] the functional is defined differently so that $\alpha = \tau \sqrt{M^2 + M_\xi^2}$ to allow invariance of the mesh equation under transformation.

Alternatively the mesh equation may be derived directly from the Equidistribution Principle (EP) [33] such that

$$\int_0^{\tilde{x}(\xi, \tilde{t})} M(\tilde{x}, \tilde{t}) d\tilde{x} = \xi \theta(t) = \xi \int_0^1 M(\tilde{x}, \tilde{t}) d\tilde{x}.$$

Upon differentiating twice with respect to ξ we obtain what is known as a quasi-static EP

$$\frac{\partial}{\partial \xi} \left\{ M(\tilde{x}(\xi, \tilde{t}), \tilde{t}) \frac{\partial}{\partial \xi} \tilde{x}(\xi, \tilde{t}) \right\} = 0. \quad (6.1.6)$$

There are two forms of the MMPDE that can be derived from (6.1.6) seen in [35]. They are chosen for their relative simplicity that allows them to be more easily discretised than other MMPDES with finite difference:

$$\text{MMPDE5} \quad \dot{\tilde{x}} = \frac{1}{\tau} \frac{\partial}{\partial \xi} \left(M \frac{\partial \tilde{x}}{\partial \xi} \right), \quad (6.1.7)$$

$$\text{MMPDE6} \quad \frac{\partial^2 \tilde{x}}{\partial \xi^2} = \frac{1}{\tau} \frac{\partial}{\partial \xi} \left(M \frac{\partial \tilde{x}}{\partial \xi} \right), \quad (6.1.8)$$

where we now denote $\tilde{x}_{\tilde{t}} = \dot{\tilde{x}}$. Here MMPDE5 has zero speed when the mesh is equidistributed. However, unlike in [36] we choose to apply MMPDE6 to our numerical scheme as MMPDE5 has been found to be not as effective as the better scaled MMPDE6. Using centred difference, we discretise MMPDE6 on our uniform computational mesh

yielding

$$\text{MMPDE6} \quad \frac{\dot{x}_{j+1} - 2\dot{x} + \dot{x}_{j-1}}{\Delta\xi^2} = \frac{1}{\tau} E_j, \quad (6.1.9)$$

$$\text{Equidistribution Term} \quad E_j = \frac{M_{j+1} + M_j}{\Delta\xi} \frac{x_{j+1} - x_j}{\Delta\xi} - \frac{M_j + M_{j-1}}{\Delta\xi} \frac{x_j - x_{j+1}}{\Delta\xi}, \quad (6.1.10)$$

We now seek to discretise (6.1.1) with finite difference on $\Omega = \check{x}_i$, a nonuniform mesh. Hence (6.1.1) becomes

$$\dot{c}_j = -U_e \frac{\Delta_{-\check{x}} c_j}{\Delta_{-\xi} \check{x}_j} + \frac{2D_e}{\delta_{0\xi}} \left(\frac{\Delta_{+\check{x}} c_j}{\Delta_{+\xi} \check{x}_j} - \frac{\Delta_{-\check{x}} c_j}{\Delta_{-\xi} \check{x}_j} \right) - K_e c_j, \quad \forall j = 1, \dots, J \quad (6.1.11)$$

Combining the discretised pde (6.1.11) and the discretised mmpde (6.1.9), we form a nonlinear system $M\mathbf{y} = \mathbf{g}(\mathbf{t}, \mathbf{y})$ for $\mathbf{y} = [\mathbf{c} \ \mathbf{x}]^T$.

6.1.6 The Choice of Monitor Function and Smoothing

The arc-length monitor function is most frequently used to equidistribute grid points along the solution gradient $c_{\check{x}}$ [11], placing more nodes where the solution changes the greatest,

$$M(\check{x}, \check{t}) = \sqrt{1 + c_{\check{x}}^2}.$$

There are other monitor functions which are based on interpolation error indicators (which require apriori knowledge of the solution) or on higher order derivatives of the solution which are more likely to be related to the error in the numerical scheme [11]. However, we are primarily interested in comparing numerical schemes to an MMDPE, rather than specifically tailoring an MMPDE scheme. Consequently we choose the most reliable and simplest monitor function.

The nonlinearity of the MMPDE when coupled with the physical pde causes the system to become very stiff. It has been shown that it is possible to make the MMPDE easier to integrate numerically by smoothing the mesh [29]. Generally the computed monitor function is very non-smooth, and we repeatedly apply the standard low-pass filter to obtain a smoother mesh.

$$M(\check{x}_j, t) \leftarrow \frac{1}{4} M(\check{x}_{j-1}, t) + \frac{1}{2} M(\check{x}_j, t) + \frac{1}{4} M(\check{x}_{j+1}, t).$$

6.1.7 A Comparison of the Different Numerical Schemes for the 1D Dispersion Equation

We consider the 1D dispersion equation (6.1.1) in the case of a maintained source at both the inlet and the outlet where (6.1.1) has a known solution. This is the same problem with known analytical solution $c^*(\check{x}, \check{t})$ used by Huang et al. [29] to compare

numerical schemes for fixed and moving meshes. Consider the following model

$$\begin{aligned}
 \text{Equation} \quad & c_{\check{t}} + U_e c_{\check{x}} = D_e c_{\check{x}\check{x}} - K_e c \quad \check{t} > 0, \quad 0 < \check{x} \leq 1, \\
 \text{Initial Condition} \quad & c(\check{x}, 0) = 0, \\
 \text{Inlet DBC} \quad & c(0, \check{t}) = 1, \\
 \text{Outlet DBC} \quad & c(1, \check{t}) = c^*(1, \check{t}) = f(\check{t}).
 \end{aligned}$$

The exact solution is given in terms of the complementary error function $\text{Erfc}(\check{x}) = \frac{2}{\sqrt{\pi}} \int_{\check{x}}^{\infty} e^{-z^2} dz$ and discriminant $\gamma = \frac{U_e + 4K_e D_e}{4D_e^2}$ such that

$$\begin{aligned}
 c^*(\check{x}, \check{t}) = \frac{1}{2} \left\{ e^{\left(\frac{U_e}{2D_e} + \sqrt{\gamma}\right)\check{x}} \text{Erfc}\left(\frac{\check{x}}{2\sqrt{D_e\check{t}}} + \sqrt{D_e\gamma\check{t}}\right) \right. \\
 \left. + e^{\left(\frac{U_e}{2D_e} - \sqrt{\gamma}\right)\check{x}} \text{Erfc}\left(\frac{\check{x}}{2\sqrt{D_e\check{t}}} - \sqrt{D_e\gamma\check{t}}\right) \right\}. \quad (6.1.12)
 \end{aligned}$$

We test the accuracy of the numerical solution of three schemes, they are 1) applying standard upwinding technique (6.1.2), 2) solving the diffusion transformed pde (6.1.3) instead of (6.1.1) and 3) applying moving mesh equation MMPDE6 (6.1.8) in conjunction with the nonuniform discretised dispersion equation (6.1.11). We measure the accuracy of each numerical scheme by three important criteria (i) global mass conservation and (ii) discrete L_2 norm error and iii) most importantly relative proportion of mass absorbed. We define exact mass at time \check{t}_n by $m_{ex}(\check{t}_n) = \int_0^1 c^*(\check{x}, \check{t}_n) d\check{x}$, then the accumulated errors are defined by:

$$\begin{aligned}
 \text{Mass Conservation} \quad & M_{err}(\check{t}_n) = \frac{1}{m_{ex}(\check{t}_n)} \int_0^1 c(\check{x}_j, \check{t}_n) d\check{x}, \\
 \text{L2 Error} \quad & L_2(\check{t}_n) = \frac{1}{m_{ex}(\check{t}_n)} \int_0^1 (c(\check{x}_m, \check{t}_n) - c^*(\check{x}_j, \check{t}_n))^2 d\check{x}, \\
 \text{Error in the Mass Absorbed} \quad & M_{aerr}(\check{t}_n) = \frac{K_e \int_0^{\check{t}_n} \int_0^1 c(\check{x}_j, \check{t}_n) d\check{x} d\check{t}}{K_e \int_0^{\check{t}_n} m_{ex}(\check{t}_n)}.
 \end{aligned}$$

We solve (6.1.1) for the three numerical schemes for $N = 30, 60, 120$ grid points, with fixed velocity $U_e = 1e - 2$, up to time $T = 1$ for two diffusion values (i) $D_e = 10^{-2}$ and (ii) $D_e = 10^{-4}$. In the case of large diffusion, we obtain a small Péclet number and solute transport is diffusion dominant. Here we expect small numerical errors as the wavefront is not so profoundly steep when compared to case (ii) where transport is dominated by convection. For each calculation we determine (a) the difference in the error of mass present $|M_{err} - 1|$, (b) the L2 error and (c) the difference in the error of mass absorbed $|M_{aerr} - 1|$.

We observe in Tables 6.1, 6.2, 6.3 that the diffusion transformation is overall the

Mass Present Error						
$D_e = 1.0e - 02$				$D_e = 1.0e - 04$		
N	Upw.	MMPDE6	$w_{\bar{t}} = D_e w_{\bar{x}\bar{x}}$	Upw.	MMPDE6	$w_{\bar{t}} = D_e w_{\bar{x}\bar{x}}$
30	1.56e-02	7.78e-03	2.92e-03	5.90e-01	7.49e-02	2.88e+00
60	7.20e-03	5.24e-03	7.29e-04	2.79e-01	4.51e-02	5.11e-01
120	3.44e-03	2.97e-03	1.82e-04	1.40e-01	2.64e-02	1.23e-01
240	1.68e-03	1.44e-03	4.55e-05	7.07e-02	1.52e-02	3.06e-02
480	8.30e-04	6.75e-04	1.13e-05	3.56e-02	8.69e-03	7.63e-03

Table 6.1: The Difference in the Error of Mass of Solute Present for the Numerical Solution of the 1D Dispersion Model using (i) Upwinding, (ii) Moving Mesh Equation MMPDE6 and (iii) a Diffusion Transformation

L2 Error						
$D_e = 1.0e - 02$				$D_e = 1.0e - 04$		
N	Upw.	MMPDE6	$w_{\bar{t}} = D_e w_{\bar{x}\bar{x}}$	Upw.	MMPDE6	$w_{\bar{t}} = D_e w_{\bar{x}\bar{x}}$
30	8.05e-05	1.97e-05	4.88e-06	1.19e-01	2.77e-03	1.81e+00
60	1.77e-05	9.01e-06	3.07e-07	3.41e-02	1.00e-03	9.96e-02
120	4.18e-06	2.93e-06	1.92e-08	1.05e-02	3.37e-04	7.05e-03
240	1.01e-06	6.92e-07	1.20e-09	3.01e-03	1.09e-04	4.64e-04
480	2.50e-07	1.52e-07	7.62e-11	8.11e-04	3.55e-05	2.94e-05

Table 6.2: The L2 Error of the Numerical Solution of the 1D Dispersion Model using (i) Upwinding, (ii) Moving Mesh Equation MMPDE6 and (iii) a Diffusion Transformation

Mass Absorption Error						
$D_e = 1.0e - 02$				$D_e = 1.0e - 04$		
N	Upw.	MMPDE6	$w_{\bar{t}} = D_e w_{\bar{x}\bar{x}}$	Upw.	MMPDE6	$w_{\bar{t}} = D_e w_{\bar{x}\bar{x}}$
30	2.01e-02	7.82e-03	7.49e-03	4.67e-01	7.06e-02	1.69e+00
60	8.40e-03	6.55e-03	1.85e-03	3.44e-01	4.55e-02	4.94e-01
120	3.77e-03	4.00e-03	4.52e-04	1.85e-01	2.87e-02	1.41e-01
240	1.78e-03	1.84e-03	1.12e-04	9.30e-02	1.78e-02	3.70e-02
480	8.62e-04	7.88e-04	2.80e-05	4.61e-02	1.10e-02	9.32e-03

Table 6.3: The Difference in the Error of Mass of Solute Absorbed for the Numerical Solution of the 1D Dispersion Model using (i) Upwinding, (ii) Moving Mesh Equation MMPDE6 and (iii) a Diffusion Transformation

most accurate in all three categories except when we solve for small diffusion with a small number of gridpoints. This is the only time the moving mesh method is the most accurate. However, the moving mesh approach is always more accurate than the upwinding scheme but becomes increasingly less so when the number of gridpoints increases removing the need to distribute nodes. The MMPDE will always do better if U_e or K_e varies though. The latter is known to vary in the intestine, $K_e = K_e(x)$, due to the variation in the villi density.

6.2 Numerically Solving The 2D Poiseuille Dispersion Model

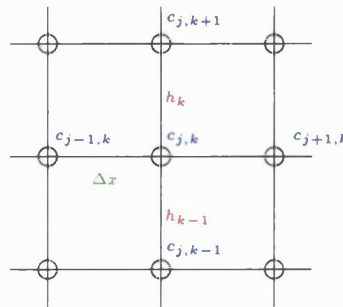
In the previous section we considered the release of a therapeutic modelled by a 1D dispersion equation (6.1.1). This was an asymptotic form of a more complex 2D Poiseuille convection dispersion model in an axisymmetric tube Ω with absorption on the boundary Γ , with governing equations

$$\begin{aligned} c_t + \epsilon u(r)c_{\tilde{x}} &= \frac{1}{P_{er}} \left(\epsilon^2 c_{\tilde{x}\tilde{x}} + c_{\tilde{r}\tilde{r}} + \frac{1}{\tilde{r}} c_{\tilde{r}} \right), & \text{in } \Omega, \\ c_{\tilde{r}} &= -D_a c, & \text{on } \Gamma. \end{aligned} \tag{6.2.1}$$

We must solve this problem numerically and we discretise (6.2.1) using finite difference operators, however, instead of a uniform-mesh, we choose a non-uniform mesh in the radial direction and a uniform mesh in the axial direction. Due to cpu limits, solving a 2D problem uses a lot of memory and a balance must be met between mesh size and cpu run time; too fine a mesh and the system takes too long to solve. Discretising with as many points as desired in the axial x and radial r direction is not possible. Our overall concern is attaining an accurate cross-sectional average of the solute concentration, the macroscopic quantity. We require a sufficient number of points in the axial direction to represent the intestine more accurately; solving for concentration at grid points every 3cm is better than every 6cm. As mentioned in Chapter 4, absorption on the boundary introduces a boundary layer, hence we wish to add more grid points in this region to capture the change in solution more accurately. We optimise by implementing a nonuniform radial mesh (size $K = 50$) with a uniform axial mesh (size $J = 200$) such that $J > K$.

6.2.1 Applying a 2D Finite Difference Scheme to the Poiseuille Dispersion Model

Consider the Poiseuille dispersion model (6.2.1) on the unit tube $0 \leq \tilde{x} \leq 1$ and $0 \leq \tilde{r} \leq 1$, for time $0 \leq t \leq T$. We denote $c_{j,k}^n$ to be the numerical approximation of the solute concentration $c_{j,k}^n \approx c(\tilde{x}_j, \tilde{r}_k, \tilde{t}_n)$ on the discretised grid for axial nodes $\tilde{x}_j = j\Delta\tilde{x}$ for $j = 0, 1, \dots, J$ and radial nodes $\{0 = \tilde{r}_0 < \tilde{r}_1 < \dots < \tilde{r}_K = 1\}$.



We define non-uniform radial spatial steps h_k for given k such that $h_k = \check{r}_{k+1} - \check{r}_k$ for $k = 0, 1, \dots, K-1$. As a result of the absorption boundary layer we distribute half the radial gridpoints, $\frac{K+1}{2}$, in the interval $[0, 0.9]$ and $\frac{K+1}{2}$ in the small interval containing the boundary $[0.9, 1]$. We apply a standard 5 point finite difference stencil for the Laplacian. Hence the discretised form of the Poiseuille dispersion equation is given by

$$\begin{aligned} \dot{c}_{j,k} &= -\epsilon u(\check{r}_k) \frac{\Delta_{-x} c_{j,k}}{\Delta \check{x}} + \frac{1}{P_{er}} \left(\epsilon^2 \frac{\delta_{\check{x}}^2 c_{j,k}}{\Delta \check{x}^2} + \frac{2}{h_{k-1} + h_k} \left(\frac{\Delta_{+\check{r}} c_{j,k}}{h_k} - \frac{\Delta_{-\check{r}} c_{j,k}}{h_{k-1}} \right) + \frac{1}{\check{r}_k} \frac{\Delta_{0\check{r}} c_{j,k}}{h_{k-1} + h_k} \right) \\ &\quad \forall j = 1, \dots, J \quad \forall k = 1, \dots, K-1 \\ 0 &= \frac{\Delta_{-\check{r}} c_{j,k}}{h_{K-1}} + D_{ar} c_{j,K} \\ &\quad \forall j = 1, \dots, J \end{aligned}$$

This forms a DAE system $M\dot{\mathbf{c}} = T\mathbf{c}$ for the concentration vectors $\dot{\mathbf{c}}, \mathbf{c} \in \mathbb{R}^{K+1(J+1) \times 1}$, block tridiagonal matrix $T \in \mathbb{R}^{(K+1)(J+1) \times (K+1)(J+1)}$ and Mass matrix $M \in \mathbb{R}^{(K+1)(J+1) \times (K+1)(J+1)}$ with zeros corresponding to the DAE boundary. However, we have yet to define the pde along the axisymmetric boundary. On the longitudinal axis, the radial term $\frac{1}{\check{r}} c_{\check{r}}$ tends to $c_{\check{r}\check{r}}$ as $\check{r} \rightarrow 0$ (by L'Hopital's rule) and we apply the symmetric boundary condition $c_{\check{r}}(\check{x}, 0, \check{t}) = 0$ and a ghost point to derive the equation at x_0

$$\dot{c}_{j,0} = -\epsilon u(\check{r}_j) \frac{\Delta_{-x} c_{j,0}}{\Delta \check{x}} + \frac{1}{P_{er}} \left(\epsilon^2 \frac{\delta_{\check{x}}^2 c_{j,0}}{\Delta \check{x}^2} + \frac{4}{h_0} \left(\frac{\Delta_{+\check{r}} c_{j,0}}{h_0} \right) \right)$$

6.2.2 A 2D Moving Mesh Scheme

The next logical and more accurate approach to solving the 2D dispersion models would be the 2D moving mesh approach. However, this is extremely complicated and for now remains out of the scope of this PhD. For further reading see [29], [33], [34], [7], [18], [32], [14], [54], [15], [16], [13]. A 2D MMPDE would be ideal in locating points at the boundary, as we did with the nonuniform mesh, but also at the head of the wavefront. It is essential when solving the model with a limited number of nodes. Hence, we could compare the 2D MMPDE against the standard nonuniform mesh approach, for the solvable problem:

$$\begin{aligned} \text{Equation} \quad c_{\check{t}} + u c_{\check{x}} &= \frac{1}{P_{er}} \left(\epsilon c_{\check{x}\check{x}} + c_{\check{r}\check{r}} + \frac{1}{\check{r}} c_{\check{r}} \right) - K_d c, \quad \check{t} > 0, \quad 0 < \check{x}, \check{r} \leq 1, \\ \text{Initial Condition} \quad c(\check{x}, 0) &= 0, \\ \text{Inlet DBC} \quad c(0, \check{r}, \check{t}) &= J_0(\beta_0 \check{r}), \\ \text{Outlet DBC} \quad c(1, \check{t}) &= c^*(1, t) = f(t), \\ \text{Absorption BC} \quad c(\check{x}, 1, \check{t})_{\check{r}} &= D_{ar} c(\check{x}, 1, \check{t}). \end{aligned}$$

Besides calculating the *mass conservation* and *L2 errors* we could measure the mass absorption error

$$\text{Error in the Mass Absorbed} \quad M_{aerr}(t^n) = \frac{\frac{D_{ar}}{P_{er}} \int_0^{t^n} \int_0^1 c(\tilde{x}_j, \tilde{r}_k, \tilde{t}_n) d\tilde{x} d\tilde{t}}{\frac{D_{ar}}{P_{er}} J_0(\beta_0) \int_0^{t^n} \int_0^1 c(\tilde{x}_j, \tilde{r}_k, \tilde{t}_n) d\tilde{x} d\tilde{t}}.$$

The higher dimensional moving mesh approach would be an invaluable tool for models with absorption boundary layers.

6.3 Numerically Solving the Peristaltic Dispersion Model

Consider an axisymmetric tube where the inelastic walls are allowed to vibrate and induce standing peristaltic waves. After a sufficient amount of time the fluid velocities become steady. We defined the nondimensional model for a diffusing solute convecting under the action of peristalsis with absorption on the boundary by Figure 6-2.

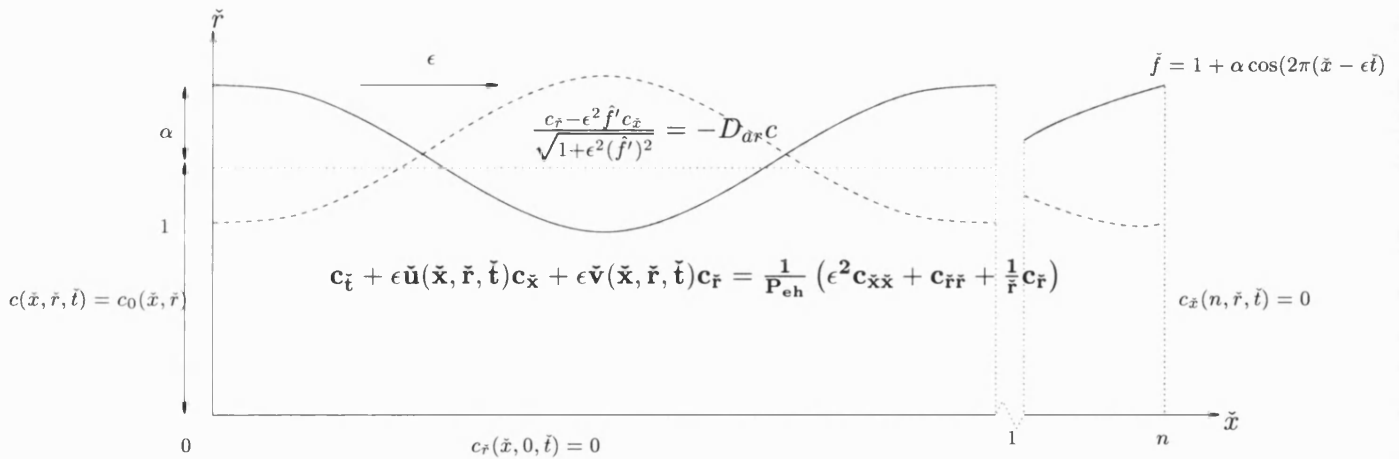


Figure 6-2: The Peristaltic Dispersion Model

By defining the function of the peristaltic boundary for all time $\tilde{f}(\tilde{x}, \epsilon \tilde{t})$, (note this is not a free boundary where the position of the membrane is unknown ahead of time), we can apply a change of coordinates from the physical peristaltic geometry (\tilde{x}, \tilde{r}) to the computational rectangular domain (χ, κ) . We note that as the wall is time dependent it is important to remember to transform the time scale $\tilde{t} \rightarrow \tau$ so that

$$\chi = \tilde{x}, \quad \kappa = \frac{\tilde{r}}{\tilde{f}(\tilde{x}, \tilde{t})}, \quad \tau = \tilde{t}. \tag{6.3.1}$$

The partial derivatives of the solute concentration may be rewritten as

$$\begin{aligned}
c_{\tilde{t}} &= c_{\chi}\chi_{\tilde{t}} + c_{\kappa}\kappa_{\tilde{t}} + c_{\tau}\tau_{\tilde{t}} = a_1c_{\kappa} + c_{\tau}, \\
c_{\tilde{r}} &= c_{\chi}\chi_{\tilde{r}} + c_{\kappa}\kappa_{\tilde{r}} + c_{\tau}\tau_{\tilde{r}} = a_2c_{\kappa}, \\
c_{\tilde{x}} &= c_{\chi}\chi_{\tilde{x}} + c_{\kappa}\kappa_{\tilde{x}} + c_{\tau}\tau_{\tilde{x}} = c_{\chi} + a_3c_{\kappa},
\end{aligned}$$

where the transformation coefficients a_i are coordinate derivatives such that:

$$\begin{aligned}
a_1 &= \kappa_{\tilde{t}} = -\frac{\tilde{r}\tilde{f}_{\tilde{t}}}{\tilde{f}} = \frac{\epsilon\kappa\tilde{f}_{\tilde{x}}}{\tilde{f}}, \\
a_2 &= \kappa_{\tilde{r}} = \frac{1}{\tilde{f}}, \\
a_3 &= \kappa_{\tilde{x}} = -\frac{\tilde{r}\tilde{f}_{\tilde{x}}}{\tilde{f}^2} = -\frac{\kappa\tilde{f}_{\tilde{x}}}{\tilde{f}},
\end{aligned}$$

We note that from the fixed frame we have the boundary property $\tilde{f}_{\tilde{t}} = -\epsilon\tilde{f}_{\tilde{x}}$. Transforming the laplacian terms is a little more complicated in the axial direction, it goes as follows

$$\begin{aligned}
c_{\tilde{x}\tilde{x}} &= (c_{\tilde{x}})_{\chi}\chi_{\tilde{x}} + (c_{\tilde{x}})_{\kappa}\kappa_{\tilde{x}} = (c_{\chi} + \kappa_{\tilde{x}}c_{\kappa})_{\chi} + (c_{\chi} + \kappa_{\tilde{x}}c_{\kappa})_{\kappa}\kappa_{\tilde{x}} \\
&= c_{\chi\chi} + \kappa_{\tilde{x}}^2c_{\kappa\kappa} + 2\kappa_{\tilde{x}}c_{\chi\kappa} + (\kappa_{\tilde{x}\tilde{x}} + \kappa_{\tilde{x}}\kappa_{\tilde{x}\kappa})c_{\kappa} \\
&= c_{\chi\chi} + \left(\frac{\kappa\tilde{f}_{\tilde{x}}}{\tilde{f}}\right)^2 c_{\kappa\kappa} - 2\left(\frac{\kappa\tilde{f}_{\tilde{x}}}{\tilde{f}}\right) c_{\chi\kappa} + \kappa\left(\frac{2\tilde{f}_{\tilde{x}}^2 - \tilde{f}\tilde{f}_{\tilde{x}\tilde{x}}}{\tilde{f}^2}\right) c_{\kappa} \\
&= c_{\chi\chi} + a_4c_{\kappa\kappa} + a_5c_{\chi\kappa} + a_6c_{\kappa}, \\
c_{\tilde{r}\tilde{r}} &= (c_{\tilde{r}})_{\kappa}\kappa_{\tilde{r}} = (\kappa_{\tilde{r}}c_{\kappa})_{\kappa}\kappa_{\tilde{r}}, = \frac{1}{\tilde{f}^2}c_{\kappa\kappa} = a_7c_{\kappa\kappa} \\
\frac{1}{\tilde{r}}c_{\tilde{r}} &= \frac{1}{\tilde{f}\kappa}c_{\kappa}\kappa_{\tilde{r}} = \frac{1}{\tilde{f}^2}c_{\kappa} = \frac{a_7}{\kappa}c_{\kappa}.
\end{aligned}$$

Substituting in the domain transformation for the peristaltic model

$$(c_{\tau} + a_1c_{\kappa}) + \epsilon\check{u}(c_{\chi} + a_3c_{\kappa}) + \epsilon\check{v}a_2c_{\kappa} = \frac{\epsilon^2}{P_{eh}}(c_{\chi\chi} + a_4c_{\kappa\kappa} + a_5c_{\chi\kappa} + a_6c_{\kappa}) + \frac{1}{P_{eh}}\left(a_7c_{\kappa\kappa} + \frac{a_7}{\kappa}c_{\kappa}\right).$$

Hence, the peristaltic model may be rewritten in the form:

$$\begin{aligned}
c_{\tau} &= \frac{\epsilon^2}{P_{eh}}c_{\chi\chi} + \left(\frac{\epsilon^2}{P_{eh}}a_4 + \frac{a_7}{P_{eh}}\right)c_{\kappa\kappa} \\
&\quad + \frac{\epsilon^2}{P_{eh}}a_5c_{\chi\kappa} - \epsilon\check{u}c_{\chi} + \left(\frac{\epsilon^2}{P_{eh}}a_5 - a_1 - \epsilon\check{u}a_3 - \epsilon\check{v}a_2 + \frac{a_7}{\kappa P_{eh}}\right)c_{\kappa} \\
&= b_1c_{\chi\chi} + b_2c_{\kappa\kappa} + b_3c_{\chi\kappa} + b_4c_{\chi} + b_5c_{\kappa}.
\end{aligned} \tag{6.3.2}$$

The absorption boundary condition must also be transformed, and in a similar manner:

$$\frac{a_2c_{\kappa} - \epsilon^2\tilde{f}'(c_{\chi} + a_3c_{\kappa})}{\sqrt{1 + \epsilon^2(\tilde{f}')^2}} = -D_{ar}c \implies (a_2 - \epsilon^2\tilde{f}'a_3)c_{\kappa} - \epsilon^2\tilde{f}'c_{\chi} = -\left(\sqrt{1 + \epsilon^2(\tilde{f}')^2}\right)D_{ar}c,$$

$$\therefore b_6c_{\kappa} - b_7c_{\chi} = -b_8D_{ar}c.$$

Consequently, the 2D peristaltic dispersion model can be represented in the rectangular ‘computational’ domain by

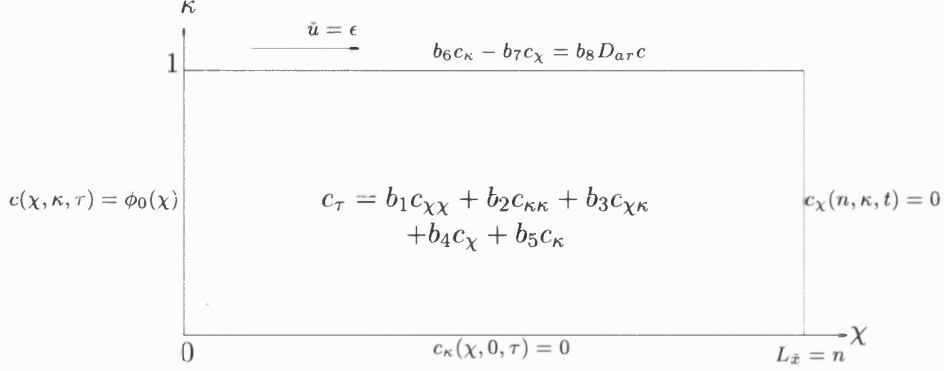


Figure 6-3: The Peristaltic Dispersion Model in the Rectangular Domain

Before we discretise the dispersion equation (6.3.2) we must determine the semi-analytic peristaltic velocities in the rectangular frame. In the physical domain they were given by

$$\begin{aligned}\tilde{u} &= 4A(\tilde{x}, \tilde{t})\tilde{r}^2 + 2B(\tilde{x}, \tilde{t}) + \epsilon^2 \left(\frac{A_{\tilde{x}\tilde{x}}(\tilde{x}, \tilde{t})}{2}\tilde{r}^4 + \frac{2A_{\tilde{x}\tilde{x}}(\tilde{x}, \tilde{t})\tilde{f}^2}{3}\tilde{r}^2 - \frac{A_{\tilde{x}\tilde{x}}(\tilde{x}, \tilde{t})\tilde{f}^4}{6} \right) + 1, \\ \tilde{v} &= -A_{\tilde{x}}(\tilde{x}, \tilde{t})\tilde{r}^3 - B_{\tilde{x}}(\tilde{x}, \tilde{t})\tilde{r} + \epsilon^2 \left(\frac{A_{\tilde{x}\tilde{x}\tilde{x}}(\tilde{x}, \tilde{t})}{12}\tilde{r}^5 + \frac{A_{\tilde{x}\tilde{x}\tilde{x}}(\tilde{x}, \tilde{t})\tilde{f}^2}{6}\tilde{r}^3 - \frac{A_{\tilde{x}\tilde{x}\tilde{x}}(\tilde{x}, \tilde{t})\tilde{f}^4}{12}\tilde{r} \right).\end{aligned}$$

Hence, using the domain transformation they may be written as

$$\begin{aligned}\tilde{u}(\chi, \kappa, \tilde{t}) &= 4A(\chi, \tilde{t})\tilde{f}^2\kappa^2 + 2B(\chi, \tilde{t}) + 1 + \epsilon^2 \left(\frac{A_{\chi\chi}(\chi, \tilde{t})}{6}\tilde{f}^4 \right) (-3\kappa^2 + 4\kappa^2 - 1), \\ \tilde{v}(\chi, \kappa, \tilde{t}) &= -A_{\chi}(\chi, \tilde{t})\tilde{f}^4\kappa^4 - B_{\chi}(\chi, \tilde{t})\tilde{f}^2\kappa^2 + \epsilon^2 \left(\frac{A_{\chi\chi\chi}(\chi, \tilde{t})}{12}\tilde{f}^5 \right) (\kappa^5 + 2\kappa^3 - \kappa).\end{aligned}$$

For the purposes of our model we assume ϵ is sufficiently small that we apply the peristaltic velocities to leading order (see Chapter 5).

6.3.1 Discretising the 2D Model with Finite Difference Operators

We solve the peristaltic dispersion model (Figure 6-3) using finite difference operations on the computational domain. Hence for an axially uniform radially nonuniform mesh we obtain

$$\begin{aligned}\dot{c}_{j,k} &= b_1 \frac{\delta_{\chi}^2 c_{j,k}}{\Delta\chi^2} + b_2 \left(\frac{2}{h_{k-1}+h_k} \right) \left(\frac{\Delta_{+\tilde{r}} c_{j,k}}{h_k} - \frac{\Delta_{-\tilde{r}} c_{j,k}}{h_{k-1}} \right) + b_3 \frac{\delta_{\chi\kappa} c_{j,k}}{2\Delta\chi(h_{k-1}+h_k)} + b_4 \frac{\Delta_{-\chi} c_{j,k}}{\Delta\chi} + b_5 \frac{\Delta_{0\kappa} c_{j,k}}{h_{k-1}+h_k}, \\ &\forall j = 1, \dots, J \quad \forall k = 1, \dots, K-1\end{aligned}$$

where we have defined the cross derivative finite difference operator by

$$\delta_{\chi\kappa} = \delta_{\chi\kappa}\psi = \psi(\chi+\Delta\chi, \kappa+\Delta\kappa) + \psi(\chi-\Delta\chi, \kappa-\Delta\kappa) - \psi(\chi-\Delta\chi, \kappa+\Delta\kappa) - \psi(\chi+\Delta\chi, \kappa-\Delta\kappa).$$

On the boundary we discretise the differential algebraic equation using upwinding in the radial direction and centred difference in the axial direction:

$$b_6 \frac{\Delta_{-\kappa} c_{j,K}}{h_K} - b_7 \frac{\delta_{-0\chi} c_{j,K}}{\Delta\chi} = b_8 D_{ar} c_{j,K}.$$

At $\tilde{r} = 0$ we implement the symmetry boundary condition $c_{\tilde{r}}(\tilde{x}, 0, \tilde{t}) = 0$. Hence the cross derivative term $c_{\tilde{x}\tilde{\kappa}}$ vanishes and the radial term simplifies to $\frac{1}{\tilde{r}} c_{\tilde{r}} = c_{\tilde{r}\tilde{r}}$. Defining $\hat{b}_2 = b_2 + \frac{a_7}{P_{er}}$, then the dispersion equation at the centreline becomes

$$\dot{c}_{j,0} = b_1 \frac{\delta_{\chi}^2 c_{j,k}}{\Delta\chi^2} + 2\hat{b}_2 \frac{\delta_{\kappa} c_{j,k}}{h_1^2} + b_4 \frac{\Delta_{-\chi} c_{j,k}}{\Delta\chi}, \quad \forall j = 1, \dots, J \quad .$$

As with the Poiseuille model we obtain a time dependent DAE system $M\dot{\mathbf{c}} = A\mathbf{c}$.

6.3.2 Numerical Scheme Instability

In the Peristaltic Dispersion Model Chapter 5 we have shown that the axial velocity $\tilde{u}(\tilde{x}, \tilde{r}, \tilde{t})$ is not always positive (see Figure 5-2) and for certain flow rates $\hat{\psi}_w$ it can take a negative value, $\tilde{u} < 0$. A consequence of this is numerical instability as a result of applying the upwinding finite difference operator. This leads to spurious oscillations that distort the mean solute concentration, see Figure 6-4(a).

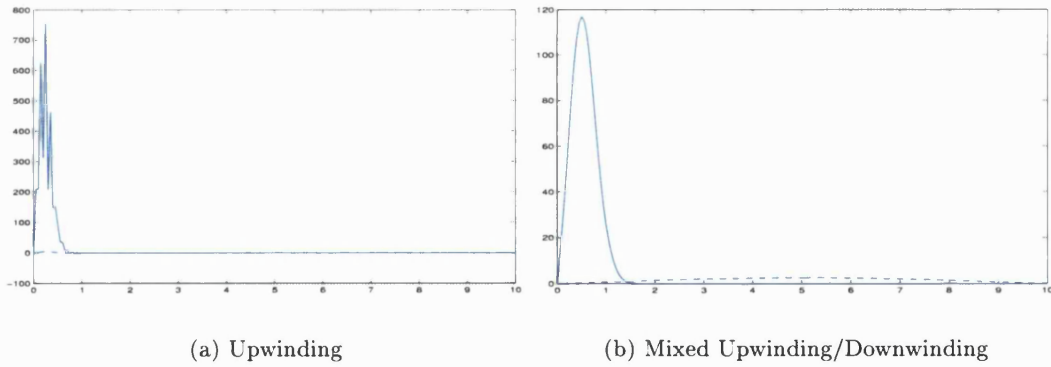


Figure 6-4: The Mean Solute Concentration of the Peristaltic Dispersion Model when using different Finite Difference Operators on the Convection Term for an example of Peristaltic Flow with Negative Velocities present. Example: Case D after 4 periods when $\epsilon = 0.156$, $\alpha = 0.3$, $\hat{\psi}_w = -0.45$, $P_{eh} = 1000$, $D_{ar} = 1$.

In Figure 6-4(a) we expected a Gaussian profile. However, spurious oscillations have occurred that are not a result of trapping as Case D has none. To compensate for the oscillations, we can apply a mixed upwinding/downwinding scheme on the convection term. We simply apply upwinding $\Delta_{-\chi}$ if the axial velocity is positive and downwinding if flow is negative. The results are shown in Figure 6-4(b) and we achieve a Gaussian

profile for the peristaltic mean solute concentration. This scheme is quite reliable with the only drawback being that the DAE solver now takes up to 10 times longer to solve as a result of checking the velocity at every point (χ_j, κ_k) for all iterations in time and possibly increased stiffness in the system.

6.4 Summary

In this Chapter we have described the numerical schemes we have used to solve our 1D and 2D dispersion models. We have used finite difference operations and applied the method of lines to convert the dispersion equations into a system of odes $M(c)c' = g(t, x, c)$ which we solved using DASSL, a DAE solver for FORTRAN.

We solved the 1D dispersion model most accurately by applying a diffusion transformation to reduce the artificial numerical dispersion. The 1D MMPDE is more accurate than the standard scheme (6.1.2) but is useful for future work if we were to model absorption as non-constant to reflect the decrease in villi, and hence the permeability of the membrane down the intestine. In this case the diffusion transformation is no longer applicable. Due to the complexity of the 2D dispersion models we could only solve the model accurately using a nonuniform mesh to locate gridpoints at the membrane to capture the boundary layer. Ideally a 2D MMPDE would be applied to capture not only steep concentration gradient at the boundary but also at the sharp wave front.

Our main effort was in solving the peristaltic dispersion model (5.1.5) which is a moving boundary problem. We applied a moving domain transformation to solve the problem on a rectangular computational domain that is fixed in time rather than the moving physical peristaltic domain. We discretised the resulting equations, shown in Figure 6-3, using standard finite difference operators on a nonuniform mesh. However, we implemented an alternating upwinding/downwinding scheme on the convection term to adapt to changes in the sign of the axial velocity to remove spurious oscillations.

Chapter 7

Conclusions

In this thesis we have been tasked with answering several questions posed by Unilever concerning the motion and absorption of solute in the intestine. They were

- How do substances flow in the small intestine?
- Can we model this flow mathematically?
- How does the fluid flow in the small intestine affect solute motion and consequently its absorption?
- Were Stoll et al. [73] correct in assuming a 1D asymptotic dispersion equation for the motion and absorption of solute in the intestine? If not, what is a more suitable model?

Our research into fluid flow in the intestine brought to our attention one of the body's main means for propelling chyme down the intestine, 'peristalsis', a series of randomly occurring waves traversing down the intestine. We modelled these intestinal contractions as a constant standing wave propagating down the intestine (Chapter 3). By assuming that chyme is sufficiently viscous we were able to apply Stokes slow flow equations. Consequently, by prescribing the moving boundary as a travelling sinusoidal function we were then able to solve for the peristaltic velocities semi-analytically.

From the derived velocity profiles we elucidated the different effects peristalsis has on fluid behaviour and in particular solute behaviour. Namely we showed that peristalsis gives rise to circulating regions known as trapping. In particular with respect to the intestine there is centreline trapping which has been shown to enhance solute mixing and absorption and even retard solute advance when compared to Poiseuille flow. We summarise our findings in the following section. We then describe how our findings affect the approach by Stoll et al. to modelling the intestine and subsequently summarise the key features of this project that are new and discuss future work.

7.1 Modelling Peristaltic Fluid Flow in the Intestine

We have investigated the behaviour of peristaltic motion to represent intestinal motion and to derive analytically for the peristaltic velocities. These velocities have elucidated different flow patterns that depend on the pressure gradient across the wavelength, $\Delta\hat{p}_\lambda$ and the amplitude of vibration of the peristaltic wave, α .

Peristalsis operates in two phases: (i) *pumping*, when there is a pressure rise across the tube, and (ii) *copumping*, when there is a pressure drop and peristalsis assists the pressure gradient in moving the fluid. We have discussed the difficulty in measuring the actual pressure gradient in the intestine and at best we can only estimate it based on the observed average velocity of chyme in the intestine u_c . We do this by determining the time mean volume flow rate \hat{Q} from u_c and then calculating the pressure gradient $\Delta\hat{p}_\lambda$ from the flow rate.

Using anatomical parameters we have shown that there should be a pressure rise across the intestine which is consistent with the illeocecal sphincter being predominantly closed. However, when the sphincter does open there should be a pressure drop driving the flow and peristalsis would operate in ‘copumping’. The pressure gradient at any given moment across the intestine is unknown and we discuss the behaviour of each type of peristaltic flow.

We have elucidated with particle paths two peristaltic phenomena; *reflux* and *trapping*. In the pumping phase fluid particles undergo reflux and centreline trapping. However, in the copumping phase fluid particles undergo either centreline trapping or detached trapping. We have shown as the flow rate increases that (i) the amount of trapping decreases and that (ii) the peristaltic flow tends to Poiseuille flow. These results are reflected in the behaviour of the mean solute concentration of solute in a peristaltic flow.

7.2 Modelling Solute Behaviour in a Peristaltic Flow

To understand solute behaviour in a peristaltic flow we modelled the solute concentration by a 2D dispersion model for solute with peristaltic velocities \mathbf{u} ,

$$c_t + \mathbf{u} \cdot \nabla c = D \nabla^2 c, \quad \text{in } \Omega.$$

Fundamental to applying the model to solute motion in the intestine is prescribing a suitable boundary condition to represent passive absorption. We applied the diffusive flux condition

$$-D \mathbf{n} \cdot \nabla c = K_a c, \quad \text{on } \Gamma,$$

to model absorption across the membrane.

We considered first the trivial case of the peristaltic dispersion model, when the

amplitude of vibration is zero. It has been shown that in this case the model reduces to the 2D Poiseuille dispersion model,

$$c_t + u(r)c_x = D\nabla^2 c, \quad \text{in } \Omega.$$

This equation is the basis of the model by Stoll et al. [73] in their model of solute motion in the intestine. For small Péclet number the equation can be reduced to a 1D dispersion process of the mean solute concentration with the solution exhibiting a Gaussian profile. As the Péclet number increases, convective fluxes dominate and the mean solute concentration \bar{c}_{po} takes the form of a negatively distorted bell curve (see Figure 4-3).

We solved the 2D peristaltic dispersion model numerically and observed that the mean solute concentration \bar{c}_{pe} was approximately \bar{c}_{po} plus some oscillatory component provided there is negligible trapping. We can remove the oscillatory term using a low pass filter to obtain a ‘cleaner’ mean solute concentration for the peristaltic model, \bar{c}_{pe}^f , which is approximately the Poiseuille mean solute concentration \bar{c}_{po} . When trapping presents itself in the peristaltic flow, the Poiseuille-like streamlines distort and \bar{c}_{pe} can no longer be represented by \bar{c}_{po} and we observe an increasingly oscillatory solution when trapping increases.

However, it is centreline trapping that greatly affects the effective velocity of the mean solute concentration. We have shown that (i) the advance of the solute front is retarded by the circulating streamlines and that (ii) solute diffuses backwards (in the wave frame sense) into trailing trapping boli. The combination of the two phenomena imply substantial mixing and convective dispersion of the solute. The results of the peristaltic model are shown by increased absorption when compared to the Poiseuille model

7.3 Stoll’s Approach to Modelling Solute in the Intestine

The basis of this thesis was the paper by Stoll et al. [73]. The authors applied a macrotransport approach [10] to the motion of solute and its absorption in the intestine. We investigated the suitability of applying their asymptotic analysis of the 2D Poiseuille dispersion model. However, we were unable to recreate the results described in Stoll et al. [73] and we were unfamiliar with the macrotransport approach. Hence, we reworked the analysis of (i) Taylor [74] for the impermeable case and (ii) Lungu et al. [52] for the permeable case, to show that their 1D asymptotic equations are the same equations derived by Stoll et al. using the macrotransport approach.

When the boundary is impermeable the macrotransport approach [10] reduces the 2D model to a 1D asymptotic equation

$$\bar{c}_t + U_e \bar{c}_x = D_e \bar{c}_{xx},$$

for the mean solute concentration which was first described by Taylor [74]. We have shown the asymptotic equation can only be applied if the following conditions are satisfied, they are (i) the 1D equation for \bar{c} is an effective representation of the full 2D model only after some time $\check{t} \gg t^* = P_{er}$ and (ii) the distance travelled by the mean solute concentration after time t^* is approximately $d = \ell P_{er}$, hence, for the unit tube we require $d \ll 1$ if we want to represent \bar{c} by the 1D equation. For the therapeutic parameters used by Stoll [73] we show that the conditions in the intestine are not met.

In the case of the permeable membrane, by reworking the analysis of Moffatt et al. [52] we were able to understand reasons why our attempt at recreating Stoll's results failed. It turned out that in all the papers by Stoll et al. [73], [10], [6] the absorption coefficient K_e is stated incorrectly resulting in abnormal levels of absorption.¹

To apply the 1D asymptotic equation to the intestine Stoll et al. [73] applied a fictitious initial condition to compensate in the short time for mass lost so that the 1D equation would be valid for all time.

We have shown by (i) rederiving the fictitious initial condition and (ii) numerically solving the 1D equation with the fictitious term and the 2D model that the fictitious term has no overall effect whatsoever. Secondly Stoll modelled peristalsis in the intestine by enhanced diffusion. We showed this was also in error by (i) stating the original formula found in [10] which clearly suggests that application of the enhanced diffusion formula by Stoll et al. violates its derivation and (ii) we solved the peristaltic dispersion model for \bar{c}_{pe} for flow with large trapping and the Poiseuille dispersion model with increased diffusion for \bar{c}_{po}^e and have shown that the mean concentration profiles look increasingly less alike. Hence peristaltic flow is far too complex to be modelled simply by enhanced diffusion.

7.4 What Aspects of the Thesis are New?

In this section we highlight for the reader, the new elements of the thesis that set it aside from previous work. We discuss our methods and results for the three main Chapters of the thesis.

7.4.1 Modelling Peristaltic Flow

In deriving the peristaltic flow (Chapter 3) we discussed the break down of the semi-analytic solution for the streamfunction as the amplitude of vibration increases. The semi-analytic solution was determined from a perturbation expansion in ϵ , the wave

¹We also found a number of calculation errors in Stoll et al. [73] when determining the dimensionless parameters.

curvature, for the biharmonic equations. Previous literature assumed $\epsilon = 0$ and took the solution to leading order. However, we have highlighted that for small but not negligible wave curvature, for example, $\epsilon \approx 0.2$, the $O(1)$ solution begins to significantly break down as α increases and it may be necessary to recover $O(\epsilon^2)$ terms. However, for the intestine $\epsilon \approx 0.15$ and we have shown, not assumed, that the $O(1)$ solution is sufficient for use.

We elucidated the different mixing attributed to peristaltic flow by plotting particle paths. We investigated the behaviour of trapping as the flow rate varies to determine the proportion of fluid in one wavelength circulating as a result of trapping. Some further analysis showed that (i) peristaltic flow tends to Poiseuille flow as the flow rate increases, (ii) trapping is maximised at the point of detachment and (iii) trapping increases as α increases.

7.4.2 Dispersion Models in Cylindrical Flow with Application to the Intestine

By nondimensionalising the 2D Poiseuille Dispersion model (Chapter 4) we have brought to the attention of the reader two important parameters ℓ and P_{er} , the length scale ratio and the radial Péclet number respectively. In reworking the analysis of Taylor's long time asymptotics of the Poiseuille dispersion model in the impermeable case, we have shown that $\ell P_{er} \ll 1$ must be very small for a good fit of the 2D Poiseuille mean solute concentration to the 1D asymptotic mean solute concentration before solute convects out of the tube. Hence for the therapeutics described in [73] the conditions for applying the asymptotic equation are not met.

For the permeable case we investigated the macrotransport approach by Stoll et al. described in [10] where they apply long time asymptotic analysis to real problems for all time by introducing a fictitious initial condition. By reworking their analysis and solving the full 2D model we have shown that this fictitious initial condition is ineffective. A clear example of this is when the boundary becomes impermeable. According to Stoll et al. the fictitious term satisfies $\bar{A}^* = 1$ but we have shown that the numerical and asymptotic solution are far from equal when ℓP_{er} is not small (see Figure 4-3). Our result casts serious doubt on applying a *macrotransport approach* to real problems. Further doubt is cast on the model by Stoll et al. when an enhanced diffusion equation is applied to simulate the effects of peristaltic flow. We later showed this to be in error too. Our research into macrotransport processes has become quite important to Unilever. They were considering to apply a macrotransport approach to a second PhD case study in the area of multiphase flows in flexible channels. Our research has highlighted the limits of such methods.

7.4.3 The Peristaltic Dispersion Model

We combined the peristaltic fluid mechanics with a dispersion model to describe the motion of a solute in a peristaltic flow. We numerically solved the 2D peristaltic dispersion model, a moving boundary problem, by transforming the moving peristaltic domain to a rectangular computational domain. To solve for the solute concentration profile when the velocity is changing we applied an alternating upwinding/downwinding finite difference operator to the convection term to remove spurious oscillations.

We have obtained five main results from solving the model, (i) peristaltic flow induces oscillations in the mean solute concentration, which for sufficiently small levels of trapping can be removed by a low pass filter to reveal an underlying Poiseuille mean solute concentration profile \bar{c}_{po} , (ii) trapping distorts the Poiseuille-like streamlines so that the mean solute concentration for such flows no longer resembles that of \bar{c}_{po} , (iii) centreline trapping retards solute motion and is seen to enhance convective dispersion by solute diffusing into trailing waves of trapping, (iv) peristalsis is too complex to be modelled by Poiseuille flow plus enhanced diffusion as suggested by Stoll as the simplification simply can not factor the effects of trapping, (v) peristaltic flow enhances absorption when compared to Poiseuille flow.

7.5 Final Thoughts

Current pharmacological models used to estimate absorption of therapeutics in the intestine oversimplify intestinal motility to plug flow. Consequently the compartment models do not accurately model gut mixing. There have been attempts at modelling the intestine more accurately by taking into account spatial and dispersion effects. None more advanced than the 1D asymptotic equation of the 2D Poiseuille dispersion model by Stoll et al. However, the asymptotics were inappropriately applied and assumed solute motion was more dispersive than it actually is. By introducing the *peristaltic dispersion model* we have modelled the peristaltic forces overlooked by previous simpler 1D models, namely reflux and trapping. We have shown that solute motion is retarded by centreline trapping, allowing solute to remain longer at the entrance to the intestine where there are more villi to absorb. The regions of circulation would greatly enhance mixing of enzymes released at the epithelial membrane with solute in the lumen.

7.6 Future Work

There were many other features of the intestine that we wanted to capture in a model which we had investigated but were unable to follow through. There are four key parts to our model of the intestine that can be investigated, namely developing a more accurate representation of (i) the geometry of the intestine, (ii) the fluid flow, (iii) the

numerical scheme and (iv) the absorption boundary condition.

The Geometry of the Intestine. We have so far assumed a fixed radius tube to represent the intestine, however, the width of the intestine decreases and so should that of the tube. There are two possible adaptations of our model. For the Poiseuille dispersion model we can prescribe a function to describe the radius of the tube and then rederive the laminar flow which will now depend on the axial coordinate as well, $u(x, r)$. We can then apply a suitable domain transformation (similar to that of the peristaltic model) to solve the dispersion model on a rectangular domain. However, for the peristaltic model with a shrinking tube, the peristaltic velocities would now be very difficult to determine as we can no longer solve the biharmonic equation in the wave frame. An alternate method must be sought.

The Fluid Flow. In this thesis we have assumed chyme in the intestine is sufficiently viscous that it can be modelled by a Newtonian fluid. However, it may be more reasonable to assume chyme behaves like a Power Law Fluid, a fluid whose viscosity decreases as the shear rate increases, e.g. water-base polymer muds. The peristaltic flow of non-Newtonian fluids has been briefly discussed in [70]. We further assumed that the peristaltic flow was steady. It would be very interesting to determine peristaltic flow in the unsteady case to observe the initial mixing of solute (an example of which is seen in [48]). We would like to understand the effects of the peripheral layer of water that surrounds the chyme on solute motion and mixing. We present in Appendix §A the effects of a peripheral layer on Poiseuille flow as a start in the modelling of peristaltic flow of fluid with nonuniform viscosity.

The 2D Numerical Scheme. We observed that the numerical solution of the 2D dispersion models suffers from (i) artificial numerical dispersion from the sharp wave front of a ‘slug’ initial condition and (ii) a boundary layer from passive absorption at the boundary. The most effective means to solve the model as accurately as possible would be to implement a 2D adaptive numerical scheme, namely a 2D MMPDE. This is quite difficult to do in practice but time permitting to develop such a scheme would be an extremely valuable tool. An alternate means for solving the peristaltic dispersion model would also be useful.

The Absorption Boundary Condition. Fundamental to modelling absorption across the epithelial layer was the absorption boundary condition. This was modelled by the flux term $-Dn \cdot \nabla c = Kc$ to represent passive diffusion. However, this was just an approximation to the unknown physical boundary condition. So far we have neglected the villi by assuming they do not affect the flow and are sufficiently small that they can be modelled as the flux boundary condition. For a more realistic model we could also determine solute motion through the villi as well, see Appendix §B for an introduction. Some asymptotic analysis may then give rise to a more accurate boundary condition where there may be slight convection and diffusion along the boundary.

Appendix A

Future Work 1: Modelling A Peripheral Layer of Water

In this section we review in more detail literature where peristaltic flow has been applied to the intestine so that we can learn and improve upon our peristaltic dispersion model as a suitable representation of solute flow in the intestine. More specifically we discuss previous work on modelling the peripheral layer of water surrounding the chyme in the intestine. We base this appendix Chapter on the variation in viscosity seen in the intestine to learn the effects of a water layer has on (i) fluid flow and (ii) solute motion.

We discuss previous efforts to model the peripheral layer by (i) two separate fluids with different flow rates and viscosity and (ii) as one fluid with slightly exponentially decaying viscosity. In the former case the flow suffered from non-uniqueness of the fluid layer interface position. In the latter the model was for axisymmetric flow but the authors applied a channel flow viscosity variation ($\check{\mu} = e^{-\nu\check{r}}$ and $\check{\mu}_{\check{r}} \neq 0$). We consider modelling the radial viscosity variation for Poiseuille flow as a basis of future work on describing the effect of a peripheral layer on peristaltic flow.

We rederive from the Navier-Stokes equation the biharmonic equations for radially varying viscosity by assuming a slowly varying solution. We model viscosity variation for a corrected axisymmetric exponential decay, $\check{\mu} = e^{-\nu\check{r}^2}$, and by applying a perturbation expansion in the small parameter ν to the biharmonic equations we obtain a semi-analytic solution for the streamfunction and velocity. We show a drop in viscosity at the boundary results in a decrease in the effective velocity and effective diffusion of the solute centroid as absorption increases. However, the viscosity drop is small and we proceed to model a larger drop in viscosity by a boundary layer function $\check{\mu}(\check{r})$ where we can prescribe the drop in viscosity and the width of the layer. We solve numerically the amended biharmonic equations to determine the velocity \check{u} using a nonuniform equidistributed mesh and determine the effective velocity. Hence, we implement the velocity into the 2D laminar flow model and elucidate the effects of the peripheral layer on the mean solute concentration.

We observe that a small peripheral layer with a large drop in viscosity results in a velocity profile with faster streamlines in the vicinity of the boundary. We can reproduce similar results by assuming that the velocity satisfies the same standard biharmonic equations but with a relaxed no-slip condition to indicate a slip velocity at the boundary. We do so by implementing the Navier-slip law

$$\tilde{u} + \lambda \tilde{u}_{\tilde{r}} = 0,$$

that implies velocity at the boundary depends on the shear stress. As $\lambda \rightarrow \infty$ the fluid flow tends to plug-like flow.

For the peristaltic case applying a variation in the viscosity to fluid flowing by peristalsis. It is no longer possible to model the radial viscosity by the exponential function seen in the earlier perturbation expansion, as that implies a nonuniform viscosity on the boundary $\tilde{r} = \tilde{f}(\tilde{x})$. If we were to add a slight modification so that $\tilde{\mu} = e^{-\frac{\nu \tilde{r}^2}{\tilde{f}(\tilde{x})}}$ to yield constant viscosity at the boundary, then we impose a periodic axial variation in viscosity $\tilde{\mu} = \tilde{\mu}(\tilde{x}, \tilde{r})$ which can not be modelled by our simplified radially varying viscosity biharmonic equations. Hence we can not apply the perturbation expansion to obtain a semi-analytic solution. Nor can we model the layer by applying a modified boundary layer function as in the Poiseuille flow case. For a small layer we suggest an alternative model where we can model the effect of the water by relaxing the no-slip condition as seen in the Poiseuille flow case.

A.1 Previous Efforts to Model the Peripheral Layer

Shukla et al. [66] modelled peristaltic flow in the intestine in a similar way to Barton [5], however, they considered the presence of a peripheral layer of mucus (observed by Guton (1971)) in the intestine surrounding the chyme core. This is due to the presence of fluid from various glands and organs being secreted into the GI tract. As much as 6 to 7 litres [21] plus a couple of litres of water from every day consumption [20]. This gastric mucus layer is approximately 0.1 cm thick with viscosity varying from $1 - 10^2$ cP, while the chyme has similar viscosity to that of faeces, about $10^3 - 10^6$ cP. Scaling the viscosity of the chyme to be one then the viscosity of the mucus layer is between 10^{-4} and 10^{-2} . Shukla modelled the peripheral layer and assumed the chyme core takes form similar to that of the wall. Hence, they found that the flow rate \hat{Q} increases if (i) the viscosity of the mucus decreases or (ii) the gastric layer thickness increases [66].

The analysis of the results is very useful and are true even though Shukla's choice of interface shape was independent of viscosity. This was later shown to violate the conservation of mass giving inaccurate results [9]. The theory was later revised by Rao et al. [63] in the axisymmetric case, however the position of the interface was non-unique for certain flow rates. Numerical results have shown that as the viscosity ratio

increases the amount of reflux decreases in the pumping case, this is consistent, since a decrease in the viscosity of the layer decreases the pressure drop over a wavelength (reflux is pressure dependent) [63].

Given that the gastric layer at the wall is less viscous than the chyme core [66], ElMisery et al. proposed the viscosity varies radially, decreasing away from the axisymmetry line [21]. It was proposed by Srivastava et al. [71] that the dimensionless form of the viscous function should take form $\check{\mu}(\check{r}) = e^{-\nu\check{r}}$, an exponentially decaying viscosity, whereby for small viscous parameter $\nu \ll 1$, the function may be simplified to $\check{\mu}(\check{r}) = 1 - \nu\check{r}$. This was applied to peristaltic flow in the presence of an endoscope [21] and later to peristaltic hydromagnetic flow [20]. This choice of function is not axisymmetric and so $\check{\mu}(\check{r}) = e^{-\nu\check{r}^2}$ would be more appropriate. To see how the change in viscosity affects fluid behaviour we must first rederive the biharmonic equations for radially varying viscosity, $\check{\mu} = \check{\mu}(\check{r})$.

A.2 Rederiving the Biharmonic Equations for Fluid Flow with a Radially Variation in Viscosity

In Chapter 3 we used the simplified version of the Navier-Stokes equation for constant fluid viscosity. The original equations takes the form

$$\rho \frac{D\mathbf{u}}{Dt} + \nabla p = \nabla \cdot (\mu(\nabla\mathbf{u} + (\nabla\mathbf{u})^T)). \quad (\text{A.2.1})$$

For constant viscosity, μ factorises out of the brackets and $\nabla \cdot ((\nabla\mathbf{u})^T) = 0$ by the continuity equation, simplifying (A.2.1) to (3.2.1). The velocity rate of strain components for an axisymmetric geometry are [65]:

$$\nabla\mathbf{u} = v_r e_r e_r + u_r e_r e_x + \frac{v}{r} e_\theta e_\theta + v_x e_x e_r + u_x e_x e_x,$$

$$(\nabla\mathbf{u})^T = v_r e_r e_r + v_x e_r e_x + \frac{v}{r} e_\theta e_\theta + u_r e_x e_r + u_x e_x e_x,$$

$$\nabla \cdot (\mu(\nabla\mathbf{u})^T) = \frac{e_r}{r} \left(\frac{\partial}{\partial r} \left(r\mu \frac{\partial v}{\partial r} \right) + \frac{\partial}{\partial x} \left(r\mu \frac{\partial u}{\partial r} \right) - \frac{\mu v}{r} \right) + \frac{e_x}{r} \left(\frac{\partial}{\partial x} \left(r\mu \frac{\partial u}{\partial x} \right) + \frac{\partial}{\partial r} \left(r\mu \frac{\partial v}{\partial x} \right) \right),$$

$$\nabla \cdot (\mu\nabla\mathbf{u}) = \frac{e_r}{r} \left(\frac{\partial}{\partial r} \left(r\mu \frac{\partial v}{\partial r} \right) + \frac{\partial}{\partial x} \left(r\mu \frac{\partial v}{\partial x} \right) - \frac{\mu v}{r} \right) + \frac{e_x}{r} \left(\frac{\partial}{\partial x} \left(r\mu \frac{\partial u}{\partial x} \right) + \frac{\partial}{\partial r} \left(r\mu \frac{\partial u}{\partial r} \right) \right).$$

Assuming viscosity varies only in the radial direction and not in the axial direction we can combine the terms and split them into radial and axial components. This yields the Navier-Stokes Equation for radially varying viscosity

$$\rho (vv_r + uv_x) + p_r = \frac{2}{r} (r\mu v_r)_r + \mu (u_r + v_x)_x - \frac{2\mu v}{r^2}, \quad (\text{A.2.2})$$

$$\rho(vu_r + uv_x) + p_x = 2r\mu u_{xx} + \frac{1}{r}(r\mu(v_x + u_r))_r. \quad (\text{A.2.3})$$

We can convert the pressure-velocity equations (A.2.2), (A.2.3) into streamfunction-vorticity notation. The streamfunction equation is given by $-\phi = L_{-1}(\psi) = \nabla \times \nabla \psi$, as seen in Chapter 3. However, for radial variation in the viscosity μ , Stokes equation $\nabla p = (\mu(r)\nabla \times \omega)$ is no longer valid and we would have to convert equations (A.2.2), (A.2.3) into streamfunction-vorticity equation manually. However, we can assume that the fluid is sufficiently viscous that the Reynolds number is sufficiently small and we can remove the nonlinear inertia terms and nondimensionalise so that

$$\begin{aligned} \check{p}_{\check{r}} &= \frac{2\epsilon^2}{\check{r}}(\check{r}\mu\check{v}_{\check{r}})_{\check{r}} + \epsilon^2\mu(\check{u}_{\check{r}} + \epsilon^2\check{v}_{\check{x}})_{\check{x}} - \frac{2\mu\check{v}\epsilon^2}{\check{r}^2}, \\ \check{p}_x &= 2\epsilon^2\check{r}\mu\check{u}_{\check{x}\check{x}} + \frac{1}{\check{r}}(\check{r}\mu(\epsilon^2\check{v}_{\check{x}} + \check{u}_{\check{r}}))_{\check{r}}. \end{aligned}$$

Hence, if the curvature of the wave is sufficiently small we may exclude $O(\epsilon^2)$ terms, and we obtain the simplified pressure-velocity equations

$$\check{p}_{\check{r}} = 0, \quad \check{p}_{\check{x}} = \frac{1}{\check{r}}(\check{r}\mu\check{u}_{\check{r}})_{\check{r}}.$$

The vorticity stream function equation is independent of the viscosity variation and for small wave number, still satisfies

$$\check{\psi}_{\check{r}\check{r}} - \frac{1}{\check{r}}\check{\psi}_{\check{r}} = -\check{\phi}.$$

Now the radial pressure gradient is negligible and the axial pressure gradient takes the form $\nabla p = \nabla \times (\mu(r)\omega)$. Hence taking the curl implies:

$$\frac{\partial}{\partial \check{r}} \left(\frac{1}{\check{r}}(\check{r}\mu\check{u}_{\check{r}})_{\check{r}} \right) = 0 \quad \Rightarrow \quad \check{\phi}_{\check{r}\check{r}} + \left(\frac{2\mu_{\check{r}}}{\mu} - \frac{1}{\check{r}} \right) \check{\phi}_{\check{r}} + \left(\frac{\mu_{\check{r}\check{r}}}{\mu} - \frac{\mu_{\check{r}}}{\check{r}\mu} \right) \check{\phi} = 0$$

Consequently the Biharmonic equations take the following form

$$\begin{aligned} \check{\psi}_{\check{r}\check{r}} - \frac{1}{\check{r}}\check{\psi}_{\check{r}} &= -\check{\phi}, \\ \check{\phi}_{\check{r}\check{r}} + \check{\mu}_1\check{\phi}_{\check{r}} + \check{\mu}_2\check{\phi} &= 0, \end{aligned} \quad (\text{A.2.4})$$

which reduces to the uniform viscous biharmonic problem when $\nu = 0$.

A.3 Deriving Fluid Flow in the Presence of a Peripheral Layer

We model the radially varying viscosity for laminar flow to understand the effect of the peripheral layer on the fluid flow. We determine the axial velocity for (i) a small

viscosity variation using a perturbation expansion for $\check{\mu}(\check{r})$ and (ii) a large viscosity variation by using a boundary layer function that prescribes the size of the boundary layer, γ , and the viscosity at the boundary, $\check{\mu}_c$.

A.3.1 Modelling the Peripheral Layer by a Weak Variation in the Viscosity

Based on work by ElMisery et al.[21], we seek a solution for the amended Biharmonic problem (A.2.4) as a power series in ν for the radially varying viscosity $\check{\mu} = e^{-\nu\check{r}^2}$. For small ν if we were to take the simplified form of the viscous equation $\check{\mu} = 1 - \nu\check{r}^2$ it would actually complicate matters as the viscous fraction derivatives would not cancel (e.g. $\check{\mu}_1, \check{\mu}_2$ do not simplify). Hence, for any ω , taking $\check{\mu} = e^{-\nu\check{r}^2}$ then the tangential vorticity equation satisfies

$$\check{\phi}_{\check{r}\check{r}} + \left(-4\nu\check{r} - \frac{1}{\check{r}}\right) \check{\phi}_{\check{r}} + (4\nu^2\check{r}^2) \check{\phi} = 0.$$

We seek a solution to (A.2.4) in the form of a perturbation expansion in ν for the vorticity, the streamfunction, velocity, and the effective velocity,

$$\check{\phi} = \check{\phi}_0 + \nu\check{\phi}_1 + \nu^2\check{\phi}_2 + \dots, \quad (\text{A.3.1})$$

$$\check{\psi} = \check{\psi}_0 + \nu\check{\psi}_1 + \nu^2\check{\psi}_2 + \dots, \quad (\text{A.3.2})$$

$$\check{u} = \check{u}_0 + \nu\check{u}_1 + \nu^2\check{u}_2 + \dots, \quad (\text{A.3.3})$$

$$\check{u} = \check{u}_0 + \nu\check{u}_1 + \nu^2\check{u}_2 + \dots \quad (\text{A.3.4})$$

Hence substituting the above power series in ν into the biharmonic equations and comparing of power of ν we obtain

$$\begin{aligned} O(1) \quad \check{\phi}_{0,\check{r}\check{r}} - \frac{1}{\check{r}}\check{\phi}_{0,\check{r}} &= 0, & \check{\psi}_{0,\check{r}\check{r}} - \frac{1}{\check{r}}\check{\psi}_{0,\check{r}} &= -\check{\phi}_0, \\ O(\nu) \quad \check{\phi}_{1,\check{r}\check{r}} - \frac{1}{\check{r}}\check{\phi}_{1,\check{r}} &= 4\check{\phi}_{0,\check{r}\check{r}}, & \check{\psi}_{1,\check{r}\check{r}} - \frac{1}{\check{r}}\check{\psi}_{1,\check{r}} &= -\check{\phi}_1, \\ O(\nu^2) \quad \check{\phi}_{2,\check{r}\check{r}} - \frac{1}{\check{r}}\check{\phi}_{2,\check{r}} &= 4\check{\phi}_{1,\check{r}\check{r}} - 4\check{\phi}_0\check{r}^2, & \check{\psi}_{2,\check{r}\check{r}} - \frac{1}{\check{r}}\check{\psi}_{2,\check{r}} &= -\check{\phi}_2. \end{aligned}$$

The following boundary conditions at the membrane and symmetry axis must apply for each order of ν :

$$\begin{aligned} O(1) \quad \check{\psi}_0(\check{x}, 0) &= 0, \quad \check{\psi}_{0,\check{r}\check{r}\check{r}}(\check{x}, 0) = 0, \quad \check{\psi}_0(\check{x}, 1) = \check{\psi}_w, \quad \check{\psi}_{0,\check{r}}(\check{x}, 1) = 0, \\ O(\nu) \quad \check{\psi}_1(\check{x}, 0) &= 0, \quad \check{\psi}_{1,\check{r}\check{r}\check{r}}(\check{x}, 0) = 0, \quad \check{\psi}_1(\check{x}, 1) = 0, \quad \check{\psi}_{1,\check{r}}(\check{x}, 1) = 0, \\ O(\nu^2) \quad \check{\psi}_2(\check{x}, 0) &= 0, \quad \check{\psi}_{2,\check{r}\check{r}\check{r}}(\check{x}, 0) = 0, \quad \check{\psi}_2(\check{x}, 1) = 0, \quad \check{\psi}_{2,\check{r}}(\check{x}, 1) = 0. \end{aligned}$$

Determining the Integrals of the Bessel Function

In calculating the effective velocities we need to calculate the following integrals $\int_0^1 \tilde{r}^n J_0(\beta_0 \tilde{r}) d\tilde{r}$ where n is odd. This requires repeated integration by parts,

$$\begin{aligned} I_0 &= \int_0^1 \tilde{r} J_0^2(\beta_0 \tilde{r}) d\tilde{r} = \frac{1}{2} (J_0^2(\beta_0) + J_1^2(\beta_0)), \\ I_1 &= \int_0^1 \tilde{r}^3 J_0^2(\beta_0 \tilde{r}) d\tilde{r} = \frac{1}{12} (3J_0^2(\beta_0) + 2J_1^2(\beta_0) - J_2^2(\beta_0)), \\ I_2 &= \int_0^1 \tilde{r}^5 J_0^2(\beta_0 \tilde{r}) d\tilde{r} = \frac{1}{60} (10J_0^2(\beta_0) + 5J_1^2(\beta_0) - 4J_2^2(\beta_0) + J_3^2(\beta_0)), \\ I_3 &= \int_0^1 \tilde{r}^7 J_0^2(\beta_0 \tilde{r}) d\tilde{r} = \frac{1}{280} (35J_0^2(\beta_0) + 14J_1^2(\beta_0) - 14J_2^2(\beta_0) + 6J_3^2(\beta_0) - J_4^2(\beta_0)). \end{aligned}$$

Determining the Zeroth Order Solution

This is the standard Poiseuille flow parabolic solution taking the form

$$\begin{aligned} \check{\psi}_0(\tilde{r}) &= A_0 \tilde{r}^4 + B_0 \tilde{r}^2 = \hat{\psi}_{wp} (2\tilde{r}^2 - \tilde{r}^4), \\ \check{u}_0(\tilde{r}) &= a_0 \tilde{r}^2 + b_0 = 4\hat{\psi}_{wp} (1 - \tilde{r}^2) = \ell p_{01}. \end{aligned}$$

Hence, from asymptotic analysis in Chapter 4 the effective velocity is found by

$$\bar{u}_0 = \frac{\int_0^1 \check{u}_0(\tilde{r}) J_0^2(\beta_0 \tilde{r}) \tilde{r} d\tilde{r}}{\int_0^1 J_0^2(\beta_0 \tilde{r}) \tilde{r} d\tilde{r}} = \hat{c} \int_0^1 (a_0 \tilde{r}^2 + b_0) J_0^2(\beta_0 \tilde{r}) \tilde{r} d\tilde{r} = \hat{c} (a_0 I_1 + b_0 I_0),$$

where

$$\hat{c} = \frac{1}{\int_0^1 J_0^2(\beta_0 \tilde{r}) \tilde{r} d\tilde{r}} = \frac{2}{J_0^2(\beta_0) + J_1^2(\beta_0)}.$$

Determining the First Order Solution

This solution is $O(\tilde{r}^2)$ larger than the previous stemming from the biharmonic problem, with solution

$$\begin{aligned} \check{\psi}_1(\tilde{r}) &= A_1 \tilde{r}^6 + B_1 \tilde{r}^4 + C_1 \tilde{r}^2 = -\frac{1}{3} \check{\psi}_w (\tilde{r}^6 - 2\tilde{r}^4 + \tilde{r}^2), \\ \check{u}_1(\tilde{r}) &= a_1 \tilde{r}^4 + b_1 \tilde{r}^2 + c_1 = -\frac{2}{3} \check{\psi}_w (3\tilde{r}^4 - 4\tilde{r}^2 + 1), \\ \bar{u}_1(\tilde{r}) &= \hat{c} \int_0^1 \check{u}_1(\tilde{r}) J_0^2(\beta_0 \tilde{r}) \tilde{r} d\tilde{r} = \hat{c} (a_1 I_2 + b_1 I_1 + c_1 I_0). \end{aligned}$$

Determining the Second Order Solution

Similarly this solution is $O(\tilde{r}^2)$ greater than the first order, hence

$$\begin{aligned} \check{\psi}_2(\tilde{r}) &= A_2 \tilde{r}^8 + B_2 \tilde{r}^6 + C_2 \tilde{r}^4 + D_2 \tilde{r}^2 = -\frac{1}{36} \check{\psi}_w (3\tilde{r}^8 - 8\tilde{r}^6 + 7\tilde{r}^4 - 2\tilde{r}^2), \\ \check{u}_2(\tilde{r}) &= a_2 \tilde{r}^6 + b_2 \tilde{r}^4 + c_2 \tilde{r}^2 + \delta_2 = -\frac{1}{9} \check{\psi}_w (6\tilde{r}^6 - 12\tilde{r}^4 + 7\tilde{r}^2 - 1), \\ \bar{u}_2(\tilde{r}) &= \hat{c} \int_0^1 \check{u}_2(\tilde{r}) J_0^2(\beta_0 \tilde{r}) \tilde{r} d\tilde{r} = \hat{c} (a_2 I_3 + b_2 I_2 + c_2 I_1 + d_2 I_0). \end{aligned}$$

A.3.2 An Example of the Effect of a Weak Drop in the Viscosity on The Effective Velocity

We determine the effect of the varying viscosity on the velocity profile in the case of a large a drop in viscosity whilst maintaining $\nu < 1$. For this example we take $\nu = 0.8$, and impose a large absorption at the boundary represented by the eigenvalue $\beta_0 = 2$ from the transcendental equation (4.4.12). We impose a flow rate $\check{\psi}_w = 50$ and graph the velocity profiles up to $O(\nu^2)$ in Figure A-1.

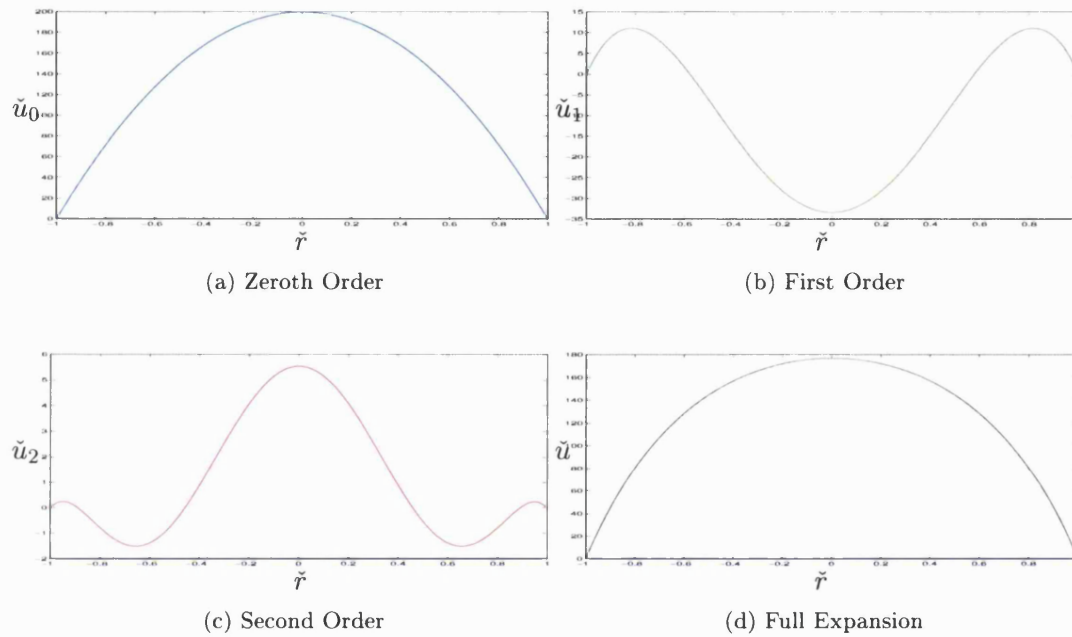


Figure A-1: Velocity Profile for varying Orders of the Perturbation Expansion

Looking at the Figure A-1(d), it is clear from the velocity profile that for decreasing viscosity, fluid flows faster at the boundary and slower at the centreline when compared to the Poiseuille case Figure A-1(a). Hence we expect the faster streamlines at the boundary to be eroded as absorption increases, resulting in a decrease in the effective velocity. We can determine the effective velocity up to order $O(\nu^2)$ and it is given by $U_e = \bar{u}_0 + \nu\bar{u}_1 + \nu^2\bar{u}_2$. In the absence of a peripheral layer the effective velocity was $U_e = \bar{u}_0 = 139.8$, and subsequently drops to $U_e = 133.9$ as $\nu \rightarrow 0.8$.

It is quite difficult to derive the effects of the drop in viscosity on the effective dispersion. It requires manipulating asymptotic analysis used in deriving Moffatt's dispersion coefficient. It is easy to show the effects numerically. We do so later.

A.3.3 Modelling the Peripheral Layer by a Boundary Layer Function for the Viscosity

The previous perturbation expansion relied on a small change in radial viscosity. If $\nu < 1$ then the viscosity at the boundary is given by $\check{\mu}_c = \check{\mu}(1) > e^{-1}$. Hence we see a gradual drop of about two-thirds in viscosity between the centreline and the wall. The actual variation of viscosity at the boundary seen with biofluids is much larger, where $\check{\mu}_c < 0.01$. Most importantly this drop occurs in a very small region at the boundary, a characteristic not captured by the function $\check{\mu} = e^{-\nu\check{r}^2}$. Hence, we derive an axisymmetric boundary layer function for the viscosity

$$\check{\mu} = Ae^{-\gamma\check{r}^2} + B = \frac{(\check{\mu}_c - 1)e^{-\gamma\check{r}^2} + (e^\gamma - \check{\mu}_1)}{e^\gamma - 1},$$

with centreline viscosity $\mu = 1$ and boundary viscosity μ_c which is defined over a small region γ at the membrane. This function is taken as the solution of the steady 1D convection diffusion pde

$$c_t + c_x = \gamma c_{xx}, \quad c(0) = 1, \quad c(1) = \check{\mu}_c,$$

which exhibits a classic boundary layer [59]. In the intestine the viscosity of chyme is approximately $10^3 - 10^6$ cP and that of the mucus layer is $1 - 10^3$ cP [66]. Hence, in nondimensional terms, there exists a boundary viscosity $\check{\mu}_c \approx 10^{-4} - 10^{-2}$ over a distance $\gamma = 0.1$.

We aim to solve the amended biharmonic equations (A.2.4) for the fluid profile to use in a 2D dispersion model, however we must solve numerically for the fluid flow. Hence, the limits on solving the dispersion model will directly affect the way we solve numerically (A.2.4) for the streamfunction and velocity. The dispersion model in Chapter 4 was given by

$$\begin{aligned} c_t + u(r)c_x &= D\nabla^2 c - K_d c, & \text{in } \Omega, \\ -Dc_r &= K_a c, & \text{on } \Gamma. \end{aligned} \tag{A.3.5}$$

Computing time and limited memory restrict the size of the mesh on which the DAE can be solved numerically. Hence, we distribute mesh points to solve the biharmonic equations numerically using a radially nonuniform mesh as seen in Chapter 6. However, we now apply the Equidistribution Principle to suitably distribute grid points to capture the boundary layer of the fluid flow. We consequently locate mesh points for the dispersion model in the same way.

Consider a mesh in the radial direction with non-uniform mesh distribution h_j for N cells. The nodes are found by $\check{r}_i = \sum_{j=1}^i h_j$ and we denote $\check{\mu}_j$ the approximation to $\check{\mu}(\check{r}_j)$. For the equidistribution principle we define a *monitor function* $M(\check{\mu}, \check{\mu}_{\check{r}}, \check{r})$ such

that for fixed mesh points at $\tilde{r} = 0, 1$ the monitor function satisfies

$$\int_{\tilde{r}_i}^{\tilde{r}_{i+1}} M(\check{\mu}, \check{\mu}_{\tilde{r}}, \tilde{r}) d\tilde{r} = \frac{1}{N} \int_0^1 M(\check{\mu}, \check{\mu}_{\tilde{r}}, \tilde{r}) d\tilde{r}.$$

An appropriate monitor functions should scale in a similar manner to the exact solution. We apply the arc-length function $M(\check{\mu}, \check{\mu}_{\tilde{r}}) = \sqrt{1 + \check{\mu}_{\tilde{r}}^2}$ so that

$$\int_{\tilde{r}_{j-1}}^{\tilde{r}_j} \sqrt{1 + \check{\mu}_{\tilde{r}}^2} d\tilde{r} = \int_{\tilde{r}_j}^{\tilde{r}_{j+1}} \sqrt{1 + \check{\mu}_{\tilde{r}}^2} d\tilde{r},$$

which can be approximated by difference methods to yield

$$\begin{aligned} h_j^2(1 + \check{\mu}_{\tilde{r}}^2)_{j-\frac{1}{2}} &= h_{j+1}^2(1 + \check{\mu}_{\tilde{r}}^2)_{j+\frac{1}{2}}, & j = 1, \dots, N-1, \\ (\check{\mu}(r_j) - \check{\mu}(r_{j-1}))^2 &= (\check{\mu}(r_{j+1}) - \check{\mu}(r_j))^2, & j = 1, \dots, N-1, \end{aligned}$$

and is solved in conjunction with the condition $\sum_{j=1}^{N-1} h_j = 1$. We compare solving the biharmonic equations for the velocity profile on (i) a nonuniform mesh with (ii) a uniform mesh.

In Figure A-2(a),(b) we observe that the equidistributed mesh captures the boundary layer, and the velocity profile displays a more prominent boundary layer not captured by the uniform mesh. We observe the fluid flow profile obtained from a uniform mesh does not differ from the standard Poiseuille flow. We observe in Figure (A-2)(d) that as absorption increases, the effective velocity of the fluid flow decreases. This is consistent with the results from the perturbation expansion for a weak drop in viscosity, only in this case the effects are more pronounced. This happens because the water layer induces much faster streamlines at the boundary and significantly slows the centreline velocity to conserve the fixed flow rate. Similarly the faster streamlines at the wall are eroded by absorption, decreasing the overall effective velocity.

A.3.4 The Effects of Modelling a Peripheral Layer on the Concentration Profile from the 2D Dispersion Model

We solve the 2D dispersion model (A.3.5) of a solute in a viscous flow surrounded by a peripheral layer of water. We consider now an example. Let the fluid flow have flow rate $\hat{\psi}_{wp} = 50$, Péclet number $Pe_r = 100$ and Damköhler number $Da_r = 1$. We are only interested in observing the effects of the peripheral layer on the mean solute concentration profile. We solve the dispersion model numerically as in Chapter 6 by applying a finite difference approach to the dispersion equation on a radially nonuniform mesh. We solve the velocity profiles for a boundary layer of size $\gamma = 0.05$ (which is consistent with the observed value in the intestine) with wall viscosity given by $\check{\mu}_c = 0.9, 0.5, 0.1, 0.001$.

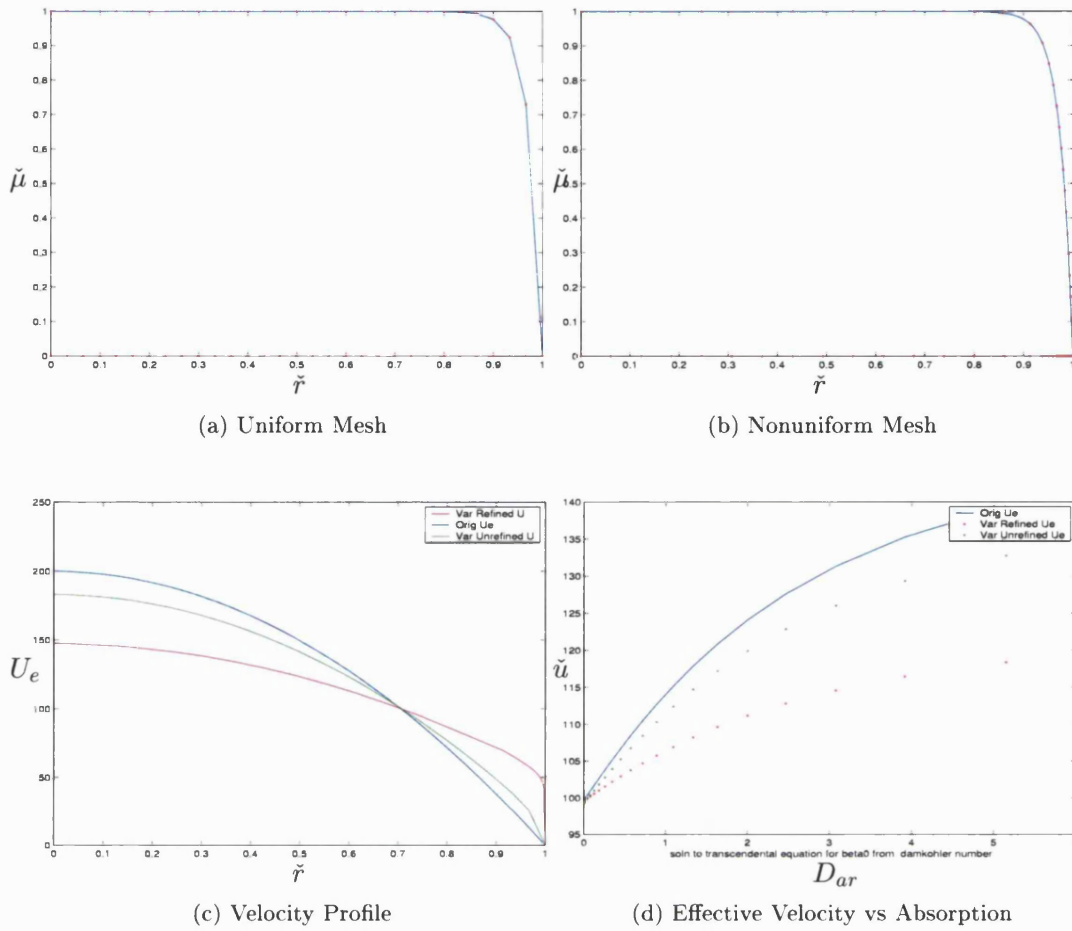


Figure A-2: The Effects of a Peripheral Layer Modelled by a Boundary Layer Function on the Fluid Flow Profile and Effective Velocity on (i) an equidistributed mesh and (ii) a uniform mesh.

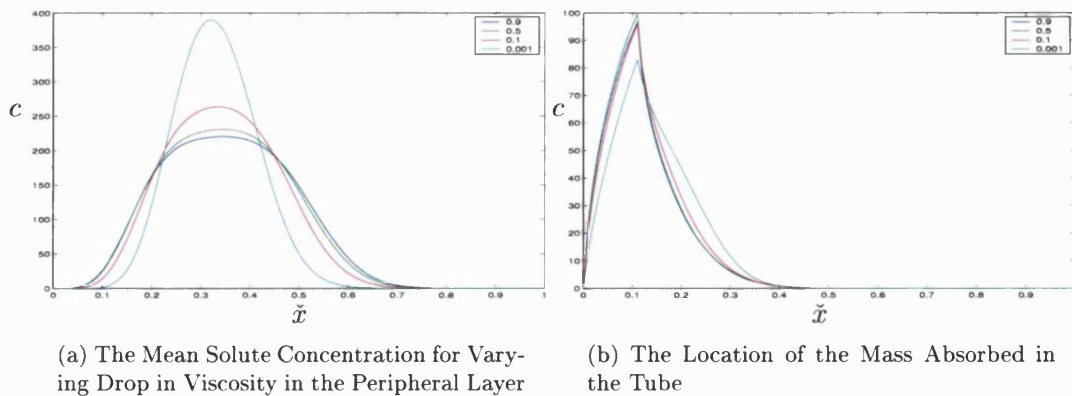


Figure A-3: The Effects of a Peripheral Layer on the 2D Dispersion Model

In Figure A-3 we observe the mean velocity of the solute centroid decreases as viscosity at the boundary decreases. This corresponds to the drop in effective velocity as faster streamlines in the boundary layer are eroded. More obvious is the effect on effective diffusion which is a more pronounced effect than that of the decrease in the effective velocity. The solute diffuses less from the decrease in convective dispersion as there are fewer slower streamlines. The increasingly plug like flow is responsible for distributing solute absorption further down the tube (see Figure A-3). However, this may not necessarily be the case in peristaltic flow.

A.4 Relaxing the No-Slip Condition

We consider laminar flow in a cylindrical tube with a peripheral layer of water. So far we have applied the no-slip condition of fluid at the boundary to represent viscous effects. The no-slip boundary condition is a core concept in fluid mechanics where there is a zero relative velocity between the fluid and the solid tube wall ($\check{u}|_{\check{r}=1} = 0$). However, 200 years ago Navier proposed a general boundary condition to incorporate fluid slip at the wall [60]. It has been observed that many foodstuffs in glass tubes exhibit a wall slip as the flowing materials squeeze out a serum to form a thin layer adjacent to the solid surface [27]. The Navier slip boundary condition is the simplest alternative to the no-slip condition and it states the the amount of slip at the wall is proportional to the tangential fluid stress at the wall. Hence, the slip velocity is a function of the wall shear stress

$$\beta\check{u} = \tau_w = \check{\mu} \left(-\frac{d\check{u}}{d\check{r}} \right), \quad \text{when } \check{r} = 1, \quad (\text{A.4.1})$$

where β is the sliding coefficient [76]. We observe the classic no-slip boundary condition as $\beta \rightarrow \infty$. In literature β is said to depend on the characteristic length of flow not just the properties of the wall and fluid [76]. Unfortunately there is no completely satisfactory method available to predict β . However, we apply the Navier-slip condition as a means to understand the affect of a peripheral layer. There are many slip-laws in use, some which exhibit a maximum and minimum value [22]. The Navier slip law can be modified for the case where there is a thin layer of a Newtonian fluid of thickness γ adjacent to the wall and is modelled by

$$\tau_w = \frac{c\check{u}_w}{\gamma}.$$

Hence the slip law can be rewritten as

$$\check{u}_w + (\mu\gamma)\check{u}_{\check{r}} = 0,$$

and we obtain the no-slip condition when $\gamma = 0$. We denote $\lambda = \mu\gamma$ to be the slip coefficient so that

$$\check{u}_w + \lambda \check{u}_{\check{r}} = 0. \quad (\text{A.4.2})$$

We consider the biharmonic equations (3.3.1) which have known solution $\check{\psi}(\check{r}) = A\check{r}^4 + B\check{r}^2$ (see §3.3). We determine the coefficients A and B from the flow rate boundary condition $\psi(1) = \psi_{wp}$ and the slip law (A.4.2) so that

$$\begin{aligned} \check{\psi}_{wp} &= \check{\psi}(1) &= A + B, \\ 0 &= \check{u}(1) + \lambda \check{u}_{\check{r}}(1) &= (4A + 2B) + \lambda(8A). \end{aligned}$$

This has streamfunction and velocity solution

$$\psi(\check{r}) = \left(\frac{(2 + 4\lambda)\psi_{wp}}{1 + 4\lambda} \right) \check{r}^2 - \left(\frac{\psi_{wp}}{1 + 4\lambda} \right) \check{r}^4, \quad (\text{A.4.3})$$

$$\check{u}_\lambda(\check{r}) = \frac{(4 + 8\lambda)\psi_{wp}}{1 + 4\lambda} - \left(\frac{4\psi_{wp}}{1 + 4\lambda} \right) \check{r}^2. \quad (\text{A.4.4})$$

Hence, we derive the slip velocity

$$\check{u}_\lambda(\check{r} = 1) = 4A + 2B = \frac{8\lambda\psi_{wp}}{1 + 4\lambda} = \delta,$$

and the centreline velocity

$$\check{u}_\lambda(\check{r} = 0) = 4A + 2B = \frac{(4 + 8\lambda)\lambda\psi_{wp}}{1 + 4\lambda}.$$

The mean velocity is given by twice the flow rate so that $\bar{V} = 2\psi_{wp}$. The limit of the velocity, \check{u} , as the slip coefficient increases is

$$\lim_{\lambda \rightarrow \infty} \check{u}_\lambda(\check{r}) = \lim_{\lambda \rightarrow \infty} (4A\check{r}^2 + 2B) = 2\psi_{wp} = \bar{V}.$$

Hence, the laminar flow tends to plug flow as $\lambda \rightarrow \infty$. We determine the effective convection by

$$U_{e\lambda} = \frac{\int_0^1 \check{u}_\lambda(r) J_0^2(\beta_0 r) r dr}{\int_0^1 J_0^2(\beta_0 r) r dr}.$$

which can be written as

$$U_{e\lambda} = \hat{c}(4AI_1 - (4 + 8\lambda)AI_0) = 4\psi_{wp}\hat{c}(I_0 - I_1) \left(\frac{1}{1 + 4\lambda} \right) + 8\psi_{wp} \left(\frac{\lambda}{1 + 4\lambda} \right).$$

Hence by differentiating $U_{e\lambda}$ with respect to λ we obtain

$$\frac{dU_{e\lambda}}{d\lambda} = \frac{4\hat{c}\psi_{wp}}{(1 + 4\lambda)^2} (I_1 - 2I_0) = -\frac{4\hat{c}\psi_{wp}}{(1 + 4\lambda)^2} \left(3J_0^2(\beta_0) + \frac{10}{3}J_1^2(\beta_0) + \frac{1}{3}J_2^2(\beta_0) \right) < 0,$$

and the effective velocity is decreasing as the slip coefficient increases.

A.5 Summary

In this section we have modelled a peripheral layer of water in the intestine by a change in viscosity of the fluid. We considered only the trivial case of peristaltic flow: Poiseuille flow case. From literature [71] it is assumed that viscosity varies according to $\check{\mu}(\check{r}) = e^{-\nu r^2}$. Hence we rederived the biharmonic equations for nonuniform viscosity and apply a perturbation expansion to derive a semi-analytical solution to the velocity profile in the uniform tube. However, the viscosity function presents a mild change in viscosity at the boundary. For a more realistic drop in viscosity as seen in the intestine we applied a more reasonable boundary layer function $\check{\mu} = Ae^{-\gamma \check{r}^2} + B$.

In this case we numerically solved for the velocity profile and showed that a peripheral layer yielded faster streamlines at the wall. As absorption increases these faster streamlines erode, leading to a decrease in effective convection and diffusion. We showed this by deriving the effective convection coefficients (as described in Chapter 4 and implementing the new velocity profile into the 2D dispersion model $c_t + \mathbf{u} \cdot \nabla c = D \nabla^2 c$ and solving numerically. From our results we have shown that for a thin water layer we can model the viscous water layer by relaxing the no-slip condition in the original biharmonic equations. Implementing the Navier-slip law $\check{u} + \lambda \check{u}_{\check{r}} = 0$ we were able to obtain an analytical solution for the velocity profile. It is then easy to show that a slip velocity at the boundary decreases the overall effective convection coefficient.

This is just an introduction to modelling the peripheral layer for the peristaltic flow case. We hope that ideas generated here will help solve for peristaltic flow with a peripheral layer, that does not yield a non-unique interface. The effects of the water layer on trapping and hence mixing would be quite important to Unilever. It may be possible to influence the size of the water layer and consequently affect solute motion to ones advantage.

Appendix B

Future Work 2: Modelling the Villi as a Porous Membrane

In this section we discuss possible future improvement of the full 2D Poiseuille dispersion model (4.4.2) by modelling the villi as a porous medium rather than a boundary condition. In previous literature [73], the villi were not specifically modelled themselves. The permeable membrane that lined the intestine was modelled by the boundary condition

$$-Dc_r = K_a c,$$

for drug diffusion D and epithelial permeability K_a . The villi and microvilli act to enhance surface area of absorption and are incorporated into the boundary condition $-Dc_r = S_a K c$, by amplifying the permeability K by the surface area S_a (a product of the villi surface area and the microvilli surface area). However, the size of the villi region decreases down the gut not only because the radius of the intestine decreases but because the villi regions also become less dense. Hence, the boundary condition $-Dc_r = S_a K c$ is crude at best and is more suitable if we were to include some axial dependency in the surface area to reflect changes in the villi structure, i.e. $-Dc_r = S_a(x) K c$.

We may incorporate the new boundary condition into (4.4.2) as a first improvement. However, the boundary condition is only an approximation of the true nature of how solute passes through the epithelium. The villi region is not sufficiently dense to assume solute particles are (i) unable to flow through the region if there is a driving pressure gradient or are (ii) unable to diffuse in the region. The assumption is less true further down the lumen as the density of villi decreases. Hence, in this section we look at free fluid flow in a tube surrounded by a porous layer. We briefly review previous work on establishing, (i) the correct interfacial boundary conditions of the fluid in the free flow and in the porous layer and (ii) the fluid boundary conditions at the outer wall of the porous medium.

Generally free fluid in a tube surrounded a porous medium has been modelled by one of two ways; 1) the *Darcy* model or 2) the *Brinkmann* model. For both models, the free fluid obeys Stokes flow

$$\mu \nabla^2 \mathbf{u}^f = -\mu \nabla p.$$

However, flow in the porous medium is assumed to satisfy in case 1) Darcy's law

$$k \nabla p = \mu \mathbf{u}^p,$$

where there is a plug flow in the medium that depends on the pressure drop, or alternatively in case 2) a combination of Stokes flow and Darcy Law

$$\nabla p = \mu_c \nabla^2 \mathbf{u}^p - \frac{\mu}{k} \mathbf{u}^p,$$

which recovers the viscous effects by imposing a no-slip at the boundary of the outer porous wall.

Consequently it is necessary to balance the free fluid Stokes equation with the Darcy or Brinkmann equation at the interfacial boundary. In the literature this has been achieved either by the Beavers-Joseph-Saffman law for the Darcy model, or for the Brinkmann equation by balancing the pressure and the velocities. We propose that we could model flow by the Brinkmann model and implement the new velocity profiles $\mathbf{u}^f, \mathbf{u}^p$ into a dispersion model where we have, 1) our standard dispersion equation,

$$c_t + \mathbf{u}^f \cdot \nabla c = \nabla(D \nabla c) - K_d c,$$

in the free fluid and 2) a dispersion equation,

$$v_t + \mathbf{u}^p \cdot \nabla v = \nabla(D \nabla v) - K_a c$$

for villi solute concentration v , in the porous villi medium where we could model absorption everywhere in the villi region. Solute is now able to flow in the porous region depending on the region's permeability and is also allowed to diffuse.

Some asymptotic analysis may allow us to reduce the porous diffusion equation to a boundary condition for the free flowing solute. This boundary condition would physiologically be more reasonable than its predecessor (4.2.1). The free fluid diffusion equation will have a non-zero velocity at the interface with slip speed depending on the shear stress and the permeability. The problem would look similar to the peripheral layer model (A.3.5) but with a new boundary condition.

B.1 Modelling Fluid Flow in a Porous Medium

Fluid flow in a channel surrounded by a permeable medium is of significant importance to engineers where many industrial processes involve modelling such phenomena. Examples include oil recovery, the manufacturing process of advanced composites and modelling underground water. Particularly coupling between groundwater and surface water presents a serious problem in predicting how pollution in lakes and rivers makes its way into a water supply. There has been various studies into accurately predicting fluid flow over such porous medium to understand the solute transport phenomena.

B.1.1 Darcy's Law

It has been widely accepted that Darcy's law is the correct model to describe steady laminar incompressible viscous flow of fluid through weakly porous media. Darcy had conducted research on the flow of water through sandbed filters. The porous medium was modelled as a collection of interconnected parallel capillary tubes where the permeability of each tube contributes to the medium's total permeability. The law assumes that permeability is independent of the medium's size and the geometry as well as the fluid, the flow rate and the pressure drop but rather the permeability is a characteristic of the porous medium. Darcy's law is applied for homogeneous isotropic mediums, that is the permeability of the porous medium is uniformly distributed and at any given point the permeability is independent of the direction. Hence, the law states that the apparent velocity \mathbf{u} is proportional to the pressure gradient ∇P in the porous medium so that,

$$\mathbf{u} = -\frac{k}{\mu} \nabla P, \quad (\text{B.1.1})$$

where μ is the dynamic viscosity of the fluid and k is the permeability of the homogeneous medium. The filtration velocity \mathbf{u} is the cross-sectional average velocity so that Darcy's law predicts a plug flow.

B.1.2 The Brinkmann Model

In many cases Darcy's law is inapplicable when fluid is flowing in a medium bounded by an impermeable boundary. The flow field can not satisfy a no flow boundary condition between the medium and the solid wall and the important transport phenomena at the boundary can not be captured by the law. Brinkmann (1947) accounted for the viscous drag and the viscous damping effects by modifying Darcy's law to be a linear semiempirical combination of (i) Stokes equation for microscopic pore level flow and (ii) Darcy's law for bulk resistance. The Brinkmann equation for a fully developed flow satisfies

$$\mu_c \nabla^2 \mathbf{u} - \frac{\mu}{k} \mathbf{u} = \nabla P, \quad (\text{B.1.2})$$

for an apparent viscosity μ_c which differs from the free fluid viscosity due to the added resistance of the porous structure. The apparent viscosity is expected to be larger than that of the fluid viscosity and is dependent on the properties of the porous media. Now the Navier-Stokes viscous resistance term has been introduced in equation (B.1.2) but the driving force is still considered to be the pressure gradient. When the permeability k is small the Darcy resistance dominates Stokes resistance and the Brinkmann equation (B.1.2) reduces to Darcy's law (B.1.1). Conversely if permeability is large, then Darcy resistance is negligible and (B.1.2) reduces to 1D steady Stokes flow. The Brinkmann model has the advantage of coping with viscous drag along walls as well as the Darcy effects in the porous medium. There are many examples of the Brinkmann model in use in flow over porous media, see [42], [8], [49], [25].

Modelling Free Fluid Flow over a Porous Medium

Consider free fluid flow over porous media. Typically flow in the non-porous channel is modelled by Stokes flow, but in literature porous flow has been modelled by either Darcy's law or the Brinkmann equation. In combining equations it is necessary to specify the location of the interface between the porous and non porous region. Even when one equation is used in both domains, for instance in a permeability step change, the interface location is required. The quantities of interest are the velocity at the interface known as the slip velocity and how far fluid penetrates into the porous medium. Porosity plays an important role, as an increase in porosity increases fluid penetration, the slip velocity and the shear.

Clearly the momentum equations describing the flow in the adjacent porous media and free fluid domain are quite different; they have different orders and are quite incompatible pdes. The fast moving flow above the interface and the slow porous medium below complicate modelling the interface velocity. For instance, Darcy's law fails to describe the penetration of high velocities into the porous medium and for shallow media, the law becomes inappropriate as velocity is no longer uniform and the viscous forces dominate. This incompatibility between the equations has resulted in a great deal of uncertainty in regards to defining appropriate boundary conditions at the interface and implies the existence of a boundary layer. Consequently the Brinkmann equation has difficulty in predicting the thickness of the layer.

A boundary condition can be found by integrating the divergence of the fluid velocity over the porous and non-porous region and applying continuity of normal velocity, a consequence of the incompressibility condition. However, for a completely determined flow it is necessary to also specify a condition on the tangential velocity component at the interface. When applying the Brinkmann equation previous authors have applied continuity of the flow; the velocities, the viscous shear stresses and the the pressure at the interface [50]. However, for more dense porous media where flow is governed

by Darcy's Law, the existence of a tangential slip velocity at the interface was demonstrated by Beavers and Joseph (1967). They developed a semi-empirical slip condition by measuring the flow rates above the porous interface and applied the laminar solution for a no-slip condition in the free region. The Beavers Joseph condition is given by

$$\gamma \left(\mathbf{u}^f \Big|_{\Gamma} - \mathbf{u}^p \right) \cdot \mathbf{t} = \sqrt{k} \mathbf{n} \cdot \nabla u^f \cdot \mathbf{t}, \quad (\text{B.1.3})$$

for the free fluid velocity u^f at the interface Γ , a porous seepage velocity u^p , the unit tangent vector to the interface \mathbf{t} , the unit normal into the fluid \mathbf{n} , a permeability k and a slip coefficient γ . The slip coefficient is a dimensionless parameter that does not depend on the viscosity of the fluid μ but rather on the geometry of the microstructure of the porous medium at the interface. Later Saffman showed by a statistical approach (later justified mathematically [56]) that the seepage velocity was much smaller than the other terms in Beavers Joseph condition so that

$$\gamma \mathbf{u}^f \Big|_{\Gamma} \cdot \mathbf{t} = \sqrt{k} \mathbf{n} \cdot \nabla u^f \cdot \mathbf{t} + O(k)$$

The Beavers Joseph condition has been thoroughly analysed to prove the unique existence of a solution to the flow in [56], [39], [40], [51], [45] and applied in [24], [44]. There are many examples of the Brinkmann model in use in flow over porous media, see [42], [8], [49], [25].

B.2 The Porous Dispersion Model

The villi and microvilli that line the intestine are very dense and greatly enhance absorption of solutes. So far they have been neglected as a physical factor in previous intestinal models, however, solute in the villi may exhibit a velocity and some diffusion, albeit small. We may model the villi region of the lumen as a porous region where we simplify the medium to that of a homogeneous isotropic region. Hence fluid flowing in the intestine is modelled by free fluid flow in a porous region.

B.2.1 Deriving the Velocity Profile

We model the intestine as a tube of radius $r = R_0$ and length $x = L_x$ with a porous region occupying $[h, R_0]$ so that $R_0 = h + \delta$ for porous radius δ . We consider an incompressible Newtonian fluid in steady flow in the tube and we assume no external forces act on the fluid. We can solve for velocities u^f and u^p in the free and porous region respectively by applying Stokes flow in the free region and the Brinkmann equation in

the porous medium.

$$\begin{aligned}\mu \nabla^2 \mathbf{u}^f &= \nabla P, & r \in [0, h], \\ \mu_c \nabla^2 \mathbf{u}^f - \frac{\mu}{k} \mathbf{u}^f &= \nabla P, & r \in [h, R_0].\end{aligned}$$

We denote μ for the fluid viscosity and μ_c for the porous viscosity. At the interface we simply apply continuity of flow and pressure.

B.2.2 Defining a Dispersion Model

For the known velocity profile we may solve two 2D coupled dispersion equations. One equation represents solute concentration $c(x, r)$ in the free fluid region, and the other models solute concentration in the villi $v(x, r)$ such that:

$$c_t + u^f(r)c_x = \nabla \cdot (D(r)\nabla c) - K_d c, \quad r \in [0, h], \quad (\text{B.2.1})$$

$$v_t + u^p(r)v_x = \nabla \cdot (D(r)\nabla v) - (K_d + K_a)v, \quad r \in [h, R_0]. \quad (\text{B.2.2})$$

Here we assume that degradation occurs in both regions with strength K_d . In reality enzymes in the villi region increase solute degradation, for simplicity we can remove the degradation rate from the villi model. We assume further that absorption occurs only in porous villi medium. We note that diffusion should vary in the free and porous region, with tighter spacing, diffusion should be much less in the villi than in the free fluid. Hence, we could model diffusion by a step function

$$\begin{aligned}D(r) &= D_f, & r \in [0, h], \\ D(r) &= kD_f, & r \in [h, R_0],\end{aligned}$$

where $k \in (0, 1)$.

B.2.3 Asymptotic Analysis

It may be possible to perform some asymptotic analysis on B.2.2 if δ is sufficiently small to reduce the villi equation it to a 1D equation for the boundary equation to B.2.1, greatly simplifying any 2D numerical scheme. Some further analysis may then reduce the 2D model to a 1D equation in order to understand the effects of the villi density on the mean solute concentration profile. This is a useful subject for further investigation.

Appendix C

Modelling Peristaltic Flow

C.1 Boundary Conditions for the Biharmonic Equations

For a regular solution of the biharmonic model, Figure 3-2, it is necessary to impose boundary condition $\hat{\psi}_{\hat{r}\hat{r}\hat{r}} = 0$ at the centreline. To prove this we convert the streamfunction-vorticity equations (3.3.1) for the case when $\epsilon = 0$ into streamfunction form

$$\hat{\psi}_{\hat{r}\hat{r}\hat{r}\hat{r}} - \frac{2}{\hat{r}}\hat{\psi}_{\hat{r}\hat{r}\hat{r}} + \frac{3}{\hat{r}^2}\hat{\psi}_{\hat{r}\hat{r}} - \frac{3}{\hat{r}^3}\hat{\psi}_{\hat{r}} = 0. \quad (\text{C.1.1})$$

We take a Taylor series expansion for $\hat{\psi} = \hat{\psi}(\hat{x}, \hat{r})$ at $\hat{r} = 0$ such that

$$\hat{\psi}(\hat{r}) = \hat{\psi}(0) + \hat{r}\hat{\psi}_{\hat{r}}(0) + \frac{\hat{r}^2}{2}\hat{\psi}_{\hat{r}\hat{r}}(0) + \frac{\hat{r}^3}{6}\hat{\psi}_{\hat{r}\hat{r}\hat{r}}(0) + \frac{\hat{r}^4}{24}\hat{\psi}_{\hat{r}\hat{r}\hat{r}\hat{r}}(0) + O(\hat{r}^5) \quad (\text{C.1.2})$$

Hence, substituting (C.1.2) into (C.1.1) for terms up to $O(\hat{r})$ we obtain

$$\begin{aligned} & \hat{\psi}_{\hat{r}\hat{r}\hat{r}\hat{r}}(0) - \frac{2}{\hat{r}} \left(\hat{\psi}_{\hat{r}\hat{r}\hat{r}}(0) + \hat{r}\hat{\psi}_{\hat{r}\hat{r}\hat{r}\hat{r}}(0) \right) + \frac{3}{\hat{r}^2} \left(\hat{\psi}_{\hat{r}\hat{r}}(0) + \hat{r}\hat{\psi}_{\hat{r}\hat{r}\hat{r}}(0) + \frac{\hat{r}^2}{2}\hat{\psi}_{\hat{r}\hat{r}\hat{r}\hat{r}}(0) \right) \\ & - \frac{3}{\hat{r}^3} \left(\hat{\psi}_{\hat{r}}(0) + \hat{r}\hat{\psi}_{\hat{r}\hat{r}}(0) + \frac{\hat{r}^2}{2}\hat{\psi}_{\hat{r}\hat{r}\hat{r}}(0) + \frac{\hat{r}^3}{6}\hat{\psi}_{\hat{r}\hat{r}\hat{r}\hat{r}}(0) \right) + O(\hat{r}) = 0 \end{aligned}$$

For a regular solution where we do not want an analytical solution that blows up at $\hat{r} = 0$ we impose $O(r^{-n})$ terms for $n \in \mathbb{N}$ to be zero. Hence comparing $O(r^{-n})$ terms in the above equation

$$\begin{aligned} O(1) & \quad \hat{\psi}_{\hat{r}\hat{r}\hat{r}\hat{r}}(0) - 2\hat{\psi}_{\hat{r}\hat{r}\hat{r}\hat{r}}(0) + \frac{3}{2}\hat{\psi}_{\hat{r}\hat{r}\hat{r}\hat{r}}(0) - \frac{1}{2}\hat{\psi}_{\hat{r}\hat{r}\hat{r}\hat{r}}(0) = 0 \\ O(\hat{r}^{-1}) & \quad -2\hat{\psi}_{\hat{r}\hat{r}\hat{r}\hat{r}}(0) + 3\hat{\psi}_{\hat{r}\hat{r}\hat{r}\hat{r}}(0) - \frac{3}{2}\hat{\psi}_{\hat{r}\hat{r}\hat{r}\hat{r}}(0) = 0 \\ O(\hat{r}^{-2}) & \quad 3\hat{\psi}_{\hat{r}\hat{r}}(0) - 3\hat{\psi}_{\hat{r}\hat{r}}(0) = 0 \\ O(\hat{r}^{-3}) & \quad -3\hat{\psi}_{\hat{r}}(0) = 0 \end{aligned}$$

Therefore, for regularity we impose $\hat{\psi}_{\hat{r}}(0) = 0$ and $\hat{\psi}_{\hat{r}\hat{r}\hat{r}}(0) = 0$.

C.2 Reflux in the Pumping Range

Lemma C.1. *Reflux occurs only in the pumping range ([64]).*

Proof. The Instantaneous flow rate Q_{ψ_a} of all fluid between the centreline and a particular streamline ψ_a is determined to be

$$\frac{Q_{\psi_a}}{2\pi} = \int_0^{r(\psi_a, x, t)} ru(x, r, t) dr = \int_0^{\bar{r}_{\psi_a}} \bar{r}(\bar{u} + \sigma) d\bar{r} = \int_0^{\bar{r}_{\psi_a}} \psi_{\bar{r}} + \bar{r}\sigma d\bar{r} = \psi_a + \sigma \frac{\bar{r}^2}{2},$$

where we have transformed from the fixed frame to the wave frame coordinate system. The time mean volume flow rate of the material up to the streamline ψ_a is given by

$$\frac{\bar{Q}}{2\pi} = \frac{1}{T} \int_0^T \frac{Q_{\psi_a}}{2\pi} = \psi_a + \frac{\sigma}{2T} \int_0^T \bar{r}^2(\psi_a, \bar{x}, t) dt = \psi_a + \frac{\lambda}{2} \int_0^\lambda \bar{r}^2 d\bar{x},$$

where the integral is now with respect to distance \bar{x} by the substitution $\bar{x} = \sigma t$. Nondimensionalising we obtain:

$$\frac{\hat{Q}_{\psi_a}}{2\pi} = \hat{\psi}_a + \frac{1}{2} \int_0^1 \hat{r}^2(\psi_a, \hat{x}, \hat{t}) d\hat{x}.$$

Let us consider the small parameter δ defined to be the difference in a streamline in the flow $\hat{\psi}$ and the streamline at the boundary $\hat{\psi}_w$ such that

$$\delta = \hat{\psi} - \hat{\psi}_w.$$

Hence δ is a small parameter for streamlines close to the wall which will have equation close to that of the boundary and thus we define their shape to be governed by a perturbation expansion on δ such that

$$\hat{r}(\hat{x}; \delta) = \hat{f}(\hat{x}) + a_1(\hat{x})\delta + a_2(\hat{x})\delta^2 + \dots \quad (\text{C.2.1})$$

Substituting (C.2.1) into (3.4.4) and expanding the powers up to $O(\delta^2)$ yields:

$$\begin{aligned} \hat{\psi} &= A(\hat{f} + a_1\delta + a_2\delta^2)^4 + B(\hat{f} + a_1\delta + a_2\delta^2)^2, \\ \hat{\psi}_w + \delta &= A(\hat{f}^4 + 4\hat{f}^3 a_q \delta + 4\hat{f}^3 a_2 \delta^2 + 6\hat{f}^2 a_1^2 \delta^2) + B(\hat{f}^2 + a_1^2 \delta^2 + 2\hat{f} a_1 \delta + 2\hat{f} a_2 \delta^2). \end{aligned}$$

Therefore, comparing orders of magnitude of δ we obtain the following equations

$$\begin{aligned} O(1) \quad \hat{\psi}_w &= A\hat{f}^4 + B\hat{f}^2, \\ O(\delta) \quad 1 &= (4\hat{f}^3 A + 2B\hat{f})a_1, \\ O(\delta^2) \quad 0 &= (4\hat{f}^3 A + 2B\hat{f})a_2 + (6\hat{f}^2 A + B)a_1^2. \end{aligned}$$

The first condition satisfies the value of the streamfunction along the peristaltic bound-

ary. Looking at the $O(\delta)$ equation we derive a_1 by

$$a_1 = \frac{1}{\hat{f}(4\hat{f}^2 + 2B)} = \frac{1}{\hat{f}\hat{u}_w} = -\hat{f}^{-1}.$$

Similarly we determine a_2 using the no-slip condition on the boundary from (3.4.4):

$$a_2 = -\frac{(6\hat{f}^2 A + B)a_1^2}{4\hat{f}^3 A + 2B\hat{f}} = \frac{6\hat{f}^2 A + B}{\hat{f}^3} = \frac{4A}{\hat{f}} - \frac{1}{2\hat{f}^3}.$$

Hence, to evaluate the instantaneous mean flow rate integral we require \hat{r}^2 from the perturbation expansion

$$\begin{aligned} \hat{r}^2 &= \hat{f}^2 + 2\hat{f}a_1\delta + a_1^2\delta^2 + 2\hat{f}a_2\delta^2 \\ &= \hat{f}^2 - 2\delta + \frac{1}{\hat{f}^2}\delta^2 + 2\hat{f}\left(\frac{4A}{\hat{f}} - \frac{1}{2\hat{f}^3}\right)\delta^2 \\ &= \hat{f}^2 - 2\delta + 8A\delta^2. \end{aligned}$$

whereby the mean flow rate becomes

$$\begin{aligned} \frac{\hat{Q}}{2\pi} &= \hat{\psi} + \frac{1}{2} \left\{ \int_0^1 \hat{f}^2 d\hat{x} - 2\delta \int_0^1 1 d\hat{x} + \delta^2 \int_0^1 8A(\hat{x}) d\hat{x} \right\} \\ &= \hat{\psi} + \frac{1}{2} \left\{ \left(1 + \frac{1}{2}\alpha^2\right) - 2\delta + \frac{1}{2}\Delta\hat{p}_\lambda\delta^2 \right\} \\ &= \hat{\psi}_w + \frac{1}{2} \left(1 + \frac{1}{2}\alpha^2\right) + \frac{1}{4}\Delta\hat{p}_\lambda\delta^2. \end{aligned}$$

We scale with respect to the mean flow rate when there is a zero pressure drop so that:

$$\frac{\hat{Q}}{\hat{Q}_0} = 1 + \left(\frac{\Delta\hat{p}_\lambda}{\hat{\psi}_w + \frac{1}{2} \left(1 + \frac{1}{2}\alpha^2\right)} \right) \delta^2 + \dots$$

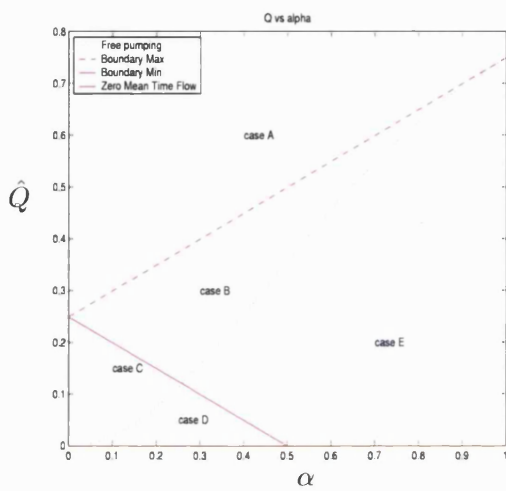
At the boundary $\delta = 0$ and the ratio of the flow rate clearly equals unity. As the instantaneous flow rate increases from the center towards the wall, if there is any net retrograde motion, the flow rate \hat{Q} will decrease. Hence, reflux exists if \hat{Q} at any point exceeds that at the wall \hat{Q}_w . So if the ratio of mean flow rate to that of the wall exceeds 1,

$$\frac{\hat{Q}}{\hat{Q}_0} > 1 \quad \Rightarrow \quad \frac{\Delta\hat{p}_\lambda}{\hat{Q}_0}\delta^2 > 0 \quad \Rightarrow \quad \Delta\hat{p}_\lambda > 0.$$

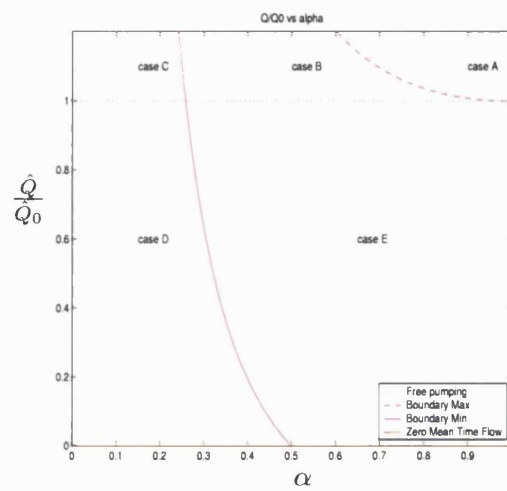
Hence a peristaltic wave acting as a pump in the absence of an assisted flow will cause a pressure rise and induce reflux. \square

C.3 Flow Rate/Pressure Drop versus Amplitude Ratio

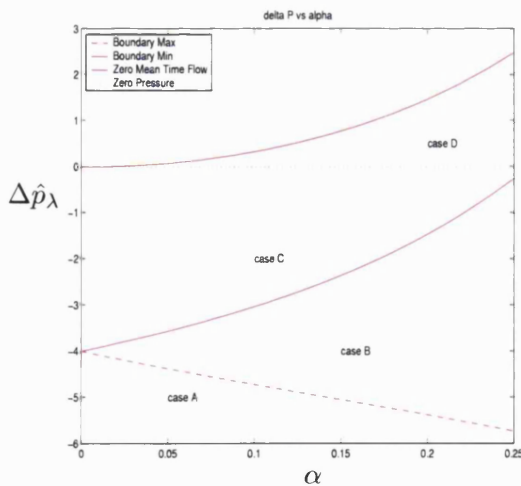
In the peristalsis chapter we have shown the existence of five different flow regions for a purely positive instantaneous mean volume flow rate, $\hat{Q} > 0$. The different flow regions were determined as a function of the flow rate, $\hat{\psi}_w$, and the amplitude of vibration, α . We show here the different regions as a function of α and (i) the instantaneous mean volume flow rate \hat{Q} , (ii) \hat{Q}/\hat{Q}_0 the instantaneous mean volume flow rate normalised with respect to a zero pressure gradient, (iii) the pressure gradient $\Delta\hat{p}_\lambda$ for small α and (iv) the pressure gradient $\Delta\hat{p}_\lambda$ for larger α .



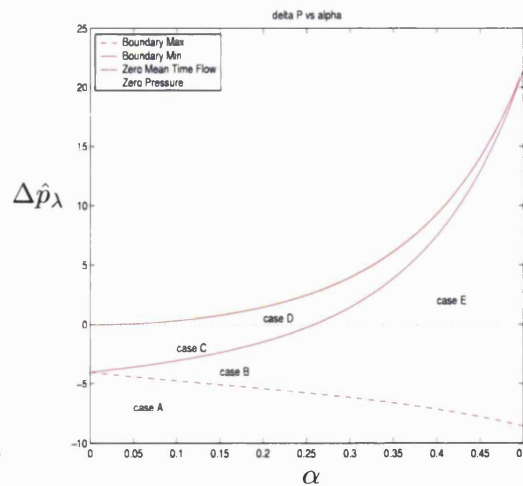
(a) Flow Types for \hat{Q}



(b) Flow Types for Normalized \hat{Q}/\hat{Q}_0 $\alpha = 1$



(c) Flow Types for Pressure Gradient up to $\alpha = 0.25$



(d) Flow Types for Pressure Gradient up to $\alpha = 0.5$

Figure C-1: Flow Types for various Amplitude Ratio

Appendix D

Dispersion Models

D.1 Poiseuille Dispersion Asymptotic Coefficients

We have shown that it is possible to apply asymptotic analysis to reduce the 2D Poiseuille dispersion model

$$c_t + \ell(1 - \tilde{r}^2)c_{\tilde{x}} = \frac{1}{P_{er}} \left(\ell^2 c_{\tilde{x}\tilde{x}} + c_{\tilde{r}\tilde{r}} + \frac{1}{\tilde{r}} c_{\tilde{r}} \right),$$

to a 1D dispersion equation

$$c_t + \left(\frac{\gamma^* \ell}{2} \right) c_{\tilde{x}} = \frac{\ell^2}{P_{er}} \left(1 + \frac{\Omega}{192} P_{er}^2 \right) c_{\tilde{x}\tilde{x}} = \frac{\alpha^* D_{ar}}{2P_{er}} c_{\tilde{x}\tilde{x}},$$

where the asymptotic factors γ^*, Ω were found to satisfy those derived in Brenner et al. [10]. However, the formula for α^* was stated incorrectly in all their work [10] [6] [73], but graphed correctly in [10]. We plot the absorption coefficient α^* as a function of the Damköhler number D_{ar} for both cases in figure (D-1), showing the enormous amount of absorption if the wrong coefficient is used.

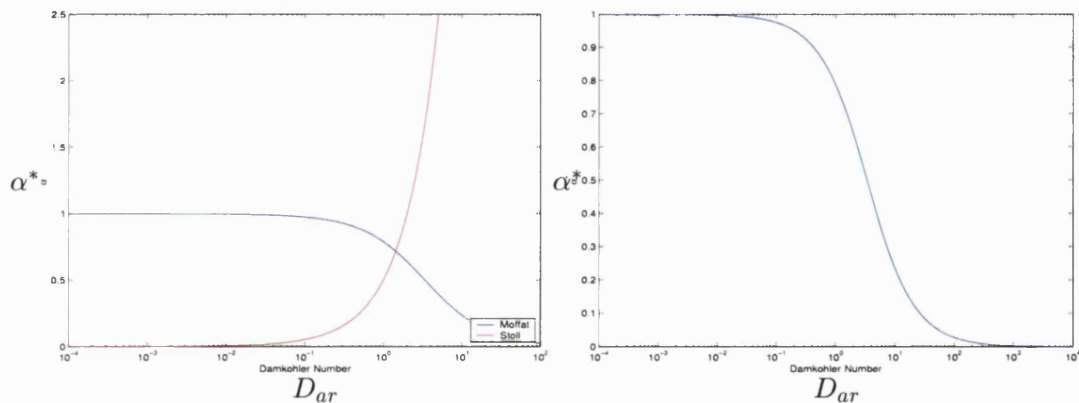


Figure D-1: A Comparison of Moffat's and Stoll's Absorption Coefficient α^*

We further plot the velocity and dispersion factor as a function of the Damköhler number, and also the root of the transcendental equation (4.4.12) and the fictitious initial condition (4.4.29).

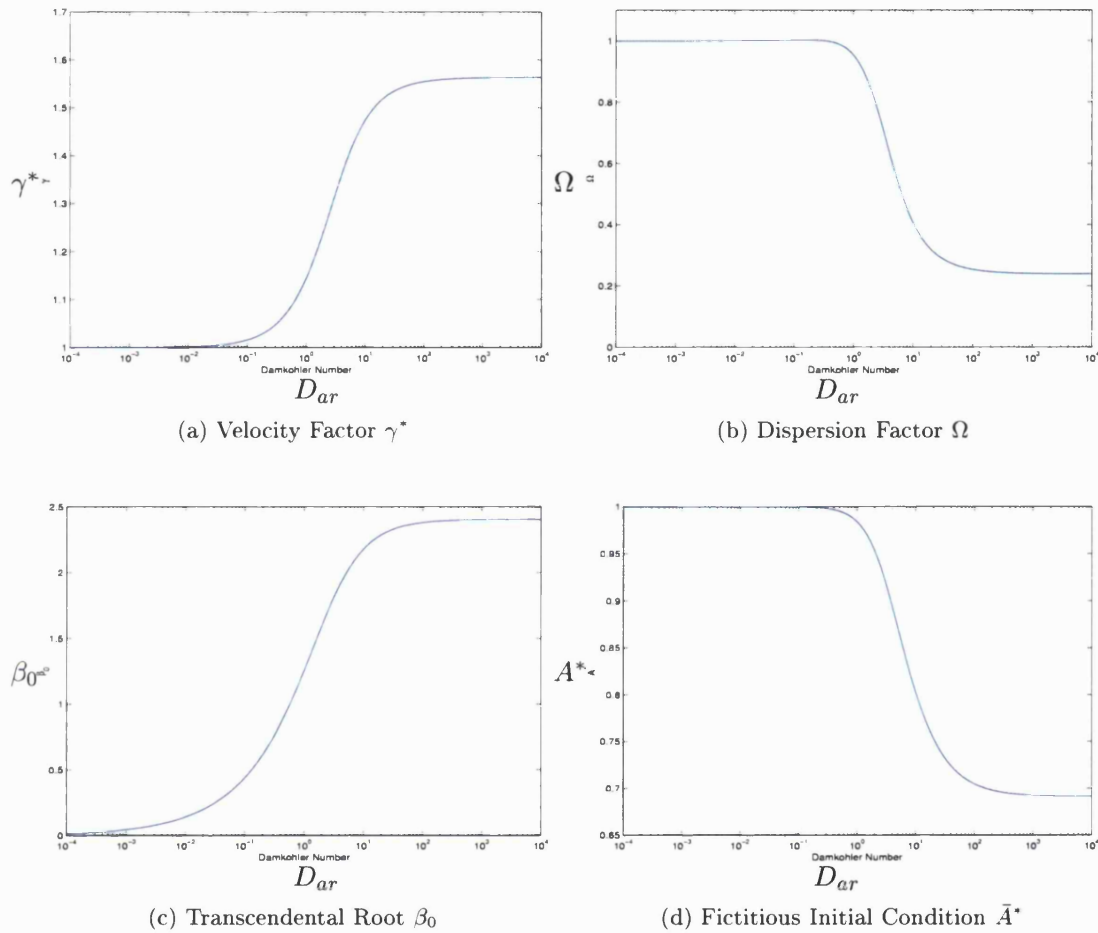


Figure D-2: Asymptotic Coefficients

Appendix E

Numerical Methods

In this section we numerically solve the peristaltic dispersion model in the absence of a semi-analytic solution. This was our first attempt at solving the dispersion model when we had not yet derived the peristaltic velocities. We must first solve the biharmonic equations in the wave frame numerically for the streamfunction $\hat{\psi}$ and we do so using the ‘fixed’ rectangular domain transformation. Hence, we derive the wave frame peristaltic velocities (\hat{u}, \hat{v}) and consequently the fixed frame velocities (\check{u}, \check{v}) . However, to implement the velocities in the peristaltic dispersion model,

$$c_{\check{t}} + \epsilon \check{u}(\check{x}, \check{r}, \epsilon \check{t}) c_{\check{x}} + \epsilon \check{v}(\check{x}, \check{r}, \epsilon \check{t}) c_{\check{r}} = \frac{1}{P_{eh}} \left(\epsilon^2 c_{\hat{x}\hat{x}} + c_{\hat{r}\hat{r}} + \frac{1}{\hat{r}} c_{\hat{r}} \right),$$

we must linearly interpolate the fixed frame velocities which we found on the ‘biharmonic mesh’ for the velocities on the ‘dispersion mesh’.

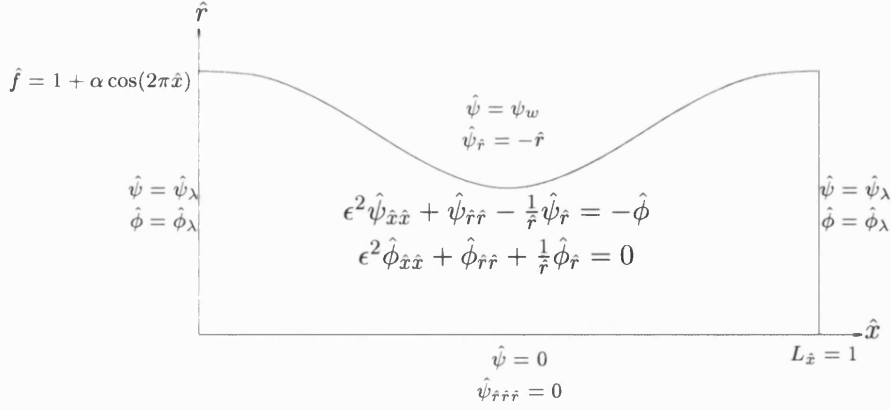
E.1 A Finite Difference Approach to Numerically Solving the Biharmonic Problem

Consider slow flow in an axisymmetric tube, where the wall undergoes standing wave oscillations. We consider the biharmonic problem for the fluid flow given in streamfunction-vorticity form by figure (E.1). We apply a rectangular coordinate transformation in the wave frame from given by

$$\hat{\chi} = \hat{x}, \quad \hat{\kappa} = \hat{r}/\hat{f}(\hat{x})$$

to obtain the biharmonic problem on a uniform domain $\Omega^c = [0, 1]^2$. We first transform the derivatives in the physical domain to those of the computational domain by

$$\begin{aligned} \hat{\psi}_{\hat{r}} &= \hat{\psi}_{\hat{\chi}} \hat{\chi}_{\hat{r}} + \hat{\psi}_{\hat{\kappa}} \hat{\kappa}_{\hat{r}} = \frac{1}{\hat{f}} \hat{\psi}_{\hat{\kappa}}, \\ \hat{\psi}_{\hat{x}} &= \hat{\psi}_{\hat{\chi}} \hat{\chi}_{\hat{x}} + \hat{\psi}_{\hat{\kappa}} \hat{\kappa}_{\hat{x}} = \hat{\psi}_{\hat{\chi}} - \left(\frac{\hat{\kappa} \hat{f}_{\hat{x}}}{\hat{f}} \right) \hat{\psi}_{\hat{\kappa}}. \end{aligned}$$



The second derivatives are consequently given by

$$\begin{aligned}\hat{\psi}_{\hat{r}\hat{r}} &= (\hat{\kappa}_{\hat{r}})^2 \hat{\psi}_{\hat{\kappa}\hat{\kappa}}, \\ \hat{\psi}_{\hat{x}\hat{x}} &= \hat{\psi}_{\hat{\chi}\hat{\chi}} + (\hat{\kappa}_{\hat{x}})^2 \hat{\psi}_{\hat{\kappa}\hat{\kappa}} + 2\hat{\kappa}_{\hat{x}} \hat{\psi}_{\hat{\chi}\hat{\kappa}} + (\hat{\kappa}_{\hat{x}\hat{x}} + \hat{\kappa}_{\hat{x}} \hat{\kappa}_{\hat{r}\hat{x}}) \hat{\psi}_{\hat{\kappa}}.\end{aligned}$$

and we obtain the biharmonic problem in the rectangular domain

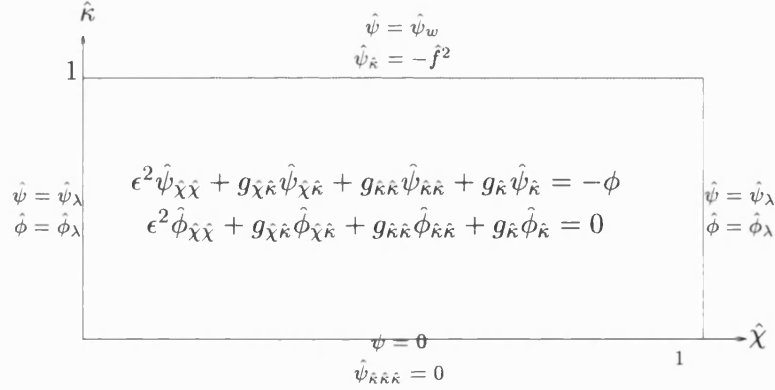


Figure E-1: The Peristaltic Biharmonic Problem in the Rectangular Computational Domain

The tensor functions g_i ($i = 1, \dots, 5$) are derived from the rectangular transformation of the cylindrical Laplacian

$$\begin{aligned}g_{\hat{\chi}\hat{\kappa}} &= \epsilon^2 \hat{\kappa}_{\hat{x}} = -\epsilon^2 \left(\frac{2\hat{\kappa}\hat{f}'}{\hat{f}} \right), \quad g_{\hat{\kappa}\hat{\kappa}} = \epsilon^2 (\hat{\kappa}_{\hat{x}})^2 + (\hat{\kappa}_{\hat{r}})^2 = \left(\frac{1 + \epsilon^2 \hat{\kappa}^2 (\hat{f}')^2}{\hat{f}^2} \right) \\ g_{\hat{\kappa}} &= \frac{\hat{\kappa}_{\hat{r}}}{\hat{f}\hat{\kappa}} + \epsilon^2 (\hat{\kappa}_{\hat{x}\hat{x}} + \hat{\kappa}_{\hat{x}} \hat{\kappa}_{\hat{r}\hat{x}}) = \left(\frac{\epsilon^2 \hat{\kappa} (2(\hat{f}')^2 - \hat{f}\hat{f}'') - \frac{1}{\hat{\kappa}}}{\hat{f}^2} \right).\end{aligned}$$

We discretise the rectangular domain into a standard uniform mesh with J, K points in

$(\hat{\chi}, \hat{\kappa})$ with spatial steps $\Delta\hat{\chi} = 1/J$ and $\Delta\hat{\kappa} = 1/K$. We denote $\hat{\psi}_{j,k}$ to be the numerical approximation of the streamfunction $\hat{\psi}_{j,k} \approx \hat{\psi}(\hat{\chi}_j, \hat{\kappa}_k)$ on the discretised grid for axial nodes $\hat{\chi}_j = j\Delta\hat{\chi}$ ($j = 0, 1, \dots, J$) and radial nodes $\hat{\kappa}_k = k\Delta\hat{\kappa}$ ($k = 0, 1, \dots, K$). The discretised biharmonic equations in finite difference are given by

$$\frac{\delta_{\hat{\chi}}^2 \hat{\psi}_{j,k}}{\Delta\hat{\chi}^2} + g_{\hat{\chi}\hat{\kappa}}(\hat{\chi}_j) \frac{\delta_{\hat{\chi}\hat{\kappa}} \hat{\psi}_{j,k}}{4\Delta\hat{\chi}\Delta\hat{\kappa}} + g_{\hat{\chi}\hat{\kappa}}(\hat{\chi}_j) \frac{\delta_{\hat{\kappa}} \hat{\psi}_{j,k}}{2\Delta\hat{\kappa}} + g_{\hat{\kappa}}(\hat{\chi}_j) \frac{\delta_{\hat{\kappa}}^2 \hat{\psi}_{j,k}}{\Delta\hat{\kappa}^2} + \hat{\phi}_{j,k} = 0, \quad (\text{E.1.1})$$

$$\frac{\delta_{\hat{\chi}}^2 \hat{\phi}_{j,k}}{\Delta\hat{\chi}^2} + g_{\hat{\chi}\hat{\kappa}}(\hat{\chi}_j) \frac{\delta_{\hat{\chi}\hat{\kappa}} \hat{\phi}_{j,k}}{4\Delta\hat{\chi}\Delta\hat{\kappa}} + g_{\hat{\chi}\hat{\kappa}}(\hat{\chi}_j) \frac{\delta_{\hat{\kappa}} \hat{\psi}_{j,k}}{2\Delta\hat{\kappa}} + g_{\hat{\kappa}}(\hat{\chi}_j) \frac{\delta_{\hat{\kappa}}^2 \hat{\phi}_{j,k}}{\Delta\hat{\kappa}^2} = 0, \quad (\text{E.1.2})$$

$\forall j = 1, \dots, J-1$ and $\forall k = 1, \dots, K-1$. As seen earlier we apply L'Hoptial's rule to approximate $\frac{1}{\hat{\kappa}} \psi_{\hat{\kappa}}$ as $\hat{\kappa} \rightarrow 0$. Hence, the tensor functions on the boundary simplify to

$$g_{\hat{\kappa}\hat{\kappa}}(\hat{\chi}_i, \hat{\kappa}_j) = \left(\frac{1 - \delta_{1j} + \epsilon^2 \hat{\kappa}^2 (\hat{f}')^2}{\hat{f}^2} \right), \quad g_{\hat{\kappa}}(\hat{\chi}_i, \hat{\kappa}_j) = \left(\frac{\epsilon^2 \hat{\kappa} (2(\hat{f}')^2 - \hat{f}\hat{f}'') - \frac{1 - \delta_{1j}}{\hat{\kappa}_j + \delta_{1j}}}{\hat{f}^2} \right),$$

for the Dirac delta function $\delta_{j,k}$, and consequently the Biharmonic equation (E.1.1) simplifies to just

$$\frac{\delta_{\hat{\chi}}^2 \hat{\psi}_{j,0}}{\Delta\hat{\chi}^2} + g_{\hat{\chi}\hat{\kappa}}(\hat{\chi}_j) \frac{\delta_{\hat{\kappa}} \hat{\psi}_{j,0}}{2\Delta\hat{\kappa}} + g_{\hat{\kappa}}(\hat{\chi}_j) \frac{\delta_{\hat{\kappa}}^2 \hat{\psi}_{j,0}}{\Delta\hat{\kappa}^2} + \hat{\phi}_{j,k} = 0, \quad \forall j = 1, \dots, J-1. \quad (\text{E.1.3})$$

The equation for $\hat{\phi}$ at $\hat{\kappa} = 0$ is not required as there are a sufficient number of boundary conditions to solve (E.1.1) and (E.1.2); four periodic conditions for $\hat{\phi}$ and $\hat{\psi}$ at $\hat{x} = 0, 1$ and two axisymmetry conditions at $\hat{\kappa} = 0$ and two fluid flow conditions at $\hat{\kappa} = 1$. At the peristaltic boundary we apply the no slip boundary condition $\psi_{\hat{\kappa}} = -\hat{f}$, which in finite difference terms is given by $\Delta_{\hat{\kappa}} \hat{\psi}_{j,K} = 2\Delta\hat{\kappa}\hat{f}$. Hence the cross derivative term simplifies to $\psi_{\hat{\chi}\hat{\kappa}} = -2\hat{f}\hat{f}_{\hat{\chi}}$, and the pde becomes

$$\frac{\delta_{\hat{\chi}}^2 \hat{\psi}_{j,K}}{\Delta\hat{\chi}^2} + g_{\hat{\kappa}\hat{\kappa}}(\hat{\chi}_j) \left(\frac{\Delta_{-\hat{\kappa}} \hat{\psi}_{j,K}}{\Delta\hat{\kappa}^2} \right) + \hat{\phi}_{ij} = 2\hat{f}\hat{f}_{\hat{\chi}} g_{\hat{\chi}\hat{\kappa}}(\hat{\chi}_j) + \frac{2\hat{f}^2}{\Delta\hat{\kappa}} g_{\hat{\kappa}\hat{\kappa}}(\hat{\chi}) + \hat{f}^2 g_{\hat{\kappa}}(\hat{\chi}), \quad \forall j = 1, \dots, J-1. \quad (\text{E.1.4})$$

At the axial boundaries, we merely apply ghost points for the periodic boundary condition $\hat{\psi}_{-1,k} = \hat{\psi}_{J-1,k}$, $\hat{\psi}_{J+1,k} = \hat{\psi}_{1,k}$ to ((E.1.1),(E.1.2)and(E.1.3)). Let $\hat{\psi}_{\mathbf{k}} = [\hat{\psi}_{1,k}, \hat{\psi}_{2,k}, \dots, \hat{\psi}_{N,k}]^T$ and $\hat{\psi} = [\hat{\psi}_1, \hat{\psi}_2, \dots, \hat{\psi}_K]$. Then $\exists A \in \mathbb{M}^{J \times JK}$ that represents the discretised form of $L_{-1}(\hat{\psi})$, with the incorporated relevant boundary conditions. Similarly for $\hat{\phi} = r\omega$, $\exists B \in \mathbb{M}^{J(K-2) \times JK}$ that represents $L_{-1}(\phi, \mu)$, $\forall j$ and for $k = 2, \dots, K-1$ which is smaller than A as we have stipulated $\hat{\phi}$ to have no boundary conditions. We then obtain the linear system for the Biharmonic problem.

$$\begin{bmatrix} D^{2J \times JK} & 0^{2J \times JK} \\ A & I^{JK \times JK} \\ 0^{J(K-2) \times JK} & B \end{bmatrix} \begin{bmatrix} \psi \\ \phi \end{bmatrix} = \begin{bmatrix} \partial \Omega^{2J \times JK} \\ \Omega^{JK \times JK} \\ 0^{J(K-2) \times JK} \end{bmatrix},$$

where (i) $\partial \Omega^{2K \times JK}$ is a matrix containing the Dirichlet boundary data for $\hat{\psi}$ at $\hat{\kappa} = 0$ and $\hat{\kappa} = 1$, (ii) D contains the location of the Dirichlet boundary and (iii) Ω contains the Neumann boundary data. This forms a linear system ($\hat{A}\mathbf{x} = \mathbf{b}$) which is easily solved for $\hat{\psi}$ and $\hat{\phi}$ in MATLAB.

E.1.1 Determining the Peristaltic Velocities from the Solution of the Biharmonic Problem in the Rectangular Domain

In order to solve the peristaltic dispersion model (6.3.2), we require fixed peristaltic velocities found from the wave frame velocities. Hence by definition of Stokes streamfunction, and by solving the biharmonic problem for $\hat{\psi}$ (E.1) we obtain axial and transverse velocities \hat{u} and \hat{v} in the wave frame. However, we must solve the peristaltic dispersion model and biharmonic equations on the rectangular computational domain Ω^c . Hence, Stokes velocities in the rectangular frame are found by the usual domain transformation. Applying appropriate symmetry and boundary conditions we obtain: We use standard centered difference on $\hat{\psi}_{\hat{\chi}}$ and $\hat{\psi}_{\hat{\kappa}}$ for $\hat{\psi}_{j,k}$ to find approximate

$$\begin{aligned} \text{Top } (\hat{\kappa}=1): \quad & \hat{u} = -1 \\ & \hat{v} = -\hat{f}' \\ \text{Bottom } (\hat{\kappa}=0): \quad & \hat{u} = \frac{1}{\hat{f}^2} \hat{\psi}_{\hat{\kappa}\hat{\kappa}} \\ & \hat{v} = 0 \\ \text{Left } (\hat{\chi}=0): \quad & \hat{u} = \frac{1}{\hat{f}^2} \frac{1}{\hat{\kappa}} \hat{\psi}_{\hat{\kappa}} \\ & \hat{v} = 0 \\ \text{Right } (\hat{\chi}=1): \quad & \hat{u} = \frac{1}{\hat{f}^2} \frac{1}{\hat{\kappa}} \hat{\psi}_{\hat{\kappa}} \\ & \hat{v} = 0 \\ \text{Internal:} \quad & \hat{u} = \frac{1}{\hat{f}^2} \frac{1}{\hat{\kappa}} \frac{\partial \hat{\psi}}{\partial \hat{\kappa}} \\ & \hat{v} = -\frac{1}{\hat{f}} \frac{1}{\hat{\kappa}} \left(\frac{\partial \hat{\psi}}{\partial \hat{\chi}} - \frac{\hat{\kappa} \hat{f}'}{\hat{f}} \frac{\partial \hat{\psi}}{\partial \hat{\kappa}} \right) \end{aligned}$$

Figure E-2: A Model to Display How to Determine Wave Frame Peristaltic Velocities from the Streamfunction Solution of the Biharmonic Problem

velocities $\hat{u}_{j,k}$ and $\hat{v}_{j,k}$. Hence, from the calculated steady wave frame velocities it is possible to solve for the fixed frame unsteady velocities in the rectangular frame by the transformation:

$$\begin{aligned} \tilde{u}(\chi, \kappa, \tilde{t}) &= \hat{u}(\hat{\chi}, \hat{\kappa}) + 1 = \hat{u}(\chi - \tilde{t}, \kappa) + 1, \\ \tilde{v}(\chi, \kappa) &= \hat{v}(\hat{\chi}, \hat{\kappa}) = \hat{v}(\chi - \tilde{t}, \kappa), \end{aligned}$$

Note that (χ, κ) is the dimensionless fixed frame rectangular coordinates and $(\hat{\chi}, \hat{\kappa})$ are the corresponding wave frame coordinates. Fixed frame velocities are periodic, $T = 1$, and so

$$\tilde{u}(\chi, \kappa, \tilde{t}) = \tilde{u}(\chi + n, \kappa, \tilde{t}) = \tilde{u}(\chi, \kappa, \tilde{t} - 1) \quad \text{for } n \in \mathbb{N}.$$

E.1.2 Determining the Pressure Gradients from the Tangential Vorticity Solution of the Biharmonic Problem in the Rectangular Frame

By Stokes slow flow equation $\nabla \times \omega = -\nabla p$ (3.2.3) we can determine the pressure gradients in the wave frame for unknown variable viscosity $\mu(\hat{r})$ by the relations:

$$\frac{\partial \hat{p}}{\partial \hat{x}} = -\frac{1}{\hat{r}} \frac{\partial \hat{\phi}}{\partial \hat{r}}, \quad \frac{\partial \hat{p}}{\partial \hat{r}} = \frac{\epsilon^2}{\hat{r}} \frac{\partial \hat{\phi}}{\partial \hat{x}}.$$

Hence, in rectangular coordinates the changes in pressure may be found with similar methods to the rectangular wave frame velocities see figure (E.1.2). At the centreline

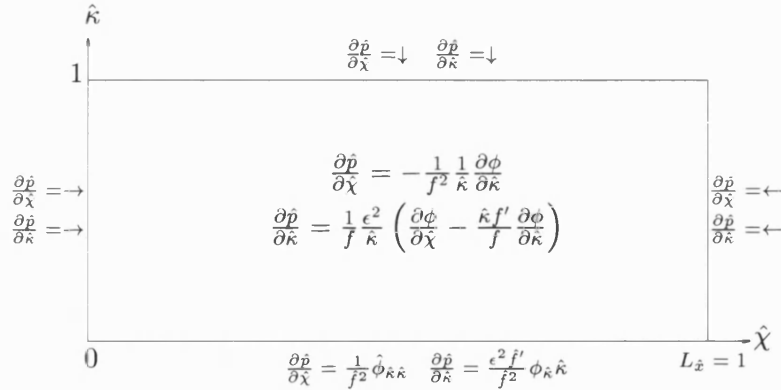


Figure E-3: A Model to Display How to Determine Pressure Gradients from the Tangential Vorticity Solution of the Biharmonic Problem

$\hat{\phi} = -\hat{r}\hat{\omega}$ and by symmetry $\hat{\phi}_{\hat{r}} = 0$. Hence $\hat{\phi}_{\hat{\kappa}} = 0$. Now $\hat{\phi}_{\hat{x}} = 0$ since $\hat{\phi}$ is zero, hence $\hat{\phi}_{\hat{\chi}} = \hat{\phi}_{\hat{x}}\hat{x}_{\hat{\chi}} + \hat{\phi}_{\hat{\kappa}}\hat{\kappa}_{\hat{\chi}} = 0$. The rectangular pressure gradients at the centreline are then found by L'Hopitals rule so that

$$\frac{\partial \hat{p}}{\partial \hat{\chi}} = \frac{\hat{\phi}_{\hat{\kappa}\hat{\kappa}}}{\hat{f}^2}, \quad \frac{\partial \hat{p}}{\partial \hat{\kappa}} = \frac{\epsilon^2 \hat{f}'}{\hat{f}^2} \hat{\phi}_{\hat{\kappa}\hat{\kappa}}.$$

E.1.3 Determining the Fixed Frame Velocities by Linearly Interpolating the Numerically Solved Wave Frame Velocities of the Biharmonic Problem

We have solved the biharmonic problem numerically and found the fixed frame axial and transverse velocities (see §E.1.1). It is only necessary to solve the biharmonic problem for one wavelength and then apply periodicity to find the velocities for $\tilde{x} > 1$. There are two ways to find the fixed frame velocities $\tilde{\mathbf{u}}$ from the wave frame velocities $\hat{\mathbf{u}}$.

In the first method we solve the biharmonic problem and the peristaltic dispersion model on the same size mesh. We prescribe the DAE solver to then solve for a uniform time step $\Delta\tilde{t}$; which we require to be an integral function of the spatial step so that at each time step \tilde{t}_n the velocities $\tilde{\mathbf{u}}_{j,k}$ can be found by rotating the wave frame velocities $\hat{\mathbf{u}}_{j,k}$. As the velocities are time dependent this would require a very small time step to reduce errors and would then require a large number of spatial steps since $\Delta\tilde{t} = \xi\Delta\hat{x}$ where ξ is the number of spatial steps a time step would jump (with $\xi = 1$ minimising the error).

This method imposes a uniform time step restriction. It requires the domain to be an integral number of wavelengths (or an integral number of wave frame mesh size $c\Delta\hat{x}$) and the biharmonic and dispersion model be solved on a very coarse mesh, which is quite costly. The peristaltic model forms a DAE system which is very stiff. Hence to solve accurately we need to allow the DAE solver to solve for time steps of its choosing which will generally be nonuniform. An alternative method is sought, and that is to linearly interpolate the velocities on the ‘biharmonic mesh’ for the velocities on the mesh used to solve the dispersion model.

We assume that the wave frame velocity profile has been solved, so $\hat{\mathbf{u}}$ is known for $\hat{x} \in [0, 1]$. Then every fixed frame velocity has a corresponding wave frame velocity

$$\tilde{u}(\chi, \kappa, \tilde{t}) = \hat{u}(\hat{\chi}, \hat{\kappa}) + 1, \quad \tilde{v}(\chi, \kappa, \tilde{t}) = \hat{v}(\hat{\chi}, \hat{\kappa}).$$

The radial component is unaffected when moving from the fixed frame to the wave frame. Therefore $\hat{\kappa} = \kappa$. However, the corresponding wave frame axial component, $\hat{\chi}$, is determined by $\hat{\chi} = \chi - \tilde{t} + n$, $n \in \mathbb{Z}$, where an arbitrary number of wavelengths is added or subtracted until $\hat{\chi} \in [0, 1]$. We discretise the wave frame into \hat{J}, \hat{K} points in $\hat{\chi}$ and $\hat{\kappa}$ respectively, and the fixed frame into J, K points for χ and κ so that

$$(\hat{\chi}_{\hat{j}}, \hat{\kappa}_{\hat{k}}) = ((\hat{j} - 1)\Delta\hat{\chi}, (\hat{k} - 1)\Delta\hat{\kappa}), \quad \hat{j} = 1, \dots, \hat{N}, \quad \hat{k} = 1, \dots, \hat{M},$$

$$\Delta\hat{\chi} = \frac{1}{\hat{N} - 1}, \quad \Delta\hat{\kappa} = \frac{1}{\hat{M} - 1},$$

$$(\chi_j, \kappa_k) = ((j-1)\Delta\chi, (k-1)\Delta\kappa) \quad j = 1, \dots, N, \quad k = 1, \dots, M,$$

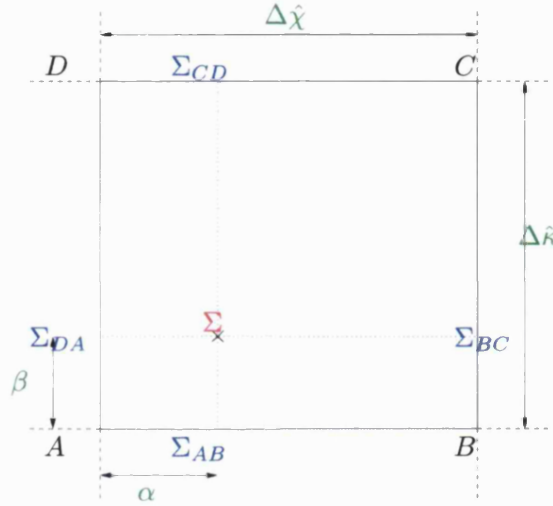
$$\Delta\chi = \frac{n}{N-1}, \quad \Delta\kappa = \frac{1}{M-1}.$$

In the discretised form, the velocity at a point, (χ_j, κ_k) , in the fixed frame is found by the velocity at a point $(\hat{\chi}_j, \hat{\kappa}_k)$, in the wave frame:

$$\tilde{u}(\chi_j, \kappa_k) = \hat{u}(\hat{\chi}_j, \hat{\kappa}_k) + 1 = \hat{u}(\chi_j - \tilde{t} + n, \kappa_k) + 1,$$

$$\tilde{v}(\chi_j, \kappa_k) = \hat{v}(\hat{\chi}_j, \hat{\kappa}_k) = \hat{v}(\hat{\chi}_j, \kappa_k),$$

which may not necessarily lie in the wave frame mesh, i.e. $(\hat{\chi}_j, \hat{\kappa}_k) \neq (\hat{\chi}_{\hat{j}}, \hat{\kappa}_{\hat{k}})$. The corresponding wave point $(\hat{\chi}_j, \hat{\kappa}_k) \equiv \Omega$ will lie in the wave frame surrounded by 4 grid points.



We define a further 4 points on the grid lines parallel to Σ :

$$A \equiv (\hat{\chi}_{\hat{j}-1}, \hat{\kappa}_{\hat{k}-1}), \quad B \equiv (\hat{\chi}_{\hat{j}}, \hat{\kappa}_{\hat{k}-1}), \quad C \equiv (\hat{\chi}_{\hat{j}}, \hat{\kappa}_{\hat{k}}), \quad D \equiv (\hat{\chi}_{\hat{j}-1}, \hat{\kappa}_{\hat{k}}),$$

$$\Sigma_{AB} \equiv (\hat{\chi}_{\hat{j}}, \hat{\kappa}_{\hat{k}-1}), \quad \Sigma_{BC} \equiv (\hat{\chi}_{\hat{j}}, \hat{\kappa}_{\hat{k}}), \quad \Sigma_{CD} \equiv (\hat{\chi}_{\hat{j}}, \hat{\kappa}_{\hat{k}}), \quad \Sigma_{DA} \equiv (\hat{\chi}_{\hat{j}-1}, \hat{\kappa}_{\hat{k}}).$$

The distances from A to Σ_{AB} and A to Σ_{DA} are defined by $\alpha = \hat{\chi}_j - \hat{\chi}_{\hat{j}-1}$ and $\beta = \hat{\kappa}_k - \hat{\kappa}_{\hat{k}-1}$ respectively. If the discretised meshes have the same radial grid spacing then $K = \hat{K}$. Hence, $\kappa_k = \hat{\kappa}_k = \hat{\kappa}_{\hat{k}}$ and the arbitrary point lies on a radial grid line. Then to find $\hat{\mathbf{u}}(\hat{\chi}_j, \hat{\kappa}_{\hat{k}})$ we need only linearly interpolate between $\hat{\mathbf{u}}(\hat{\chi}_{\hat{j}-1}, \hat{\kappa}_{\hat{k}})$ and $\hat{\mathbf{u}}(\hat{\chi}_{\hat{j}}, \hat{\kappa}_{\hat{k}})$.

Only when $J = \hat{J}$ and $\Delta t = \xi \Delta \hat{\chi} / \sigma$ would the arbitrary point lie on an axial grid line, $\hat{\chi}_j = \hat{\chi}_{\hat{j}}$, and we need only linearly interpolate in the radial direction to find $\hat{\mathbf{u}}(\hat{\chi}_{\hat{j}}, \hat{\kappa}_k)$. However, for non-superimposing meshes, it is necessary to linearly interpolate for $\hat{\mathbf{u}}(\hat{\chi}_j, \hat{\kappa}_k)$ in 2 Dimensions. The wave frame velocity at points on the

grid in (E.1.3) parallel to Σ are found by:

$$\begin{aligned}\hat{\mathbf{u}}_{\Sigma_{AB}} &= \hat{\mathbf{u}}_A + \alpha \mathbf{m}_{AB}, & \mathbf{m}_{AB} &= \frac{\hat{\mathbf{u}}_B - \hat{\mathbf{u}}_A}{\Delta \hat{\chi}}, \\ \hat{\mathbf{u}}_{\Sigma_{BC}} &= \hat{\mathbf{u}}_B + \beta \mathbf{m}_{BC}, & \mathbf{m}_{BC} &= \frac{\hat{\mathbf{u}}_C - \hat{\mathbf{u}}_B}{\Delta \hat{\kappa}}, \\ \hat{\mathbf{u}}_{\Sigma_{CD}} &= \hat{\mathbf{u}}_D + \alpha \mathbf{m}_{CD}, & \mathbf{m}_{CD} &= \frac{\hat{\mathbf{u}}_C - \hat{\mathbf{u}}_D}{\Delta \hat{\chi}}, \\ \hat{\mathbf{u}}_{\Sigma_{DA}} &= \hat{\mathbf{u}}_A + \beta \mathbf{m}_{DA}, & \mathbf{m}_{DA} &= \frac{\hat{\mathbf{u}}_D - \hat{\mathbf{u}}_A}{\Delta \hat{\kappa}}.\end{aligned}$$

Therefore, $\hat{\mathbf{u}}_{\Sigma}$ can be found by radially linearly interpolating between $\hat{\mathbf{u}}_{\Sigma_{AB}}$ and $\hat{\mathbf{u}}_{\Sigma_{CD}}$ or axially linearly interpolating between $\hat{\mathbf{u}}_{\Sigma_{DA}}$ and $\hat{\mathbf{u}}_{\Sigma_{BC}}$.

Proof. Define $\mathbf{V}_{\hat{\kappa}}$ to be the radial linear interpolant of $\hat{\mathbf{u}}_{\Sigma}$ between $\hat{\mathbf{u}}_{\Sigma_{AB}}$ and $\hat{\mathbf{u}}_{\Sigma_{CD}}$, and define \mathbf{V}_p to be the axial linear interpolant of $\hat{\mathbf{u}}_{\Sigma}$ between $\hat{\mathbf{u}}_{\Sigma_{DA}}$ and $\hat{\mathbf{u}}_{\Sigma_{BC}}$. Then:

$$\mathbf{V}_{\hat{\kappa}} = \hat{\mathbf{u}}_{\Sigma_{AB}} + \beta \mathbf{m}_{\hat{\kappa}}, \quad \mathbf{m}_{\hat{\kappa}} = \frac{\hat{\mathbf{u}}_{\Sigma_{CD}} - \hat{\mathbf{u}}_{\Sigma_{AB}}}{\Delta \hat{\kappa}}, \quad \mathbf{V}_{\hat{\chi}} = \hat{\mathbf{u}}_{\Sigma_{DA}} + \alpha \mathbf{m}_{\hat{\chi}}, \quad \mathbf{m}_{\hat{\chi}} = \frac{\hat{\mathbf{u}}_{\Sigma_{BC}} - \hat{\mathbf{u}}_{\Sigma_{DA}}}{\Delta \hat{\chi}}.$$

Expanding $\mathbf{V}_{\hat{\kappa}}$ into the original 4 surrounding grid points $\hat{\mathbf{u}}_A, \hat{\mathbf{u}}_B, \hat{\mathbf{u}}_C, \hat{\mathbf{u}}_D$ implies:

$$\begin{aligned}\mathbf{V}_{\hat{\kappa}} &= (\hat{\mathbf{u}}_A + \alpha \mathbf{m}_{AB}) + \beta \left(\frac{\hat{\mathbf{u}}_{\Sigma_{CD}} - \hat{\mathbf{u}}_{\Sigma_{AB}}}{\Delta \hat{\kappa}} \right) \\ &= \left(\hat{\mathbf{u}}_A + \alpha \left(\frac{\hat{\mathbf{u}}_B - \hat{\mathbf{u}}_A}{\Delta \hat{\chi}} \right) \right) + \beta \left(\frac{(\hat{\mathbf{u}}_D + \alpha \mathbf{m}_{DC}) - (\hat{\mathbf{u}}_A + \alpha \mathbf{m}_{AB})}{\Delta \hat{\kappa}} \right) \\ &= \hat{\mathbf{u}}_A + \alpha \left(\frac{\hat{\mathbf{u}}_B - \hat{\mathbf{u}}_A}{\Delta \hat{\chi}} \right) + \beta \left(\frac{\hat{\mathbf{u}}_D - \hat{\mathbf{u}}_A}{\Delta \hat{\kappa}} \right) + \alpha \beta \left(\frac{\mathbf{m}_{DC} - \mathbf{m}_{AB}}{\Delta \hat{\kappa}} \right) \\ &= \hat{\mathbf{u}}_A + \alpha \left(\frac{\hat{\mathbf{u}}_B - \hat{\mathbf{u}}_A}{\Delta \hat{\chi}} \right) + \beta \left(\frac{\hat{\mathbf{u}}_D - \hat{\mathbf{u}}_A}{\Delta \hat{\kappa}} \right) + \alpha \beta \left(\frac{\hat{\mathbf{u}}_C + \hat{\mathbf{u}}_A - \hat{\mathbf{u}}_B - \hat{\mathbf{u}}_D}{\Delta \hat{\chi} \Delta \hat{\kappa}} \right),\end{aligned}$$

Expanding $\mathbf{V}_{\hat{\chi}}$ into the original 4 surrounding grid points $\hat{\mathbf{u}}_A, \hat{\mathbf{u}}_B, \hat{\mathbf{u}}_C, \hat{\mathbf{u}}_D$ implies:

$$\begin{aligned}\mathbf{V}_{\hat{\chi}} &= (\hat{\mathbf{u}}_A + \beta \mathbf{m}_{DA}) + \alpha \left(\frac{\hat{\mathbf{u}}_{\Sigma_{BC}} - \hat{\mathbf{u}}_{\Sigma_{DA}}}{\Delta \hat{\chi}} \right) \\ &= \left(\hat{\mathbf{u}}_A + \beta \left(\frac{\hat{\mathbf{u}}_D - \hat{\mathbf{u}}_A}{\Delta \hat{\kappa}} \right) \right) + \alpha \left(\frac{(\hat{\mathbf{u}}_B + \beta \mathbf{m}_{BC}) - (\hat{\mathbf{u}}_A + \beta \mathbf{m}_{DA})}{\Delta \hat{\chi}} \right) \\ &= \hat{\mathbf{u}}_A + \beta \left(\frac{\hat{\mathbf{u}}_D - \hat{\mathbf{u}}_A}{\Delta \hat{\kappa}} \right) + \alpha \left(\frac{\hat{\mathbf{u}}_B - \hat{\mathbf{u}}_A}{\Delta \hat{\chi}} \right) + \alpha \beta \left(\frac{\mathbf{m}_{BC} - \mathbf{m}_{DA}}{\Delta \hat{\chi}} \right) \\ &= \hat{\mathbf{u}}_A + \alpha \left(\frac{\hat{\mathbf{u}}_B - \hat{\mathbf{u}}_A}{\Delta \hat{\chi}} \right) + \beta \left(\frac{\hat{\mathbf{u}}_D - \hat{\mathbf{u}}_A}{\Delta \hat{\kappa}} \right) + \alpha \beta \left(\frac{\hat{\mathbf{u}}_C + \hat{\mathbf{u}}_A - \hat{\mathbf{u}}_B - \hat{\mathbf{u}}_D}{\Delta \hat{\chi} \Delta \hat{\kappa}} \right).\end{aligned}$$

Therefore, $\hat{\mathbf{u}}_{\Sigma} = \mathbf{V}_{\hat{\chi}} = \mathbf{V}_{\hat{\kappa}}$, a 2D linear interpolant, made up of linear interpolations in the axial direction AB , radial direction AD and a cross product radial axial term. The equations hold when $(\hat{\chi}_j, \hat{\kappa}_k)$ lie on the wave frame grid lines. \square

E.2 How to Apply the Low Pass Filter to Remove Noise

To test our hypothesis that peristalsis contributes to the mean solute concentration profile in superimposed oscillations we remove the oscillatory terms using a Low Pass Filter a technique used in noise reduction. We apply in MATLAB the Fast Fourier Transform (FFT) at the end time $\check{t} = T$ to express the set of discretised mean solute values \bar{c}_j at nodes $\check{x}_j = j\Delta\check{x}$ as a combination of samples of periodic functions of different frequencies. The FFT maps from the set of N mean values to a set of N complex numbers, where the FFT constructs complex vector f_j ¹ defined by

$$f_j = \sum_{k=1}^N \bar{c}_j e^{-2\pi i(j-1)(k-1)/N}.$$

As \bar{c}_j is real then f_j is symmetric so that $f_j = \bar{f}_{N+2-j}$. The contribution of noise to a signal appears as terms in FFT centered on index $N/2$. Hence the effects of noise from peristaltic can be reduced by suppressing these values. So we multiply the FFT of the mean concentration by a symmetric vector which sets the central section of the FFT to zero:

$$\begin{cases} g_j = 1 & j \leq M, \\ g_j = 1 & j \geq N + 2 - M, \\ g_j = 0 & \text{otherwise,} \end{cases}$$

and obtain the vector $\mathbf{h} = \mathbf{g} \cdot \mathbf{f}$. We choose M small enough to remove noise but large enough to retain detail of \bar{c} . Consequently we obtain the cleaner mean solute concentration from taking the inverse Laplace transform of h .

¹This f is not the same as the prescribed boundary $f(x)$.

Bibliography

- [1] M. Abramowitz and I.A. Stegun. *Handbook of Mathematical Functions*. Dover, New York, 1964.
- [2] Agoram, B., Woltosz, W.S., Bolger, M.B. Predicting the Impact of Physiological and Biochemical Processes on Oral Drug Bioavailability. *Advanced Drug Delivery Reviews*, 50:S41–S67, 2001.
- [3] Amidon, G.L., Lennernas, H., Shah, V.P., Crison, J.R. A Theoretical Basis for a Biopharmaceutics Drug Classification: The Correlation of In-Vitro Drug Product Dissolution and In-Vivo Bioavailability. *Pharmaceutical Research*, 12:3:413–420, 1995.
- [4] Aris, R. Unsteady Convective Diffusion with Interphase Mass Transfer. *Proc Roy Soc Lond A Mat*, 333:115–132, 1973.
- [5] Barton, C., Raynor, S. Peristaltic Flow in Tubes. *Bulletin of Mathematical Biophysics*, 30:663–680, 1968.
- [6] Batycky, R.P., Edwards, D.A, Brenner, H. Thermal Taylor Dispersion Phenomena in Nonadiabatic Systems. *Chemical Engineering Communications*, 130:53–104, 1994.
- [7] Beckett, G., Mackenzie, J.A., Robertson, M.L. Adaptive mesh movement - the MMPDE approach and its applications. *Journal of Computational Physics*, 168:500–518, 2001.
- [8] Bhatt, B.S., Sacheti, N.C. Flow Past a Porous Spherical Shell using the Brinkman Model. *Journal of Physics D: Applied Physics*, 27:37–41, 1994.
- [9] Brasseur, J.G., Corrsin, S. The Influence of a Peripheral Layer of Different Viscosity on Peristaltic Pumping with Newtonian Fluids. *Journal of Fluid Mechanics*, 174:495–519, 1987.
- [10] D.A. Brenner H., Edwards. *Macrotransport Processes*. Butterworth-Heineman, MA, USA, 1993.

- [11] Budd, C.J., Koomullil, G.P., Stuart, A.M. On the Solution of Convection-Diffusion Boundary Value Problems using Equidistributed Grids. *SIAM Journal of Scientific Computing*, 120:2:591–618, 1998.
- [12] Burns, J.C., Parkes, T. Peristaltic Motion. *Journal of Fluid Mechanics*, 29:4:731–743, 1967.
- [13] Cao, W., Carretero-Gonzalez, R., Huang, W., Russell, R.D. Variational Mesh Adaptation Methods for Axisymmetrical Problems. *SIAM Journal of Numerical Analysis*, 41:1:235–257, 2003.
- [14] Cao, W., Huang, W., Russell, R.D. A Study of Monitor Functions for Two-Dimensional Adaptive Mesh Generation. *SIAM Journal of Scientific Computing*, 20:6:1978–1994, 1999.
- [15] Cao, W., Huang, W., Russell, R.D. A Moving Mesh Method Based on the Geometric Conservation Law. *SIAM Journal of Scientific Computing*, 24:1:118–142, 2002.
- [16] Cao, W., Huang, W., Russell, R.D. Approaches for Generating Moving Adaptive Meshes: Location versus Velocity. *Applied Numerical Mathematics*, 47:121–138, 2003.
- [17] Carlsson, F., Sen, M., Löfdahl, L. Analytical Studies of Flow Effects due to Vibrating Walls. *Journal of Fluid Mechanics*, Submitted 2002.
- [18] Cenicerros, H.D., Hou, T.Y. An Efficient Dynamically Adaptive Mesh for Potentially Singular Solutions. *Journal of Computational Physics*, 172:609–639, 2001.
- [19] Christensen, J., Glover, J.R., Macagno, E.O., Singerman, R.B., Weisbrodt, N.W. Statistics of Contractions at a point in the Human Duodenum. *American Journal of Physiology*, 221:1818–1823, 1971.
- [20] El Hakeem, A., El Naby, A.E., El Misery, A.E.M., El Shamy, I.I. Hydromagnetic Flow of Fluid with Variable Viscosity in a Uniform Tube with Peristalsis. *Journal of Physics A: Mathematical and General*, 36:8535–8547, 2003.
- [21] El Misery, A.M., Hakeem, A.E., Naby, A.E., El Nagar, A.H. Effects of a Fluid with Variable Viscosity and an Endoscope on Peristaltic Motion. *Journal of the Physical Society of Japan*, 72:1:89–93, 2003.
- [22] Georgiou, G.C., Crochet, M.J. Time-Dependent Compressible Extrudate-Swell Problem with Slip at the Wall. *Journal of Rheology*, 38:6:1745–1755, 1994.
- [23] Grass, G.M. Simulation Models to Predict Oral Drug Absorption from In Vitro Data. *Advanced Drug Delivery Reviews*, 23:199–219, 1997.

- [24] Hahn, S., Je, J., Choi, H. Direct Numerical Simulation of Turbulent Channel flow with Permeable Walls. *Journal of Fluid Mechanics*, 450:259–285, 2002.
- [25] Haji-Sheikh, A., Vafai, K. Analysis of Flow and Heat Transfer in Porous Media imbedded inside Various Shaped Ducts. *International Journal of Heat and Mass Transfer*, 47:1889–1905, 2004.
- [26] Hardy, G. Nutraceuticals and Functional Foods: Introduction and Meaning . *Nutrition*, 16:688–689, 2000.
- [27] Higgs, S.J. An Investigation into the Flow Behaviour of Complex Non-Newtonian Foodstuffs. *Journal of Physics D: Applied Physics*, 7:1184–1191, 1974.
- [28] Ho, N.F.H., Park, J.Y., Ni, P.F., Hiyuchi, W, I. Advanced Quantitative and Mechanistic Approaches in Interfacing Gastrointestinal Drug Absorption Studies in Animals and Humans. *American Pharmaceutical Association*, pages 27–106, 1983.
- [29] Huang, W. Variational Mesh Adaptation: Isotropy and Equidistribution. *Journal of Computational Physics*, 174:903–924, 2001.
- [30] Huang, W., Ren, Y., Russell, R.D. Moving Mesh Partial Differential Equations (MMPDEs) Base on the Equidistribution Principle. *SIAM Journal on Numerical Analysis*, 31:3:709–730, 1994.
- [31] Huang, W., Russell, R.D. Analysis of Moving Mesh Partial Differential Equations with Spatial Smoothing. *SIAM Journal of Scientific Computing*, 34:3:1106–1126, 1997.
- [32] Huang, W., Russell, R.D. Moving Mesh Strategy based on a Gradient Flow Equation for Two-Dimensional Problems. *SIAM Journal of Scientific Computing*, 20:3:998–1015, 1999.
- [33] Huang, W., Russell, R.D. Adaptive mesh movement - the MMPDE approach and its applications. *Journal of Computational and Applied Mathematics*, 128:383–398, 2001.
- [34] Huang, W., Sun, W. Variational Mesh Adaptation II: Error Estimates and Monitor Functions. *Journal of Computational PHysics*, 184:619–648, 2003.
- [35] Huang, W., Zheng, L., Zhan, X.. Moving Mesh Methods Based on Moving Mesh Partial Differential Equations. *Journal of Computational Physics*, 113:2:279–290, 1994.

- [36] Huang, W., Zheng, L., Zhan, X.. Adaptive Moving Mesh Methods for Simulating One Dimensional Groundwater Problems with Sharp Moving Fronts. *International Journal for Numerical Methods in Engineering*, 54:11:1579–1603, 2002.
- [37] Hwu, T., Sobey, I.J., Bellhouse, B.J. Observation of Concentration Dispersion in Unsteady Deflected Flows . *Chemical Engineering Science*, 51:3373–3390, 1996.
- [38] Hwu, T., Sobey, I.J., Bellhouse, B.J. Simulation of Concentration Dispersion in Unsteady Deflected Flows. *Chemical Engineering Science*, 52:3233–3242, 1997.
- [39] Jaeger, W., Mikelic, A. On the Interface Boundary Condition of Beavers, Joseph and Saffman. *SIAM Journal of Applied Mathematics*, 60:4:1111–1127, 2000.
- [40] Jaeger, W., Mikelic, A., Neuss, N. Asymptotic Analysis of the Laminar Viscous Flow over a Porous Bed. *SIAM Journal of Scientific Computing*, 22:6:2006–2028, 2001.
- [41] Jaffrin, M.Y., Shapiro, A.H. Peristaltic Pumping. *Annual Review of Fluid Mechanics*, 37:4:13–35, 1971.
- [42] James, D.F., Davis, A.M.J. Flow at the Interface of a Model Fibrous Porous Medium. *Journal of Fluid Mechanics*, 426:47–72, 2001.
- [43] Jensen, O.E., Grotber, J.B. The Spreading of Heat or Soluble Surfactant along a Thin Liquid Film. *Physical Fluids A*, 5:58–68, 1993.
- [44] Jeong, J. Slip Boundary Condition on an Idealized Porous Wall. *Physics of Fluids*, 13:7:1884–1890, 2001.
- [45] Layton, W.J., Schieweck, F., Yotov, I. Coupling Fluid Flow with Porous Media Flow. *SIAM Journal of Numerical Analysis*, 40:2195–2218, 2003.
- [46] R.J. LeVeque. *Numerical Methods for Conservation Laws*. Birkhauser Verlag, Dover, 1992.
- [47] Lew, H.S., Fung, Y.C., Lowenstein, C.B. Peristaltic Carrying and Mixing of Chyme in the Small Intestine (An Analysis of A Mathematical Model of Peristalsis Of the Small Intestine. *Journal of Biomechanics*, 4:297–315, 1971.
- [48] Li, M., Brasseur, J.G. Non-steady Peristaltic Transport in finite-length tubes. *Journal of Fluid Mechanics*, 248:129–151, 1993.
- [49] Lin, J., Hwang, C. Static and Dynamic Characteristics of Long Porous Journal Bearings: use of the Brinkman-extended Darcy Model. *Journal of Physics D: Applied Physics*, 27:634–643, 1994.

- [50] Lin, J., Lu, R., Yang, C. Derivation of Porous Squeeze-fil Reynolds equation using the Brinkman Model and its Application. *Journal of Physics D: Applied Physics*, 34:3217–3223, 2001.
- [51] Looker, J.R., Carnie, S.L. The Hydrodynamics of an Oscillating Porous Sphere. *Physics of Fluids*, 16:1:62–72, 2004.
- [52] Lungu, E.M., Moffatt, H.K. The Effect of Wall Conductance on Heat Diffusion in Duct Flow. *Journal of Engineering Mathematics*, 16:121–136, 1982.
- [53] Macagno, E.O., Christensen, J. Fluid Mechanics of the Duodenum. *Annual Review of Fluid Mechanics*, 12:139–158, 1980.
- [54] Mackenzie, J.A. The Efficient Generation of Simple Two-Dimensional Adaptive Grids. *SIAM Journal of Scientific Computing*, 19:4:1340–1365, 1998.
- [55] Mackenzie, J.A., Robertson, M.L. The Numerical Solution of One-Dimensional Phase Change Problems Using an Adaptive Moving Mesh Method. *Journal of Computational Physics*, 161:537–557, 2000.
- [56] Mikleic, A, Paoli, L. Homogenisation of the Inviscid Incompressible Fluid Flow through a 2D Porous Medium. *Proceedings of the American Mathematical Society*, 127:7:2019–2028, 1999.
- [57] J.D. Moffatt. *Absorbing the Nutrients from the Small Intestine*. <http://www.hillstrath.on.ca/moffatt/bio3a/digestive/intestin.htm>, 1997.
- [58] K.W. Morton. *Numerical Solution of Partial Differential Equations*. Cambridge University Press, Cambridge, 1994.
- [59] K.W. Morton. *Numerical Solution of Convection-Diffusion Problems*. Chapman & Hall, London, 1996.
- [60] Navier, C.L.M.H. Sur le Lois du Mouvement des Fluides. *Memoires de l'Academie Royale des Sciences de l'Institut de France*, 1:414–416, 1823.
- [61] J.M. Ottino. *The Kinematics of mixing: Stretching, Chaos, and Transport*. Cambridge University Press, Cambridge, 1989.
- [62] G.A. Piersol. *Piersol's Human Anatomy 9th Edition*. J.B. Lippincott Co., Philadelphia, 1930.
- [63] Rao, A.R., Usha, S. Peristaltic Transport of Two Immiscible Viscous Fluids in a Circular Tube. *Journal of Fluid Mechanics*, 298:271–285, 1995.

- [64] Shapiro, A.H., Jaffrin, M.Y., Weinberg, S.L. Peristaltic Pumping with Long Wavelengths at Low Reynolds Number. *Journal of Fluid Mechanics*, 37:4:799–825, 1969.
- [65] F.S. Sherman. *Viscous Flow*. McGraw-Hill Education, UK, 1990.
- [66] Shukla, J.B., Parihar, R.S., Rao, B.R.P., Gupta, S.P. Effects of Peripheral-Layer Viscosity on Peristaltic Transport of a Bio-Fluid. *Journal of Fluid Mechanics*, 97:2:225–237, 1980.
- [67] Singerman, R.B.J., Macagno, E.O., Glover, J.R., Christensen, J. Stochastic Model of Contractions at a Point in the Duodenum. *American Journal of Physiology*, 229:3:612–617, 1975.
- [68] Sinko, P.J., Leesman, G.D., Amidon, G.L. Predicting Fraction Dose Absorbed in Humans Using a Macroscopic Mass Balance Approach. *Pharmaceutical Research*, 8:8:979–988, 1991.
- [69] Sobey, I.J. Dispersion Caused By Separation During Oscillatory Flow Through a Furrowed Channel. *Chemical Engineering Science*, 40:2129–2134, 1985.
- [70] Srivastava, L.M., Srivastava, V.P. Peristaltic Transport of a Non-Newtonian Fluid: Applications to the Vas Deferens and Small Intestine. *Annals of Biomedical Engineering*, 13:137–153, 1985.
- [71] Srivastava, L.M., Srivastava, V.P., Sinha, S.N. Peristaltic Transport of a Physiological Fluid part 1: Flow in Non-Uniform Geometry. *Biorheology*, 20:153–166, 1983.
- [72] Stockie, J.M., Mackenzie, J.A., Russell, R.D. A Moving Mesh Method for One-Dimensional Hyperbolic Conservation Laws. *SIAM Journal of Scientific Computing*, 22:5:1791–1813, 2001.
- [73] Stoll, B.R., Batycky, R.P., Leipold, H.R., Milstein, S., Edwards, D.A. A Theory of Molecular Absorption from the Small Intestine. *Chemical Engineering Science*, 55:473–489, 2000.
- [74] Taylor, G. Dispersion of Soluble Matter in Solvent Flowing Slowly through a Tube. *Proc Roy Soc Lond A Mat*, 219:186–203, 1953.
- [75] A.J. Vander. *Human Physiology: The Mechanism of Body Function*. McGraw Hill Publishing Co., New Delhi, 1975.
- [76] Watanabe, K., Udagawa, Y., Udagawa, H. Drag Reduction of Newtonian Fluid in a Circular Pipe with a Highly Water-Repellent Wall. *Journal of Fluid Mechanics*, 381:225–238, 1999.

-
- [77] Yu, L.X., Amidon, G.L. Saturable small intestinal drug absorption in humans: modelling and interpretaion of cefatrizine data. *European Journal of Pharmaceutics and Biopharmaceutics*, 45:199–203, 1998.